Università degli Studi di Cagliari

DOTTORATO DI RICERCA
In Scienze e Tecnologie Chimiche

Ciclo XXX

TITOLO TESI

Functional ordered mesoporous silica in nanomedicine: target and drug delivery systems.

Settore scientifico disciplinari di afferenza

CHIM/02

Presentata da:	Valentina Nairi
Coordinatore Dottorato	Prof. Stefano Enzo
Tutor	Prof. Andrea Salis

Esame finale anno accademico 2016 – 2017
Tesi discussa nella sessione d'esame di marzo 2018

Università degli Studi di Cagliari

DOTTORATO DI RICERCA
In Scienze e Tecnologie Chimiche

Ciclo XXX

TITOLO TESI

Functional ordered mesoporous silica in nanomedicine: target and drug delivery systems.

Settore scientifico disciplinari di afferenza

CHIM/02

Presentata da:	Valentina Nairi
Coordinatore Dottorato	Prof. Stefano Enzo
Tutor	Prof. Andrea Salis

Esame finale anno accademico 2016 – 2017
Tesi discussa nella sessione d'esame di marzo 2018

To my family

Acknowledgements

Thanks are due to Ministero dell'Istruzione, dell'Università e della Ricerca (MIUR) that financed my PhD course.

A sincere thanks goes to my supervisors Prof. Andrea Salis and Prof. Maura Monduzzi for their valuable advice and encouragement during these three years.

A special acknowledgement Dr. Marco Piludu, from the Department of Biomedical Sciences of University of Cagliari, for his precious and invaluable assistance for the realization of this thesis project and for TEM measurements.

I also would like to thanks Prof. Maria Francesca Casula for TEM and TGA measurements, Prof. Valeria Sogos, Dr. Maura Fanti, Dr. Marinella Nieddu, and Dr. Cristian Antonio Caria for cells internalization experiments and optical microscopy and flow cytometry measurements.

A particular thanks is dedicated to Prof. Maria Vallet-Regì from Universidad Complutense de Madrid, that allowed me to carry out part of my PhD work in her research group. Furthermore, I want to thanks Dr. Alejandro Baeza to include me into his project and Dr. Gonzalo Villaverde for his teaching, friendship, encouragement and advice both at academic and personal level.

A special acknowledgement is dedicated to Federica, my colleague, for all the moments shared in these three years, and to Dr. Luca Medda and Dr. Francesca Cugia for the precious advices. I also want to thanks all the students that have

worked with me Federico, Sara, Silvia, Eloisa, and Laura who contributed to the realization of this work.

Thanks to Arianna, Cristina, Nicola, Giorgia, Stefania, Miguel, Natividad, Patricia, Juan Luis for their support and friendship shown in one of the most important and difficult periods of my life.

Finally, I want to thank my family, for supporting me and for always believing in me.

List of publications

I. **Adsorption and release of ampicillin antibiotic from ordered mesoporous silica.** V. Nairi, L. Medda, M. Monduzzi and A. Salis *J. Colloid Interface Sci.*, (2017) 497, 217-225.
DOI: 10.1016/j.jcis.2017.03.021

II. **Double sequential encrypted targeting sequence: A new concept for bone cancer treatment.** G. Villaverde, V. Nairi, A. Baeza and M. Vallet-Regì *Chem.–Eur. J.*, (2017) 23, 7174-7179.
DOI: 10.1002/chem.201605947

III. **Mesoporous silica nanoparticles functionalized with hyaluronic acid and chitosan biopolymers. Effect of functionalization on cell internalization.** A. Salis, M. Fanti, L. Medda, V. Nairi, F. Cugia, M. Piludu, V. Sogos and M. Monduzzi *ACS Biomater. Sci. Eng.*, (2016) 2, 741-751. DOI: 10.1021/acsbiomaterials.5b00502

IV. **Interaction between bovine serum albumin and mesoporous silica nanoparticles functionalized with biopolymers.** V. Nairi, S. Medda, M. Piludu, M. F. Casula, M. Vallet-Regì, M. Monduzzi and A. Salis *Chem. Eng. J.* (2018) *In press.* DOI: 10.1016/j.cej.2018.01.011.

V. **Mesoporous silica nanoparticles functionalized with hyaluronic acid. Effect of the biopolymer chain length on cell internalization.** V. Nairi, S. Magnolia, M. Piludu, M. Nieddu, C. A. Caria, V. Sogos, M. Vallet-Regì, M. Monduzzi and A. Salis *Colloids Surf. B* (2018) *In press.*
DOI: 10.1016/j.colsurfb.2018.02.019.

Abstarct

Ordered mesoporous materials (OMMs) are characterized by high surface area (up to 1000 m^2/g), high pore volume (1-3 cm^3/g) and narrow pore size (2-30 nm) distribution. These features make OMMs very interesting matrices for applications in several fields. Recently, mesoporous silica nanoparticles (MSNs), a subclass of OMMs, have had great development as nanocarriers for drug delivery, particularly for cancer treatment. Present chemotherapeutic drugs are highly toxic and, besides to kill cancer cells, they can also damage healthy ones. For these reasons, in the last years, researchers focused on the fabrication of smart delivery systems to control the release of the drug only in the diseased tissue.

This thesis focused on different aspects of the use of OMMs, particularly MSNs, as drug delivery systems. Firstly, how different features of OMMs (surface area, pore size and surface charge) can affect the adsorption and release of drugs was investigated. Ampicillin, a penicillin-like β-lactam antibiotic was firstly loaded on MCM-41, SBA-15, and amino-functionalized SBA-15, then its release in simulated physiological conditions was studied (**Paper I**). Common target systems have the disadvantage that the targeting molecule can be recognized by several receptors. A possible strategy to solve this issue is that the targeting molecule is hidden by preparing a double sequential targeting system. To this purpose biphosphonate was used as a tissue target to recognize a diseased bone, and an encrypted cellular target, Arg-Gly-Asp (RGD) was used to improve the internalization in human osteosarcoma cells (**Paper II**). The effect of surface charge on the internalization of MCM-41-type MSNs, functionalized with chitosan (CHIT) and hyaluronic acid (HA) biopolymers, on 3T3 mouse fibroblast

cells was then investigated (**Paper III**). The opposite surface charge of the biopolymer-functionalized MSNs (negative for MSN-HA and positive for MSN-CHIT) give a different interaction with BSA, used as a model protein to investigate the formation of the protein corona (**Paper IV**). Finally, MSNs were functionalized with HA samples having three different molecular weights (HA_S, HA_M, and HA_L). The effect of HA molecular weight on the internalization of HA-MSNs particles on HeLa cells was evaluated (**Paper V**).

Summary

ACKNOWLEDGEMENTS .... **III**

LIST OF PUBLICATIONS .... **V**

ABSTARCT .... **VI**

1 NANOMEDICINE **1**

1.1 CRITICISM TO CURRENT CANCER THERAPIES 2
1.2 NANOCARRIERS FOR CANCER TREATMENT 3
1.2.1 Polymeric nanoparticles 4
1.2.2 Liposomes 5
1.2.3 Cubosomes 5
1.2.4 Dendrimers 6
1.2.5 Gold nanoparticles (GNPs) 6
1.2.6 Quantum dots (QDs) 7
1.2.7 Ordered mesoporous materials and mesoporous silica nanoparticles 7

2 ORDERED MESOPOROUS MATERIALS **8**

2.1 SYNTHESIS OF OMMS 11
2.2 OMMS FUNCTIONALIZATION 13
2.3 APPLICATIONS 15
2.4 USE OF OMMS IN NANOMEDICINE 17
2.4.1 Tissue engineering 17
2.4.2 Drug delivery 19

3 MSNS IN NANOMEDICINE **21**

3.1 COMPOSITION AND PH OF TUMOR MICROENVIRONMENT 21
3.2 TARGET SYSTEMS 23
3.2.1 Passive targeting 23
3.2.2 Active targeting 25
3.3 STIMULI-RESPONSIVE SYSTEMS 26
3.3.1 Internal stimuli 27
3.3.2 External stimuli 31

4 MSNS IN PHYSIOLOGICAL MEDIA: ADSORPTION OF PROTEINS, CELLULAR UPTAKE AND GRAFTING OF BIOMOLECULES **34**

4.1 PROTEIN CORONA 34
4.2 CELLULAR UPTAKE 35
4.3 TARGETING MOLECULES AND BIOPOLYMERS 38
4.3.1 Chitosan 38
4.3.2 Hyaluronic acid 41
4.3.3 Arg-Gly-Asp (RGD) sequence 44

5 EXPERIMENTAL TECHNIQUES **46**

5.1 N_2 ADSORPTION/DESORPTION ISOTHERMS 46
5.2 SMALL-ANGLE X-RAYS SCATTERING (SAXS) 49
5.3 DYNAMIC LIGHT SCATTERING (DLS) 52
5.4 ELECTROPHORETIC LIGHT SCATTERING (ELS) 53
5.5 TRANSMISSION ELECTRON MICROSCOPY (TEM) 55

6 RESULTS **59**

6.1 STUDY OF ADSORPTION AND RELEASE OF AMPICILLIN FROM OMMS (PAPER I) 60
6.2 SYNTHESIS OF A DOUBLE SEQUENTIAL TARGETING SYSTEM (PAPER II) 62
6.3 CELLULAR UPTAKE IN 3T3 CELLS OF MSNS FUNCTIONALIZED WITH CHIT AND HA (PAPER III) 64
6.4 MSNS FUNCTIONALIZED WITH CHIT AND HA AND THEIR INTERACTION WITH BOVINE SERUM ALBUMIN (BSA) (PAPER IV) 66
6.5 STUDY OF THE EFFECT OF THE HA CHAIN LENGTH ON INTERNALIZATION OF MSN-HA IN HELA CELLS (PAPER V) 67

7 CONCLUSIONS **71**

8 REFERENCES **75**

APPENDIX **118**

PAPER I **119**

PAPER II **120**

PAPER III **121**

PAPER IV **122**

PAPER V **123**

1 Nanomedicine

Cancer disease kills every year millions of people. In order to reduce mortality due to this disease researchers have focused their attention on new treatments and techniques of prevention and diagnosis [1]. Nanomedicine is a branch of medicine that exploits the new advances in the field of nanotechnology. The term *Nanotechnology* was coined during the National Nanotechnology Initiative in 2000 to define the study of nanomaterials, that is, materials with dimensions between 0.1 and 100 nm [2]. Due to their peculiar dimensions, nanomaterials exhibit special and different physical, chemical and biological features and properties which are not shown by a material with the same chemical composition but a bigger size [3,4]. For these reasons nanomaterials are having a great development in medicine for several applications such as imaging [5], gene therapy [6] and drug delivery [7–9]. In particular, nanomaterials are becoming of great interest in oncology as nanocarriers of chemotherapic drugs. The small size of the nanocarriers allows to exploit the cancer microenvironment features, in particular the vascular abnormalities of the tumor, to improve the penetration into the cancer tissue where the chemotherapic drug is finally released [10].

The development of nanomedicine is the result of an interdisciplinary work which, beside medicine, involves chemistry, molecular medicine, biochemistry, materials sciences and nanotechnology. In particular, nanomedicine requires knowledge in [3]:

1. Chemistry: synthesis of drug delivery systems and their surface modification (to improve nanoparticles biocompatibility and modulate drug loading and release).
2. Biology and pathophysiology: to identify efficient target systems.
3. Physics: to study the physical properties of nanomaterials that can help researchers (engineers and material scientists) to the discovery of new materials and systems.

1.1 Criticism to current cancer therapies

Currently chemotherapy and radiotherapy are the most widespread therapies for cancer treatment. In vitro studies show that chemotherapy and radiotherapy cause damage and structural defects on DNA which may result in cells death [11]. Without entering into the details of the mechanisms involved in chemo- and radio-therapies, it should be remarked that the current therapies need the administration of a high amounts of drug (or radiation doses) that lead to the occurrence of effects not only in the tumor tissue, but also in healthy cells [12,13]. A possible solution to these disadvantages may come from nanomedicine. Researchers are working to develop smart nanocarriers which, once injected in the blood flow, are able to release the chemotherapic drugs only when the diseased tissue has been reached.

1.2 Nanocarriers for cancer treatment

In the last 25 years several types of nanocarriers have been synthesized and widely developed in particular for drug administration and clinical tests. The design of new nanocarriers should consider the following parameters [14]:

- Size
- Composition
- Coating and functionalization
- Drug loading capacity

Not only the features previously listed are important to define the destiny of nanocarriers in the human body. Indeed a body fluid is composed by proteins, peptides and several electrolytes that can interact with the nanocarriers' surface changing their surface properties. These changes can affect the therapeutic efficacy of the nanosystem and its final fate. For example, nanocarriers injected in the blood flow can be phagocytized and eliminated by leukocytes that have the task to eliminate every putative danger. Another critical point is the capacity of nanocarriers to reach and to release, with a controlled rate, the drug in the tumor tissue only. All these issues have been investigated and possible solutions based on the use of different nanocarriers have been proposed [9]. In the following paragraphs the most studied nanocarriers will briefly be described (Fig. 1.1).

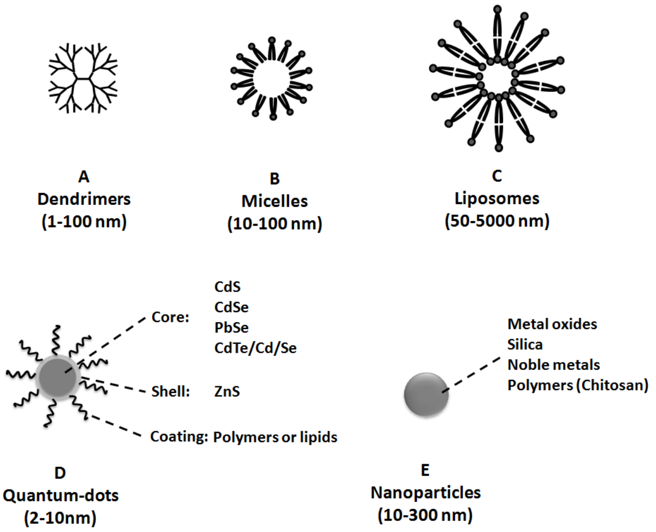

Figure 1.1 Examples of nanocarriers: dendrimers (A), micelles (B), liposomes (C), quantum-dots (D), and nanoparticles (E). Adapted from ref. [8].

1.2.1 Polymeric nanoparticles

The first polymeric nanoparticles were synthesized by Khanna and Speiser in 1969 which proposed epoxy resins beads as nanocarriers for drug delivery [15]. Subsequently researchers focused their attention on the possibility to use other natural polymers, such as proteins (albumin) and polysaccharides (chitosan and heparin), or synthetic polymers such as poly(lacticacid), poly(glycolic acid), and their co-polymers, poly(lactide-co-glycolide) [16–19]. Polymeric nanoparticles are generally biocompatible and chemically stable if compared with the most common nanomaterials. For their high biocompatibility and biodegradability, low toxicity, mucoahdesivity, and hemostatic and antimicrobial activity, chitosan-based nanoparticles have found important developments in nanomedicine as nanocarriers for drug delivery systems [20–22]. In particular, the swelling potential of chitosan at low pH values makes these nanoparticles excellent candidates as pH-responsive systems [23,24].

1.2.2 Liposomes

Liposomes are micro-particulate or colloidal carriers with size between 0.05 and 5.0 μm, composed of an aqueous volume entrapped in membrane-like lipid (phospho- and sphingo-lipids) layers [25]. Originally liposomes were used for the study of biological membranes, but starting from the end of 1970 they were introduced for biomedical applications [26]. Liposomes' structure is able to incorporate bio-active molecules (i. e. nucleids acid, DNA) or drugs (amphotericin B, doxorubicin and cis-platinum) [14,25,27] reducing their toxic effects on the healthy tissues. Another important feature of liposomes is the possibility to modify their surface and composition with biocompatible polymers like PEG or antibodies [28] to increase the circulation time in these systems, and to control the accumulation and the release of the drug in the desired site. Furthermore the recent discovery that liposomes are sensitive to heat, ultrasounds, light, and changes of pH, allows to exploit them as stimuli-responsive systems [29–31].

1.2.3 Cubosomes

Cubosomes are lipid-based nanoparticles with a bicontinuous liquid-crystalline phase stabilized by pluronics copolymer [32,33]. As result of the possibility to load at the same time with a fluorophore probes (that emit in IR or UV-Vis range) and a anti-cancer drug (i. e. quercetin or camptothecin) cubosomes are being studied for theranostic nanomedicine [34–36].

1.2.4 Dendrimers

Dendrimers, introduced as drug delivery nanocarriers in the 1990s [37], are highly branched polymeric macromolecules that have size between 1-100 nm. The drug can be encapsulated into the free space of the dendrimers' structure through physical interactions, but can also be linked to the external functional groups with covalent bonds [38]. To solve the problem of the controlled and targeted release, dendrimers have recently been used to realize stimuli-responsive systems. PEGylated polyamidoamine (PAMAM) [39] and poly(L-glutamic acid) [40] dendrimers are able to release the drug as a response to a pH variation. Similarly, thermosensitive systems were synthesized by using codendrimers which contain in their structure PAMAM and oligoethylene dendron [41].

1.2.5 Gold nanoparticles (GNPs)

Gold nanoparticles (GNPs), synthesized for the first time by Faraday in 1850, were used for biological applications in 1971 by Faulk and Taylor to invent the immunogold staining procedure [9,42]. In this technique targeting agents, like antibodies, are labeled with GNPs to visualize cellular components through electron microscopy [43,44]. Subsequently, due to their biocompatible nature, rapid synthesis and easy size and shape control, GNPs were used as nanocarriers for the delivery of proteins, peptides, nucleic acids, anticancer agents and as molecular probes [9,45]. Moreover GNPs are able to penetrate into cancer cells preventing their replication. Another important feature of these materials is the possibility to functionalize their external surface with a variety of ligands to modify their physical and chemical properties [46]. Furthermore GNPs were recently used for several biomedical applications, i.e. cancer diagnosis, immunoassays, protein assays, etc [45].

1.2.6 Quantum dots (QDs)

Researchers discovered quantum dots (QDs), light-emitting fluorescent inorganic nanoparticles, for the first time in the 1980s. QDs are semiconductors with dimensions of several nanometers (2-10 nm) and high citotoxicity that find application for theranostics, either alone or associated with other nanomaterials. The use of QDs has two important disadvantages: i) they are composed by heavy metals, ii) these metals accumulate in the body [9].

1.2.7 Ordered mesoporous materials and mesoporous silica nanoparticles

Ordered mesoporous materials (OMMs) and mesoporous silica nanoparticles (MSNs), synthesized for the first time in the 1990s, recently are widely used in nanomedicine. As will be described in more detail in chapters 2 and 3, OMMs and MSNs present structural properties that make them great candidates for tissue engineering and as depot systems in drug delivery.

2 Ordered mesoporous materials

Before 1990's zeolites were the main microporous (pore diameter < 20 Å) inorganic solids used for water treatment and heterogeneous catalysis [47–49]. In 1992 the researchers of the Mobil Oil Corporation synthesized a new family of ordered mesoporous materials (OMMs), known with the acronym of MCM (Mobile Composite of Matter) with a pore diameter in the mesopores' range (20 - 500 Å) [50]. At the same time Inagaki et al. synthesized a very similar material characterized by hexagonal structure [51]. All these materials present outstanding textural and structural features and high thermal stability [52] (see Table 2.1).

Table 2.1 Comparison among structural, physical, and chemical properties of zeolites and OMMs. Adapted from ref [52].

Property	**Zeolites**	**OMMs**
Crystalline	Yes	No
Surface area	<700 m^2g^{-1}	<2000 m^2g^{-1}
Pore size	≤1 nm	2-50 nm
Pore volume	0.1-0.5 cm^3	<1 cm^3
Diffusivity	Low	High
Thermal stability	High	Medium

Chemical stability	High	Limited
Chemical versatility	Low	Medium to low
Metal site density	Low	Variable
Lewis acidity	High	Low
Bronsted acidity	Bridging Si(OH)/Al hydroxyl groups	Medium / Increased by functional groups in the pore wall
Basicity	Arise from the oxygen framework	Introduced by functional groups in the pore wall
Chirality	Difficult to achieve	Easily obtained

The first synthesized MCM (Mobile Composite of Matter) materials had a variety of pore sizes and ordered structures. For example the materials named MCM-41, MCM-48 and MCM-50 have hexagonal, cubic and lamellar structures, respectively (Fig. 2.1) [53]. MCM materials are synthesized by means of a basic aqueous solution of a cationic surfactant (i.e. cetyl trimethylammonium bromide, CTAB) to which a silica precursor (i.e. tetraethyl orthosilicate, TEOS) is added. The type and concentration of surfactant, the surfactant/silica ratio, the reaction pH [54,55], but also ionic strength, temperature and counterion charge [50] play important roles for the synthesis of these materials.

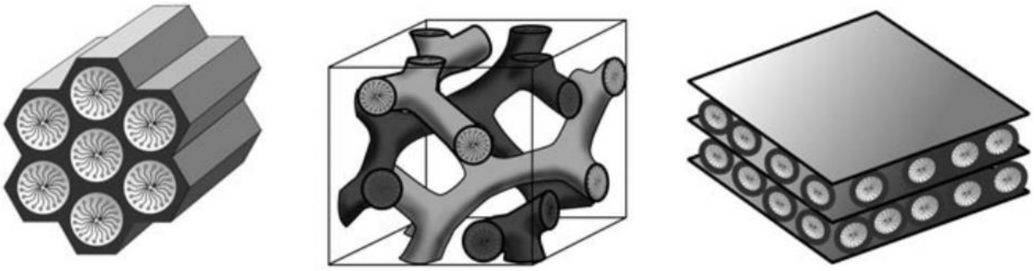

Figure 2.1 Schematic representation of ordered structures of MCM-41 (hexagonal), MCM-48 (cubic), and MCM-50 (lamellar). This picture is reproduced from ref. [56].

Another class of OMMs, discovered in 1998, is the "Santa Barbara Amorphous" (SBA) family. SBA materials are synthesized using nonionic surfactants, like pluronic copolymers (polyethylene oxide and polypropylene oxide). Before 1998 these surfactants were mainly used for the synthesis of disordered mesoporous alumina and silicate, in acidic media [57–60]. Materials with cubic (SBA-11, SBA-14 and SBA-16) and hexagonal (SBA-12 and SBA-15) structure belong to this family [57]. Besides MCM and SBA materials also other OMMs have been synthesized with different ordered structures and properties. Table 2.2 lists the most common materials.

Table 2.2. List of the most common ordered mesoporous materials. Table adapted from ref. [61].

Materials	Surfactant	Remarks	Structure
MCM-41	CTAB	Synthesis in basic conditions	Hexagonal
MCM-48	C_nTMA+ (Cn=14-18)	/	Cubic
MCM-50	CTAB	/	Lamellar
SBA-1	$C_{16}TEABr$ C_nTAB (n=14, 16)	Synthesis in acidic conditions	Cubic
SBA-3	C_nTMA+ (n=14-18)	Synthesis in acidic conditions	Hexagonal

SBA-11	Brij56($C_{16}EO_{10}$)	/	Cubic
SBA-15	P123, P85, P65	Synthesis in acidic conditions	Hexagonal
SBA-16	F127($EO_{106}PO_{70}EO_{106}$)	/	Cubic
FDU-1	B50-6600($EO_{39}PO_{47}EO_{39}$)	Large caged	Cubic
FDU-5	P123($EO_{20}PO_{70}EO_{20}$)	Large-pore silica, synthesis with EISA method	Cubic
FDU-12	F127($EO_{106}PO_{70}EO_{106}$)	Ultralarge carged, adding inorganic salts and TMB	Cubic
CMI-1	Brij56($C_{16}EO_{10}$)	Synthesis in acidic conditions	Hexagonal
MSU-H	P123($EO_{20}PO_{70}EO_{20}$)	Synthesis at neutral pH, adding inorganic salts	Hexagonal
KIT-5	F127($EO_{106}PO_{70}EO_{106}$)	Synthesis with n-butanol, in weakly acidic conditions	Cubic
KIT-6	P123 ($EO_{20}PO_{70}EO_{20}$)	Synthesis with *n*-butanol, in low concentration of acid	Cubic

2.1 Synthesis of OMMs

Kresge and co-workers in 1992 were the first to investigate the OMMs formation mechanism [54]. They proposed a liquid crystal templating (LCT) mechanism consisting of two main steps:

1. The formation of the ordered structure due to the self-assembly of surfactant molecules;

2. Hydrolysis of the silica precursor (TEOS) followed by the silica condensation around the previously formed ordered structure.

The LCT mechanism for the formation of mesoporous materials was criticized by Monnier et al. [62]. A more complex cooperative templating mechanism (CTM) (Fig. 2.2), characterized by the following three steps, was then proposed [63–65]:

1. Formation of surfactant micelles;
2. Hydrolysis of the silica precursor (TEOS) followed by silica polymerization;
3. Adsorption of the silica polymers on the micelles surface and formation of the ordered structure.

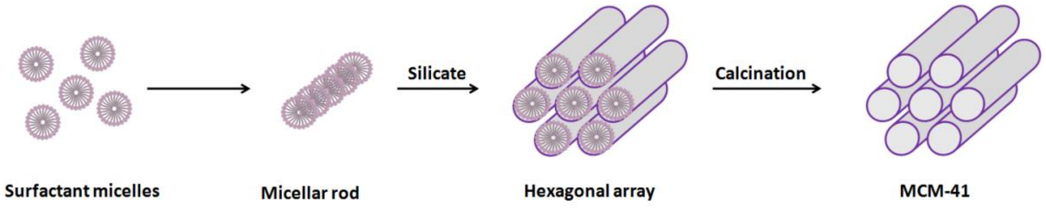

Figure 2.2. Scheme of synthesis of mesoporous materials according with CTM.

Whatever the mechanism, the synthesis of OMMS ends with the removal of the surfactant by calcination or solvent extraction.

The use of small-angle X-Ray scattering (SAXS) has been crucial to elucidate the CTM. The SAXS analysis of the synthesis mixture, carried out at different reaction times, demonstrated that surfactant molecules cannot arrange to form an ordered structure before adding the silica precursor [63]. The attractive interactions between the surfactant template and the silica precursor, affected by the reaction conditions, play a fundamental role in the formation of the ordered structure. The reaction can take place in a range of conditions, i.e. in basic or acidic media - where silanols of polymerizing silica are deprotonated or protonated respectively - and using an ionic (anionic or cationic) or nonionic surfactant as schematically shown in Fig. 2.3 [53,56]. Briefly, at basic pH, silanols are negatively charged, and can establish an attractive interaction with the polar heads of cationic surfactants. This interaction leads to the formation of the ordered structure (Fig. 2.3a). In the same pH conditions the use of an anionic surfactant requires the mediation of a cation to establish an attractive interaction with the deprotonated silanols (Fig. 2.3b). Similar mechanisms are responsible of the structure's formation in acidic media (Fig. 2.3 c-d) [53,56]. Finally, the formation of the ordered structure when nonionic surfactants are used, is due to the formation of hydrogen bonds with the silanols of the polymerizing silica (Fig 2.3e) [53,56].

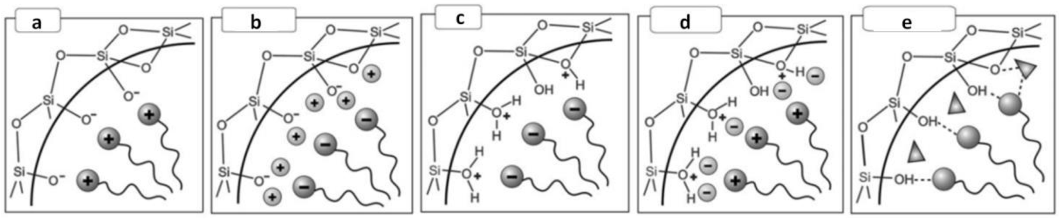

Figure 2.3. Interactions between the silica precursor and the surfactant (ionic or nonionic) in basic, acidic and neutral media. Adapted from ref. [56].

2.2 OMMs functionalization

A key feature of silica-based OMMs material is the possibility to functionalize their external and internal surface. Fig. 2.4 shows the three strategies of functionalization: i) post-synthesis functionalization; ii) one pot synthesis and functionalization (co-condensation); iii) synthesis of periodic mesoporous organosilicas [56].

1. *Grafting or post-synthesis functionalization.* This process consists in the reaction between the surface silanol groups of OMMs and a $(R'O)_3SiR$ organosilane [56], (chlorosilane $ClSiR_3$ or silazanes $HN(SiR_3)_3$) or more commonly alkoxysilanes [66] (i. e. 3-aminopropyl triethoxysilane or 3-mercaptopropyltrimethoxysilane). This process does not modify the ordered structure of the material [66], but usually affects the textural features (i.e. surface area, pore volume and pore size) [56]. The difficulty of this process is to ensure an homogeneous distribution of organic groups, due to the preferential reactivity of organosilanes for the pore openings during the initial stages of the functionalization. This may hinder its diffusion into the pore channels [56]. Another disadvantage is the need of two steps, that is synthesis and functionalization [66].
2. *Co-condensation.* This process, also known as direct synthesis or one-pot synthesis [56], is based on the direct reaction and condensation between the silica precursor and an organoalcoxysilane in the presence of a surfactant (template agent). The obtained material presents organic residues covalently bound to the pore walls with an homogeneous distribution [66]. The main disadvantage of the co-condensation process is the possibility to alter the ordered structure [66]. Moreover the final step, involving the removal of the surfactant template, can only be done by

solvent extraction since the commonly used calcination would destroy the functionalized material [56,66].

3. *Synthesis of periodic mesoporous organosilicas (PMOs).* This process is used to introduce organic groups into the silica framework [66]. For this kind of reaction a bridged organosilica precursors of the type $(R'O)_3Si-R-Si(OR')_3$ is used. The organic groups are homogeneously incorporated in the three-dimensional network structure [66]. These materials show higher surface area (up to 1800 m^2/g) and thermal stability than the materials functionalized through the previously described processes, but often exhibit a disordered pore size distribution [56].

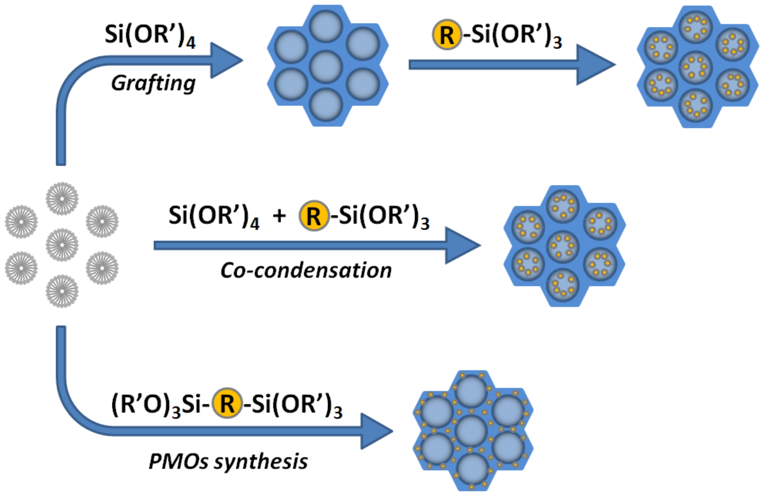

Figure 2.4. Scheme of different method of functionalization (post-synthesis and co-condensation) and synthesis of PMOs.

2.3 Applications

To date OMMs have been used for several applications.

1. *Catalysis and biocatalysis.* The large pores size of OMMs eases the mass transport and, consequently, catalytic reactions that involve bulky

substrates and/or products. In order to prepare an OMM catalyst catalytic active metals or metal oxide nanoparticles, such as Pt [67], Pd [68], and ZnO [69], need to be included into the structure (Fig. 2.5). Moreover, particularly for SBA materials, the pore size are large enough to permit enzyme immobilization. Several enzymes, such as cytochrome c [70,71], lipases [72], lysozyme [73–75], mioglobina [75], laccase [76], glucose oxidase [77], horseradish peroxidase [77–79] were used. Recently hybrid mesoporous materials, such as mesoporous silica-carbon (MSC) nanocomposites were introduced as catalyst supports for hosting metal catalysts [80,81]. The use of OMMs shows several advantages because of the possibility to: i) perform the reactions in mild conditions; ii) reduce the reaction time; iii) regenerate the catalysts without loss of catalytic activity.

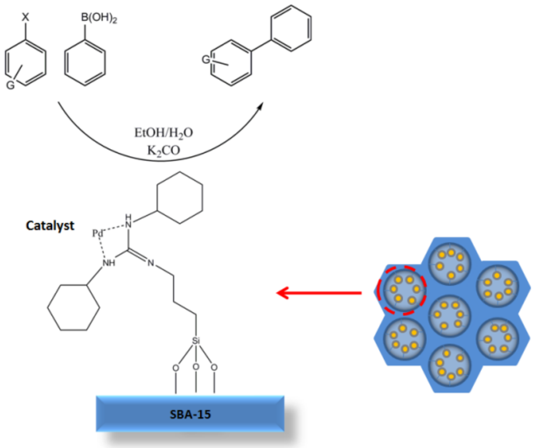

Figure 2.5. Suzuki-Miyaura reaction catalyzed by Pd included into the structure of SBA-15.

2. *Environmental applications.* The porous structure, the high surface area and the easy functionalization of OMMs allow to remove metal ions, i.e. Hg(II) [82] and Cu(II) [83], or other polluting (i.e. dyes [84,85] and polycyclic hydrocarbons [86]) molecules from waste waters (Fig. 2.6).

Functionalized OMMs are also useful for the specific recognition of heavy metal ions or polluting molecules. Another important use of these materials is for the capture of CO_2 from gas stream and flue gases [87–89].

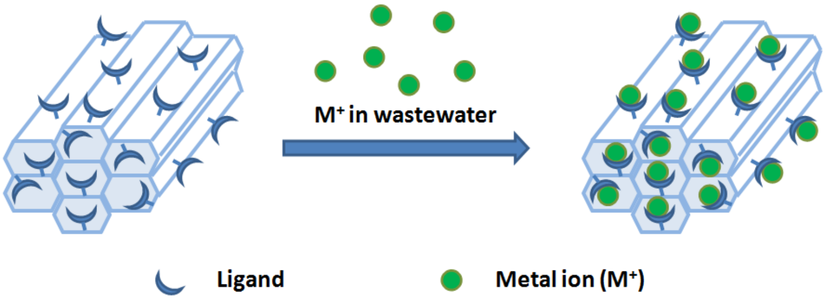

Figure 2.6. Schematic representation of OMSs modified with selective ligand for metal ions capture.

2.4 Use of OMMs in nanomedicine

As introduced in par. 1.2.7, OMMs are very important materials for nanomedicine. OMMs features - high surface areas (up than and 1400 m^2/g), high pore volumes (1-3 cm^3/g) and narrow pore size distributions (2-30 nm) the possibility to modify their external and internal surface and their biocompatibility - make them excellent candidates in tissue engineering and drug delivery [50,54,90].

2.4.1 Tissue engineering

Tissue engineering is defined as the creation and reconstruction of damage tissue using biomaterials [91]. Among the materials used for tissue engineering OMMs allows the immobilization of peptides or growth factors into the pore channels that can promote the growth of the new bone tissue [92,93]. Several studies demonstrated that OMMs are biocompatible materials [94] (as first-generation biomaterials) [95–97] and resorbable (as second-generation biomaterials) [98,99]. OMMs belong to the third-generation of biomaterials due to their capability to interact with the surrounding living tissues thus improving the bone regeneration [100–103]. When these materials are soaked in a simulated body fluid (SBF), the formation of an hydroxyapatite-like (HAP) layer around the surface of the material takes place without damaging its ordered structure [94], as schematically shown in Fig. 2.7. As shown in Table 2.3, not all materials have bioactive response, as for example MCM-41 materials. The best solution to accelerate the bioactive response is to add a small amount of bioactive glasses to OMMs. The use of the Evaporation-Induced Self-Assembly (EISA) method [104] allows to obtain mesoporous glasses with a combination between properties of OMMs and bioglasses. The higher surface area of mesoporous glasses if compared with that of bioglasses favors the contact with SBF and, consequently, it accelerates the formation of the HAP layer [94].

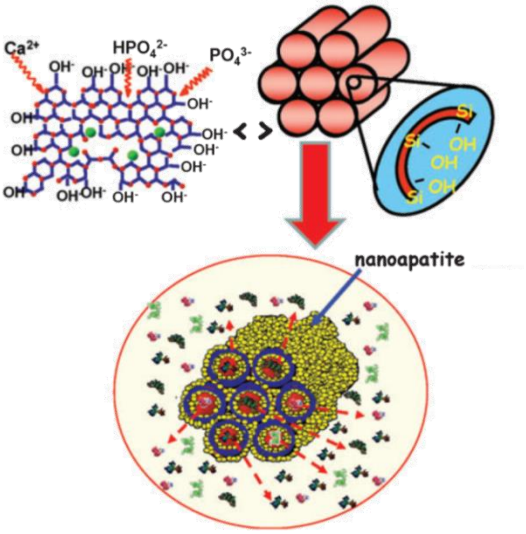

Figure 2.7. Formation of the HAP-layer on OMMs surface in SBF. This picture is reproduced from ref. [105].

Table 2.3. Examples of bioactivity for several OMMs. Adapted from ref. [105].

Material	Capability to form of an HAP-like layer	Time in SBF
MCM-41	No	60 days
MCM-48	Yes	60 days
SBA-15	Yes	30 days
1%P-doped-MCM-41	Yes	15 days
Bioglasses	Yes	3 days
10%Glass-90%MCM-41	Yes	1 day
Mesoporous glasses	Yes	1 h

2.4.2 Drug delivery

Although OMMs were synthesized in the 1990s it took about ten years to see the first possible medical application of OMMs. Indeed, in 2001 Vallet-Regì et al. [106] demonstrated the possibility to use MCM-41 as carrier for drug delivery. Indeed, the ordered porous structure allows the immobilization into the pore channels of therapeutic molecules and their controlled release [73,74,107–109]. Several studies demonstrated that OMMs (i.e. MSE, SBA-15, MCM-41) can be successfully used as depot systems for antibiotic [110–116], anti-anflammatory [117–119] or chemotherapeutic drugs [120–122]. The importance in the use of OMMs in medicine is the possibility to administrate the drug only in the desired site, for example in the inflamed or tumor tissue, without damaging the healthy one. Furthermore, this allows the administration to the patient of a lower amount of the drug thus solving problems such as sensitivity, bacterial resistance, or superinfections [123,124]. Moreover, the possibility to modify their surface with several organic groups [66,107,110,119] is an important factor that, as demonstrated by Sevimli et al. [110], affect the drug loading and release since the interaction between the support and the drug changes. Recently, in particular in the field of chemotherapy, the use of mesoporous silica nanoparticles (MSNs) is having great development. In addition to the typical characteristics of OMSs, MSNs have very small particle size, thus they can be administrated by injection and transported in various sites of the human body by the bloodstream [125,126], and then internalized by cells [127]. The easy functionalization allows to modify the external surface of MSNs with targeting or stimuli-responsive agents to obtain target or stimuli-responsive systems. Briefly, the former are recognized by receptors overexpressed in cancer cells able to bind the targeting agent and to allow MSNs to reach the tumor tissue. The latter consists in the grafting of capping agents able to close and open the pores under determined stimuli (external or internal to the body, like pH and temperature change, redox reactions or the application of a magnetic field). These particular properties of MSNs will be discussed in detail in Chapter 3.

3 MSNs in nanomedicine

3.1 Composition and pH of tumor microenvironment

The knowledge of the biological characteristics and the microenvironment of the tumor tissue is of fundamental importance to develop new effective therapies. Tumor tissue contains several types of cells, i.e. endothelial cells, fibroblasts, macrophages, neutrophils, dendritic cells, and cytotoxic T lymphocytes [11], as schematically represented in Fig. 3.1. The extracellular matrix of tumor tissues contains, among others, growth factors, cytokines and structural proteins (collagen and elastin) [128]. The modification of the composition of the extracellular matrix causes abnormal inter- and intracellular signaling, leading to irregularities in cell proliferation, growth and cytoskeleton reorganization [128]. Furthermore, tumor tissue presents activated platelets because it is considered by the organism as an injured tissue. While for injured tissues the stimulus for the activation of platelets ends when the tissue is repaired, for tumors the stimulus persists allowing its growth with the stimulation of angiogenesis [128]. The abnormal vascularization, that characterizes tumors, is the cause of the irregular oxygenation. To solve this issue, cancer cells use glycolysis in place of the oxidative phosphorylation, ensuring the survival and proliferation, and hence the cancer progression. This process causes an increase in the lactate level which, in turn, leads to a decrease in pH values of extra-cellular and intra-cellular environment [11]. Indeed, tumor tissue is characterized by pH values lower than the healthy pH=7.4. Furthermore the intra-cellular pH_{in} (pH_{in}=5.0-6.0) is lower than the extra-cellular pH_{ex} (pH_{ex}=6.5-7.2) [129–132]. Another important feature is the capability of cancer cells to overexpress proteins, i. e. integrins [133–139] or CD44 receptor [140–146] which are able to recognize and bind target molecules.

The knowledge of the tumor microenvironment has allowed the development of smart drug delivery systems. The use of mesoporous silica nanoparticles (MSNs) as nanodevices for cancer treatment could be more effective with the grafting on their external surface of targeting agents which can be recognized by specific receptors. A further grafting of molecules sensitive to either internal (pH, enzymatic and redox reactions) and external stimuli (light, temperature and magnetic field) would permit the release of the drug *in situ*. These two aspects will be discussed in detail in the following paragraphs.

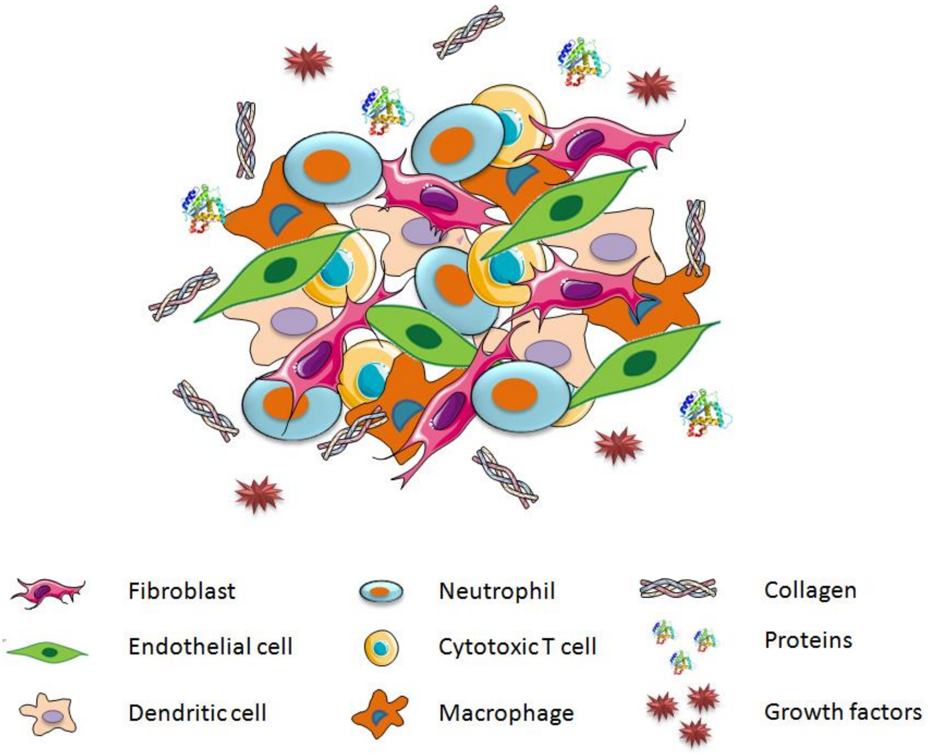

Figure 3.1. Schematically representation of tumor tissue and its components.

3.2 Target systems

Targeted drug delivery is a method that enables the delivery of drugs or therapeutic molecules from nanocarriers in the diseased tissue preferentially. The main advantages of this method are the reduction of the dose of drug administered to the patient and of side effects on the healthy tissues. Two strategies are possible, namely: passive targeting and active targeting.

3.2.1 Passive targeting

In a cancer tissue blood vessels are abnormal in form and architecture, with large pores and fenestrations of few hundred nanometers [147]. Consequently the vascularization is irregular and heterogeneous in the tissue. All these features can favor the penetration and the accumulation of macromolecules or nanocarriers, namely liposomes or nanoparticles, within the tumor tissue much more than in the other tissues. This phenomenon was discovered for the first time by Maeda and co-workers in 1986 [148]. They observed that macromolecules with molecular weight > 50 kDa tend to accumulate in tumor tissues more than in the healthy tissues and persist there for long time increasing their concentration by 70-fold. This effect is known as the "enhanced permeability and retention" (EPR) effect. EPR effect received great interest for the development of new cancer treatments in nanomedicine. The EPR effect is addressed by tumor features [149]:

i. the nature of the vascular bed and the presence of functional lymphatic vessels;
ii. tumor characteristics: size, type, and location;
iii. tumor stage: primary, advanced or metastatic;

iv. the capability of macrophages' penetration in tumor tissue that in turn is influenced by patient age and gender, and by tumor type and treatment.

The knowledge of all these factors can help to realize new smart drug delivery systems which are able to deeply penetrate into the tumor tissue and release the drug in the desired site. Particles accumulation is affected by their circulation time and their capability to overcome biological barriers. These phenomena are strongly related to their features: i) size; ii) shape and iii) surface properties.

1. *Size.* When nanoparticles are used as drug delivery systems their ideal size should be in the range 50-300 nm [125,127,150]. Nanoparticles of smaller size, i.e. < 10 nm are easily eliminated by the kidneys. On the other hand, particles with size > 400 nm do not diffuse and accumulate into the interstitial tumor tissue without being internalized into cancer cells [151].
2. *Shape.* Length/width ratio (L/W) is an important parameter to control cellular uptake. Indeed nanoparticles' shape can affect non-specific cell internalization. Huang et al. studied the effect of MSNs shape on cellular uptake [152]. They demonstrated that nanoparticles with big values of L/W, typical of rod-shaped MSNs, are internalized more easily than spherical ones (L/W=1) as a result of their high contact surface. In this case the orientation of the nanoparticles will respect to the cellular membrane is decisive.
3. *Surface properties.* Once injected in the blood flow, the fate of nanoparticles mainly depends on the properties of their external surface. In order to increase the circulation time and ensure the accumulation of

MSNs into the tumor tissue it is necessary to avoid the "opsonization" process. This process is based on the adsorption of opsonin proteins on MSNs surface which result in their rapid elimination by the mononuclear phagocyte system (also known as reticulo-endothelial system). Surface modifications of MSNs allows to avoid opsonization. Polyethylene glycol (PEG) is widely used to this purpose because of its steric hindrance, and the capability to repel opsonins from its chains, thus increasing the circulation time of the system [153]. This effect increases with increasing PEG molecular weight [138,154]. Furthermore, to promote cellular internalization an effective strategy is to modify MSNs surface with amine groups that are positively charged in physiological conditions [155]. In this way nanoparticles can interact electrostatically with the negatively charged membrane phospholipids, and promote the endocytosis mechanism of internalization [155,156].

3.2.2 Active targeting

It is known that cancer cells, organs, tissues and organelles overexpress receptors able to recognize particular molecules as, for example, peptides, proteins, antibodies, saccharides, aptamers or other small molecules (Fig. 3.2).

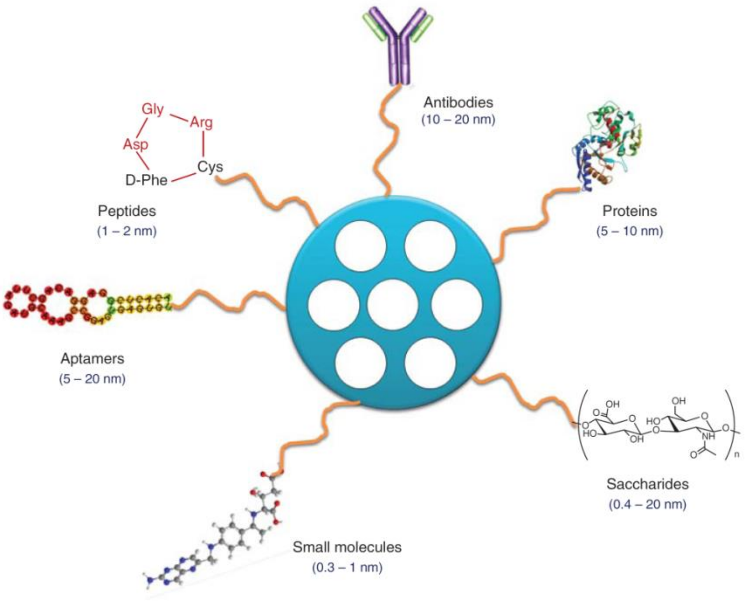

Figure 3.2. Example of active target molecules on MSNs. This picture is reproduced from ref. [125].

Functionalized MSNs' surfaces can link one of these type of molecules to obtain active-target drug delivery systems. The efficacy of these systems depends on the abundance and function of receptors in the tumor tissue, as well as on the degree of nanoparticles functionalization. Some of the most common target molecules are: antibodies, proteins, peptides, aptamers, and saccharides (see chapter 4).

3.3 Stimuli-responsive systems

The controlled release of the drug in the desired site is another important goal of nanomedicine. Stimuli-responsive systems are able to release the drug only when they undergo a specific internal or external stimulus (Fig 3.3). The pore channels of opportunely functionalized MSNs can be loaded with a drug, and then closed with a capping agent that prevents the drug release. The most common capping agents are:

i. metal or metal oxide nanoparticles;

ii. coatings of organic molecules linked at the surface through pH-, temperature-, redox- or light-sensitive bond

iii. polymers that change their conformation with a change of pH or temperature.

Furthermore, two types of stimuli can be used to this purpose: i) internal; and ii) external [125,157,158].

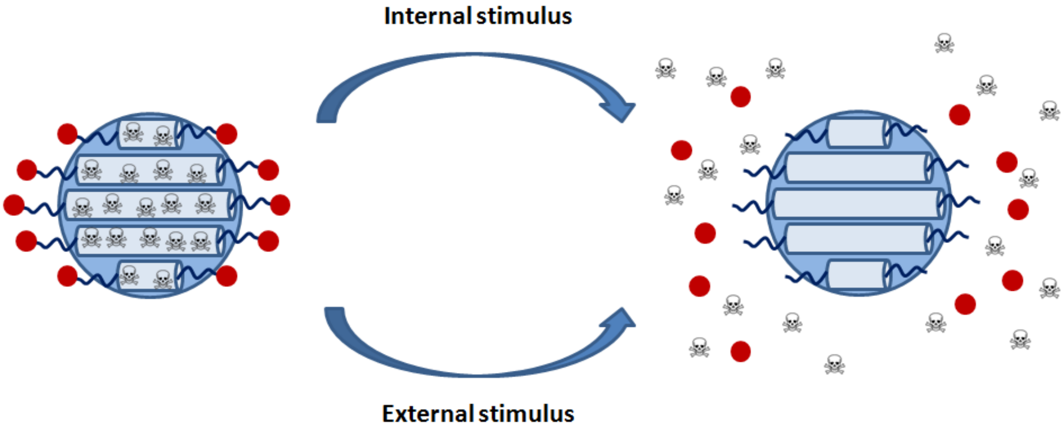

Figure 3.3. Examples of internal and external stimuli-responsive MSNs.

3.3.1 Internal stimuli

3.3.1.1 pH

As explained at par. 3.1, the evolution of inflammation or cancer disease results in lower pH values of extra-cellular (pH_{ex}=6.5-7.2) and intra-cellular (pH_{in}=5.0-6.0) fluids. Differences in pH are also observed among the different cell compartments and organelles [129–132]. It is possible to exploit these pH variations to realize efficient pH-responsive systems, for example by linking on the MSNs surface a capping agent with a pH-sensitive bond. Pores of MSNs, previously loaded with the drug can be closed with organic molecules as cucurbit[6]uril [159], cyclodextrins [160–162] or crown ethers [163] that form inclusion complexes with the previously grafted groups on MSNs surface. These complexes are broken at low pH values allowing the drug release as shown in Fig. 3.4.

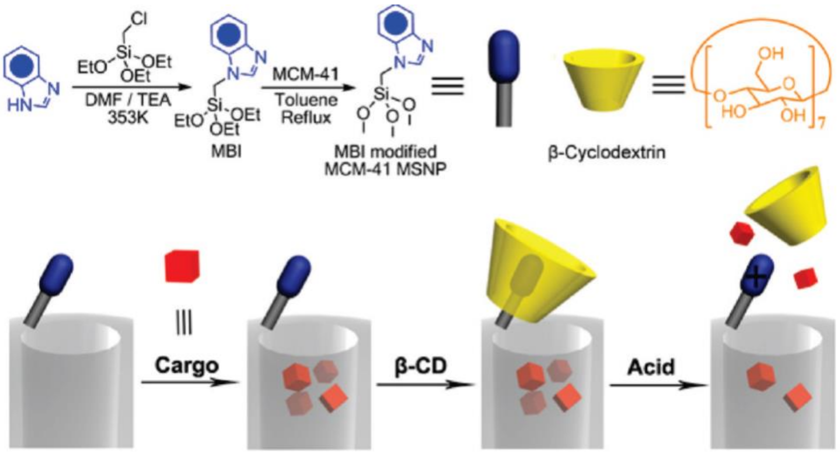

Figure 3.4. Schematic representation of pH-responsive system based on MSNs and cyclodextrins as capping agent[160].

Also gold nanoparticles [164,165], iron oxide [166] and cerium oxide [167] or molecules with high molecular weight [168] are frequently used as capping agents. They bind pH-cleavable linkers (i.e. acetals, hydrazone and boronate) placed on the MSNs surface at neutral or slightly basic pH values. A pH decrease breaks these bonds allowing the opening of the pore and the drug release (see Fig.3.5).

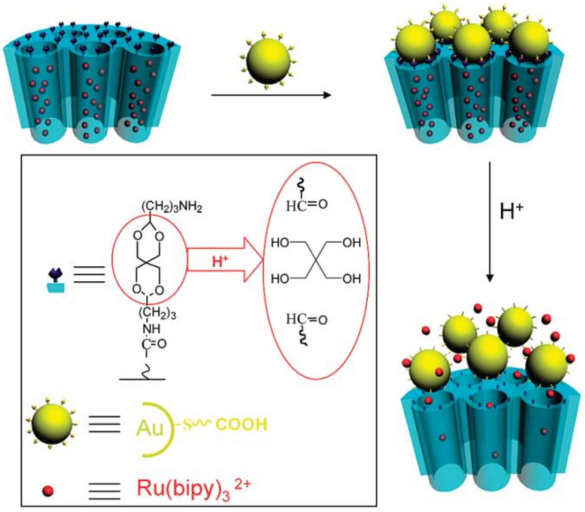

Figure 3.5. Graphical representation of gold nanoparticles-capped MSNs [164].

Another strategy is the functionalization of MSNs external surface with polymers (capping polymers) with acid/base properties (Fig. 3.6). Chitosan (CHIT) is one of the most used pH-sensitive polymer to realize stimuli-responsive systems. In physiological conditions (pH=7.4) CHIT chains interact with each other through hydrogen bonds, and close the pores. At acidic pH values amino groups of the CHIT chains are protonated, thus producing repulsion forces that break the hydrogen bonds network. This causes the elongation of chains and consequently the opening of the pores allowing the drug release. Others polymers were recently used for the synthesis of pH-sensitive systems such as poly(4-vinylpyridine) [169], poly(4-vinylphenybronic acid-co-2- dimethylamino)-ethyl acrylate [170] and DNA fragments [171].

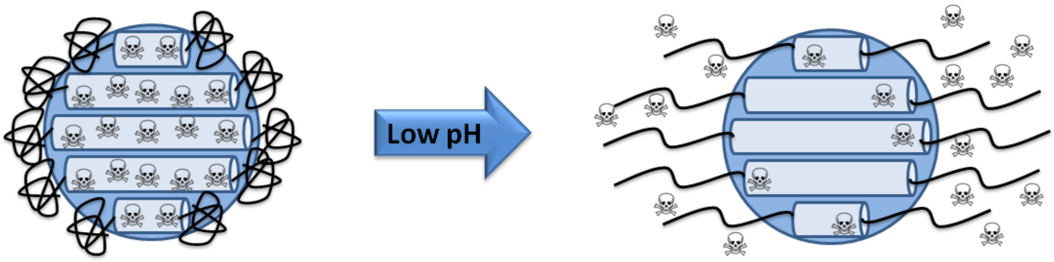

Figure 3.6. Schematic representation of a pH-responsive system.

3.3.1.2 Redox

In the human body reductive species, such as glutathione (GSH), able to break disulfide (S-S) bond are present. GSH occurs in different concentrations inside (10 mM) and outside (20 μM) the cells of healthy and diseased tissues [20,172–174]. The high concentration of GSH in the intracellular environment induces the breaking of the disulfide bond and so the release of the drug only when MSNs are internalized by the cells. Several systems have recently been synthesized using capping agents linked through redox-sensitive bonds [172,175–180].

3.3.1.3 Enzymes

Several tumors overexpress enzymes involved in tumor progression and metastasis. It is possible to exploit their capacity to break particular bonds to make stimuli-responsive and controlled release systems. In this case MSNs can be grafted with capping agents, such as cyclodextrins or rotaxanes, through enzyme-sensitive linkers that can be broken this causing the opening of the pore. Singh and co-workers [181] described a system based on MSNs grafted with a polymeric shell formed by a protease-sensitive sequence. Other enzymes such as glucose oxidase [182] and enzymes of the gastrointestinal tract [183] have been exploited to realize stimuli-responsive systems.

3.3.2 External stimuli

3.3.2.1 Light

Light, particularly UV radiation, can be used as an external stimulus to trigger drug release [184–186]. Light-sensitive systems use MSNs whose pores have been closed by capping agents linked through a light-sensitive bond. More recently NIR-sensitive systems have been prepared. For example Lin and co-workers synthesized a drug delivery system based on MSNs grafted with coumarin conjugated to an anticancer drug linked through a NIR-sensitive bond, as schematically represented in Fig. 3.7. The NIR radiation breaks this bond, the pores open and the drug is released [187]. Following this work other research groups focused on these kind of systems as a result of the great penetration capacity of NIR radiation [188,189].

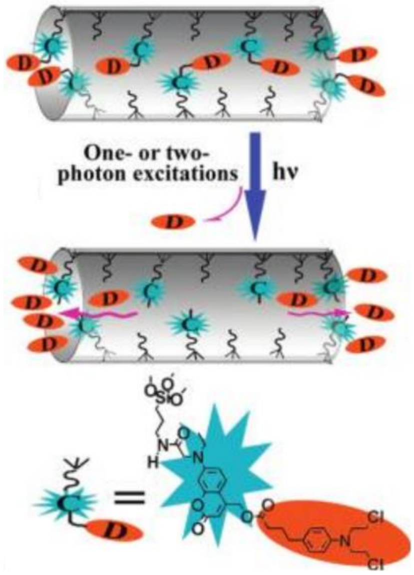

Figure 3.7. Scheme of the drug release process activated by NIR radiation [187].

3.3.2.2 Temperature

Other systems which permit the drug release only in the diseased site are thermo-responsive systems. Indeed diseases as cancer, infections or inflammations cause an increase of 4-5°C of the tissue temperature [190,191]. The external functionalization of MSNs with thermo-sensitive polymers permit to exploit this temperature gradient and release the therapeutic molecules only in the desired site. A polymer already used for this type of systems is poly-N-isopropylacrylamide (PNIPAAm) (Fig. 3.8) synthesized for the first time by Schild [192]. PNIPAAm has a low critical solution temperature (LCST) of 32°C. Below this temperature PNIPAAm is hydrated, hence its chains are swollen and obstruct the MSNs pores, thus preventing the drug release. At temperatures above 33°C, water is released, polymer's structure collapses causing the opening of the pores and the release of the drug [192,193]. Other polymers such as the copolymer formed by units of N-isopropylacrylamide and 3-(methacryloxypropyl)trimethoxysilane [194] or poly(DMAEMA-co-3-dimethyl(methacryloyloxyethyl)ammonium propanesulfonate) [195] have been used. More recently MSNs were coated with the biodegradable polymer poly(2-dimethylamino)ethylmethacrylate [196], that belongs to the class of polyampholites, namely zwitterionic polymers, with acid or basic groups in their chains that are both dissociated in water solution.

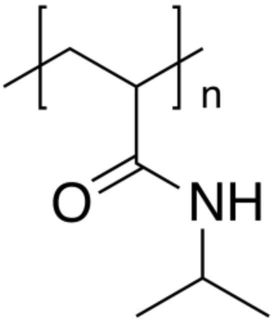

Figure 3.8. Structure of PNIPAAm.

3.3.2.3 Magnetic field

Enclosing magnetic components in the structure of MSNs the system becomes sensitive to a stimulus induced by an external magnetic field. Superparamagnetic iron oxide nanoparticles (SPIONs) are frequently used to this purpose [197–200]. They transform the magnetic field in heat with two different mechanisms: Brownian and Nell fluctuations that are caused by the rapid rotation of the nuclei and the magnetic moment respectively [125,201]. SPIONs, located at the entrance of MSNs pores, obstruct the drug release that is allowed only after the application of the magnetic field.

4 MSNs in physiological media: adsorption of proteins, cellular uptake and grafting of biomolecules

As described in the previous chapter, opportunely functionalized MSNs can be excellent target and stimuli-responsive systems for drug delivery. Surface modification of MSNs affects not only their chemical and physical properties, but also their behavior into the biological environment and biocompatibility [202,203]. When put in contact with a biological medium, MSNs can interact with several biomolecules, such as proteins, metalloproteins, glycolipids, and peptides. Indeed, it is possible that these biomolecules are adsorbed on MSNs' surface changing their chemical and biological properties [204].

4.1 Protein corona

Nanoparticles (NPs) dispersed in a biological medium seek to reduce their surface energy through the adsorption of biomolecules (proteins, peptides, or glycolipids) occurring in the medium. The formation of a layer of biomolecules, known as *protein corona* (PC), is due to the physico-chemical interactions established between the NPs and the biomolecules [205,206]. NPs features [207], such as, their chemical composition [208], size [209], shape [210], surface charge [2,211,212], and hydrophilic/hydrophobic character [2] affect the formation of the PC. Other important factors that affect the formation of the PC are the composition of the biological medium, the proteins concentration in blood plasma, temperature, administration route, as well as composition of the cell membrane

[205,213]. PC can be composed of two layers of proteins known as *hard corona* (HC) and *soft corona* (SC) characterized by proteins bound through strong and weak interactions to NPs' surface, respectively [206,214,215]. The formation of either HC or SC depends on medium composition including protein concentration, but also on the NPs external charge, and the affinity of proteins towards the NPs surface [213]. Firstly, highly concentrated proteins, like serum albumins, and immunoglobulins, are adsorbed on the NPs' surface. Subsequently these are replaced by other proteins, such as fibrinogen and apolipoproteins, which occur with lower concentrations but show higher affinities toward NPs [216]. This process is known as the "Vroman effect" [216,217]. The formation of the PC modifies the surface charge and hydrophilic/hydrophobic character of NPs [218], thus affecting the fate of NPs in terms of cellular uptake [214] and cytotoxicity [219].

4.2 Cellular uptake

Cellular uptake can occur through several mechanisms affected by the size of the considered carrier (Fig. 4.1.) [220]:

1. Phagocytosis: internalization of solid particles by specific cells;
2. Pinocytosis: internalization of extracellular molecules dissolved in a fluid-phase. Two different pathways are possible:

- Macropinocytosis: uptake through pockets formed by the introflection of cell membrane;

- Endocytosis: receptor-mediated uptake of extracellular molecules due to the modification of the cell membrane.

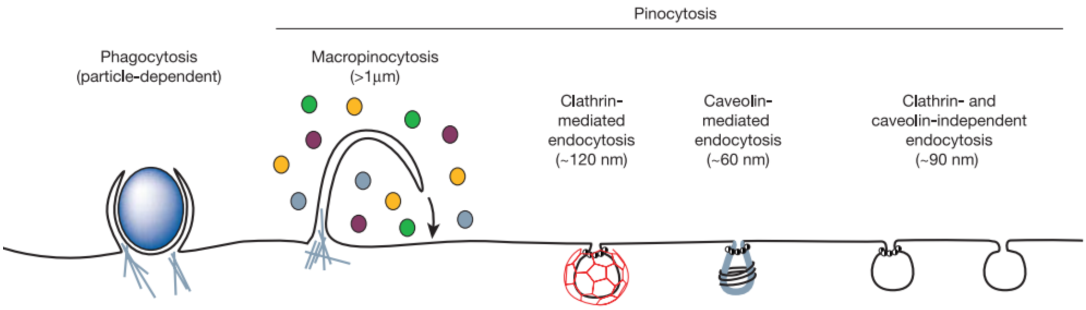

Figure 4.1. Representation of several internalization mechanisms. This picture is reproduced from ref. [220].

The kinetics, amount and mechanism of cell internalization are affected by several parameters, i.e.: incubation conditions, type of cells, and type and purity of nanomaterial. MSNs' surface properties, as well their size and shape, can affect their interaction with cell membrane, and consequently the mechanism of cellular internalization [155]. Neutral polymers, such as PEG, grafted on MSNs' surface are able to reduce the nonspecific adsorption of proteins and favor the cellular uptake through the endocytosis mechanism. Similarly, the use of zwitterionic ligands allows to minimize nonspecific proteins' adsorption, but on the other hand they reduce interactions between NPs and cells, and thus the internalization. The behavior of charged NPs is different. Since the cell membranes are negatively charged (due to their phospholipid composition), negatively charged NPs experiment repulsive electrostatic forces that contrast their uptake [155]. In this case the internalization can occur only through nonspecific binding between the scarce cationic sites of the phospholipid membrane and NPs (Fig. 4.2A). On the contrary the attractive forces established between positively charged NPs and the cellular membrane favor the cell internalization [221] (Fig. 4.2B).

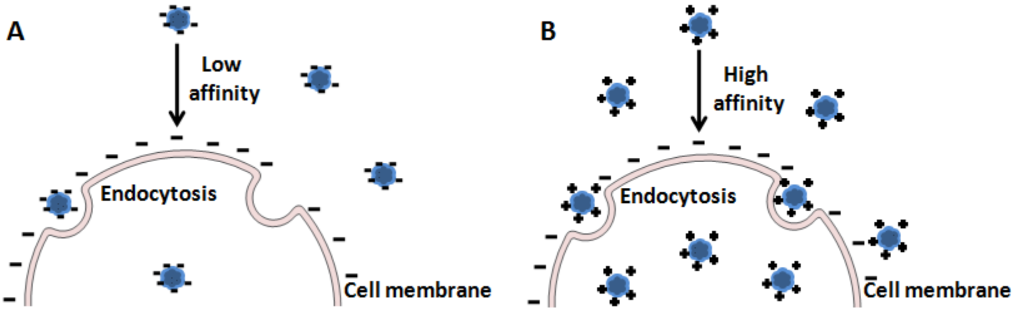

Figure 4.2. Schematic illustration of negatively (A) and positively (B) charged nanoparticles interaction with phospholipid membrane.

It has been observed that positively charged MSNs are able to escape endosomes and enter the cytoplasm and the nucleus [222]. The grafting of positively charged polymers, such as chitosan (see paragraph 4.3.1), on MSNs surface is a promising strategy to improve the interaction between MSNs and cell membranes. Alternatively the bioadhesive properties of MSNs can be improved by functionalizing their external surface with biomolecules recognized by the receptors occurring on the cell membrane. Among these molecules hyaluronic acid (HA), (see par. 4.3.2) is an excellent candidate. Recent studies have demonstrated that HA grafted on MSNs surface improves the molecular recognition and the bioadhesive properties towards biological barriers [223]. Peptides, such as cilengitide, adnectin, and RGD (Arg-Gly-Asp), are another example of biomolecules able to improve the cellular uptake of compounds and nanocarriers [224,225]. Among them, RGD recognized by $\alpha_v\beta_3$-integrins, has recently been used to coat MSNs to prepare a target drug delivery system for cancer therapy [226].

4.3 Targeting molecules and biopolymers

Due to the importance of the external functionalization for improving MSNs' uptake and biocompatibility and to realize smart target systems, this paragraph describes the three biomolecules used for this work, namely: chitosan, hyaluronic acid, and RGD.

4.3.1 Chitosan

Chitosan (CHIT), discovered for the first time in 1811 by Braconnot [227], is a polysaccharide with a chemical structure similar to that of cellulose. CHIT consists of a linear chain of thousands of β-(1-4) linked D-glucose units where the hydroxyl in C2 position is replaced with an amino group [228–230] (Fig. 4.3b). CHIT is extracted from the shells of crustaceans (i. e. crabs, prawns, lobsters and shrimps), the exoskeleton of insects, and the cell walls of fungi (*Aspergillus* and *Mucor*) obtained from the waste of food industry [228]. CHIT production requires the deacylation of chitin according to the reaction shown in Fig. 4.3 [227,228]:

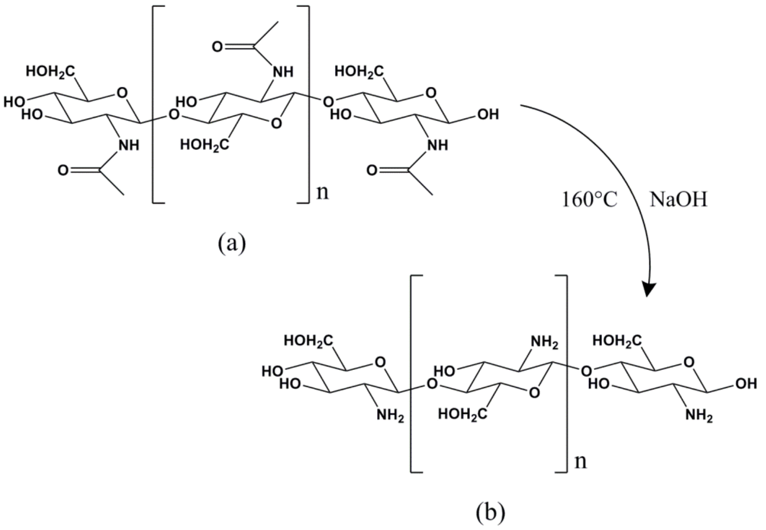

Figure 4.3. Deacetylation of chitin (a) to produce of chitosan (b).

The presence of amino groups confers to CHIT a cationic nature at physiological pH. The positive charged amino groups can interact with the anionic groups of lipoteichoic acids and lipopolysaccharides present in Gram-positive and Gram-negative membrane respectively. This process allows the destruction of the membrane and is the basis of the antimicrobial activity of CHIT [227,229,231].

CHIT presents several properties like biocompatibility, biodegradability, non-toxicity and good humidity adsorption as well as antibacterial, analgesic, antitumor, hemostatic, hypocholesterolemic, antimicrobian, and antioxidant effects [228]. CHIT features allow to realize several types of scaffolds useful for biomedical applications (i.e. tissue engineering of bone, cartilage, and cutaneous wound healing, and drug delivery) [229,232,233]. The most common CHIT-based scaffolds and their main applications are listed (Table 4.1).

Table 4.1. List of the most common CHIT-based scaffolds and their applications.

Type of scaffold	Application	Ref.
Nanoparticles	Drug delivery	[22,234–237]
Hydrogels	Tissue engineering/Drug delivery	[238–240] [241–243]
Sponges	Tissue engineering/Drug delivery	[244] [245,246]
Films	Tissue engineering	[247,248]
Porous nanofibers	Drug delivery/Tissue engineering	[249,250] [251,252]

CHIT has a pH-responsive behavior due to its acid/base properties. In particular, in aqueous solution at neutral pH, CHIT can assume spherical, random coil and rigid rod shape conformations. This is due to the hydrogen bonds established between the amino and hydroxyl groups of the polymer's chain. CHIT amino groups have a pK_a value around 6-6.5 [253,254], so that they are fully protonated at acidic pH. This makes the hydrogen bonds less effective, because repulsive electrostatic forces prevail [255]. This mechanism is exploited by several pH-responsive systems based on CHIT, that is, nanoparticles [256,257], microcapsules [258], hydrogels [259,260], and nanospheres [261]. Recently, CHIT was used as capping agent for MSNs to control the drug release. Indeed, as schematically represented in Fig. 4.4, at physiological pH the hydrogen bonds between polymer's chains of CHIT - grafted on the external surface of MSNs - induce their contraction and consequently the closure of the pores which prevent the unwanted drug release. When CHIT coated MSNs reach inflamed/cancer cells, which have an acidic pH (see par. 3.1), CHIT chains disentangle due to repulsive forces established among protonated amino groups thus allowing the drug release (Fig. 4.4) [114,255,262,263].

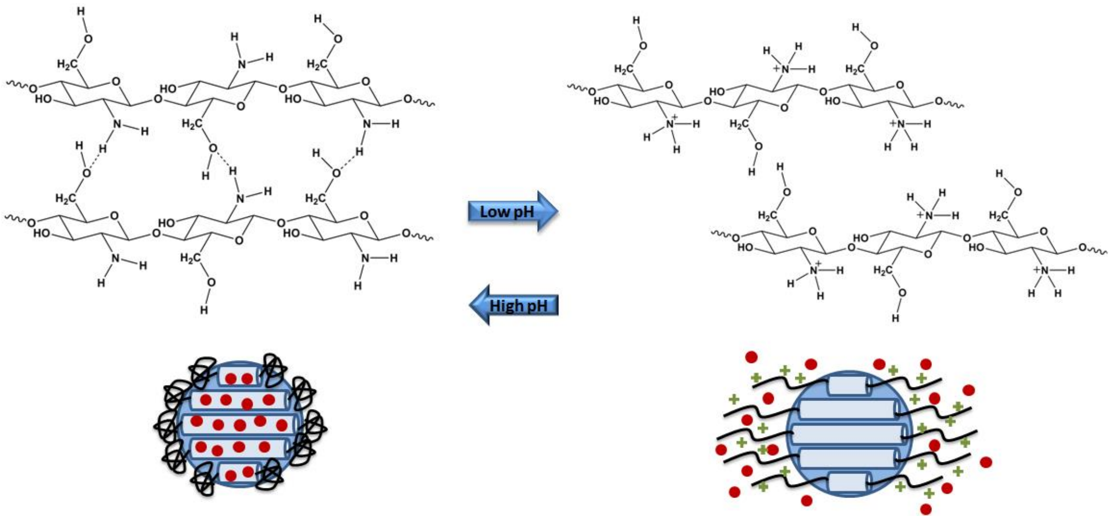

Figure 4.4. Scheme of the pH-responsive MSNs functionalized with CHIT.

4.3.2 Hyaluronic acid

Hyaluronic acid (HA) was discovered for the first time in 1934 by Meyer and Palmer in the bovine vitreous humor [264]. HA is a polysaccharide with a primary structure consisting of a linear chain of N-acetyl-D-glucosammine and β-glucuronic acid (Fig. 4.5). Its secondary structure can be described as a tape-like 2-fold helices, due to the 180° twisting of each disaccharide unit, while, the interactions among the hydrophobic 8 CH groups induce a bending of the chain causing the formation of a network similar to β-sheets [265]. HA is susceptible to degradation caused by changes of pH and temperature, or by mechanical, ultrasonic and enzymatic stresses. The conditions of the external environment, can also affect the polymer structure and consequently its physicochemical properties. For example HA viscoelasticity in aqueous solution is affected by the presence of sugars [266,267], salts [267], phospholipids [268]. Viscoelasticity is also affected by pH changes which cause variations in the ionization degree of the polymer's chain. Gibbs et al. found that HA solutions have higher viscoelastic properties at pH 2.5 rather than at pH 7.0. Since the pK_a value of HA carboxylic groups is around 3 [269–271], at neutral pH values the negatively charged HA chains repel themselves thus decreasing the viscoelasticity of the solution [272]. Commercial HA is obtained by extraction from synovial fluid, umbilical cord, skin and rooster comb, or from bacterial fermentation. HAs of different origin have different molecular weights and chain lengths. In the human body HA is synthesized by the enzyme HA-synthase (Has). There are three isoforms of Has: Has1, Has2 and Has3. Has2 is responsible of the synthesis of HA with MW $\approx 2 \cdot 10^6$ Da, whereas Has3 is involved in the synthesis of HA with MW $< 3 \cdot 10^5$ Da [273]. Most HA is contained in the human skin (about 5 g, one-third of the total), both in the dermis and in the epidermis. In particular HA is present in mammalian skin, but also in all organs of vertebrates and in the extracellular matrix (ECM) of soft connective tissues [265].

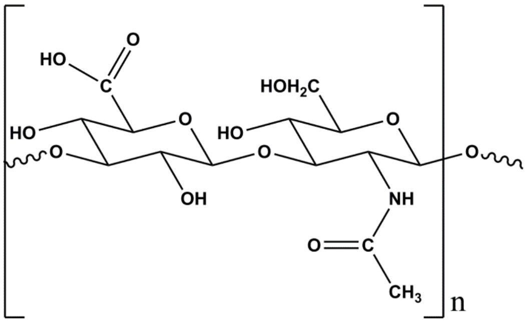

Figure 4.5. Structure of Hyaluronic Acid.

HA-based scaffolds, associated with stem cells and growth factors, are widely used for tissue engineering to obtain biocompatible and functional tissues. These are very interesting because of their biocompatibility, degradability, chemical functionalization, and capability to regulate the inflammatory chemokines, receptors, metalloproteinases and tissue inhibitors. HA-based scaffolds can also be used in combination with other materials. For example HA combined with fibrin, tricalcium phosphate, collagen, alginate and silk fibroin were used for the regeneration of cartilage lesions, while mesenchymal stem cells (MSCs), collagen type I and chitosan were found to promote the osteogenesis [274]. HA-based scaffolds have also the capability to be integrated into the wound tissue, contributing to the healing process, thus improving the generation of granulation and connective tissue along with new blood vessels.

HA is recognized by cluster determinant 44 (CD44) receptors overexpressed in several cancer cells (for example HeLa and HCT-116). For this reason HA was recently used to functionalize carriers for drug delivery systems as for example dendrimers [140], micelles [275], and ceramides [142] or HA-grafted graphene quantum dots [146], carbon nanotubes [144,145] as well as silica mesoporous nanoparticles [276]. Zhao et al. [277] and Wang et al. [223] compared the behavior of HA-grafted MSNs incubated with CD44 receptor-positive cells (HCT-116 and HeLa cells) and receptor-negative cell lines (NIH-3T3 cells). They demonstrated that MSNs are better internalized in HCT-116 and HeLa cells than in NIH-3T3.

4.3.3 Arg-Gly-Asp (RGD) sequence

Arginine-Glycine-Aspartate (RGD) sequence (see Fig. 4.6) is a tripeptide, discovered for the first time in 1984 [278], occurring in several proteins such as fibrinogen, fibronectine, vitronectin, collagen type I and von Willebrand factor [279,280].

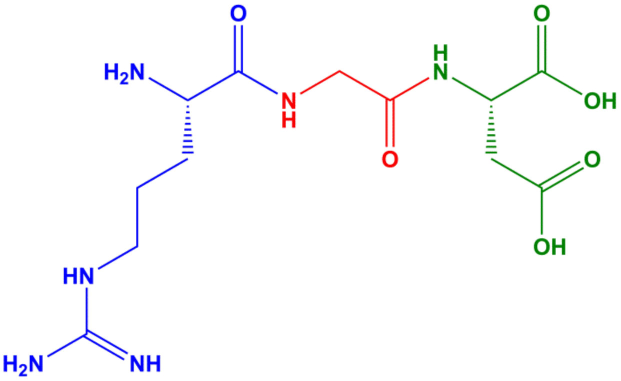

Figure 4.6. Structure of RGD.

In the human body RGD plays the important role to mediate the interaction between proteins, such as fibrinogen [279] and fibronectin [281] and their receptors. In 1987 Plow et al. investigated how the efficacy of RGD is affected by the presence of other amino acids adjacent to that sequence. They found that the addition of amino acids, in particular at the carboxy-terminus, can reduce the activity of the RGD-containing peptides [279]. Integrin $\alpha_v\beta_3$ are particular receptors overexpressed in fibroblasts, epithelial cells, and in many solid tumors: melanoma, glioblastoma, breast, prostate, pancreatic, ovarian, and cervical cancer [133,282]. They are able to recognize the RGD sequence that can act as targeting agent [283]. Researchers might take advantage of this property for the synthesis of new target drug delivery systems. Recently micelles [284], liposomes [285–289], inorganic nanoparticles [290–292], as well as MSNs [293–296] were functionalized with RGD to improve the cellular uptake and to assure that the drug is released preferentially in the desired site. In these works, authors compared the internalization in several $\alpha_v\beta_3$ integrin-positive tumor cells (U87, HL-7702 and HEH293 cells) with the $\alpha_v\beta_3$ integrin-negative ones (MCF-7 and LO2) using bare and the RGD-grafted systems. Through flow cytometry and fluorescent microscopy, they demonstrated that the internalization of nanocarriers is accelerated and increased by the presence of the targeting agent and that the uptake is mediated by an endocytosis process. It was also demonstrated that the same sequence (Arg-Gly-Asp) does not affect the drug loading and release or the cytotoxic effect of the system [297]. Finally it is worth mentioning that several researchers synthesized double-responsive MSNs systems. For example Xu and co-workers realized a dual-receptor system with RGD and HA to increase the cellular uptake in cells that overexpress $\alpha_v\beta_3$ and CD44 receptors, thus enhancing the cytotoxic effect [297].

5 Experimental techniques

5.1 N_2 adsorption/desorption isotherms

Gas adsorption/desorption is a nondestructive technique used to determine surface area, pore size distribution and pore volume of porous materials. During the measurement, the pressure of the gas increases from vacuum to saturation pressure, and then decreases back to vacuum. By plotting the amount of adsorbed and desorbed gas (usually nitrogen at the temperature of -196°C) as a function of the equilibrium gas pressure (or relative pressure, p/p_0) the adsorption/desorption isotherms are obtained. Fig. 5.1 shows the six isotherms classified by IUPAC. Type I and II are related to microporous and macroporous materials, respectively. Type III is originated from both non-porous and macroporous solids. Type IV and V isotherms are characteristic of mesoporous materials for which gas adsorption occurs via the formation of a multilayer of N_2 molecules that gives the capillary condensation phenomenon. Finally, type VI represents the formation of a multilayer on a uniform non-porous surface.

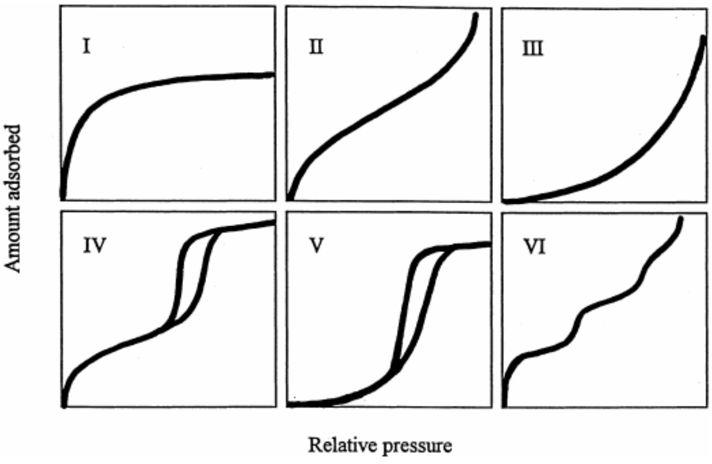

Figure 5.1. IUPAC classification of gas adsorption/desorption isotherms.

Usually, capillary condensation and evaporation do not occur at the same pressure. This give rise to the hysteresis loops shown in Fig 5.2. The H1 hysteresis is characterized by parallel vertical branches derived from the adsorption on materials with a narrow distribution of mesopores. H2 type hysteresis (with a triangular shape) is associated to materials with a complex structure, i.e. materials with narrow windows or with relatively uniform channel-like pores. H3 type hysteresis is derived from the adsorption on the surface of materials constituted by aggregates of plate-like particles forming slit-like pores. Finally, H4 type hysteresis is obtained for the adsorption/desorption in narrow slit-shaped pores or materials with large mesopores embedded in a matrix with pores of much smaller size.

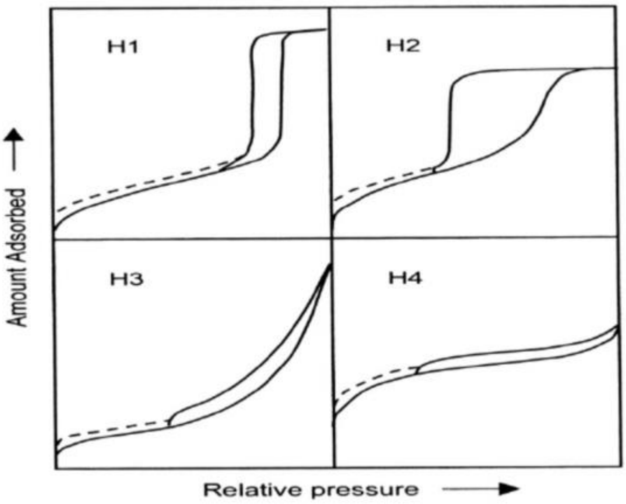

Figure 5.2. IUPAC classification of hysteresis loops.

From adsorption and desorption data, it is possible to obtain the surface area, pore volume and pore size distribution of the porous materials. The most commonly used methods for the calculation of these parameters are:

1. **Surface area.** The Brunauer-Emmet-Teller (BET) equation (eq. 5.1) is commonly used to calculate the surface area [298]:

$$\frac{1}{v\left(\frac{p}{p_0-1}\right)} = \frac{1}{cv_m} + \frac{c-1}{cv_m} \cdot \frac{p}{p_0} \tag{5.1}$$

where v is the volume of adsorbed gas, v_m is the volume of adsorbed gas necessary to form a monolayer, c is the BET constant, p and p_0 are the equilibrium and the saturation gas pressures, respectively. The surface area (S_{BET}) of a porous sample is calculated by:

$$S_{BET} = \frac{v_m N s}{a} \tag{5.2}$$

where N is the Avogadro's number, s is the adsorption cross section of the adsorbing species and a is the mass of the sample.

2. **Pore size.** Barrett-Joyner-Halenda (BJH) method, based on the Kelvin equation (eq. 5.3), is used to calculate the pore size [299]:

$$ln \frac{p}{p_0} = \frac{-2\sigma V}{RT} \cdot \frac{1}{r} \tag{5.3}$$

where r is the radius of the capillary, σ is the surface tension, V is the molar volume of the adsorbate, R is the ideal gas constant, and T the absolute temperature. In the BJH method, pore size distribution is graphically represented as dVp/ddp as a function of d_p (where V_p is the volume of mesopores and dp is the pore radius for cylindrical pores).

N_2-adsorption isotherms were used to measure the surface area, pore volume, and the pore size distribution of the mesoporous silica sample synthesized in this thesis work.

5.2 Small-angle X-rays scattering (SAXS)

X-rays, an electromagnetic radiation characterized by a wavelength between 0.01 and 10 nm, were discovered in 1895 by Wilhelm Conrad Rontgen. X-rays can be used to characterize the structure of solid and liquid materials. Small angle X-rays scattering (SAXS) is a technique widely used for the analysis of nanometric structures. SAXS is based on the elastic scattering of photons, that is the scattered and the incident radiations have exactly the same wavelength. No exchange of energy occurs when the x-ray photons hit the electrons of the sample. More in detail, elastic (Rayleigh and Thomson) scattering is produced when x-ray photons collides with the electrons of a sample. Due to this interaction, the electrons oscillate at the same frequency of the photon and emit radiations with the same wavelength of the incident radiation. The whole process takes place without energy transfer. The neighboring electrons of the sample oscillate in phase producing coherent waves that interfere among them. These interferences generate a pattern which give information about the structure of the material. The SAXS pattern is usually presented as a plot of scattering intensity, $I(q)$ in function of the scattering vector, q [300]:

$$q = \frac{4\pi}{\lambda} sin\theta \qquad [\mathrm{nm}^{-1}] \qquad (5.4)$$

The distance between the planes (d) is correlated to the scattering vector (q) through the following relation:

$$d = \frac{2\pi}{q} \qquad (5.5)$$

A scheme of a SAXS experiment is represent in Fig 5.3. Briefly, the incident radiation r_i hits the sample, and is scattered by its electrons. The scattered radiation, r_s, reaches the detector that records a value of $I(q)$ for each value of q.

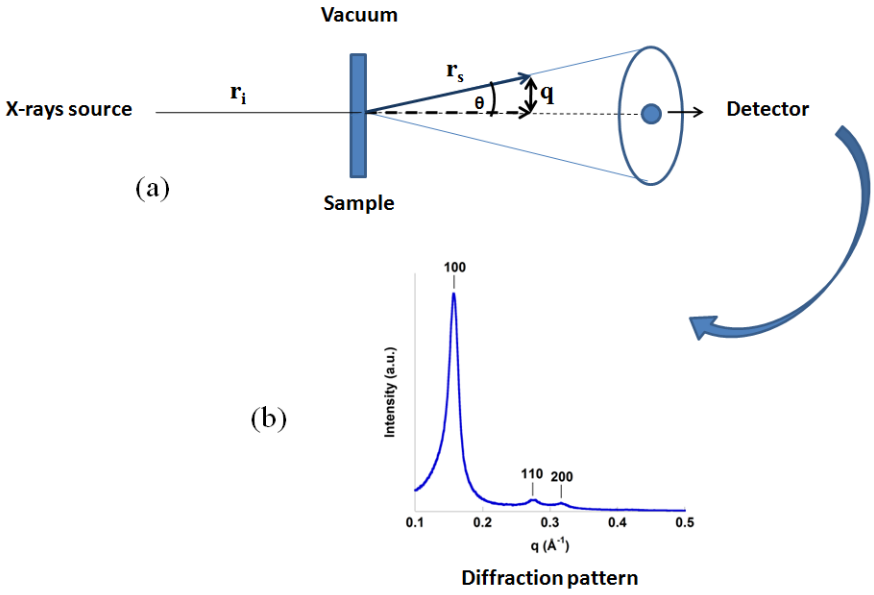

Figure 5.3 Scheme of a SAXS (a) experiment and (b) pattern of a mesoporous silica material with an hexagonal structure.

Scattered waves give constructive interference only if Bragg's law is satisfied:

$$n\lambda = 2dsin\theta \qquad (5.6)$$

where λ is the wavelength, d is the distance between the scattering planes, θ is the angle between the planes of the sample and the incident beam (Fig. 5.4). A constructive interference is obtained only for $n = 1, 2, 3,...$etc..

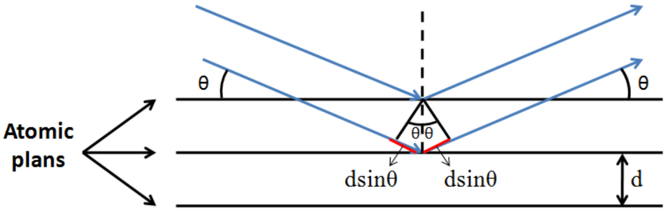

Figure 5.4 Representation of the Bragg's law.

According with Bragg's law the greater is d, the smaller is the scattering angle θ. In practice, the long range order of mesoporous silica samples (SBA-15, MCM-41, etc.) can be investigated at small angles which correspond to low q values. Through SAXS analysis is also possible to obtain the lattice parameter (a). For hexagonal structures the lattice parameter a is calculated by:

$$a = d \cdot \frac{2}{\sqrt{3}}\sqrt{(h^2 + k^2 + hk)} \qquad (5.7)$$

Where d is the distance between the plans, h and k are the Miller indexes.

5.3 Dynamic light scattering (DLS)

Dynamic light scattering (DLS) measures the fluctuations of the intensity of the scattered light due to the Brownian motions of particles suspended in a liquid medium. The intensity fluctuations are analyzed by a correlator which builds the correlation function G(τ) [301]:

$$G(\tau) = A \cdot [1 + Bexp(-2D_T q^2 \tau)] \tag{5.8}$$

Where A and B are the baseline and the intercept of the correlation function, respectively; D_T is the diffusion coefficient, τ is the correlator time delay, and q is the scattering vector:

$$q = \frac{4\pi n}{\lambda_0} sin\frac{\theta}{2} \tag{5.9}$$

where, n is the refractive index of the dispersant, λ_0 is the wavelength of the incident radiation, and θ is the scattering angle. DLS technique is mainly used to measure particles size. Indeed, D_T is related through the Stokes-Einstein equation (eq. 5.10) to the hydrodynamic diameter (d_H) [301,302]:

$$D_T = \frac{kT}{3\pi\eta d_H} \tag{5.10}$$

where k is the Boltzmann's constant, T is the absolute temperature, and η is the viscosity. d_H is the diameter of an hypothetical rigid sphere which has the same

D_T of the particle. In this work of thesis, DLS was used to measure the d_H of MSNs in particular to confirm the external functionalization. Furthermore, DLS measurements are very useful to investigate the behavior of polymer-grafted MSNs (MSN-HA and MSN-CHIT) in aqueous media of different composition.

5.4 Electrophoretic light scattering (ELS)

A charged colloidal particle dispersed in a solution produces an asymmetric distribution of ions generating an electrical double layer. The double layer around the particle can be divided in two regions that is the *Stern* layer, the inner layer where the ions are strongly bound to the particle, and the diffuse layer (at larger distances from the particle surface) where the ions are only weakly bound (Fig. 5.5).

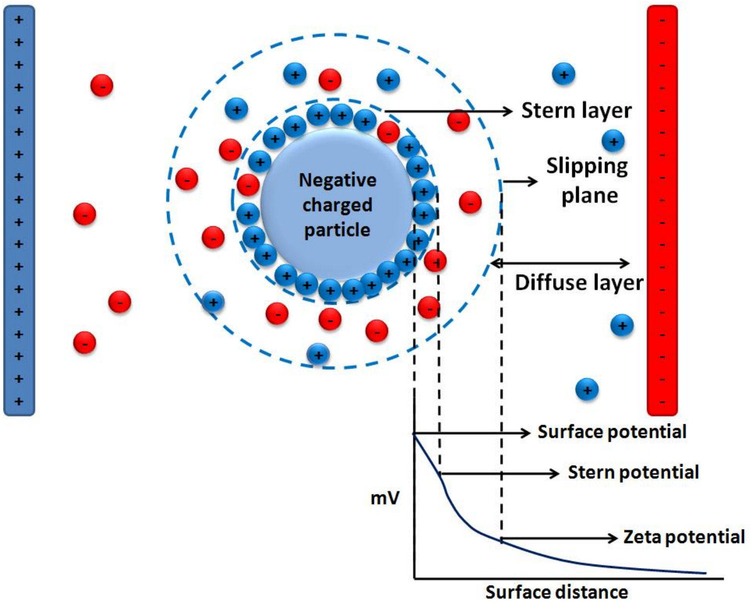

Figure 5.5. Schematic representation of an electrophoretic experiment.

If an electric field is applied across the solution, the charged particles are attracted by the oppositely charged electrode [303]. Viscous forces oppose to the particle movement induced by the electric field. When the equilibrium between these opposing forces is reached, the particles move with a constant velocity, called electrophoretic mobility U_e. In the diffuse layer there is an area (slipping plane) where the ions are stably bound to the particle and move with it. The particle with the bound solvent molecules and ions which moves in the electric field is called 'electrokinetic unit'. The electric potential at the slipping plane is called zeta potential (ζ) and it is related to the U_e through the Henry equation [303]:

$$U_e = \frac{2\varepsilon\zeta f(ka)}{3\eta} \tag{5.11}$$

where, ε is the solvent permittivity, η is the solution viscosity, κ is the inverse Debye length, a is the particle radius, and $f(\kappa a)$ is the Henry function. The value of $f(\kappa a)$ ranges between 1 (Huckel limit) and 1.5 (Smoluchowski limit). The former is used for small particles in low dielectric constant media (generally non-aqueous media), while the latter is used for large particles (> 0.2 μm) dispersed in aqueous media with electrolyte concentrations higher than 10 mM [304].

Electrophoretic light scattering (ELS), determines U_e and, consequently, ζ by means of the Doppler effect. Indeed, the frequency of the light scattered by the charged particles moving in the electric field is slightly different from that of the incident light. The Doppler shift ($\Delta\nu$) is related to the electrophoretic mobility, U_e, through the equation:

$$\Delta\nu = 2U_e \frac{\sin\left(\frac{\theta}{2}\right)}{\lambda} \tag{5.12}$$

where θ is the scattering angle and λ is the wavelength of the incident light. Zeta potential is finally calculated through eq. 5.11.

5.5 Transmission electron microscopy (TEM)

TEM exploits the interaction between electrons and matter to determine the structure of a sample with high resolution. The resolving power (R) of a microscope is its capability to create individual images of objects and is related to the wavelength of the incident radiation λ through the eq. 5.13.

$$R = \frac{0.61\lambda}{n\, sin\theta} \tag{5.13}$$

where n is the refractive index of the medium, and θ is half-open angle subtended to the lens. For an optical microscope the value of R is between 200-300 nm. It is possible to reduce this value with the use of a radiation with smaller values of λ. The wavelength of the electrons is calculated through the *de Broglie* equation:

$$\lambda = \frac{h}{p} = \frac{h}{mv} \tag{5.14}$$

where m and v are the mass and velocity of the electron, respectively.

When a difference of potential is applied, electrons are accelerated with a kinetic energy (V_e) and a wavelength:

$$\lambda = \frac{h}{\left(2mev\cdot\left(1+{}^{ev}/_{2mc^2}\right)\right)^{1/2}} \tag{5.15}$$

Replacing *v* from the de Broglie law, we obtain that the value of λ is:

$$\lambda \approx \frac{1.23}{V^{1/2}} \tag{5.16}$$

From this relationship it follows that for an electron microscope R = 0.1-0.3 nm [305] and, consequently, it is possible to obtain larger magnifications than with a traditional optical microscope. The main components of an electron microscope (Fig. 5.6) are:

- **Electrons source:** it is generally constituted by a filament of tungsten that generates electrons through thermionic effect when left to reach incandescence;
- **Condenser lenses:** they direct the light on the sample;
- **Objective and projector lenses:** they create the first image of the sample;
- **Fluorescent screen:** it creates the enlarged image of the sample.

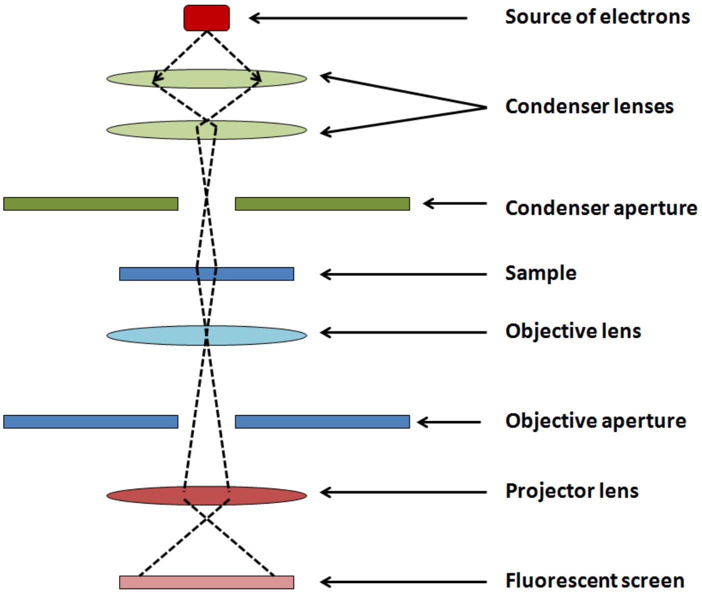

Figure 5.6. Schematic representation of the electron microscope.

In this thesis TEM analysis was used for the structural characterization of mesoporous silica samples. In Fig. 5.7 some example of TEM micrographs are shown. SBA-15 sample (Fig. 5.7a-b) is characterized by particles with size around 1 µm, while MCM-41 has smaller particles, with size in the range between 60-100 nm (Fig. 5.7c). TEM images are useful also to confirm the ordered structure of the samples. Indeed, as shown in Fig. 5.9, for all materials it is possible to see cylindrical pore channels.

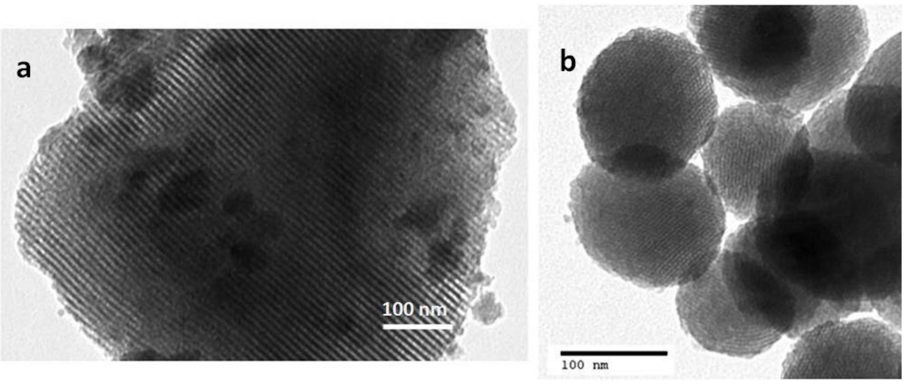

Figure 5.7. TEM micrographs of SBA-15 (a-b) and MCM-41 (c).

In this thesis TEM was also used to monitor MSNs' cellular internalization (see Fig. 5.8a) and adsorption of gold-conjugated proteins on MSNs' surface to investigate the formation of protein corona (Fig. 5.8b).

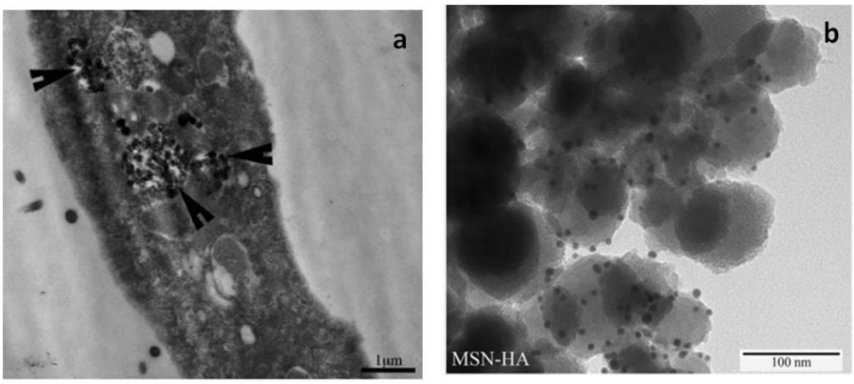

Figure 5.10. HA-grafted MSNs internalized in mouse fibroblasts 3T3 cells (a) and GNP-BSA adsorbed on MSN-HA surface (b).

6 Results

This thesis was aimed to study SBA-15 and MCM-41 mesoporous silica samples for biomedical applications. The texture and the structure of the synthesized materials were characterized through N_2 adsorption/desorption isotherms, SAXS, and TEM. The functionalization of the mesoporous silica samples was verified by means of Fourier-transform infrared spectroscopy (FTIR) and thermogravimetric analysis (TGA). DLS and ELS were used to determinate hydrodynamic diameter and zeta potential of the studied systems under different conditions. This work can be divided in five main parts:

1. Effect of particle size, surface area, pore size and surface charge on the adsorption and release of ampicillin antibiotic from mesoporous silica samples.
2. Synthesis of a double sequential targeting system based on RGD peptide.
3. Study of the internalization of MSNs functionalized with CHIT and HA in 3T3 cells.
4. Investigation of the mechanism of formation of the protein corona on a model system constituted by HA and CHIT functionalized MSNs interacting with bovine serum albumin.
5. Study of the effect of the HA chain length on MSN-HA internalization in HeLa cells.

The following paragraphs give a quick overview of the studies carried out in this thesis. The detailed description of the experimental work, of the obtained results, and of the main conclusions is reported in the attached papers (see appendix section).

6.1 Study of adsorption and release of ampicillin from OMMs (Paper I)

MCM-41, SBA-15 and SBA-15-NH$_2$ (amino-functionalized SBA-15) were used as supports for the investigation of the adsorption and release of ampicillin. Adsorption isotherms showed in Fig 6.1A, described by the Langmuir model, highlighted a maximal loading of 278 mg/g and 237 mg/g for MCM-41 and SBA-15 respectively. The higher amount of ampicillin loaded on MCM-41 sample could be due to the higher surface area which derives from its smaller pore size. Surface charge is another important factor that affects the adsorption process. Indeed, for SBA-15-NH$_2$ the maximal loading recorded was 333 mg/g. This value was justified as a result of the electrostatic interactions between the support and the drug which, in the adsorption conditions (pH=7.4), are positively and negatively charged, respectively (see Fig. 6.1B).

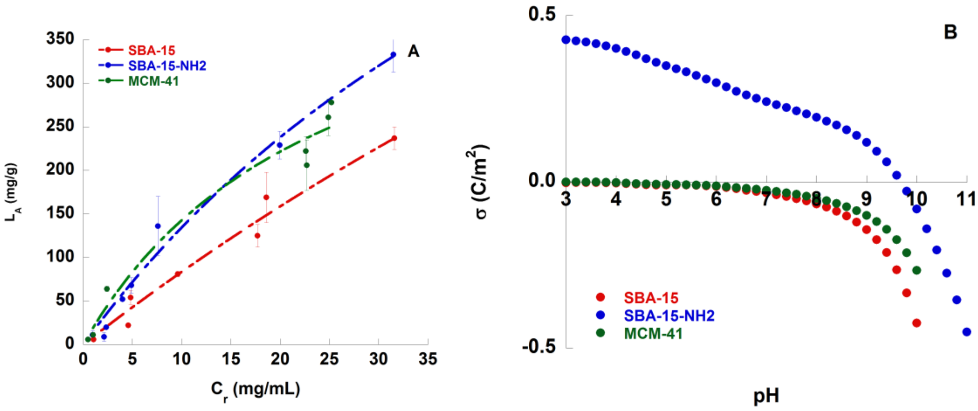

Figure 6.1 Adsorption isotherms (A) and surface charge density versus pH (B) of SBA-15, SBA-15-NH$_2$ and MCM-41.

Kinetic studies of the drug adsorption on mesoporous silica samples, (Fig. 6.2A), allowed the estimation of the adsorption rate constant on OMMs samples. We can observe a decrease of the adsorption rate, according with the series MCM-41>SBA-15>SBA-15-NH2. This trend can be justified with the smaller particles size of MCM-41 that permit a faster diffusion into pore channels. On the other hand, although SBA-15-NH2 shows a lower adsorption rate, it can reach a higher loading. Finally, the release of ampicillin was studied. The release was fast from MCM-41 and SBA-15 and sustained from SBA-15-NH2. Although the first two materials are characterized by different pore size, both carry a negative surface charge at physiological pH (=7.4). Under the same conditions also ampicillin is negatively charged. Hence, repulsive forces established between the drug and the support result in a high release rate at pH 7.4. On the contrary, the sustained release of ampicillin from SBA-15-NH2 is the result of the attractive forces established between the positively charged material and the negatively charged drug (see Fig. 6.2B).

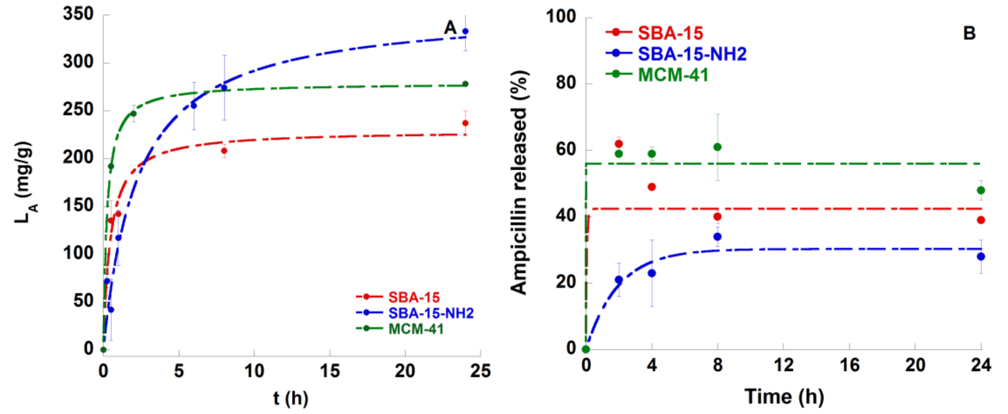

Figure 6.2 Kinetics of adsorption (A) and release (B) of ampicillin from SBA-15, SBA-15-NH$_2$ and MCM-41.

From this study, it emerges that the adsorption and release processes are affected by the surface charge more than by pore size.

6.2 Synthesis of a double sequential targeting system (Paper II)

A common problem of target systems is that the molecule used as targeting agent can be recognized by several receptors. The strategy which was used to solve this issue is the synthesis of a double sequential targeting system. This consists of a tissue target, the alendronate (ALN) and a cellular target, the amino acid sequence Arg-Gly-Asp (RGD), linked together by a PEG chain. The bone tissue was simulated by using hydroxyapatite. Fluorescence microscopy was used to compare the capacity of FITC-labeled BF and RGD to bound HAP tablets. The obtained results demonstrated that ALN is able to recognize the diseased bone. Then the efficiency of the cellular target was investigated. RGD is encrypted inside an oligopeptide sequence (Arg-Pro-Gly-Arg-Asp-Gly-Arg-Cys), so to make this target available, it is necessary to break the link Pro-Gly. This job can be done by Cathepsin K (CK), an enzyme overproduced in the malignant tissues. To confirm this hypothesis the RGD$_{\text{encrypted}}$ peptide was soaked in an acid solution of CK and the obtained product was isolated and analyzed by matrix-assisted laser desorption/ionization (MALDI) time-of-flight/time-of-flight (TOF/TOF) spectrometry. Also the internalization on human osteosarcoma (HOS) cells was studied for PEG-RGD, PEG-RGD$_{\text{encrypted}}$ and the complete system PEG-RGD$_{\text{encrypted}}$-ALN. Flow cytometry data showed a that HOS cells internalized 8%, 12% and 20% of PEG-RGD, PEG-RGD$_{\text{encrypted}}$-ALN and PEG-RGD$_{\text{encrypted}}$, respectively (Fig. 6.3).

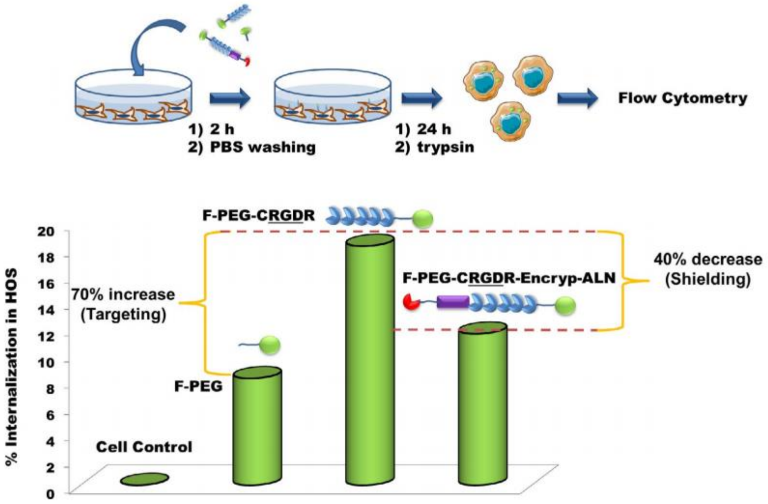

Figure 6.3 Internalization of PEG F-PEG (fluorescently labeled), F-PEG-CRGDR and F-PEG-CRGDR$_{\text{encryped}}$-ALN in HOS.

Finally the complete system was first put in contact with HAP tablets and then placed on the upper sheet of transwells and the cells were cultured on the bottom, and soaked in an acid solution of CK, as schematically shown in Fig. 6.4A. In this case flow cytometry showed fluoresce in the 90% of HOS cells, confirming the internalization (Fig. 6.4B).

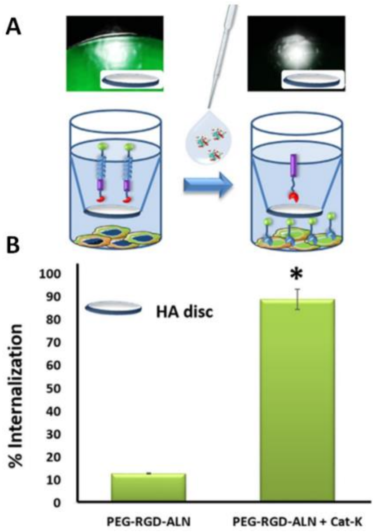

Figure 6.4 Scheme of the CK responsive behavior of F-PEG-CRGDR$_{\text{encrypted}}$-ALN in HOS. Fluorescence microscopy of the HA discs with F-PEG-CRGDR$_{\text{encrypted}}$-ALN (A) and percentage of internalized F-PEG-CRGDR$_{\text{encrypted}}$ (B) before and after CK treatment.

This preliminary study demonstrated the efficiency of the double sequential target system PEG-RGD$_{encrypted}$-ALN and its possible application for drug delivery.

6.3 Cellular uptake in 3T3 cells of MSNs functionalized with CHIT and HA (Paper III)

MCM-41-type MSNs were firstly functionalized with amino groups (MSN-NH$_2$) and then with CHIT and HA polysaccharides to obtain MSN-CHIT and MSN-HA samples. The MTS assay carried out after 24 h of contact with 3T3 cells showed that all these materials favor the cell growth, confirming their high biocompatibility. Important differences were highlighted for the cellular uptake after an exposure time of 24 h and a concentration of MSNs of 100 μg/mL.

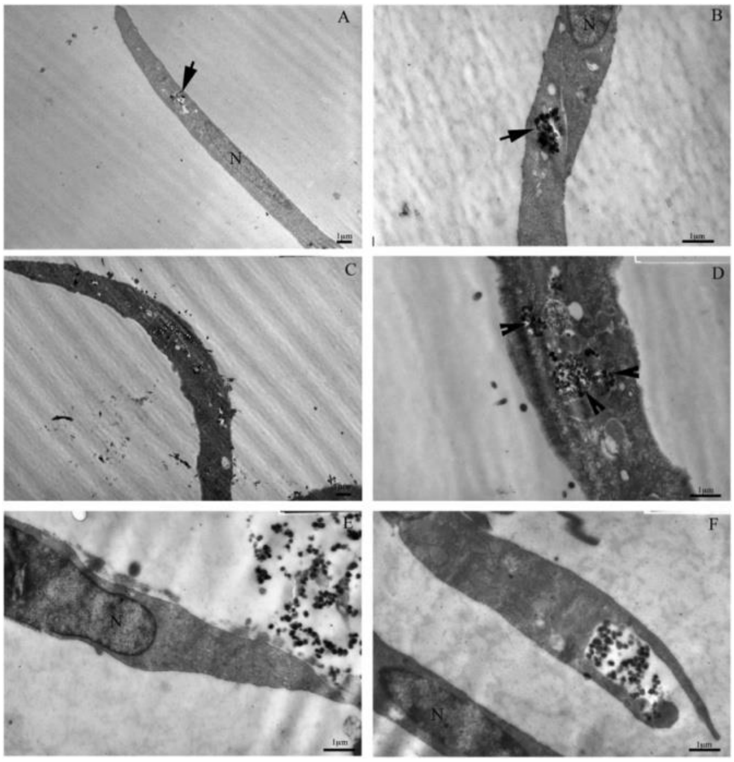

Figure 6.5 Electron micrographs of 3T3 mouse fibroblasts incubated for 24 h with 100 μg/mL of MSNs, and then left to grow for other 24 h in the culture medium. (A-B) MSN-NH$_2$, (C-D) MSN-HA, (E-F) MSN-CHIT.

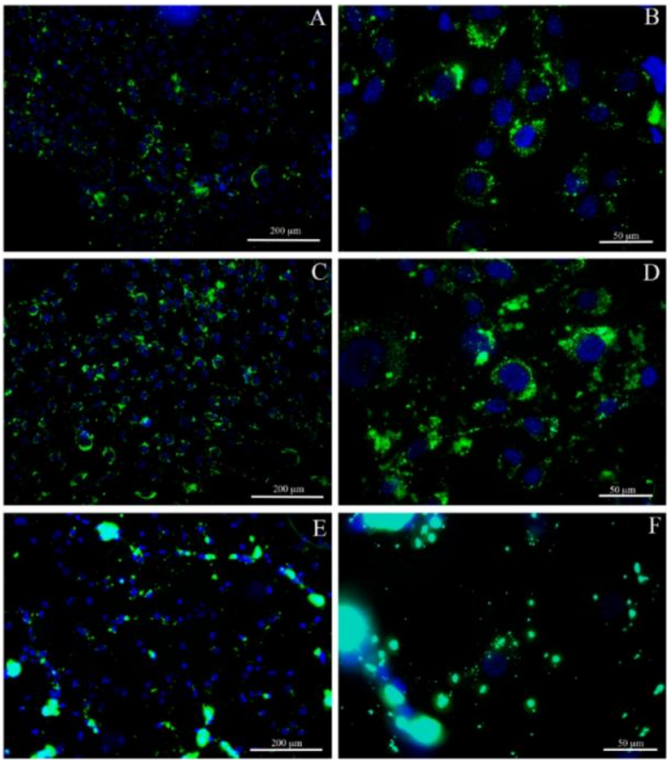

Figure 6.6 Images of fluorececscent microscopy of 3T3 mouse fibroblasts incubated for 24 h with 100 µg/mL of MSNs, and then left to grow for other 24 h in the culture medium. (A-B) MSN-NH_2, (C-D) MSN-HA, (E-F) MSN-CHIT.

Through TEM (Fig. 6.5) and fluorescence (Fig. 6.6) microscopies it has been demonstrated that MSN-NH_2 and MSN-HA were internalized, while MSN-CHIT sample formed large aggregates which could not be internalized by 3T3 cells. Flow cytometry quantified these data, showing for MSN-NH_2 and MSN-HA samples a percentage of cells able to internalize nanoparticles of 79% and 100% respectively. Moreover, the formation of aggregates of MSN-CHIT sample was confirmed by ELS measurements. Indeed, zeta potential values passed from +40 mV in water to −6.7 mV in cell culture medium. This can be attributed to a loss of colloidal stability. All these results highlight that the external functionalization with HA improve the cellular uptake. On the contrary, the interaction between

CHIT-coated MSNs and the components of the medium favor the formation of large aggregates that prevent cell uptake.

6.4 MSNs functionalized with CHIT and HA and their interaction with bovine serum albumin (BSA) (Paper IV)

The same functionalized HA and CHIT functionalized MSNs were used to study the interaction with BSA and the formation of a *protein corona*. All the samples were suspended in a BSA aqueous solution at pH = 7.4 and T = 37°C for 24 h, and then characterized by TEM (Fig. 6.7 A-C), TGA (Fig. 6.7 D-F) and ELS (Tab. 6.1). All these techniques confirmed the interactions between MSNs and BSA proteins.

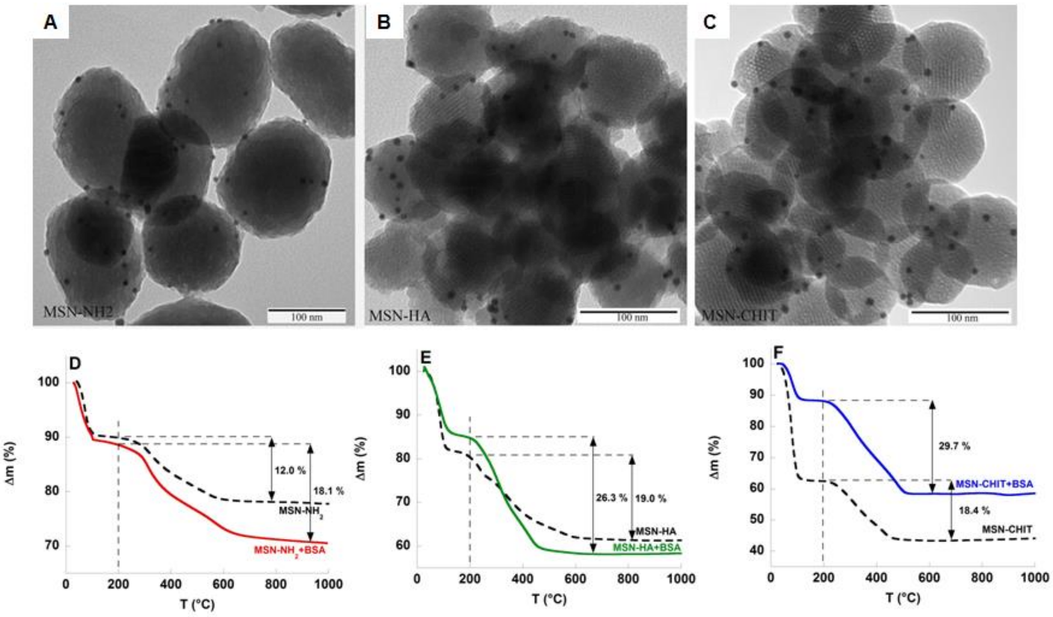

Figure 6.7 Electron micrographs and mass loss percentage of MSN-NH_2+BSA-GNPs (A-D) MSN-HA+BSA-GNPs (B-E) and MSN-CHIT+BSA-GNPs (C-F).

At our experimental pH BSA has a negative net charge (IEP ≈ 4.7) thus it was able to interact with materials with opposite (MSN-NH_2 and MSN-CHIT) charge.

Table 6.1 Characterization of biopolymer-functionalized MSNs and BSA-loaded MSNs. Zeta potential (ζ) in distilled water at 37°C and loading of BSA (L_{BSA}).

Sample	**ζ (mV)**	**L_{BSA} (mg/g)**
MSN	-20.0±0.2	-
MSN-NH_2	+30.6±0.5	-
MSN-HA	-14.8±0.9	-
MSN-CHIT	+10.1±0.3	-
MSN-NH_2+BSA	+9.3±0.3	65
MSN-HA+BSA	-18.5±0.4	79
MSN-CHIT+BSA	-7.7±0.6	127

Surprisingly, BSA also interacted with the negatively charged MSN-HA particles. This can be explained by the action of both electrostatic and non-electrostatic van der Waals interactions that take place in biological systems.

6.5 Study of the effect of the HA chain length on internalization of MSN-HA in HeLa cells (Paper V)

The effect of HA chain length of MSN-HA samples on cell internalization was finally investigated. HA with different molecular weights: HA_S=8-15 kDa, HA_M=30-50 kDa, and HA_L=90-130 kDa was grafted on the external surface of MSNs. The different behavior of MSN-NH_2, MSN-HA_S, MSN-HA_M and MSN-

HA_L was investigated through DLS and ELS measurements at pH 7.4 to simulate biological conditions. An apparently anomalous low value of d_H for MSN-HA_L at pH 7.4 was assigned to the high molecular weight of the polymer and its conformation at this pH value. All the samples (MSN-NH_2, MSN-HA_S, MSN-HA_M and MSN-HA_L) were incubated at 37°C and 4°C for 4 h with HeLa cells to evaluate through optical and electron microscopies the cellular uptake (Fig 6.8 and Fig. 6.9).

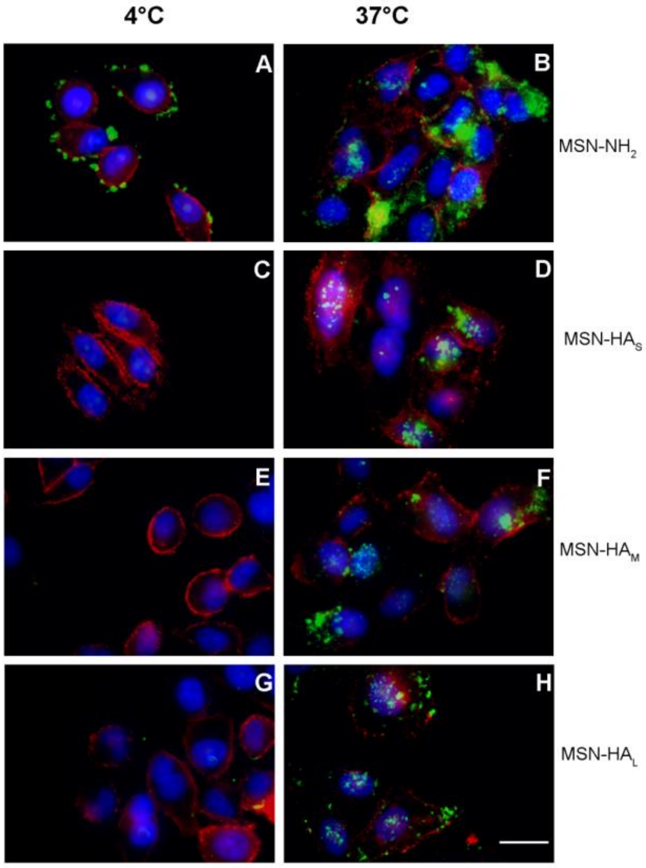

Figure 6.8 Internalization of MSNs using fluorescence microscopy of HeLa cells incubated for 4 h with 50 µg/mL of FITC-MSNs: (A-B) MSN-NH_2, (C-D) MSN-HA_S, (E-F) MSN-HA_M, (G-H) MSN-HA_L. Cell membranes are immunostained with CD44 antibody (red) and nuclei are stained with Hoechst (blue). Bar: 20 µm.

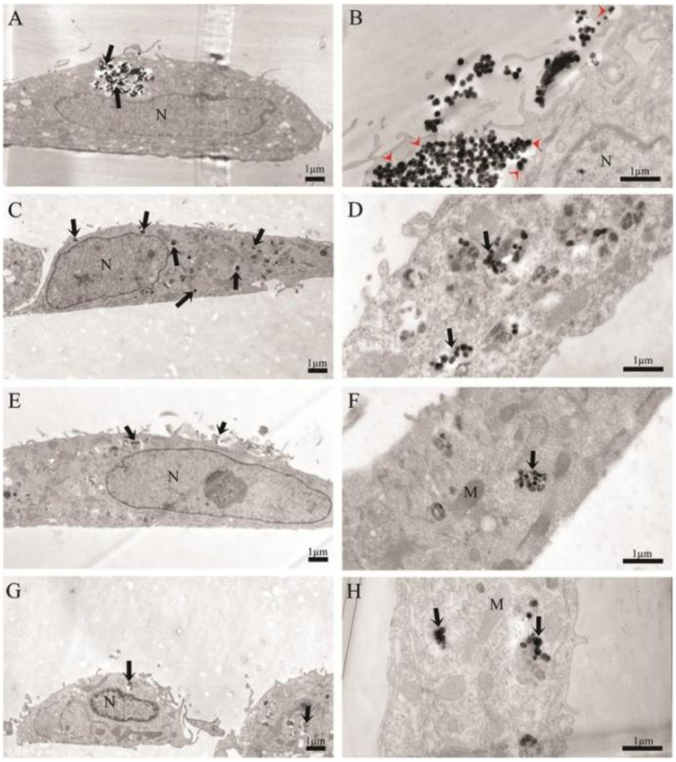

Figure 6.9 Electron micrographs of HeLa cells incubated for 24h: (A-B) MSN-NH_2, (C-D) MSN-HA_S, (E-F) MSN-HA_M, (G-H) MSN-HA_L.

At 37°C all the samples were internalized by HeLa cells through ATP-dependent endocytosis, particularly MSN-NH_2 and MSN-HA_S, as confirmed by flow cytometry data. In the case of MSN-HA_S another factor seems to be at work. Indeed, HeLa cells are CD44-receptors positive, that is they are able to recognize HA and thus to improve cellular uptake as shown in Fig. 6.10. On the contrary, internalization does not take place at 4°C due to the inhibition of the ATP-dependent endocytosis which mediates the process at low temperature. With this study we demonstrated that the chain length of HA is an important factor that can affect the cellular uptake of MSN-HA particles, and needs to be considered for the realization of target drug delivery systems.

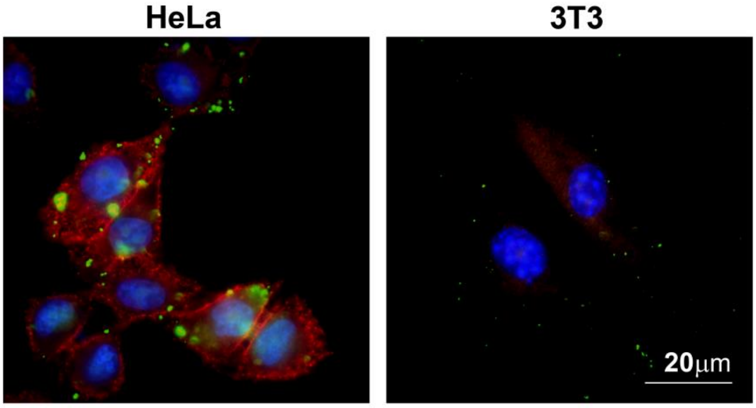

Fig. 6.10 Fluorescence microscopy images of HeLa and 3T3 cells treated for 4 h at 37°C with FITC labeled MSN-HA$_S$. Cell membranes are immunostained with CD44 antibody (red) and nuclei are stained with Hoechst (blue). Bar: 20 μm.

7 Conclusions

In the last years nanomaterials (size 1-100 nm) are having a great development in medicine for several applications such as imaging, gene therapy and drug delivery due to their peculiar physical, chemical and biological properties. The aim of this thesis work was to investigate OMMs (SBA-15 and MCM-41) as depot systems and carriers for biomedical applications. In particular three main aspects were studied:

1. the effect of functionalization of OMMs on the drug adsorption and release phenomena;
2. the possibility to synthesize a new a double target system;
3. the effect of the external functionalization on cell internalization and on the interaction with proteins.

We have demonstrated that drug adsorption and release phenomena are affected by the properties of the material such as pore size and particle size, and especially by their surface charge. In particular for the amino-functionalized material (SBA-15-NH_2) we have obtained the most interesting results. Indeed the attractive electrostatic interaction established between SBA-15-NH_2 and ampicillin (positively and negatively charged respectively at pH 7.4) favor the drug adsorption and hence the obtainment of the highest loading of ampicillin (L=333 mg/g). On the contrary, the same forces slow down the release rate causing a sustained release of ampicillin from this carrier. Another important result is that the concentration of ampicillin in the release solution is 145 μg/mL. This concentration of ampicillin is comparable with that needed in the human serum (80-110 μg/mL for adults and 177-200 μg/mL for children). These studies demonstrated that, in order to obtain a sustained drug release, the chemical nature of the matrix's surface plays a role which is more important than its textural features. This makes SBA-15-NH_2 matrix is a suitable candidate as depot system for local sustained release of ampicillin.

The goal of the second part of the thesis was to try to solve the problem of non-selective targets. For this reason a double target system, that is a system presenting two different targeting molecules, was synthesized. The first is an alendronate, a tissular targeting, able to link the tumoral bone tissue. The second is the peptide known as RGD, recognized by $\alpha_v\beta_3$-integrins overexpressed by several tumor cells, as human osteosarcoma (HOS) cells, used for our studies. As schematically reported in Fig. 7.1 the alendronate is bound through PEG to a peptide chain where the RGD is hidden to avoid that it could be recognized by other cells different from HOS cells.

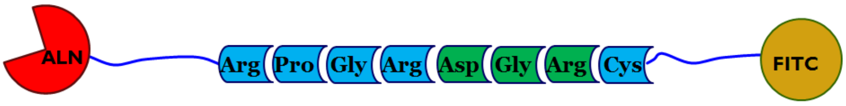

Figure 7.1 Scheme of the double target systems.

This preliminary study showed the efficacy of our double target systems. The planned next step is the functionalization of MSNs with the previously described systems (Fig. 7.1) for the synthesis of a smart target systems usable as a carrier for anticancer drugs against bone cancer.

The last part of the thesis work focused on MSNs external functionalization with biopolymers, such as chitosan (CHIT) and hyaluronic acid (HA). The different features of HA and CHIT affect the cell internalization. The first improve cellular internalization, while the second gave rise to the formation of aggregates, too large to be internalized by the cells. In order to justify this behavior it is very important to consider that a body fluid is constituted by various molecules i.e. proteins, peptides and electrolytes that can interact with the polymer-layer that covers MSNs. As previously described in section 1.2 and 4.1, the adsorption of molecules on the external surface of MSNs cause the formation of a "protein corona" that affects their surface properties and in particular their surface charge. Our studies have demonstrated that the functionalization with HA and CHIT, affects in different way the adsorption of body fluid components. A change in the zeta potential from -7.2 to -10 for MSN-HA and from +40 to -6.7 for MSN-CHIT passing from water to the cell culture medium, composed by proteins, peptides and electrolytes. The adsorption of these components on the surface of functionalized MSNs can justify the decrease in zeta potential values. In particular, in the last case the sign change from a positive value to a negative one highlights a change in the surface properties. This is likely the cause the loss of stability of the MSN-CHIT particles, which form large aggregates that prevent the cellular internalization. We observed a decrease in the surface charge also when MSNs were soaked in a solution of BSA at pH 7.4 (used to simulate a body fluid), highlighting the formation of the protein corona. The establishment of attractive electrostatic forces favors the formation of the protein corona as shown in the case of MSN-NH_2 and MSN-CHIT. It is also important to consider not only electrostatic forces but also van der Waals interactions play a key role. Indeed, in the case of MSN-HA the adsorption of BSA is not justified by electrostatics, but rather by non-electrostatic interactions occurring between functionalized MSNs and BSA, which favored the formation of the protein corona.

Furthermore, it has been found that cellular uptake is affected not only by the chemical nature of the polymer but also by its molecular weight. Cellular internalization experiments, carried out both at 37°C and at 4°C, suggested that the mechanism of internalization is the ATP-dependent endocytosis mediated by CD44 receptors overexpressed by HeLa cells. This mechanism is inhibited at low temperature. The obtained results showed also that the increase of the molecular weight causes a decrease in the cellular uptake.

All these results highlight the importance of OMMs in general and MSNs in particular as nanocarriers for the development of targeting drug delivery systems for cancer treatment.

8 References

[1] H.A. Halpin, M.M. Morales-Suarez-Varela, J.M. Martin-Moreno, Chronic Disease Prevention and the New Public Health, Public Health Reviews. 32 (2010) 120–154. doi:10.1007/BF03391595.

[2] P. Aggarwal, J.B. Hall, C.B. McLeland, M.A. Dobrovolskaia, S.E. McNeil, Nanoparticle interaction with plasma proteins as it relates to particle biodistribution, biocompatibility and therapeutic efficacy, Advanced Drug Delivery Reviews. 61 (2009) 428–437. doi:10.1016/j.addr.2009.03.009.

[3] K. Riehemann, S.W. Schneider, T.A. Luger, B. Godin, M. Ferrari, H. Fuchs, Nanomedicine - Challenge and perspectives, Angewandte Chemie - International Edition. 48 (2009) 872–897. doi:10.1002/anie.200802585.

[4] Y. Chen, H. Chen, J. Shi, In vivo bio-safety evaluations and diagnostic/therapeutic applications of chemically designed mesoporous silica nanoparticles, Advanced Materials. 25 (2013) 3144–3176. doi:10.1002/adma.201205292.

[5] M. Ferrari, Cancer nanotechnology: opportunities and challenges, Nature Reviews Cancer. 5 (2005) 161–171. doi:10.1038/nrc1566.

[6] J. Tabernero, G.I. Shapiro, P.M. LoRusso, A. Cervantes, G.K. Schwartz, G.J. Weiss, L. Paz-Ares, D.C. Cho, J.R. Infante, M. Alsina, M.M. Gounder, R. Falzone, J. Harrop, A.C.S. White, I. Toudjarska, D. Bumcrot, R.E. Meyers, G. Hinkle, N. Svrzikapa, R.M. Hutabarat, V.A. Clausen, J. Cehelsky, S. V. Nochur, C. Gamba-Vitalo, A.K. Vaishnaw, D.W.Y. Sah, J.A. Gollob, H.A. Burris, First-in-humans trial of an RNA interference therapeutic targeting VEGF and KSP in cancer patients with liver involvement, Cancer Discovery. 3 (2013) 406–417. doi:10.1158/2159-8290.CD-12-0429.

[7] S. Shen, M. Liu, T. Li, S. Lin, R. Mo, Recent progress in nanomedicine-based combination cancer therapy using a site-specific co-delivery strategy,

Biomater. Sci. 5 (2017) 1367–1381. doi:10.1039/C7BM00297A.

[8] E.J. Campos, A. Campos, J. Martins, A.F. Ambrósio, Opening eyes to nanomedicine: Where we are, challenges and expectations on nanotherapy for diabetic retinopathy, Nanomedicine: Nanotechnology, Biology, and Medicine. 13 (2017) 2101–2113. doi:10.1016/j.nano.2017.04.008.

[9] S. Hassan, G. Prakash, A. Bal Ozturk, S. Saghazadeh, M. Farhan Sohail, J. Seo, M. Remzi Dokmeci, Y.S. Zhang, A. Khademhosseini, Evolution and clinical translation of drug delivery nanomaterials, Nano Today. 15 (2017) 91–106. doi:10.1016/j.nantod.2017.06.008.

[10] F. Danhier, O. Feron, V. Préat, To exploit the tumor microenvironment : Passive and active tumor targeting of nanocarriers for anti-cancer drug delivery, Journal of Controlled Release. 148 (2015) 135–146. doi:10.1016/j.jconrel.2010.08.027.

[11] E. Hirata, E. Sahai, Tumor Microenvironment and Differential Responses to Therapy, Cold Spring Harbor Perspectives in Medicine. 7 (2017) 1–14. doi:10.1101/cshperspect.a026781.

[12] B. Xiao, L. Ma, D. Merlin, Nanoparticle-mediated co-delivery of chemotherapeutic agent and siRNA for combination cancer therapy, Expert Opinion on Drug Delivery. 14 (2017) 65–73. doi:10.1080/17425247.2016.1205583.

[13] A.J. Primeau, A. Rendon, D. Hedley, L. Lilge, I.F. Tannok, The Distribution of the Anticancer Drug Doxorubicin in Relation to Blood Vessels in Solid Tumors, Clinical Cancer Research. 11 (2005) 8782–8788. doi:10.1158/1078-0432.CCR-05-1664.

[14] D. Mehn, P. Iavicoli, N. Cabaleiro, S. Even, F. Caputo, O. Geiss, L. Calzolai, F. Rossi, D. Gilliland, Analytical ultracentrifugation for analysis of doxorubicin loaded liposomes, International Journal of Pharmaceutics. 523 (2017) 320–326. doi:10.1016/j.ijpharm.2017.03.046.

[15] S.C. Khanna, P. Speiser, Epoxy Resin Beads as a Pharmaceutical Dosage Form I: Method of Preparation, Journal of Pharmaceutical Sciences. 58 (1969) 1114–1116. doi:10.1002/jps.2600581120.

[16] M.. Hans, A.. Lowman, Biodegradable nanoparticles for drug delivery and targeting, Current Opinion in Solid State and Materials Science. 6 (2002) 319–327. doi:10.1016/S1359-0286(02)00117-1.

[17] K. Cho, X. Wang, S. Nie, Z. Chen, D.M. Shin, Therapeutic nanoparticles for drug delivery in cancer, Clinical Cancer Research. 14 (2008) 1310–1316. doi:10.1158/1078-0432.CCR-07-1441.

[18] A. Kumari, S.K. Yadav, S.C. Yadav, Biodegradable polymeric nanoparticles based drug delivery systems, Colloids and Surfaces B: Biointerfaces. 75 (2010) 1–18. doi:10.1016/j.colsurfb.2009.09.001.

[19] N. Han, L. Pang, J. Xu, H. Hyun, J. Park, Y. Yeo, Development of Surface-Variable Polymeric Nanoparticles for Drug Delivery to Tumors, Molecular Pharmaceutics. 14 (2017) 1538–1547. doi:10.1021/acs.molpharmaceut.7b00050.

[20] S.C. Park, Y.M. Kim, J.K. Lee, N.H. Kim, E.J. Kim, H. Heo, M.Y. Lee, J.R. Lee, M.K. Jang, Targeting and synergistic action of an antifungal peptide in an antibiotic drug-delivery system, Journal of Controlled Release. 256 (2017) 46–55. doi:10.1016/j.jconrel.2017.04.023.

[21] S.A. Agnihotri, N.N. Mallikarjuna, T.M. Aminabhavi, Recent advances on chitosan-based micro- and nanoparticles in drug delivery, Journal of Controlled Release. 100 (2004) 5–28. doi:10.1016/j.jconrel.2004.08.010.

[22] T. Wang, J. Hou, C. Su, L. Zhao, Y. Shi, Hyaluronic acid-coated chitosan nanoparticles induce ROS-mediated tumor cell apoptosis and enhance antitumor efficiency by targeted drug delivery via CD44, Journal of Nanobiotechnology. 15 (2017) 1–12. doi:10.1186/s12951-016-0245-2.

[23] Z. Karimi, S. Abbasi, H. Shokrollahi, G. Yousefi, M. Fahham, L. Karimi,

O. Firuzi, Pegylated and amphiphilic Chitosan coated manganese ferrite nanoparticles for pH-sensitive delivery of methotrexate: Synthesis and characterization, Materials Science and Engineering: C. 71 (2017) 504–511. doi:10.1016/j.msec.2016.10.008.

[24] M. Arif, Q.-J. Dong, M.A. Raja, S. Zeenat, Z. Chi, C.-G. Liu, Development of novel pH-sensitive thiolated chitosan/PMLA nanoparticles for amoxicillin delivery to treat Helicobacter pylori, Materials Science and Engineering: C. 83 (2017) 17–24. doi:10.1016/j.msec.2017.08.038.

[25] A. Sharma, U.S. Sharma, Liposomes in drug delivery: Progress and limitations, International Journal of Pharmaceutics. 154 (1997) 123–140. doi:10.1016/S0378-5173(97)00135-X.

[26] M. Mezei, V. Gulasekharam, Liposomes - a selective drug delivery system for the topical route of administration I. Lotion dosage form, Life Sciences. 26 (1980) 1473–1477. doi:10.1016/0024-3205(80)90268-4.

[27] N. Seetharamu, E. Kim, H. Hochster, F. Martin, F. Muggia, Phase II study of liposomal cisplatin (SPI-77) in platinum-sensitive recurrences of ovarian cancer, Anticancer Research. 30 (2010) 541–545.

[28] V.H.L. Lee, H. Ghandehari, T.M. Allen, P.R. Cullis, Liposomal drug delivery systems: From concept to clinical applications, Advanced Drug Delivery Reviews. 65 (2013) 36–48. doi:10.1016/j.addr.2012.09.037.

[29] Y. Lee, D.H. Thompson, Stimuli-responsive liposomes for drug delivery, Wiley Interdisciplinary Reviews: Nanomedicine and Nanobiotechnology. 9 (2017) 1–40. doi:10.1002/wnan.1450.

[30] S. Ganta, H. Devalapally, A. Shahiwala, M. Amiji, A review of stimuli-responsive nanocarriers for drug and gene delivery, Journal of Controlled Release. 126 (2008) 187–204. doi:10.1016/j.jconrel.2007.12.017.

[31] H.S. O’Neill, C.C. Herron, C.L. Hastings, R. Deckers, A. Lopez Noriega, H.M. Kelly, W.E. Hennink, C.O. McDonnell, F.J. O’Brien, E. Ruiz-

Hernández, G.P. Duffy, A stimuli responsive liposome loaded hydrogel provides flexible on-demand release of therapeutic agents, Acta Biomaterialia. 48 (2017) 110–119. doi:10.1016/j.actbio.2016.10.001.

[32] J. Gustafsson, H. Ljusberg-Wahren, M. Almgren, K. Larsson, Cubic Lipid−Water Phase Dispersed into Submicron Particles, Langmuir. 12 (1996) 4611–4613. doi:10.1021/la960318y.

[33] M. Monduzzi, H. Ljusberg-Wahren, K. Larsson, A 13C NMR Study of Aqueous Dispersions of Reversed Lipid Phases, Langmuir. 16 (2000) 7355–7358. doi:10.1021/la0000872.

[34] C. Caltagirone, A.M. Falchi, S. Lampis, V. Lippolis, V. Meli, M. Monduzzi, L. Prodi, J. Schmidt, M. Sgarzi, Y. Talmon, R. Bizzarri, S. Murgia, Cancer-cell-targeted theranostic cubosomes, Langmuir. 30 (2014) 6228–6236. doi:10.1021/la501332u.

[35] S. Murgia, A.M. Falchi, V. Meli, K. Schill??n, V. Lippolis, M. Monduzzi, A. Rosa, J. Schmidt, Y. Talmon, R. Bizzarri, C. Caltagirone, Cubosome formulations stabilized by a dansyl-conjugated block copolymer for possible nanomedicine applications, Colloids and Surfaces B: Biointerfaces. 129 (2015) 87–94. doi:10.1016/j.colsurfb.2015.03.025.

[36] S. Murgia, S. Bonacchi, A.M. Falchi, S. Lampis, V. Lippolis, V. Meli, M. Monduzzi, L. Prodi, J. Schmidt, Y. Talmon, C. Caltagirone, Drug-loaded fluorescent cubosomes: Versatile nanoparticles for potential theranostic applications, Langmuir. 29 (2013) 6673–6679. doi:10.1021/la401047a.

[37] R. Wiwattanapatapee, B. Carreno-Gomez, N. Malik, R. Duncan, PAMAM dendrimers as a potential oral drug delivery system : uptake by everted rat intestinal sacs in-vitro, Journal of Pharmacy and Pharmacology. 50 (1998) 99.

[38] H. Hsu, J. Bugno, S. Lee, S. Hong, Dendrimer-based nanocarriers: a versatile platform for drug delivery, WIREs Nanomedicine and

Nanobiotehnology. 9 (2017) 1–21. doi:10.1002/wnan.1409.

[39] S. Zhu, M. Hong, G. Tang, L. Qian, J. Lin, Y. Jiang, Y. Pei, Partly PEGylated polyamidoamine dendrimer for tumor-selective targeting of doxorubicin: The effects of PEGylation degree and drug conjugation style, Biomaterials. 31 (2010) 1360–1371. doi:10.1016/j.biomaterials.2009.10.044.

[40] Y. Pu, S. Chang, H. Yuan, G. Wang, B. He, Z. Gu, The anti-tumor efficiency of poly(L-glutamic acid) dendrimers with polyhedral oligomeric silsesquioxane cores, Biomaterials. 34 (2013) 3658–3666. doi:10.1016/j.biomaterials.2013.01.082.

[41] Y. Guo, Y. Zhao, J. Zhao, M. Han, A. Zhang, X. Wang, Codendrimer from Polyamidoamine (PAMAM) and Oligoethylene Dendron as a Thermosensitive Drug Carrier, Bioconjugate Chemistry. 25 (2014) 24–31. doi:10.1021/bc300560p.

[42] W. Page Faulk, G. Malcolm Taylor, Communication to the editors. An immunocolloid method for the electron microscope, Immunochemistry. 8 (1971) 1081–1083. doi:10.1016/0019-2791(71)90496-4.

[43] J.L. West, N.J. Halas, Engineered Nanomaterials for Biophotonics Applications: Improving Sensing, Imaging, and Therapeutics, Annual Review of Biomedical Engineering. 5 (2003) 285–292. doi:10.1146/annurev.bioeng.5.011303.120723.

[44] M. Piludu, L. Medda, F. Cugia, M. Monduzzi, A. Salis, Silver Enhancement for Transmission Electron Microscopy Imaging of Antibody Fragment–Gold Nanoparticles Conjugates Immobilized on Ordered Mesoporous Silica, Langmuir. 31 (2015) 9458–9463. doi:10.1021/acs.langmuir.5b02830.

[45] K.S. Siddiqi, A. Husen, Recent advances in plant-mediated engineered gold nanoparticles and their application in biological system, Journal of Trace

Elements in Medicine and Biology. 40 (2017) 10–23. doi:10.1016/j.jtemb.2016.11.012.

[46] M. Ghorbani, H. Hamishehkar, Decoration of gold nanoparticles with thiolated pH-responsive polymeric (PEG- b -p(2-dimethylamio ethyl methacrylate- co -itaconic acid) shell: A novel platform for targeting of anticancer agent, Materials Science and Engineering: C. 81 (2017) 561–570. doi:10.1016/j.msec.2017.08.021.

[47] R.S. Bowman, Applications of surfactant-modified zeolites to environmental remediation, Microporous and Mesoporous Materials. 61 (2003) 43–56. doi:10.1016/S1387-1811(03)00354-8.

[48] S. Kesraoui-Ouki, C.R. Cheeseman, R. Perry, Natural zeolite utilisation in pollution control: A review of applications to metals' effluents, Journal of Chemical Technology & Biotechnology. 59 (1994) 121–126. doi:10.1002/jctb.280590202.

[49] Y. Tao, H. Kanoh, L. Abrams, K. Kaneko, Mesopore-Modified Zeolites : Preparation , Characterization , and Applications, (2006) 896–910. doi:10.1021/cr040204o.

[50] J.S. Beck, K.D. Schmitt, J.B. Higgins, J.L. Schlenkert, New Family of Mesoporous Molecular Sieves Prepared with Liquid Crystal Templates, Journal of American Chemical Society. 114 (1992) 10834–10843. doi:10.1021/ja00053a020.

[51] S. Inagaki, Y. Fukushima, K. Kuroda, Synthesis of highly ordered mesoporous materials from a layered polysilicate, Journal of the Chemical Society, Chemical Communications. 0 (1993) 680–682. doi:10.1039/c39930000680.

[52] J. Liang, Z. Liang, R. Zou, Y. Zhao, Heterogeneous Catalysis in Zeolites, Mesoporous Silica, and Metal-Organic Frameworks, Advanced Materials. 29 (2017) 1701139–1701159. doi:10.1002/adma.201701139.

[53] Z.A. Alothman, A review: Fundamental aspects of silicate mesoporous materials, Materials. 5 (2012) 2874–2902. doi:10.3390/ma5122874.

[54] C.T. Kresge, M.E. Leonowicz, W.J. Roth, J.C. Vartuli, J.S. Beck, Ordered mesoporous molecular sieves synthesized by liquid-crystal template mechanism, Nature. 359 (1992) 710–712. doi:10.1038/355242a0.

[55] Liquid-crystalline phases as templates for the synthesis of mesoporous silica, Nature. 378 (1995) 366–368.

[56] F. Hoffmann, M. Cornelius, J. Morell, M. Fröba, Silica-Based Mesoporous Organic–Inorganic Hybrid Materials, Angewandte Chemie International Edition. 45 (2006) 3216–3251. doi:10.1002/anie.200503075.

[57] D. Zhao, Q. Huo, J. Feng, B.F. Chmelka, G.D. Stucky, Nonionic Triblock and Star Diblock Copolymer and Oligomeric Surfactant Syntheses of Highly Ordered, Hydrothermally Stable, Mesoporous Silica Structures, Journal of American Chemical Society. 120 (1998) 6024–6036. doi:Doi 10.1021/Ja974025i.

[58] D. Zhao, J. Feng, Q. Huo, N. Melosh, G. Fredrickson, B. Chmelka, G. Stucky, Triblock copolymer syntheses of mesoporous silica with periodic 50 to 300 angstrom pores, Science (New York, N.Y.). 279 (1998) 548–52. doi:10.1126/science.279.5350.548.

[59] S. a Bagshaw, T.J. Pinnavaia, Mesoporous Alumina Molecular Sieves, Angewandte Chemie International Edition In English. 35 (1996) 1102–1105. doi:10.1002/anie.199611021.

[60] S.A. Bagshaw, E. Prouzet, T.J. Pinnavaia, Porous inorganic oxide materials prepared by non-ionic surfactant templating route, Journal of Cleaner Production. 269 (1995) 1242–1244. doi:10.1016/S0959-6526(97)80819-0.

[61] Y. Wan, D. Zhao, On the controllable soft-templating approach to mesoporous silicates, Chemical Reviews. 107 (2007) 2821–2860. doi:10.1021/cr068020s.

[62] A. Monnier, F. Schuth, Q. Huo, D. Kumar, D. Margolese, R.S. Maxwell, G.D. Stucky, M. Krishnamurty, P. Petroff, A. Firouzi, M. Janicke, B.F. Chmelka, Coopertive formation of inorganic-organic interfaces in the synthesis of silicates mesostructures, Science. 261 (1993) 1299–1303.

[63] T. Kjellman, V. Alfredsson, The use of in situ and ex situ techniques for the study of the formation mechanism of mesoporous silica formed with non-ionic triblock copolymers, Chem. Soc. Rev. 42 (2013) 3777–3791. doi:10.1039/C2CS35298B.

[64] M. Lindén, S.A. Schunk, F. Schüth, In situ X-ray diffraction study of the initial stages of formation of MCM-41 in a tubular reactor, Angewandte Chemie - International Edition. 37 (1998) 821–823. doi:10.1002/(SICI)1521-3773(19980403)37:6<821::AID-ANIE821>3.0.CO;2-I.

[65] V. Alfredsson, H. Wennerstrom, The Dynamic Association Processes Leading from a Silica Precursor to a Mesoporous SBA-15 Material, Accounts of Chemical Research. 48 (2015) 1891–1900. doi:10.1021/acs.accounts.5b00165.

[66] E. Magner, Immobilisation of enzymes on mesoporous silicate materials, Chemical Society Reviews. 42 (2013) 6213–6222. doi:10.1039/c2cs35450k.

[67] Y. Cao, R. Ran, Y. Chen, X. Wu, D. Weng, Nanostructured platinum in ordered mesoporous silica as novel efficient catalyst for propane total oxidation, RSC Adv. 6 (2016) 30170–30175. doi:10.1039/C5RA27303J.

[68] H. Veisi, A. Amini Manesh, N. Eivazi, A.R. Faraji, Palladium nanoparticles supported on 1,3-dicyclohexylguanidine functionalized mesoporous silica SBA-15 as highly active and reusable catalyst for the Suzuki–Miyaura cross-coupling reaction, RSC Adv. 5 (2015) 20098–20107. doi:10.1039/C4RA14668A.

[69] O. Hamid, M.A. Chari, C. Van Nguyen, J.E. Chen, S.M. Alshehri, E. Yanmaz, S.A. Hossain, Y. Yamauchi, K.C.W. Wu, ZnO-loaded mesoporous silica (KIT-6) as an efficient solid catalyst for production of various substituted quinoxalines, Catalysis Communications. 90 (2017) 111–115. doi:10.1016/j.catcom.2016.10.026.

[70] J. Deere, E. Magner, J.G. Wall, B.K. Hodnett, Mechanistic and structural features of protein adsorption onto mesoporous silicates, Journal of Physical Chemistry B. 106 (2002) 7340–7347. doi:10.1021/jp0139484.

[71] S. Hudson, E. Magner, J. Cooney, B. Kieran, Methodology for the immobilization of enzymes onto mesoporous materials, Journal of Physical Chemistry B. 109 (2005) 19496–19506. doi:10.1021/jp052102n.

[72] M. Zheng, X. Xiang, S. Wang, J. Shi, Q. Deng, F. Huang, R. Cong, Lipase immobilized in ordered mesoporous silica: A powerful biocatalyst for ultrafast kinetic resolution of racemic secondary alcohols, Process Biochemistry. 53 (2017) 102–108. doi:10.1016/j.procbio.2016.12.005.

[73] M.S. Bhattacharyya, P. Hiwale, M. Piras, L. Medda, D. Steri, M. Piludu, A. Salis, M. Monduzzi, Lysozyme Adsorption and Release from Ordered Mesoporous Materials, The Journal of Physical Chemistry C. 114 (2010) 19928–19934. doi:10.1021/jp1078218.

[74] L. Medda, M.F. Casula, M. Monduzzi, A. Salis, Adsorption of Lysozyme on Hyaluronic Acid Functionalized SBA-15 Mesoporous Silica: A Possible Bioadhesive Depot System, Langmuir. 30 (2014) 12996–13004. doi:10.1021/la503224n.

[75] M.M. Lynch, J. Liu, M. Nigra, M.O. Coppens, Chaperonin-Inspired pH Protection by Mesoporous Silica SBA-15 on Myoglobin and Lysozyme, Langmuir. 32 (2016) 9604–9610. doi:10.1021/acs.langmuir.6b02832.

[76] A. Salis, M. Pisano, M. Monduzzi, V. Solinas, E. Sanjust, Laccase from Pleurotus sajor-caju on functionalised SBA-15 mesoporous silica:

Immobilisation and use for the oxidation of phenolic compounds, Journal of Molecular Catalysis B: Enzymatic. 58 (2009) 175–180. doi:10.1016/j.molcatb.2008.12.008.

[77] F. Pitzalis, M. Monduzzi, A. Salis, A bienzymatic biocatalyst constituted by glucose oxidase and Horseradish peroxidase immobilized on ordered mesoporous silica, Microporous and Mesoporous Materials. 241 (2017) 145–154. doi:10.1016/j.micromeso.2016.12.023.

[78] H. Takahashi, B. Li, T. Sasaki, C. Miyazaki, T. Kajino, S. Inagaki, Immobilized enzymes in ordered mesoporous silica materials and improvement of their stability and catalytic activity in an organic solvent, Micropor Mesopor Mat. 44–45 (2001) 755–762. doi:10.1016/S1387-1811(01)00257-8.

[79] H. Takahashi, B. Li, T. Sasaki, C. Miyazaki, T. Kajino, S. Inagaki, Catalytic Activity in Organic Solvents and Stability of Immobilized Enzymes Depend on the Pore Size and Surface Characteristics of Mesoporous Silica, Chemistry of Materials. 12 (2000) 3301–3305. doi:10.1021/cm000487a.

[80] Y. Wan, H. Wang, Q. Zhao, M. Klingstedt, O. Terasaki, D. Zhao, Ordered Mesoporous Pd/Silica−Carbon as a Highly Active Heterogeneous Catalyst for Coupling Reaction of Chlorobenzene in Aqueous Media, Journal of the American Chemical Society. 131 (2009) 4541–4550. doi:10.1021/ja808481g.

[81] J. Ren, P. Hao, W. Sun, R. Shi, S. Liu, Ordered mesoporous silica-carbon-supported copper catalyst as an efficient and stable catalyst for catalytic oxidative carbonylation, Chemical Engineering Journal. 328 (2017) 673–682. doi:10.1016/j.cej.2017.07.101.

[82] M.R. Awual, Novel nanocomposite materials for efficient and selective mercury ions capturing from wastewater, Chemical Engineering Journal. 307 (2017) 456–465. doi:10.1016/j.cej.2016.08.108.

[83] Q. Meng, X. Zhang, C. He, G. He, P. Zhou, C. Duan, Multifunctional mesoporous silica material used for detection and adsorption of Cu2+in aqueous solution and biological applications in vitro and in vivo, Advanced Functional Materials. 20 (2010) 1903–1909. doi:10.1002/adfm.201000080.

[84] A. Kunamneni, I. Ghazi, S. Camarero, A. Ballesteros, F.J. Plou, M. Alcalde, Decolorization of synthetic dyes by laccase immobilized on epoxy-activated carriers, Process Biochemistry. 43 (2008) 169–178. doi:10.1016/j.procbio.2007.11.009.

[85] P. Peralta-Zamora, C.M. Pereira, E.R.L. Tiburtius, S.G. Moraes, M.A. Rosa, R.C. Minussi, N. Durán, Decolorization of reactive dyes by immobilized laccase, Applied Catalysis B: Environmental. 42 (2003) 131–144. doi:10.1016/S0926-3373(02)00220-5.

[86] M. Alcalde, T. Bulter, M. Zumárraga, H. García-Arellano, M. Mencía, F.J. Plou, A. Ballesteros, Screening Mutant Libraries of Fungal Laccases in the Presence of Organic Solvents, Journal of Biomolecular Screening. 10 (2005) 624–631. doi:10.1177/1087057105277058.

[87] R.S. Franchi, P.J.E. Harlick, A. Sayari, Applications of pore-expanded mesoporous silica. 2. Development of a high-capacity, water-tolerant adsorbent for CO2, Industrial and Engineering Chemistry Research. 44 (2005) 8007–8013. doi:10.1021/ie0504194.

[88] S. Park, J. Bang, J. Choi, S.H. Lee, J.H. Lee, J.S. Lee, 3-Dimensionally disordered mesoporous silica (DMS)-containing mixed matrix membranes for CO2and non-CO2 greenhouse gas separations, Separation and Purification Technology. 136 (2014) 286–295. doi:10.1016/j.seppur.2014.09.016.

[89] C.F. Martín, M.B. Sweatman, S. Brandani, X. Fan, Wet impregnation of a commercial low cost silica using DETA for a fast post-combustion CO2 capture process, Applied Energy. 183 (2016) 1705–1721. doi:10.1016/j.apenergy.2016.09.081.

[90] C.-Y. Chen, H. Li, M.E. Davis, Studies on mesoporous materials I . Synthesis and characterization of MCM-41, Microporous Materials. 2 (1993) 17–26.

[91] C. Zhao, A. Tan, G. Pastorin, H.K. Ho, Nanomaterial scaffolds for stem cell proliferation and differentiation in tissue engineering, Biotechnology Advances. 31 (2013) 654–668. doi:10.1016/j.biotechadv.2012.08.001.

[92] J.M. Rosenholm, J. Zhang, M. Linden, C. Sahlgren, Mesoporous silica nanoparticles in tissue engineering – a perspective, Nanomedicine. 11 (2016) 391–402. doi:10.2217/nnm.15.212.

[93] C.G. Trejo, D. Lozano, M. Manzano, J.C. Doadrio, A.J. Salinas, S. Dapía, E. Gómez-Barrena, M. Vallet-Regí, N. García-Honduvilla, J. Buján, P. Esbrit, The osteoinductive properties of mesoporous silicate coated with osteostatin in a rabbit femur cavity defect model, Biomaterials. 31 (2010) 8564–8573. doi:10.1016/j.biomaterials.2010.07.103.

[94] T. Kokubo, H. Takadama, How useful is SBF in predicting in vivo bone bioactivity?, Biomaterials. 27 (2006) 2907–2915. doi:10.1016/j.biomaterials.2006.01.017.

[95] M. Korim, S. Scholes, A. Unsworth, R. Power, Retrieval analysis of alumina ceramic-on-ceramic bearing couples, Acta Orthopaedica. 85 (2014) 133–140. doi:10.3109/17453674.2014.894390.

[96] A. Tofighi, Calcium Phosphate Bone Cement (CPBC): Development, Commercialization and Future Challenges., Key Engineering Materials. 493–494 (2012) 349–354. doi:10.4028/www.scientific net/KEM.493-494.349.

[97] T. Tateiwa, I.C. Clarke, G. Pezzotti, L. Sedel, T. Kumakura, T. Shishido, K. Yamamoto, Surface Micro-Analyses of Long-Term Worn Retrieved “‘OstealTM’” Alumina Ceramic Total Hip Replacement, Journal of Biomedical Materials Research. Part B, Applied Biomaterials. 83 (2007)

562–570. doi:10.1002/jbmb.

[98] L.L. Hench, R.J. Splinter, W.C. Allen, T.K. Greenlee, Bonding mechanisms at the interface of ceramic prosthetic materials, Journal of Biomedical Materials Research. 5 (1971) 117–141. doi:10.1002/jbm.820050611.

[99] J. Wilson, G.H. Pigott, F.J. Schoen, L.L. Hench, Toxicology and biocompatibility of bioglasses, Journal of Biomedical Materials Research. 15 (1981) 805–817. doi:10.1002/jbm.820150605.

[100] J. Wilson, S.B. Low, Bioactive ceramics for periodontal treatment: Comparative studies in the patus monkey, Journal of Applied Biomaterials. 3 (1992) 123–129. doi:10.1002/jab.770030208.

[101] I.D. Xynos, A.J. Edgar, L.D.K. Buttery, L.L. Hench, J.M. Polak, Ionic Products of Bioactive Glass Dissolution Increase Proliferation of Human Osteoblasts and Induce Insulin-like Growth Factor II mRNA Expression and Protein Synthesis, Biochemical and Biophysical Research Communications. 276 (2000) 461–465. doi:10.1006/bbrc.2000.3503.

[102] I.D. Xynos, M.V.J. Hukkanen, J.J. Batten, L.D. Buttery, L.L. Hench, J.M. Polak, Bioglass ®45S5 Stimulates Osteoblast Turnover and Enhances Bone Formation In Vitro: Implications and Applications for Bone Tissue Engineering, Calcified Tissue International. 67 (2000) 321–329. doi:10.1007/s002230001134.

[103] L.L. Hench, The future of bioactive ceramics, Journal of Materials Science: Materials in Medicine. 26 (2015) 86. doi:10.1007/s10856-015-5425-3.

[104] C.J. Brinker, Y. Lu, A. Sellinger, H. Fan, Evaporation-Induced Self-Assembly: Nanostructures Made Easy, Advanced Materials. 11 (1999) 579–585.

[105] M. Vallet-Regí, Nanostructured mesoporous silica matrices in nanomedicine, Journal of Internal Medicine. 267 (2010) 22–43.

doi:10.1111/j.1365-2796.2009.02190.x.

[106] M. Vallet-Regi, A. Rámila, R.P. Del Real, J. Pérez-Pariente, A new property of MCM-41: Drug delivery system, Chemistry of Materials. 13 (2001) 308–311. doi:10.1021/cm0011559.

[107] A.L. Doadrio, J.M. Sánchez-Montero, J.C. Doadrio, A.J. Salinas, M. Vallet-Regí, A molecular model to explain the controlled release from SBA-15 functionalized with APTES, Microporous and Mesoporous Materials. 195 (2014) 43–49. doi:10.1016/j.micromeso.2014.04.019.

[108] N.Ž. Knežević, J.-O. Durand, Large pore mesoporous silica nanomaterials for application in delivery of biomolecules, Nanoscale. 7 (2015) 2199–2209. doi:10.1039/C4NR06114D.

[109] D. Berger, L. Bajenaru, S. Nastase, R.-A. Mitran, C. Munteanu, C. Matei, Influence of structural, textural and surface properties of mesostructured silica and aluminosilicate carriers on aminoglycoside uptake and in vitro delivery, Microporous and Mesoporous Materials. 206 (2015) 150–160. doi:10.1016/j.micromeso.2014.12.022.

[110] F. Sevimli, A. Yılmaz, Surface functionalization of SBA-15 particles for amoxicillin delivery, Microporous and Mesoporous Materials. 158 (2012) 281–291. doi:10.1016/j.micromeso.2012.02.037.

[111] A.L. Doadrio, E.M.B. Sousa, J.C. Doadrio, J. Pérez Pariente, I. Izquierdo-Barba, M. Vallet-Regí, Mesoporous SBA-15 HPLC evaluation for controlled gentamicin drug delivery, Journal of Controlled Release. 97 (2004) 125–132. doi:10.1016/j.jconrel.2004.03.005.

[112] E.I. Basaldella, M.S. Legnoverde, Functionalized silica matrices for controlled delivery of cephalexin, Journal of Sol-Gel Science and Technology. 56 (2010) 191–196. doi:10.1007/s10971-010-2293-7.

[113] M. Vallet-Regì, J.C. Doadrio, A.L. Doadrio, I. Izquierdo-Barba, J. Perez-Pariente, Hexagonal ordered mesoporous material as a matrix for the

controlled release of amoxicillin, Solid State Ionics. 172 (2004) 435–439. doi:10.1016/j.ssi.2004.04.036.

[114] A. Pourjavadi, Z.M. Tehrani, Mesoporous Silica Nanoparticles (MCM-41) Coated PEGylated Chitosan as a pH-Responsive Nanocarrier for Triggered Release of Erythromycin, International Journal of Polymeric Materials and Polymeric Biomaterials. 63 (2014) 692–697. doi:10.1080/00914037.2013.862534.

[115] G.F. Andrade, V.S. Gomide, A.C. da Silva Júnior, A.M. Goes, E.M.B. de Sousa, An in situ synthesis of mesoporous SBA-16/hydroxyapatite for ciprofloxacin release: in vitro stability and cytocompatibility studies, Journal of Materials Science: Materials in Medicine. 25 (2014) 2527–2540. doi:10.1007/s10856-014-5273-6.

[116] D. Molina-Manso, M. Manzano, J.C. Doadrio, G. Del Prado, A. Ortiz-Pérez, M. Vallet-Regì, E. Gòmez-Barrena, J. Esteban, Usefulness of SBA-15 mesoporous ceramics as a delivery system for vancomycin, rifampicin and linezolid: A preliminary report, International Journal of Antimicrobial Agents. 40 (2012) 252–256. doi:10.1016/j.ijantimicag.2012.05.013.

[117] A. Szegedi, M. Popova, I. Goshev, J. Mihály, Effect of amine functionalization of spherical MCM-41 and SBA-15 on controlled drug release, Journal of Solid State Chemistry. 184 (2011) 1201–1207. doi:10.1016/j.jssc.2011.03.005.

[118] Q. Gao, Y. Xu, D. Wu, W. Shen, F. Deng, Synthesis, characterization, and in vitro pH-controllable drug release from mesoporous silica spheres with switchable gates, Langmuir. 26 (2010) 17133–17138. doi:10.1021/la102952n.

[119] A. Szegedi, M. Popova, I. Goshev, S. Klébert, J. Mihály, Controlled drug release on amine functionalized spherical MCM-41, Journal of Solid State Chemistry. 194 (2012) 257–263. doi:10.1016/j.jssc.2012.05.030.

[120] S. Rahmani, J.O. Durand, C. Charnay, L. Lichon, M. Férid, M. Garcia, M. Gary-Bobo, Synthesis of mesoporous silica nanoparticles and nanorods: Application to doxorubicin delivery, Solid State Sciences. 68 (2017) 25–31. doi:10.1016/j.solidstatesciences.2017.04.003.

[121] Y. Jiao, S. Shen, Y. Sun, X. Jiang, W. Yang, A Functionalized Hollow Mesoporous Silica Nanoparticles-Based Controlled Dual-Drug Delivery System for Improved Tumor Cell Cytotoxicity, Particle & Particle Systems Characterization. 32 (2015) 222–233. doi:10.1002/ppsc.201400115.

[122] Y. Yan, J. Fu, X. Liu, T. Wang, X. Lu, Acid-responsive intracellular doxorubicin release from click chemistry functionalized mesoporous silica nanoparticles, RSC Advances. 5 (2015) 30640–30646. doi:10.1039/C5RA00059A.

[123] M. Catauro, F. Papale, G. Roviello, C. Ferone, F. Bollino, M. Trifuoggi, C. Aurilio, Synthesis of SiO2 and CaO rich calcium silicate systems via sol-gel process: Bioactivity, biocompatibility, and drug delivery tests, Journal of Biomedical Materials Research - Part A. 102 (2014) 3087–3092. doi:10.1002/jbm.a.34978.

[124] S. Kamath, S. Sinha, E. Shaari, D. Young, A.C. Campbell, Role of topical antibiotics in hip surgery: A prospective randomised study, Injury. 36 (2005) 783–787. doi:10.1016/j.injury.2005.01.001.

[125] A. Baeza, M. Colilla, M. Vallet-Regí, Advances in mesoporous silica nanoparticles for targeted stimuli-responsive drug delivery, Expert Opinion on Drug Delivery. 12 (2015) 319–337. doi:10.1517/17425247.2014.953051.

[126] L.B. de O. Freitas, L. de M. Corgosinho, J.A.Q.A. Faria, V.M. dos Santos, J.M. Resende, A.S. Leal, D.A. Gomes, E.M.B. de Sousa, Multifunctional mesoporous silica nanoparticles for cancer-targeted, controlled drug delivery and imaging, Microporous and Mesoporous Materials. 242 (2017) 271–283. doi:10.1016/j.micromeso.2017.01.036.

[127] J. Rejman, V. Oberle, I.S. Zuhorn, D. Hoekstra, Size-dependent internalization of particles via the pathways of clathrin- and caveolae-mediated endocytosis, Biochemical Journal. 377 (2004) 159–169. doi:10.1042/bj20031253.

[128] S. Misra, P. Heldin, V.C. Hascall, N.K. Karamanos, S.S. Skandalis, R.R. Markwald, S. Ghatak, Hyaluronan-CD44 interactions as potential targets for cancer therapy, FEBS Journal. 278 (2011) 1429–1443. doi:10.1111/j.1742-4658.2011.08071.x.

[129] I.F. Tannock, D. Rotin, Acid pH in tumors and its potential for therapeutic exploitation., Cancer Research. 49 (1989) 4373–4384. doi:2545340.

[130] J. Ko, K. Park, Y.S. Kim, M.S. Kim, J.K. Han, K. Kim, R.W. Park, I.S. Kim, H.K. Song, D.S. Lee, I.C. Kwon, Tumoral acidic extracellular pH targeting of pH-responsive MPEG-poly(β-amino ester) block copolymer micelles for cancer therapy, Journal of Controlled Release. 123 (2007) 109–115. doi:10.1016/j.jconrel.2007.07.012.

[131] F. Danhier, O. Feron, V. Préat, To exploit the tumor microenvironment: Passive and active tumor targeting of nanocarriers for anti-cancer drug delivery, Journal of Controlled Release. 148 (2010) 135–146. doi:10.1016/j.jconrel.2010.08.027.

[132] G. Yan, J. Wang, L. Hu, X. Wang, G. Yang, S. Fu, X. Cheng, P. Zhang, R. Tang, Stepwise targeted drug delivery to liver cancer cells for enhanced therapeutic efficacy by galactose-grafted, ultra-pH-sensitive micelles, Acta Biomaterialia. 51 (2017) 363–373. doi:10.1016/j.actbio.2017.01.031.

[133] H. Dehari, Y. Ito, T. Nakamura, M. Kobune, K. Sasaki, N. Yonekura, G. Kohama, H. Hamada, Enhanced antitumor effect of RGD fiber-modified adenovirus for gene therapy of oral cancer, Cancer Gene Therapy. 10 (2003) 75–85. doi:10.1038/sj.cgt.7700529.

[134] K. Shi, J. Li, Z. Cao, P. Yang, Y. Qiu, B. Yang, Y. Wang, Y. Long, Y. Liu,

Q. Zhang, J. Qian, Z. Zhang, H. Gao, Q. He, A pH-responsive cell-penetrating peptide-modified liposomes with active recognizing of integrin $\alpha_v\beta_3$ for the treatment of melanoma, Journal of Controlled Release. 217 (2015) 138–150. doi:10.1016/j.jconrel.2015.09.009.

[135] A. Dal Corso, M. Caruso, L. Belvisi, D. Arosio, U. Piarulli, C. Albanese, F. Gasparri, A. Marsiglio, F. Sola, S. Troiani, B. Valsasina, L. Pignataro, D. Donati, C. Gennari, Synthesis and Biological Evaluation of RGD Peptidomimetic-Paclitaxel Conjugates Bearing Lysosomally Cleavable Linkers, Chemistry - A European Journal. 21 (2015) 6921–6929. doi:10.1002/chem.201500158.

[136] J. Zhang, Z.-F. Yuan, Y. Wang, W.-H. Chen, G.-F. Luo, S.-X. Cheng, R. Zhuo, X. Zhang, Multifunctional Envelope-Type Mesoporous Silica Nanoparticles for Tumor-Triggered Targeting Drug Delivery, Journal of American Chemical Society. 135 (2013) 5068–5073. doi:/10.1021/ja312004m.

[137] C. Feng, X. Li, C. Dong, X. Zhang, X. Zhang, Y. Gao, RGD-modified liposomes enhance efficiency of aclacinomycin A delivery : evaluation of their effect in lung cancer, Drug Design, Development and Therapy. 9 (2015) 4613–4620. doi:10.2147/DDDT.S85993.

[138] M. Saraswathy, G.T. Knight, S. Pilla, R.S. Ashton, S. Gong, Multifunctional drug nanocarriers formed by cRGD-conjugated βCD-PAMAM-PEG for targeted cancer therapy, Colloids and Surfaces B: Biointerfaces. 126 (2015) 590–597. doi:10.1016/j.colsurfb.2014.12.042.

[139] W. Yao, P. Xu, J. Zhao, L. Ling, X. Li, B. Zhang, N. Cheng, Z. Pang, RGD functionalized polymeric nanoparticles targeting periodontitis epithelial cells for the enhanced treatment of periodontitis in dogs, Journal of Colloid and Interface Science. 458 (2015) 14–21. doi:10.1016/j.jcis.2015.07.032.

[140] P. Kesharwani, L. Xie, S. Banerjee, G. Mao, S. Padhye, F.H. Sarkar, A.K. Iyer, Hyaluronic acid-conjugated polyamidoamine dendrimers for targeted

delivery of 3,4-difluorobenzylidene curcumin to CD44 overexpressing pancreatic cancer cells, Colloids and Surfaces B: Biointerfaces. 136 (2015) 413–423. doi:10.1016/j.colsurfb.2015.09.043.

[141] G. Mattheolabakis, L. Milane, A. Singh, M.M. Amiji, Hyaluronic acid targeting of CD44 for cancer therapy: from receptor biology to nanomedicine, Journal of Drug Targeting. 23 (2015) 605–618. doi:10.3109/1061186X.2015.1052072.

[142] J.-Y. Lee, U. Termsarasab, J.-H. Park, S.Y. Lee, S.-H. Ko, J.-S. Shim, S.-J. Chung, H.-J. Cho, D.-D. Kim, Dual CD44 and folate receptor-targeted nanoparticles for cancer diagnosis and anticancer drug delivery, Journal of Controlled Release. 236 (2016) 38–46. doi:10.1016/j.jconrel.2016.06.021.

[143] G. Li, Y. Gao, Y. Cui, T. Zhang, R. Cui, Y. Jiang, J. Shi, Overexpression of CD44 is associated with the occurrence and migration of non-small cell lung cancer, Molecular Medicine Reports. 14 (2016) 3159–3167. doi:10.3892/mmr.2016.5636.

[144] H. Yao, Y. Zhang, L. Sun, Y. Liu, The effect of hyaluronic acid functionalized carbon nanotubes loaded with salinomycin on gastric cancer stem cells, Biomaterials. 35 (2014) 9208–9223. doi:10.1016/j.biomaterials.2014.07.033.

[145] X. Cao, L. Tao, S. Wen, W. Hou, X. Shi, Hyaluronic acid-modified multiwalled carbon nanotubes for targeted delivery of doxorubicin into cancer cells, Carbohydrate Research. 405 (2015) 70–77. doi:10.1016/j.carres.2014.06.030.

[146] Abdullah-Al-Nahain, J.-E. Lee, I. In, H. Lee, K.D. Lee, J.H. Jeong, S.Y. Park, Target Delivery and Cell Imaging Using Hyaluronic Acid-Functionalized Graphene Quantum Dots, Molecular Pharmaceutics. 10 (2013) 3736–3744. doi:10.1021/mp400219u.

[147] H. Maeda, H. Nakamura, J. Fang, The EPR effect for macromolecular drug

delivery to solid tumors: Improvement of tumor uptake, lowering of systemic toxicity, and distinct tumor imaging in vivo, Advanced Drug Delivery Reviews. 65 (2013) 71–79. doi:10.1016/j.addr.2012.10.002.

[148] Y. Matsumura, H. Maeda, A new concept for macromolecular therapies in cancer chemotherapy: mechanism of tumortropic accumulation of proteins and the antitumor agents Smancs, Cancer Research. 46 (1986) 6387–6392.

[149] U. Prabhakar, H. Maeda, R.K. Jain, E.M. Sevick-Muraca, W. Zamboni, O.C. Farokhzad, S.T. Barry, A. Gabizon, P. Grodzinski, D.C. Blakey, Challenges and key considerations of the enhanced permeability and retention effect for nanomedicine drug delivery in oncology, Cancer Research. 73 (2013) 2412–2417. doi:10.1158/0008-5472.CAN-12-4561.

[150] I.I. Slowing, B.G. Trewyn, S. Giri, V.S.Y. Lin, Mesoporous silica nanoparticles for drug delivery and biosensing applications, Advanced Functional Materials. 17 (2007) 1225–1236. doi:10.1002/adfm.200601191.

[151] M.E. Davis, Z. (Georgia) Chen, D.M. Shin, Nanoparticle therapeutics: an emerging treatment modality for cancer, Nature Reviews Drug Discovery. 7 (2008) 771–782. doi:10.1038/nrd2614.

[152] X. Huang, X. Teng, D. Chen, F. Tang, J. He, The effect of the shape of mesoporous silica nanoparticles on cellular uptake and cell function, Biomaterials. 31 (2010) 438–448. doi:10.1016/j.biomaterials.2009.09.060.

[153] J.L. Townson, Y.S. Lin, J.O. Agola, E.C. Carnes, H.S. Leong, J.D. Lewis, C.L. Haynes, C.J. Brinker, Re-examining the size/charge paradigm: Differing in vivo characteristics of size- and charge-matched mesoporous silica nanoparticles, Journal of the American Chemical Society. 135 (2013) 16030–16033. doi:10.1021/ja4082414.

[154] J.M. Harris, R.B. Chess, Effect of pegylation on pharmaceuticals, Nature Reviews Drug Discovery. 2 (2003) 214–221. doi:10.1038/nrd1033.

[155] A. Verma, F. Stellacci, Effect of Surface Properties on Nanoparticlea-Cell

Interactions, Small. 6 (2010) 12–21. doi:10.1002/smll.200901158.

[156] O. Harush-Frenkel, N. Debotton, S. Benita, Y. Altschuler, Targeting of nanoparticles to the clathrin-mediated endocytic pathway, Biochemical and Biophysical Research Communications. 353 (2007) 26–32. doi:10.1016/j.bbrc.2006.11.135.

[157] Y. Kuthati, P.-J. Sung, C.-F. Weng, C.-Y. Mou, C.-H. Lee, Functionalization of Mesoporous Silica Nanoparticles for Targeting, Biocompatibility, Combined Cancer Therapies and Theragnosis, Journal of Nanoscience and Nanotechnology. 13 (2013) 2399–2430. doi:10.1166/jnn.2013.7363.

[158] A.F. Moreira, D.R. Dias, I.J. Correia, Stimuli-responsive mesoporous silica nanoparticles for cancer therapy: A review, Microporous and Mesoporous Materials. 236 (2016) 141–157. doi:10.1016/j.micromeso.2016.08.038.

[159] S. Angelos, N.M. Khashab, Y.W. Yang, A. Trabolsi, H.A. Khatib, J.F. Stoddart, J.I. Zink, pH clock-operated mechanized nanoparticles, Journal of the American Chemical Society. 131 (2009) 12912–12914. doi:10.1021/ja9010157.

[160] H. Meng, M. Xue, T. Xia, Y. Zhao, F. Tamanoi, J.F. Stoddart, J.I. Zink, A.E. Nel, Autonomous in Vitro Anticancer Drug Release from Mesoporous Silica Nanoparticles by pH-Sensitive Nanovalves, Journal of the American Chemical Society. 132 (2010) 12690–12697. doi:10.1021/ja104501a.

[161] Y.-J. Cheng, G.-F. Luo, J.-Y. Zhu, X.-D. Xu, X. Zeng, D.-B. Cheng, Y.-M. Li, Y. Wu, X.-Z. Zhang, R.-X. Zhuo, F. He, Enzyme-Induced and Tumor-Targeted Drug Delivery System Based on Multifunctional Mesoporous Silica Nanoparticles, ACS Applied Materials & Interfaces. 7 (2015) 9078–9087. doi:10.1021/acsami.5b00752.

[162] L. Chen, Z. Zhang, X. Yao, X. Chen, X. Chen, Intracellular pH-operated mechanized mesoporous silica nanoparticles as potential drug carries,

Microporous and Mesoporous Materials. 201 (2015) 169–175. doi:10.1016/j.micromeso.2014.09.023.

[163] S. Lee, X. Zhu, Y.-X.J. Wang, S. Xuan, Q. You, W. Chan, C. Wong, F. Wang, J.C. Yu, C.H.K. Cheng, K.C. Leung, Ultrasound, pH, and Magnetically Responsive Crown-Ether-Coated Core/Shell Nanoparticles as Drug Encapsulation and Release Systems, ACS Applied Materials & Interfaces. 5 (2013) 1566–1574. doi:10.1021/am4004705.

[164] R. Liu, Y. Zhang, X. Zhao, A. Agarwal, L.J. Mueller, P. Feng, pH-responsive nanogated ensemble based on gold-capped mesoporous silica through an acid-labile acetal linker, Journal of the American Chemical Society. 132 (2010) 1500–1501. doi:10.1021/ja907838s.

[165] L. Cui, H. Lin, C. Yang, X. Han, T. Zhang, F. Qu, Synthesis of Multifunctional Fe_3O_4 @mSiO_2 @Au Core-Shell Nanocomposites for pH-Responsive Drug Delivery, European Journal of Inorganic Chemistry. 2014 (2014) 6156–6164. doi:10.1002/ejic.201402671.

[166] Q. Gan, X. Lu, Y. Yuan, J. Qian, H. Zhou, X. Lu, J. Shi, C. Liu, A magnetic, reversible pH-responsive nanogated ensemble based on Fe_3O_4 nanoparticles-capped mesoporous silica, Biomaterials. 32 (2011) 1932–1942. doi:10.1016/j.biomaterials.2010.11.020.

[167] C. Xu, Y. Lin, J. Wang, L. Wu, W. Wei, J. Ren, X. Qu, Nanoceria-Triggered Synergetic Drug Release Based on CeO_2 -Capped Mesoporous Silica Host-Guest Interactions and Switchable Enzymatic Activity and Cellular Effects of CeO_2, Advanced Healthcare Materials. 2 (2013) 1591–1599. doi:10.1002/adhm.201200464.

[168] W. Cheng, J. Nie, L. Xu, C. Liang, Y. Peng, G. Liu, T. Wang, L. Mei, L. Huang, X. Zeng, pH-Sensitive Delivery Vehicle Based on Folic Acid-Conjugated Polydopamine-Modified Mesoporous Silica Nanoparticles for Targeted Cancer Therapy, ACS Applied Materials & Interfaces. 9 (2017) 18462–18473. doi:10.1021/acsami.7b02457.

[169] A. Abbaszad Rafi, M. Mahkam, S. Davaran, H. Hamishehkar, A Smart pH-responsive Nano-Carrier as a Drug Delivery System: A hybrid system comprised of mesoporous nanosilica MCM-41 (as a nano-container) & a pH-sensitive polymer (as smart reversible gatekeepers): Preparation, characterization and in vitro release st, European Journal of Pharmaceutical Sciences. 93 (2016) 64–73. doi:10.1016/j.ejps.2016.08.005.

[170] Y.J. Chang, X.Z. Liu, Q. Zhao, X.H. Yang, K.M. Wang, Q. Wang, M. Lin, M. Yang, P(VPBA-DMAEA) as a pH-sensitive nanovalve for mesoporous silica nanoparticles based controlled release, Chinese Chemical Letters. 26 (2015) 1203–1208. doi:10.1016/j.cclet.2015.08.005.

[171] C. Chen, F. Pu, Z. Huang, Z. Liu, J. Ren, X. Qu, Stimuli-responsive controlled-release system using quadruplex DNA-capped silica nanocontainers, Nucleic Acids Research. 39 (2011) 1638–1644. doi:10.1093/nar/gkq893.

[172] L. Chen, X. Zhou, W. Nie, Q. Zhang, W. Wang, Y. Zhang, C. He, Multifunctional Redox-Responsive Mesoporous Silica Nanoparticles for Efficient Targeting Drug Delivery and Magnetic Resonance Imaging, ACS Applied Materials & Interfaces. 8 (2016) 33829–33841. doi:10.1021/acsami.6b11802.

[173] L. Maggini, I. Cabrera, A. Ruiz-Carretero, E.A. Prasetyanto, E. Robinet, L. De Cola, Breakable mesoporous silica nanoparticles for targeted drug delivery, Nanoscale. 8 (2016) 7240–7247. doi:10.1039/C5NR09112H.

[174] Z.-Y. Li, J.-J. Hu, Q. Xu, S. Chen, H. Jia, Y.-X. Sun, R.-X. Zhuo, X.-Z. Zhang, A redox-responsive drug delivery system based on RGD containing peptide-capped mesoporous silica, Journal of Materials Chemistry B. 3 (2015) 39–44. doi:10.1039/C4TB01533A.

[175] X. Chen, H. Sun, J. Hu, X. Han, H. Liu, Y. Hu, Transferrin gated mesoporous silica nanoparticles for redox-responsive and targeted drug delivery, Colloids and Surfaces B: Biointerfaces. 152 (2017) 77–84.

doi:10.1016/j.colsurfb.2017.01.010.

[176] J. Jiao, X. Li, S. Zhang, J. Liu, D. Di, Y. Zhang, Q. Zhao, S. Wang, Redox and pH dual-responsive PEG and chitosan-conjugated hollow mesoporous silica for controlled drug release, Materials Science and Engineering: C. 67 (2016) 26–33. doi:10.1016/j.msec.2016.04.091.

[177] Y. Wang, Y. Cui, Y. Zhao, B. He, X. Shi, D. Di, Q. Zhang, S. Wang, Fluorescent carbon dot-gated multifunctional mesoporous silica nanocarriers for redox/enzyme dual-responsive targeted and controlled drug delivery and real-time bioimaging, European Journal of Pharmaceutics and Biopharmaceutics. 117 (2017) 105–115. doi:10.1016/j.ejpb.2017.03.019.

[178] K. Park, S.S. Park, Y.H. Yun, C.-S. Ha, Mesoporous silica nanoparticles functionalized with a redox-responsive biopolymer, Journal of Porous Materials. 24 (2017) 1215–1225. doi:10.1007/s10934-017-0361-x.

[179] Q. Zhao, S. Wang, Y. Yang, X. Li, D. Di, C. Zhang, T. Jiang, S. Wang, Hyaluronic acid and carbon dots-gated hollow mesoporous silica for redox and enzyme-triggered targeted drug delivery and bioimaging, Materials Science and Engineering: C. 78 (2017) 475–484. doi:10.1016/j.msec.2017.04.059.

[180] J. Zhang, M. Niemelä, J. Westermarck, J.M. Rosenholm, Mesoporous silica nanoparticles with redox-responsive surface linkers for charge-reversible loading and release of short oligonucleotides, Dalton Transactions. 43 (2014) 4115–4126. doi:10.1039/c3dt53071j.

[181] N. Singh, A. Karambelkar, L. Gu, K. Lin, J.S. Miller, C.S. Chen, M.J. Sailor, S.N. Bhatia, Bioresponsive Mesoporous Silica Nanoparticles for Triggered Drug Release, Journal of the American Chemical Society. 133 (2011) 19582–19585. doi:10.1021/ja206998x.

[182] E. Aznar, R. Villalonga, C. Giménez, F. Sancenón, M.D. Marcos, R.

Martínez-Máñez, P. Díez, J.M. Pingarrón, P. Amorós, Glucose-triggered release using enzyme-gated mesoporous silica nanoparticles, Chemical Communications. 49 (2013) 6391–6393. doi:10.1039/c3cc42210k.

[183] B. Kumar, S. Kulanthaivel, A. Mondal, S. Mishra, B. Banerjee, A. Bhaumik, I. Banerjee, S. Giri, Mesoporous silica nanoparticle based enzyme responsive system for colon specific drug delivery through guar gum capping, Colloids and Surfaces B: Biointerfaces. 150 (2017) 352–361. doi:10.1016/j.colsurfb.2016.10.049.

[184] Y. Zhu, M. Fujiwara, Installing dynamic molecular photomechanics in mesopores: A multifunctional controlled-release nanosystem, Angewandte Chemie - International Edition. 46 (2007) 2241–2244. doi:10.1002/anie.200604850.

[185] N.K. Mal, M. Fujiwara, Y. Tanaka, Photocontrolled reversible release of guest molecules from coumarin- modified mesoporous silica, Nature. 421 (2003) 350–353. doi:10.1038/nature01337.1.

[186] G. Wang, J. Dong, T. Yuan, J. Zhang, L. Wang, H. Wang, Visible Light and pH Responsive Polymer-Coated Mesoporous Silica Nanohybrids for Controlled Release, Macromolecular Bioscience. 16 (2016) 990–994. doi:10.1002/mabi.201600008.

[187] Q. Lin, Q. Huang, C. Li, C. Bao, Z. Liu, F. Li, L. Zhu, Anticancer Drug Release from a Mesoporous Silica Based Nanophotocage Regulated by Either a One- or Two-Photon Process, Journal of the American Chemical Society. 132 (2010) 10645–10647. doi:10.1021/ja103415t.

[188] Y.-T. Chang, P.-Y. Liao, H.-S. Sheu, Y.-J. Tseng, F.-Y. Cheng, C.-S. Yeh, Near-Infrared Light-Responsive Intracellular Drug and siRNA Release Using Au Nanoensembles with Oligonucleotide-Capped Silica Shell, Advanced Materials. 24 (2012) 3309–3314. doi:10.1002/adma.201200785.

[189] L. Cui, F. Zhang, Q. Wang, H. Lin, C. Yang, T. Zhang, R. Tong, N. An, F.

Qu, NIR light responsive core–shell nanocontainers for drug delivery, J. Mater. Chem. B. 3 (2015) 7046–7054. doi:10.1039/C5TB00709G.

[190] J. Li, J. Zeng, X. Jia, L. Liu, T. Zhou, P. Liu, pH, temperature and reduction multi-responsive polymeric microspheres as drug delivery system for anti-tumor drug: Effect of middle hollow layer between pH and reduction dual-responsive cores and temperature sensitive shells, Journal of the Taiwan Institute of Chemical Engineers. 74 (2017) 238–245. doi:10.1016/j.jtice.2016.07.013.

[191] O. Onaca, R. Enea, D.W. Hughes, W. Meier, Stimuli-Responsive Polymersomes as Nanocarriers for Drug and Gene Delivery, Macromolecular Bioscience. 9 (2009) 129–139. doi:10.1002/mabi.200800248.

[192] H.G. Schild, Poly(N-isopropylacrylamide): experiment, theory and application, Progress in Polymer Science. 17 (1992) 163–249. doi:10.1016/0079-6700(92)90023-R.

[193] J.C. Rueda, K. Contreras, R. Coello, M. Lomer, H. Komber, S. Zschoche, B. Voit, Characterization of new thermo-responsive hydrogels for optical sensing applications, 6572 (2007) 1–7. doi:10.1117/12.720426.

[194] E. Ugazio, L. Gastaldi, V. Brunella, D. Scalarone, S.A. Jadhav, S. Oliaro-Bosso, D. Zonari, G. Berlier, I. Miletto, S. Sapino, Thermoresponsive mesoporous silica nanoparticles as a carrier for skin delivery of quercetin, International Journal of Pharmaceutics. 511 (2016) 446–454. doi:10.1016/j.ijpharm.2016.07.024.

[195] J. Sun, Z. Yu, C. Hong, C. Pan, Biocompatible Zwitterionic Sulfobetaine Copolymer-Coated Mesoporous Silica Nanoparticles for Temperature-Responsive Drug Release, Macromolecular Rapid Communications. 33 (2012) 811–818. doi:10.1002/marc.201100876.

[196] J.T. Sun, Z.Q. Yu, C.Y. Hong, C.Y. Pan, Biocompatible zwitterionic

sulfobetaine copolymer-coated mesoporous silica nanoparticles for temperature-responsive drug release, Macromolecular Rapid Communications. 33 (2012) 811–818. doi:10.1002/marc.201100876.

[197] J. An, X. Zhang, Q. Guo, Y. Zhao, Z. Wu, C. Li, Glycopolymer modified magnetic mesoporous silica nanoparticles for MR imaging and targeted drug delivery, Colloids and Surfaces A: Physicochemical and Engineering Aspects. 482 (2015) 98–108. doi:10.1016/j.colsurfa.2015.04.035.

[198] Yi-Hsin Lien, Jhaol-Huei Wu, Jiunn-Wang Liao, Tzong-Ming Wu, In vitro Evaluation of the Thermosensitive and Magnetic Nanoparticles for the Controlled Drug Delivery of Vitamin D3, Macromolecular Research. 21 (2013) 511–518. doi:10.1007/s13233-013-1047-0.

[199] W.-H. Chen, G.-F. Luo, Q. Lei, F.-Y. Cao, J.-X. Fan, W.-X. Qiu, H.-Z. Jia, S. Hong, F. Fang, X. Zeng, R.-X. Zhuo, X.-Z. Zhang, Rational design of multifunctional magnetic mesoporous silica nanoparticle for tumor-targeted magnetic resonance imaging and precise therapy, Biomaterials. 76 (2016) 87–101. doi:10.1016/j.biomaterials.2015.10.053.

[200] E. Che, Y. Gao, L. Wan, Y. Zhang, N. Han, J. Bai, J. Li, Z. Sha, S. Wang, Paclitaxel/gelatin coated magnetic mesoporous silica nanoparticles: Preparation and antitumor efficacy in vivo, Microporous and Mesoporous Materials. 204 (2015) 226–234. doi:10.1016/j.micromeso.2014.11.013.

[201] Y. Chen, H. Zhang, X. Cai, J. Ji, S. He, G. Zhai, Multifunctional mesoporous silica nanocarriers for stimuli-responsive target delivery of anticancer drugs, RSC Adv. 6 (2016) 92073–92091. doi:10.1039/C6RA18062K.

[202] Y. Chen, H. Chen, J. Shi, In Vivo Bio-Safety Evaluations and Diagnostic/Therapeutic Applications of Chemically Designed Mesoporous Silica Nanoparticles, Advanced Materials. 25 (2013) 3144–3176. doi:10.1002/adma.201205292.

[203] H. Meng, M. Xue, T. Xia, Z. Ji, D.Y. Tarn, J.I. Zink, A.E. Nel, Use of Size and a Copolymer Design Feature To Improve the Biodistribution and the Enhanced Permeability and Retention Effect of Doxorubicin-Loaded Mesoporous Silica Nanoparticles in a Murine Xenograft Tumor Model, ACS Nano. 5 (2011) 4131–4144. doi:10.1021/nn200809t.

[204] J.E. Gagner, S. Shrivastava, X. Qian, J.S. Dordick, R.W. Siegel, Engineering nanomaterials for biomedical applications requires understanding the nano-bio interface: A perspective, Journal of Physical Chemistry Letters. 3 (2012) 3149–3158. doi:10.1021/jz301253s.

[205] L. Treuel, G.U. Nienhaus, Toward a molecular understanding of nanoparticle-protein interactions, Biophysical Reviews. 4 (2012) 137–147. doi:10.1007/s12551-012-0072-0.

[206] S. Laurent, C. Burtea, C. Thirifays, F. Rezaee, M. Mahmoudi, Significance of cell "observer" and protein source in nanobiosciences, Journal of Colloid and Interface Science. 392 (2013) 431–445. doi:10.1016/j.jcis.2012.10.005.

[207] M. Mahmoudi, I. Lynch, M.R. Ejtehadi, M.P. Monopoli, F.B. Bombelli, S. Laurent, Protein−Nanoparticle Interactions: Opportunities and Challenges, Chemical Reviews. 111 (2011) 5610–5637. doi:10.1021/cr100440g.

[208] Z. Deng, G. Mortimer, T. Schiller, A. Masumeci, D. Martin, M. RF, Differential plasma protein binding to metal oxide nanoparticles, Nanotechnology. 20 (2009) 455101–455109. doi:10.1088/0957-4484/20/45/455101.

[209] S. Tenzer, D. Docter, S. Rosfa, A. Wlodarski, J. Kuharev, A. Rekik, S.K. Knauer, C. Bantz, T. Nawroth, C. Bier, J. Sirirattanapan, W. Mann, L. Treuel, R. Zellner, M. Maskos, H. Schild, R.H. Stauber, Nanoparticle size is a critical physicochemical determinant of the human blood plasma corona: A comprehensive quantitative proteomic analysis, ACS Nano. 5 (2011) 7155–7167. doi:10.1021/nn201950e.

[210] M.C. Cox, K.J. Barnham, T. a Frenkiel, J.D. Hoeschele, a B. Mason, Q.Y. He, R.C. Woodworth, P.J. Sadler, Identification of platination sites on human serum transferrin using (13)C and (15)N NMR spectroscopy., Journal of Biological Inorganic Chemistry : JBIC : A Publication of the Society of Biological Inorganic Chemistry. 4 (1999) 621–631.

[211] S. Laurent, M. Mahmoudi, Superparamagnetic iron oxide nanoparticles: Promises for diagnosis and treatment of cancer, International Journal of Molecular Epidemiology and Genetics. 2 (2011) 367–390. doi:10.1021/cn100100e.

[212] I. Lynch, K.A. Dawson, Protein-nanoparticle interactions, Nano Today. 3 (2008) 40–47. doi:10.1016/S1748-0132(08)70014-8.

[213] I. Lynch, K.A. Dawson, Protein-nanoparticle interactions, Nano Today. 3 (2008) 40–47. doi:10.1016/S1748-0132(08)70014-8.

[214] P. Foroozandeh, A.A. Aziz, Merging worlds of nanomaterials and biological environment: factors governing protein corona formation on nanoparticles and its biological consequences., Nanoscale Research Letters. 10 (2015) 221–232. doi:10.1186/s11671-015-0922-3.

[215] M. Lundqvist, J. Stigler, T. Cedervall, T. Berggård, M.B. Flanagan, I. Lynch, G. Elia, K. Dawson, The evolution of the protein corona around nanoparticles: A test study, ACS Nano. 5 (2011) 7503–7509. doi:10.1021/nn202458g.

[216] M.S. Ehrenberg, A.E. Friedman, J.N. Finkelstein, G. Oberdörster, J.L. McGrath, The influence of protein adsorption on nanoparticle association with cultured endothelial cells, Biomaterials. 30 (2009) 603–610. doi:10.1016/j.biomaterials.2008.09.050.

[217] L. Vroman, A.L. Adams, G.C. Fischer, P.C. Munoz, Interaction of High Molecular Weight Kininogen, Factor XII, and Fibrinogen in Plasma at Interfaces, 55 (1980) 156–159.

[218] G. Villaverde, A. Baeza, G.J. Melen, A. Alfranca, M. Ramirez, M. Vallet-Regí, A new targeting agent for the selective drug delivery of nanocarriers for treating neuroblastoma, J. Mater. Chem. B. 3 (2015) 4831–4842. doi:10.1039/C5TB00287G.

[219] M.T. Ortega, J.E. Riviere, K. Choi, N.A. Monteiro-Riviere, Biocorona formation on gold nanoparticles modulates human proximal tubule kidney cell uptake, cytotoxicity and gene expression, Toxicology in Vitro. 42 (2017) 150–160. doi:10.1016/j.tiv.2017.04.020.

[220] S.D. Conner, S.L. Schmid, Regulated portals of entry into the cell, Nature. 422 (2003) 37–44. doi:10.1038/nature01451.

[221] E.C. Cho, J. Xie, P.A. Wurm, Y. Xia, Understanding the role of surface charges in cellular adsorption versus internalization by selectively removing gold nanoparticles on the cell surface with a I 2/KI etchant, Nano Letters. 9 (2009) 1080–1084. doi:10.1021/nl803487r.

[222] J.E. Fuller, G.T. Zugates, L.S. Ferreira, H.S. Ow, N.N. Nguyen, U.B. Wiesner, R.S. Langer, Intracellular delivery of core-shell fluorescent silica nanoparticles, Biomaterials. 29 (2008) 1526–1532. doi:10.1016/j.biomaterials.2007.11.025.

[223] Z. Wang, Y. Tian, H. Zhang, Y. Qin, D. Li, L. Gan, F. Wu, Using hyaluronic acid-functionalized pH stimuli-responsive mesoporous silica nanoparticles for targeted delivery to CD44-overexpressing cancer cells, International Journal of Nanomedicine. Volume 11 (2016) 6485–6497. doi:10.2147/IJN.S117184.

[224] S. Sengupta, A. Kulkarni, Design Principles for Clinical Efficacy of Cancer Nanomedicine: A Look into the Basics, ACS Nano. 7 (2013) 2878–2882. doi:10.1021/nn4015399.

[225] A. Accardo, D. Tesauro, G. Morelli, Peptide-based targeting strategies for simultaneous imaging and therapy with nanovectors, Polymer Journal. 45

(2013) 481–493. doi:10.1038/pj.2012.215.

[226] L. Pan, J. Liu, Q. He, J. Shi, MSN-Mediated Sequential Vascular-to-Cell Nuclear-Targeted Drug Delivery for Efficient Tumor Regression, Advanced Materials. 26 (2014) 6742–6748. doi:10.1002/adma.201402752.

[227] T. Dai, M. Tanaka, Y.-Y. Huang, M.R. Hamblin, Chitosan preparations for wounds and burns: antimicrobial and wound-healing effects, Expert Review of Anti-Infective Therapy. 9 (2011) 857–879. doi:10.1586/eri.11.59.

[228] S. Islam, M.A.R. Bhuiyan, M.N. Islam, Chitin and Chitosan: Structure, Properties and Applications in Biomedical Engineering, Journal of Polymers and the Environment. 25 (2017) 854–866. doi:10.1007/s10924-016-0865-5.

[229] A. Oryan, S. Sahvieh, Effectiveness of chitosan scaffold in skin, bone and cartilage healing, International Journal of Biological Macromolecules. 104 (2017) 1003–1011. doi:10.1016/j.ijbiomac.2017.06.124.

[230] M. Ahmad, K. Manzoor, S. Singh, S. Ikram, Chitosan centered bionanocomposites for medical specialty and curative applications: A review, International Journal of Pharmaceutics. 529 (2017) 200–217. doi:10.1016/j.ijpharm.2017.06.079.

[231] C. Qin, H. Li, Q. Xiao, Y. Liu, J. Zhu, Y. Du, Water-solubility of chitosan and its antimicrobial activity, Carbohydrate Polymers. 63 (2006) 367–374. doi:10.1016/j.carbpol.2005.09.023.

[232] F. Croisier, C. Jérôme, Chitosan-based biomaterials for tissue engineering, European Polymer Journal. 49 (2013) 780–792. doi:10.1016/j.eurpolymj.2012.12.009.

[233] Y. Xu, D. Xia, J. Han, S. Yuan, H. Lin, C. Zhao, Design and fabrication of porous chitosan scaffolds with tunable structures and mechanical properties, Carbohydrate Polymers. 177 (2017) 210–216.

doi:10.1016/j.carbpol.2017.08.069.

[234] A.M. De Campos, A. Sánchez, M.J. Alonso, Chitosan nanoparticles: A new vehicle for the improvement of the delivery of drugs to the ocular surface. Application to cyclosporin A, International Journal of Pharmaceutics. 224 (2001) 159–168. doi:10.1016/S0378-5173(01)00760-8.

[235] A.M. De Campos, Y. Diebold, E.L.S. Carvalho, A. Sánchez, M.J. Alonso, Chitosan nanoparticles as new ocular drug delivery systems: In vitro stability, in vivo fate, and cellular toxicity, Pharmaceutical Research. 21 (2004) 803–810. doi:10.1023/B:PHAM.0000026432.75781.cb.

[236] V. Zamora-Mora, M. Fernández-Gutiérrez, Á. González-Gómez, B. Sanz, J.S. Román, G.F. Goya, R. Hernández, C. Mijangos, Chitosan nanoparticles for combined drug delivery and magnetic hyperthermia: From preparation to in vitro studies, Carbohydrate Polymers. 157 (2017) 361–370. doi:10.1016/j.carbpol.2016.09.084.

[237] M. Arif, Q.-J. Dong, M.A. Raja, S. Zeenat, Z. Chi, C.-G. Liu, Development of novel pH-sensitive thiolated chitosan/PMLA nanoparticles for amoxicillin delivery to treat Helicobacter pylori, Materials Science and Engineering: C. 83 (2017) 17–24. doi:10.1016/j.msec.2017.08.038.

[238] K.E. Crompton, J.D. Goud, R. V. Bellamkonda, T.R. Gengenbach, D.I. Finkelstein, M.K. Horne, J.S. Forsythe, Polylysine-functionalised thermoresponsive chitosan hydrogel for neural tissue engineering, Biomaterials. 28 (2007) 441–449. doi:10.1016/j.biomaterials.2006.08.044.

[239] H. Tan, C.R. Chu, K.A. Payne, K.G. Marra, Injectable in situ forming biodegradable chitosan-hyaluronic acid based hydrogels for cartilage tissue engineering, Biomaterials. 30 (2009) 2499–2506. doi:10.1016/j.biomaterials.2008.12.080.

[240] K. Madhumathi, K.T. Shalumon, V.V.D. Rani, H. Tamura, T. Furuike, N. Selvamurugan, S. V. Nair, R. Jayakumar, Wet chemical synthesis of

chitosan hydrogel-hydroxyapatite composite membranes for tissue engineering applications, International Journal of Biological Macromolecules. 45 (2009) 12–15. doi:10.1016/j.ijbiomac.2009.03.011.

[241] K. Kiene, F. Porta, B. Topacogullari, P. Detampel, J. Huwyler, Self-assembling chitosan hydrogel: A drug-delivery device enabling the sustained release of proteins, Journal of Applied Polymer Science. 135 (2018) 1–6. doi:10.1002/app.45638.

[242] S. Yu, X. Zhang, G. Tan, L. Tian, D. Liu, Y. Liu, X. Yang, W. Pan, A novel pH-induced thermosensitive hydrogel composed of carboxymethyl chitosan and poloxamer cross-linked by glutaraldehyde for ophthalmic drug delivery, Carbohydrate Polymers. 155 (2017) 208–217. doi:10.1016/j.carbpol.2016.08.073.

[243] J. Xu, M. Tam, S. Samaei, S. Lerouge, J. Barralet, M.M. Stevenson, M. Cerruti, M.M. Stevenson, M.M. Stevenson, Mucoadhesive chitosan hydrogels as rectal drug delivery vessels to treat ulcerative colitis, Acta Biomaterialia. 48 (2017) 247–257. doi:10.1016/j.actbio.2016.10.026.

[244] Y.C. Lin, F. jui Tan, K.G. Marra, S.S. Jan, D.C. Liu, Synthesis and characterization of collagen/hyaluronan/chitosan composite sponges for potential biomedical applications, Acta Biomaterialia. 5 (2009) 2591–2600. doi:10.1016/j.actbio.2009.03.038.

[245] T. Furuike, T. Chaochai, D. Komoto, H. Tamura, Adsorption and Desorption Behaviors of Bovine Serum Albumin on Gelatin/Chitosan Sponge, Journal of Materials Science and Chemical Engineering. 5 (2017) 109–120. doi:10.4236/msce.2017.51015.

[246] L. Racine, G. Costa, E. Bayma-Pecit, I. Texier, R. Auzély-Velty, Design of interpenetrating chitosan and poly(ethylene glycol) sponges for potential drug delivery applications, Carbohydrate Polymers. 170 (2017) 166–175. doi:10.1016/j.carbpol.2017.04.060.

[247] H.K. Varma, Y. Yogogawa, F.F. Espinosa, Y. Kawamoto, K. Nishizawa, F. Nagata, T. Kameyama, Porous calcium phosphate coating over phosphorylated chitosan film by a biomimetic method, Biomaterials. 20 (1999) 879–884. doi:10.1016/S0142-9612(98)00243-9.

[248] T.-J. Lu, F.-Y. Chiu, H.-Y. Chiu, M.-C. Chang, S.-C. Hung, Chondrogenic differentiation of mesenchymal stem cells in three-dimensional chitosan film culture, Cell Transplantation. 26 (2016) 417–427. doi:10.3727/096368916X693464.

[249] Z. Cui, Z. Zheng, L. Lin, J. Si, Q. Wang, X. Peng, W. Chen, Electrospinning and crosslinking of polyvinyl alcohol/chitosan composite nanofiber for transdermal drug delivery, Advances in Polymer Technology. (2017) 1–12. doi:10.1002/adv.21850.

[250] M.G. Lancina, R.K. Shankar, H. Yang, Chitosan nanofibers for transbuccal insulin delivery, Journal of Biomedical Materials Research Part A. 105 (2017) 1252–1259. doi:10.1002/jbm.a.35984.

[251] Y. Zhang, J.R. Venugopal, A. El-Turki, S. Ramakrishna, B. Su, C.T. Lim, Electrospun biomimetic nanocomposite nanofibers of hydroxyapatite/chitosan for bone tissue engineering, Biomaterials. 29 (2008) 4314–4322. doi:10.1016/j.biomaterials.2008.07.038.

[252] A. Subramanian, D. Vu, G.F. Larsen, H.-Y. Lin, Preparation and evaluation of the electrospun chitosan/PEO fibers for potential applications in cartilage tissue engineering., Journal of Biomaterials Science. Polymer Edition. 16 (2005) 861–73. doi:10.1163/1568562054255682.

[253] S. Bashir, Y.Y. Teo, S. Ramesh, K. Ramesh, Synthesis, characterization, properties of N-succinyl chitosan-g-poly (methacrylic acid) hydrogels and in vitro release of theophylline, Polymer (United Kingdom). 92 (2016) 36–49. doi:10.1016/j.polymer.2016.03.045.

[254] P. Sahu, S.K. Kashaw, V. Kushwah, S. Sau, S. Jain, A.K. Iyer, pH

responsive biodegradable nanogels for sustained release of bleomycin, Bioorganic and Medicinal Chemistry. 25 (2017) 4595–4613. doi:10.1016/j.bmc.2017.06.038.

[255] W.T. Liu, Y. Yang, P.H. Shen, X.J. Gao, S.Q. He, H. Liu, C.S. Zhu, Facile and simple preparation of pH-sensitive chitosan-mesoporous silica nanoparticles for future breast cancer treatment, Express Polymer Letters. 9 (2015) 1068–1075. doi:10.3144/expresspolymlett.2015.96.

[256] C.-Y. Chuang, T.-M. Don, W.-Y. Chiu, Synthesis of chitosan-based thermo- and pH-responsive porous nanoparticles by temperature-dependent self-assembly method and their application in drug release, American Chemical Society, Polymer Preprints, Division of Polymer Chemistry. 47 (2009) 5126–5136. doi:10.1002/pola.

[257] C.-Y. Chuang, T.-M. Don, W.-Y. Chiu, Synthesis and properties of chitosan-based thermo- and pH-responsive nanoparticles and application in drug release, American Chemical Society, Polymer Preprints, Division of Polymer Chemistry. 47 (2009) 2798–2810. doi:10.1002/pola.

[258] J. Wei, X.-J. Ju, X.-Y. Zou, R. Xie, W. Wang, Y.-M. Liu, L.-Y. Chu, Multi-Stimuli-Responsive Microcapsules for Adjustable Controlled-Release, Advanced Functional Materials. 24 (2014) 3312–3323. doi:10.1002/adfm.201303844.

[259] D. Jocic, A. Tourrette, P. Glampedaki, M.M.C.G. Warmoeskerken, Application of temperature and pH responsive microhydrogels for functional finishing of cotton fabric, Materials Technology. 24 (2009) 14–23. doi:10.1179/175355509X417963.

[260] M. He, C.C. Chu, Dual stimuli responsive glycidyl methacrylate chitosan-quaternary ammonium hybrid hydrogel and its bovine serum albumin release, Journal of Applied Polymer Science. 130 (2013) 3736–3745. doi:10.1002/app.39635.

[261] Q. Yang, Y. Zhu, B. Luo, F. Lan, Y. Wu, Z. Gu, pH-Responsive magnetic nanospheres for the reversibly selective capture and release of glycoproteins, J. Mater. Chem. B. 5 (2017) 1236–1245. doi:10.1039/C6TB02662A.

[262] A. Popat, J. Liu, G.Q. (Max) Lu, S.Z. Qiao, A pH-responsive drug delivery system based on chitosan coated mesoporous silica nanoparticles, Journal of Materials Chemistry. 22 (2012) 11173–11178. doi:10.1039/c2jm30501a.

[263] X. Hu, Y. Wang, B. Peng, Chitosan-capped mesoporous silica nanoparticles as pH-responsive nanocarriers for controlled drug release, Chemistry - An Asian Journal. 9 (2014) 319–327. doi:10.1002/asia.201301105.

[264] W. Palmer, K.M. John, Polysaccharide of Vitreous Humor, Ophthalmology. 107 (1934) 629–634.

[265] Y.-H. Liao, S.A. Jones, B. Forbes, G.P. Martin, M.B. Brown, Hyaluronan: Pharmaceutical Characterization and Drug Delivery, Drug Delivery. 12 (2005) 327–342. doi:10.1080/10717540590952555.

[266] Y. Kobayashi, A. Okamoto, K. Nishinari, Viscoelasticity of hyaluronic acid with different molecular weights., Biorheology. 31 (1994) 235–44.

[267] Y. Mo, T. Takaya, K. Nishinari, K. Kubota, A. Okamoto, Effects of sodium chloride, guanidine hydrochloride, and sucrose on the viscoelastic properties of sodium hyaluronate solutions, Biopolymers. 50 (1999) 23–34. doi:10.1002/(SICI)1097-0282(199907)50:1<23::AID-BIP3>3.0.CO;2-G.

[268] P. Ghosh, N. Hutadilok, N. Adam, A. Lentini, Interactions of hyaluronan (hyaluronic acid) with phospholipids as determined by gel permeation chromatography, multi-angle laser-light-scattering photometry and 1H-NMR spectroscopy, International Journal of Biological Macromolecules. 16 (1994) 237–244. doi:10.1016/0141-8130(94)90028-0.

[269] L.J. Lapcik, S. de Smedt, L. Lapcik, J. Demeester, P. Chabrecek,

Hyaluronan: Preparation, Structure, Properties and Applications, Chemical Reviews. 88 (1998) 2663–2681. doi:10.1021/cr941199z.

[270] A. Umerska, K.J. Paluch, I. Inkielewicz-Stepniak, M.J. Santos-Martinez, O.I. Corrigan, C. Medina, L. Tajber, Exploring the assembly process and properties of novel crosslinker-free hyaluronate-based polyelectrolyte complex nanocarriers, International Journal of Pharmaceutics. 436 (2012) 75–87. doi:10.1016/j.ijpharm.2012.07.011.

[271] K. Tømmeraas, P.O. Wahlund, Poly-acid properties of biosynthetic hyaluronan studied by titration, Carbohydrate Polymers. 77 (2009) 194–200. doi:10.1016/j.carbpol.2008.12.021.

[272] D.A. Gibbs, E.W. Merrill, K.A. Smith, E.A. Balazs, Rheology of hyaluronic acid, Biopolymers. 6 (1968) 777–791. doi:10.1002/bip.1968.360060603.

[273] A.P. Spicer, T.K. Nguyen, Mammalian hyaluronan synthases: investigation of functional relationships in vivo, Biochemical Society Transactions. 27 (1999) 109–115. doi:10.1042/bst0270109.

[274] S. Mathews, R. Bhonde, P.K. Gupta, S. Totey, A novel tripolymer coating demonstrating the synergistic effect of chitosan, collagen type 1 and hyaluronic acid on osteogenic differentiation of human bone marrow derived mesenchymal stem cells, Biochemical and Biophysical Research Communications. 414 (2011) 270–276. doi:10.1016/j.bbrc.2011.09.071.

[275] Y. Zhong, K. Goltsche, L. Cheng, F. Xie, F. Meng, C. Deng, Z. Zhong, R. Haag, Hyaluronic acid-shelled acid-activatable paclitaxel prodrug micelles effectively target and treat CD44-overexpressing human breast tumor xenografts in??vivo, Biomaterials. 84 (2016) 250–261. doi:10.1016/j.biomaterials.2016.01.049.

[276] M. Yu, S. Jambhrunkar, P. Thorn, J. Chen, W. Gu, C. Yu, Hyaluronic acid modified mesoporous silica nanoparticles for targeted drug delivery to

CD44-overexpressing cancer cells., Nanoscale. 5 (2013) 178–83. doi:10.1039/c2nr32145a.

[277] Q. Zhao, J. Liu, W. Zhu, C. Sun, D. Di, Y. Zhang, P. Wang, Z. Wang, S. Wang, Dual-stimuli responsive hyaluronic acid-conjugated mesoporous silica for targeted delivery to CD44-overexpressing cancer cells, Acta Biomaterialia. 23 (2015) 147–156. doi:10.1016/j.actbio.2015.05.010.

[278] M.D. Pierschbacher, E. Ruoslahti, Cell attachment activity of fibronectin can be duplicated by small synthetic fragments of the molecule, Nature. 309 (1984) 30–33. doi:10.1038/309030a0.

[279] E.F. Plow, M.D. Pierschbacher, E. Rouslahti, G. Marguerie, M.H. Ginsberg, Arginyl-Glycyl-Aspartic acid sequences and fibrinogen binding to platelets, Blood Journal. 70 (1987) 110–115.

[280] B.K. Brandley, R.L. Schnaar, Covalent attachment of an Arg-Gly-Asp sequece peptide to derivatizable polyacrylamide surfaces: Support of fibroblast adhesion and long-term growth, Analytical Biochemistry. 172 (1988) 270–278. doi:10.1016/0003-2697(88)90442-3.

[281] S.E. D’Souza, M.H. Ginsberg, S.C.T. Lam, E.F. Plow, Chemical cross-linking of arginyl-glycyl-aspartic acid peptides to an adhesion receptor on platelets, Journal of Biological Chemistry. 263 (1988) 3943–3951.

[282] J.S. Desgrosellier, D.A. Cheresh, Integrins in cancer: biological implications and therapeutic opportunities, Nature Reviews Cancer. 10 (2010) 9–22. doi:10.1038/nrc2748.

[283] P.C. Letourneau, I. V. Pech, S.L. Rogers, S.L. Palm, J.B. McCarthy, L.T. Furcht, Growth cone migration across extracellular matrix components depends on integrin, but migration across glioma cells does not, Journal of Neuroscience Research. 21 (1988) 286–297. doi:10.1002/jnr.490210221.

[284] H. Ruan, X. Chen, C. Xie, B. Li, M. Ying, Y. Liu, M. Zhang, X. Zhang, C. Zhan, W. Lu, W. Lu, Stapled RGD Peptide Enables Glioma-Targeted Drug

Delivery by Overcoming Multiple Barriers, ACS Applied Materials & Interfaces. 9 (2017) 17745–17756. doi:10.1021/acsami.7b03682.

[285] C. Chen, Z. Duan, Y. Yuan, R. Li, L. Pang, J. Liang, X. Xu, J. Wang, Peptide-22 and Cyclic RGD Functionalized Liposomes for Glioma Targeting Drug Delivery Overcoming BBB and BBTB, ACS Applied Materials & Interfaces. 9 (2017) 5864–5873. doi:10.1021/acsami.6b15831.

[286] T. Zuo, Y. Guan, M. Chang, F. Zhang, S. Lu, T. Wei, W. Shao, G. Lin, RGD(Arg-Gly-Asp) internalized docetaxel-loaded pH sensitive liposomes: Preparation, characterization and antitumor efficacy in vivo and in vitro, Colloids and Surfaces B: Biointerfaces. 147 (2016) 90–99. doi:10.1016/j.colsurfb.2016.07.056.

[287] C. Dong, C. Feng, X. Li, X. Zhang, X. Zhang, Y. Gao, RGD-modified liposomes enhance efficiency of&nbsp;aclacinomycin A delivery: evaluation of their effect in lung cancer, Drug Design, Development and Therapy. 9 (2015) 4613–4620. doi:10.2147/DDDT.S85993.

[288] K. Shi, J. Li, Z. Cao, P. Yang, Y. Qiu, B. Yang, Y. Wang, Y. Long, Y. Liu, Q. Zhang, J. Qian, Z. Zhang, H. Gao, Q. He, A pH-responsive cell-penetrating peptide-modified liposomes with active recognizing of integrin α<inf>v</inf>β<inf>3</inf> for the treatment of melanoma, Journal of Controlled Release. 217 (2015) 138–150. doi:10.1016/j.jconrel.2015.09.009.

[289] W. Fei, Y. Zhang, S. Han, J. Tao, H. Zheng, Y. Wei, J. Zhu, F. Li, X. Wang, RGD conjugated liposome-hollow silica hybrid nanovehicles for targeted and controlled delivery of arsenic trioxide against hepatic carcinoma, International Journal of Pharmaceutics. 519 (2017) 250–262. doi:10.1016/j.ijpharm.2017.01.031.

[290] H. Zhao, M. Wang, P. Zhou, Q. Wang, Z. Zhou, D. Wang, H. Yang, S. Yang, RGD-conjugated titanium dioxide nanoparticles: targeted near-infrared photothermal therapy for αvβ3 integrin overexpressed cancer cells,

Journal of Materials Science. 52 (2017) 13356–13364. doi:10.1007/s10853-017-1083-9.

[291] B. Adibi-Motlagh, A.S. Lotfi, A. Rezaei, E. Hashemi, Cell attachment evaluation of the immobilized bioactive peptide on a nanographene oxide composite, Materials Science and Engineering: C. 82 (2017) 323–329. doi:10.1016/j.msec.2017.05.039.

[292] N. Zhao, Z. Yang, B. Li, J. Meng, Z. Shi, P. Li, S. Fu, RGD-conjugated mesoporous silica-encapsulated gold nanorods enhance the sensitization of triple-negative breast cancer to megavoltage radiation therapy, International Journal of Nanomedicine. Volume 11 (2016) 5595–5610. doi:10.2147/IJN.S104034.

[293] X. Wu, Z. Han, R.M. Schur, Z.R. Lu, Targeted Mesoporous Silica Nanoparticles Delivering Arsenic Trioxide with Environment Sensitive Drug Release for Effective Treatment of Triple Negative Breast Cancer, ACS Biomaterials Science and Engineering. 2 (2016) 501–507. doi:10.1021/acsbiomaterials.5b00398.

[294] G. Pan, T. Jia, Q. Huang, Y. Qiu, J. Xu, P. Yin, T. Liu, Mesoporous silica nanoparticles (MSNs)-based organic/inorganic hybrid nanocarriers loading 5-Fluorouracil for the treatment of colon cancer with improved anticancer efficacy, Colloids and Surfaces B: Biointerfaces. 159 (2017) 375–385. doi:10.1016/j.colsurfb.2017.08.013.

[295] Y. You, H. Hu, L. He, T. Chen, Differential Effects of Polymer-Surface Decoration on Drug Delivery, Cellular Retention, and Action Mechanisms of Functionalized Mesoporous Silica Nanoparticles, Chemistry - An Asian Journal. 10 (2015) 2744–2754. doi:10.1002/asia.201500769.

[296] H. Hu, F. Arena, E. Gianolio, C. Boffa, E. Di Gregorio, R. Stefania, L. Orio, S. Baroni, S. Aime, Mesoporous silica nanoparticles functionalized with fluorescent and MRI reporters for the visualization of murine tumors overexpressing α v β 3 receptors, Nanoscale. 8 (2016) 7094–7104.

doi:10.1039/C5NR08878J.

[297] H. Xu, Z. Wang, Y. Li, Y. Guo, H. Zhou, Y. Li, F. Wu, Preparation and characterization of a dual-receptor mesoporous silica nanoparticle–hyaluronic acid–RGD peptide targeting drug delivery system, RSC Adv. 6 (2016) 40427–40435. doi:10.1039/C6RA03113G.

[298] S. Brunauer, P.H. Emmett, E. Teller, Adsorption of Gases in Multimolecular Layers, Journal of the American Chemical Society. 60 (1938) 309–319. doi:10.1021/ja01269a023.

[299] E.P. Barrett, L.G. Joyner, P.P. Halenda, The Determination of Pore Volume and Area Distributions in Porous Substances. I. Computations from Nitrogen Isotherms, Journal of the American Chemical Society. 73 (1951) 373–380. doi:10.1021/ja01145a126.

[300] L. Boldon, F. Laliberte, L. Liu, Review of the fundamental theories behind small angle X-ray scattering, molecular dynamics simulations, and relevant integrated application, Nano Reviews. 6 (2015) 25661–25681. doi:10.3402/nano.v6.25661.

[301] Malvern Instruments, Dynamic Light Scattering: An Introduction in 30 Minutes, Technical Note. (2000) 1–8. http://www.malvern.com/En/Products/Technology/Dynamic-Light-Scattering/.

[302] M. Kaasalainen, V. Aseyev, E. von Haartman, D.Ş. Karaman, E. Mäkilä, H. Tenhu, J. Rosenholm, J. Salonen, Size, Stability, and Porosity of Mesoporous Nanoparticles Characterized with Light Scattering, Nanoscale Research Letters. 12 (2017) 74–83. doi:10.1186/s11671-017-1853-y.

[303] Malvern Instruments, Electrophoretic Light Scattering (ELS), Technology. (2015) 1. http://www.malvern.com/en/products/technology/electrophoretic-light-scattering/.

[304] Malvern instruments, Zeta Potential theory, Zetasizer Nano Series User

Manual. (2004) 207. http://www.biophysics.bioc.cam.ac.uk/files/Zetasizer_Nano_user_manual_Man0317-1.1.pdf.

[305] H. Ma, K.-J. Shieh, T.X. Qiao, Study of transmission electron microscopy (TEM) and scanning electron microscopy (SEM), Nature and Science. 4 (2006) 14–22.

Appendix

Paper I

Reprinted with permission from:

Adsorption and release of ampicillin antibiotic from ordered mesoporous silica.

V. Nairi, L. Medda, M. Monduzzi and A. Salis *J. Colloid Interface Sci.*, 2017, 497, 217-225.

DOI: 10.1016/j.jcis.2017.03.021

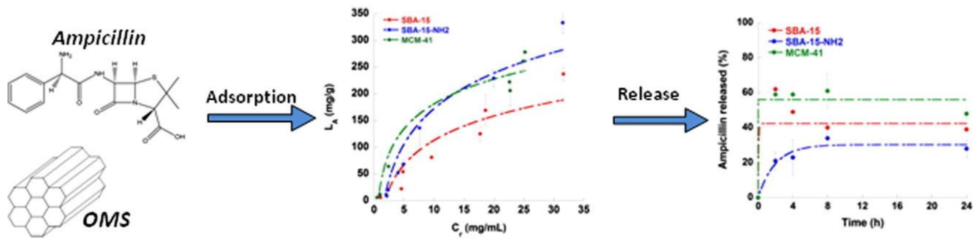

Journal of Colloid and Interface Science 497 (2017) 217–225

Contents lists available at ScienceDirect

Journal of Colloid and Interface Science

journal homepage: www.elsevier.com/locate/jcis

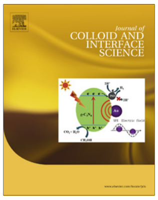

Regular Article

Adsorption and release of ampicillin antibiotic from ordered mesoporous silica

Valentina Nairi, Luca Medda, Maura Monduzzi *, Andrea Salis *

Department of Chemical and Geological Sciences, University of Cagliari-CSGI and CNBS, Cittadella Universitaria, S.S. 554 bivio Sestu, 09042 Monserrato, CA, Italy

GRAPHICAL ABSTRACT

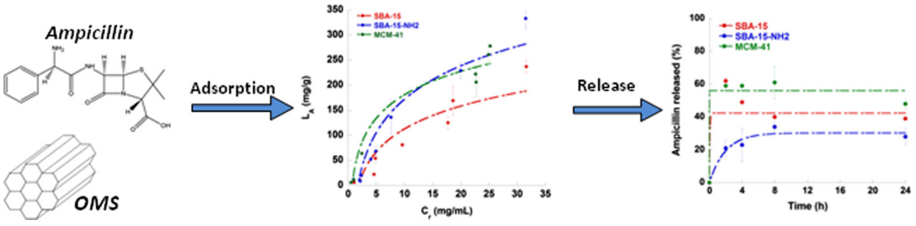

ARTICLE INFO

Article history:
Received 15 December 2016
Revised 27 February 2017
Accepted 3 March 2017
Available online 6 March 2017

Keywords:
Ampicillin
Ordered mesoporous silica
Functionalization
Adsorption
Drug delivery

ABSTRACT

In this work the adsorption and the release of ampicillin - a β-lactam penicillin-like antibiotic - from MCM-41, SBA-15, and (amino functionalized) SBA-15-NH$_2$ ordered mesoporous silica (OMS) materials were investigated. The silica matrices differ for their pore size (SBA-15 vs. MCM-41) mainly, and also for surface charge (SBA-15 and MCM-41, vs. SBA-15-NH$_2$). OMS samples were characterized through small-angle X-rays scattering (SAXS), transmission electron microscopy (TEM), N$_2$ adsorption–desorption isotherms, Fourier transform infrared spectroscopy (FTIR), thermogravimetric analysis (TGA), and potentiometric titrations. The quantification of immobilized and released ampicillin was monitored by mean of UV–Vis spectroscopy. Experimental adsorption isotherms evidenced that ampicillin's loading is not related to the pore size (d_{BJH}) of the adsorbent. Indeed the maximal loadings were 237 mg/g for SBA-15 (d_{BJH} = 6.5 nm), 278 mg/g for MCM-41 (d_{BJH} = 2.2 nm), and 333 mg/g for SBA-15-NH$_2$ (d_{BJH} = 5.6 nm). Loading seems, instead, to be related to the surface charge density (σ) of the sorbent surface. Indeed, at pH 7.4 ampicillin drug is negatively charged and likely prefers to interact with SBA-15-NH$_2$ ($\sigma_{SBA\text{-}15\text{-}NH2} = +0.223\ C\ m^{-2}$) rather than the slightly negatively charged silicas ($\sigma_{SBA\text{-}15} = -0.044\ C\ m^{-2}$ and $\sigma_{MCM\text{-}41} = -0.033\ C\ m^{-2}$). Similarly, ampicillin release is affected by interfacial interactions. Indeed, we found a burst release from pure silica samples (SBA-15 and MCM-41), whereas a sustained one from SBA-15-NH$_2$ sample. We explain this behavior as a result of an attractive interaction between the protonated amino group of SBA-15-NH$_2$ and the negatively charged carboxylate group of ampicillin. In summary, in order to obtain a sustained drug release, the chemical nature of the matrix's surface plays a role which is more important than its textural features. SBA-15-NH$_2$ matrix is hence a suitable candidate for local sustained release of antibiotic drugs.

1. Introduction

Osseointegration was discovered in 1969 when Branemark observed that a piece of titanium inserted in a rabbit bone was

---

* Corresponding authors.

E-mail addresses: monduzzi@unica.it (M. Monduzzi), asalis@unica.it (A. Salis).

http://dx.doi.org/10.1016/j.jcis.2017.03.021

not easily removed because anchored in the tissue [1]. The osseointegration process begins after the surgical insertion of an implant and is possible when the material is biocompatible, and allows for the spontaneous formation of hydroxyapatite layers [2]. However, after the implant insertion inflammatory processes (as peri-implantitis) can occur [3]. This can cause the loss of the supporting bone [1] and different types of osteomyelitis [4]. These diseases can be treated with systemic administration of antibiotic or anti-inflammatory drugs (via injection or ingestion) to prevent necrosis and bone neoformation that can degenerate in a chronic state [4,5]. This type of antibiotic therapy is highly inefficient. Indeed, only a low amount of drug can reach the infected region, so that the therapy needs to be repeated several times. Moreover, large amounts of administrated drugs can cause several drawbacks such as sensitivity, bacterial resistance, or superinfections. The proposed solution to all these problems is the *'in situ'* drug administration [5,6]. Nowadays different materials - i.e. antibiotic-impregnated cements, pastes, powders, degradable sponges or fleeces - are used in orthopedic surgery [7]. Nevertheless, only few nanomaterials can both easily be osseointegrated and slowly release antibiotic or anti-inflammatory drugs [5,8–11].

Ordered mesoporous silicas (OMSs), firstly synthesized in the early 90s [12,13], are interesting matrices for drug delivery [4,14–23]. Relevant features of OMSs are the high surface area (up to 1000 m^2/g), the narrow distribution of the pores size (2–30 nm), the high pore volume (1–3 cm^3/g) and the possibility to introduce several types of surface functional groups [24–30]. Moreover, OMSs display high biocompatibility [19,31–34] and allow for osseointegration if placed in a simulated body fluid [9,11]. All these features make OMSs very interesting matrices for biomedical applications as depot carriers for *'in situ'* controlled drug release. The use of OMS for drug delivery, dates back to 2001, when Vallet-Regì et al. studied the immobilization of ibuprofen on MCM-41 [35]. After that pioneering work the drug-loading capacity, and the sustained drug release from OMSs (i.e. MCM-41 and SBA-15) with different antibiotic or anti-inflammatory drugs - i.e. ibuprofen [36–38], gentamicin [39] and amoxicillin [25,40,41] - were widely investigated. Moreover, those studies showed how to modulate the drug loading and the release kinetics by functionalizing the surface of OMS samples [14,17,25,36,37,42,43], or by changing the pH, at which the drug loading is carried out [14,38,42,44,45].

Ampicillin is a penicillin-like molecule belonging to the class of β-lactam antibiotics, useful for the treatment of infections mediated by both gram-negative and gram-positive bacteria [5,7]. Ampicillin is usually administered in combination with sulbactam [46–48], a powerful and highly specific inhibitor of β-lactamases [49]. In particular, the therapeutic ampicillin dosage is 1.5–12 g/day for adults and 150 mg/kg/day for children [46]. After the administration, the maximal concentration of ampicillin in blood serum mainly depends on the patient's age. For adults (from 20 to 65 years) who have been administered with 2 g of ampicillin, the maximal measured concentration is about 80–110 μg/mL [50]. While for children (from 1 to 12 years) a dose of 40–80 mg/kg every 6 h results in an ampicillin concentration of 177–200 μg/mL [51]. Due to its high purity and low cost, ampicillin can be used as a model drug for a better understanding of the processes that regulate the adsorption and the release of therapeutic molecules from OMS-based depot systems. Recently, the release of ampicillin from different materials - amorphous silica, calcium silicate, silica/polycaprolactone, and $xCaO{\cdot}SiO_2$ - was studied [5,52]. These studies showed that the rate of release is affected by the chemical composition of the used material. Singh et al. used silica-based nanotubes for the adsorption and release of ampicillin [53]. They found that both adsorption and release rates are determined by the pore size of the carrier.

The aim of this work is to understand which, between the textural features and the chemical nature of the surface, plays the most important role to address the adsorption and release phenomena of ampicillin antibiotic from ordered mesoporous silica. To this purpose we compared the behavior of three different OMS samples, namely, SBA-15, SBA-15-NH_2 and MCM-41. In particular, we investigated the effect of pore size (SBA-15 versus MCM-41) and surface charge (SBA-15 versus SBA-15-NH_2) toward ampicillin adsorption (isotherms and kinetics) and release in simulated physiological conditions.

2. Materials and methods

2.1. Chemicals

Tetraethoxysilane (TEOS, 98%), pluronic copolymer 123 (EO_{20}-$PO_{70}EO_{20}$), cetyltrimethylammonium bromide (CTAB, >99%), (3-aminopropyl)triethoxysilane (APTES, >98%), sodium hydroxide, hydrochloride acid (37%), ampicillin sodium salt, acetic acid (>99.7%), sodium acetate (>99%), sodium dihydrogen phosphate (99.0%), and sodium phosphate dibasic (≥99.5%) were purchased from Sigma-Aldrich (Milan, Italy). Standard buffers at pH 1, 4, 6, 9, and 10 were purchased from Hanna Instruments (Szeged, Hungary). All chemical reagents were used without further purification.

2.2. Synthesis and characterization of SBA-15, MCM-41, and SBA-15-NH_2 samples

SBA-15 and MCM-41 were synthesized according to the methods reported in Refs. [27,54,55] respectively. We just remind that the synthesis occurs with a cooperative templating mechanism between TEOS and either Pluronic copolymer 123 (SBA-15) or CTAB (MCM-41). The organic surfactants were removed by calcination at 550 °C for 5 h. The functionalized SBA-15-NH_2 was prepared using APTES through a post-functionalization method described in Ref. [27]. The resulting solid was filtered and washed with acetone and dried overnight under vacuum at room temperature.

All materials were characterized through N_2 adsorption–desorption isotherms (texture), SAXS and TEM (structure), FTIR (functional groups), potentiometric titrations (surface charge density, σ), and thermogravimetric analysis (TGA). Textural analysis was carried out on an ASAP 2020 instrument, by determining the N_2 adsorption/desorption isotherm at 77 K. Before analysis MCM-41 and SBA-15 samples were heated at 250 °C at a rate of 1 °C/min under vacuum for 12 h, while SBA-15-NH_2 was heated at 110 °C at the rate of 1 °C/min under vacuum for 24 h. The Brunauer-Emmett-Teller (BET) and Barrett-Joyner-Halenda (BJH) method, calculated from the desorption branch of N_2 isotherm, were used to calculate surface area, pore volume and pore size distribution respectively. Small-angle X-ray scattering (SAXS) pattern was recorded with a S3-MICRO SWAXS camera system (HECUS X-ray Systems, Graz, Austria), as elsewhere reported [27]. Thin-walled 2 mm glass capillaries were filled with the sample for the scattering experiments. The scattering patterns were recorded for 1 h. Transmission electron microscopy (TEM) images were obtained on a JEOL 100S microscope, finely ground samples were placed directly onto formvar-coated electron microscopy nickel grids. Fourier transform infrared (FTIR) studies were conducted with a Bruker Tensor 27 spectrophotometer equipped with a diamond-ATR accessory and a DTGS detector. A number of 256 scans at a resolution of 2 cm^{-1} were averaged from wave number 4000 to 400 cm^{-1}. Surface charge density (σ vs. pH curves) of all samples was determined through potentiometric titrations which were carried out through an automatic titrator, Titrando 836 from Methrom (Herizau, Switzerland). The titration method is described in detail in Ref. [56]. Thermogravimetric analysis (TGA) was carried out in the range 25–1000 °C (heating rate = 10 $°C \cdot min^{-1}$), and under oxygen flow (flow rate = 50 $mL \cdot min^{-1}$) by mean of a Mettler-Toledo TGA/STDA 851.

2.3. Ampicillin adsorption and release from mesoporous silica samples

The adsorption isotherm of ampicillin on mesoporous silica (SBA-15, MCM-41, SBA-15-NH_2) was carried out by suspending different samples (50 mg each) of mesoporous silica in 50 mM phosphate buffer (pH 7.4) solutions having ampicillin concentrations in the range between 0.5 and 25 mg/mL. The suspensions were kept under rotation for 24 h at 298 K. The adsorbed amount of ampicillin was obtained by calculating the difference between the initial and the final (equilibrium) concentration of ampicillin in the adsorption solution. The concentration of ampicillin was determined through a calibration curve (in the concentration range 0.1–2.0 mg/mL) by measuring the absorbance at $\lambda = 268$ nm through a Cary UV–Vis spectrophotometer. After the immobilization ampicillin-loaded silica samples were collected through centrifugation, dried under vacuum, and analyzed through ATR-FTIR to assess the drug immobilization. The adsorption kinetics experiments of ampicillin adsorption on OMS samples were carried out similarly to what done for the isotherms. The only difference is that liquid samples were withdrawn at different fixed times (in the range 0–24 h) from the OMS/ampicillin suspension and analyzed through UV–Vis to assess the residual ampicillin concentration in the liquid phase.

In vitro drug release was carried out by suspending 50 mg of ampicillin-loaded mesoporous silica in 25 mL of 50 mM phosphate buffer saline solution (PBS: pH 7.4 and 0.15 M NaCl) at 37 °C in an orbital shaker (120 rpm). At fixed time intervals, a volume of 5 mL of solution was withdrawn and the same volume of PBS was replaced to maintain sink conditions. The amount of released ampicillin was quantified through UV–Vis spectrophotometry, using a calibration curve in the concentration range 0.1–2.0 mg/mL (100–2000 μg/mL). The amount of ampicillin released was calculated taking into account the dilution caused by the introduction of fresh PBS after each withdrawal [57].

3. Results and discussion

3.1. Characterization of OMSs

Fig. 1 shows the adsorption/desorption N_2 isotherms of SBA-15, SBA-15-NH_2 and MCM-41. SBA-15 and SBA-15-NH_2 exhibit a type IV isotherm with a sharp increase of N_2 volume adsorption at the relative pressure of p/p° = 0.6–0.7. The H1 hysteresis cycle is associated to a channel-like mesoporous structure. Respect to the curve of SBA-15, that of SBA-15-NH_2 is shifted toward low adsorbed nitrogen volumes. This result is consistent with a decrease of the pore volume due to the functionalization step with APTES.

MCM-41 isotherm strongly differs from that of SBA-15 and SBA-15-NH_2. It shows a similar increase of N_2 volume adsorption but at a lower relative pressure, between 0.2 and 0.4 p/p°, as expected by the smaller pores of MCM-41. In this case the isotherm is reversible and does not show any appreciable hysteresis loop. Table 1 reports the values of surface area, pore size, and pore volume for the three mesoporous silica samples.

Samples were also characterized through SAXS technique (Fig. 2a). SBA-15 and SBA-15-NH_2 show the typical pattern of hexagonal phases, with an intense peak and two weak peaks due to the reflections of (1 0 0), (1 1 0) and (2 0 0) planes, respectively. This confirms that the functionalization of SBA-15 with APTES does not modify the ordered hexagonal structure. Also MCM-41 shows a SAXS pattern with the three typical peaks of hexagonal phases but, in this case, they occur at higher *q* (scattering vector) values than those recorded for the other two OMSs. This is due to the reciprocal relationship which occurs between plane distance, *d*, and the scattering vector, *q*, ($d = 2\pi/q$). The lattice parameter (*a*) determined by SAXS measurements was 113.4 Å for SBA-15 and SBA-15-NH_2, and 40.1 Å for MCM-41 (Table 1).

Fig. 2b–d show TEM micrographs of the three mesoporous silica samples. It can be seen that MCM-41 sample is constituted by quasi-spherical nanoparticles with diameters in the range 60–100 nm (Fig. 2b), whereas SBA-15 and SBA-15-NH_2 samples have bigger particles with sizes around 1.0 μm (Fig. 2c and d). The TEM images show the cylindrical channels for all samples.

The FTIR spectra of SBA-15 and MCM-41 (Fig. 3a) show two intense peaks at 1060 and 800 cm^{-1} assigned to the asymmetric and symmetric stretching vibrations of Si—O—Si group, respectively. Moreover, a peak at 450 cm^{-1} is due to the deformation modes of the O—Si—O group [25]. The peak at 960 cm^{-1} is attributed to Si—OH stretching [58,59]. SBA-15-NH_2 sample shows a spectrum similar to those of SBA-15 and MCM-41 (Fig. 3a) but, in addition, we observe a weak peak around 1558 cm^{-1} (Fig. 3b)

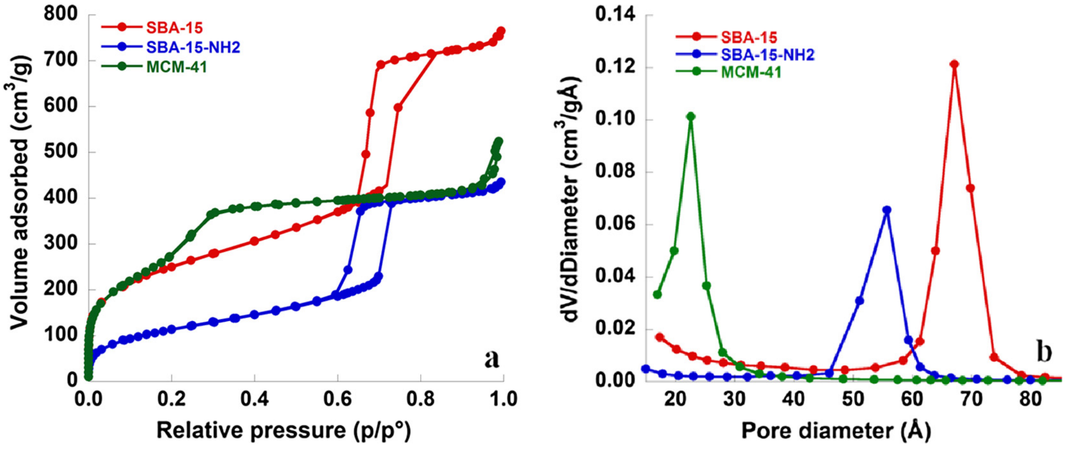

Fig. 1. Adsorption/desorption N_2 isotherms (a) and pore size distribution (b) of SBA-15, SBA-15-NH_2 and MCM-41.

Table 1
Surface area, pore volume, and pore size of SBA-15, SBA-15-NH_2 and MCM-41.

Sample	[a]S_{BET} (m^2/g)	[b]Pore volume (cm^3/g)	[c]$d_{BJH-Des}$ (Å)	[d]a (Å)
SBA-15	867	1.23	64.5	113.4
SBA-15-NH_2	408	0.69	55.7	113.4
MCM-41	1169	0.91	22.3	40.1

[a] Surface area calculated by the BET method (pressure range 0–1 p/p°).
[b] Pore volume (calculated at p/p°=0.99).
[c] Pore diameter calculated by applying the BJH method to the desorption branch of the isotherm.
[d] Lattice parameter obtained by SAXS.

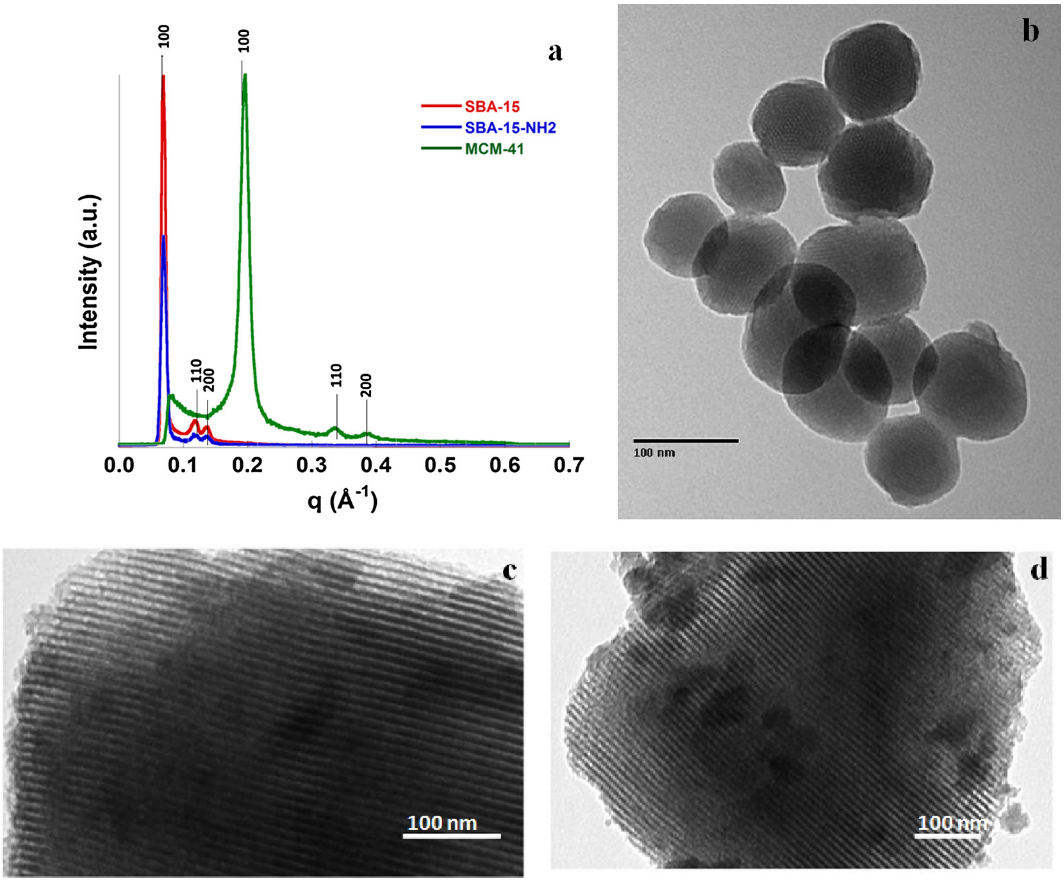

Fig. 2. Structural characterization of OMS samples. (a) SAXS pattern of SBA-15, SBA-15-NH_2 and MCM-41. Transmission electron microscopy images of MCM-41 (b), SBA-15 (c), SBA-15-NH_2 (d).

attributed to the bending of $-NH_2$, which confirms the amino-functionalization [25,60,61]. Thermogravimetric analysis (TGA) of OMS samples was then carried out. Fig. 4 shows the comparison among the percentage mass loss (Δm) profiles as a function of temperature for OMS samples. The mass loss observed for all samples at $T < 200$ °C can be ascribed to the removal of humidity and to the condensation of surface silanols. This last likely occurring for the pure silica samples (i.e. MCM-41 and SBA-15). Above 200 °C only SBA-15-NH_2 has a consistent mass loss ($\Delta m = 9.4\%$) due to the burning of organic groups. This is a further confirmation of the occurred functionalization with APTES.

Fig. 5 shows the surface charge density (σ) versus pH curves obtained for the three OMS samples. SBA-15 and MCM-41 samples show a very similar trend, that is, the surface charge is close to zero at acidic pH and becomes negative for pH > 6. It can be noticed that for pH > 8, SBA-15 surface charge is more negative than that of MCM-41. This may be due to a slightly more acidic behavior of SBA-15 silanols compared to those of MCM-41 [62]. As a result of the functionalization, the surface charge density of SBA-15-NH_2 becomes highly positive at acidic pH values. σ remains positive up to pH = 9.7, which is the point of zero charge of that material. Consequently, at the pH value used to immobilize the ampicillin (pH = 7.4) SBA-15 and MCM-41 carry a slightly negative surface charge ($\sigma_{SBA-15} = -0.044$ C m^{-2} and $\sigma_{MCM-41} = -0.033$ C m^{-2}) while SBA-15-NH_2 has a highly positive surface charge ($\sigma_{SBA-15-NH2} = +0.223$ C m^{-2}). At that pH, ampicillin carries a negative net charge ($pk_{aCOOH} = 2.96$, $pk_{aNH3} = 7.22$) [63]. Hence its adsorption on SBA-15-NH_2 would involve attractive electrostatic interactions. This will be discussed further in next paragraphs.

3.2. Determination of the adsorption isotherms and kinetics of ampicillin on OMSs

The different OMS samples, SBA-15, SBA-15-NH_2 and MCM-41, were then used as carriers for the adsorption of ampicillin antibiotic. The adsorption isotherms ($T = 298$ K) were determined

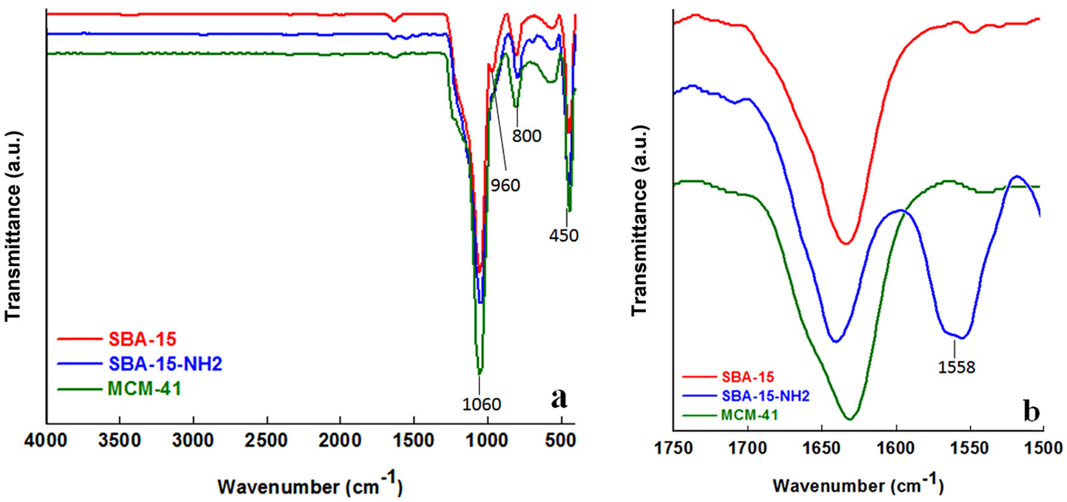

Fig. 3. FTIR spectra of SBA-15, SBA-15-NH$_2$ and MCM-41.

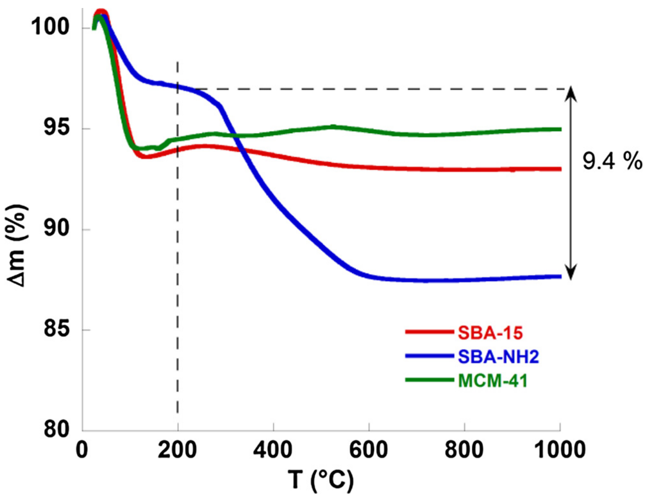

Fig. 4. TG analysis for SBA-15, SBA-15-NH$_2$, and MCM-41 samples.

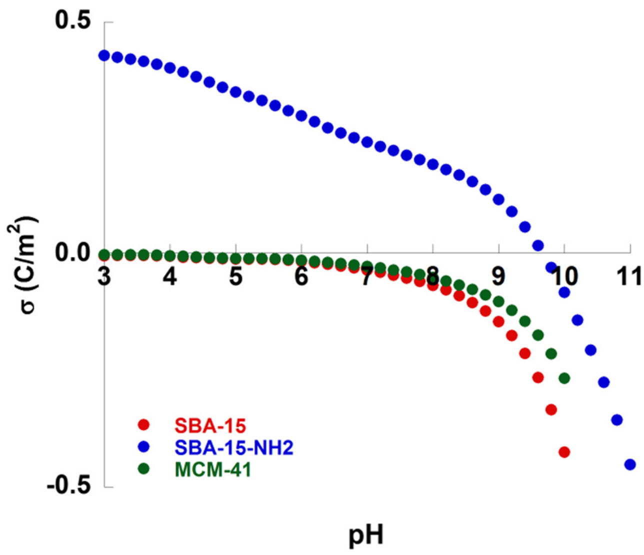

Fig. 5. Surface charge density versus pH curves for SBA-15, SBA-15-NH$_2$ and MCM-41 obtained by potentiometric titrations.

plotting the loading of ampicillin on OMS (L_A, mg$_{\mathrm{ampicillin}}$/g$_{\mathrm{OMS}}$) versus the equilibrium concentration of ampicillin in the adsorbing solution (C_r, mg$_{\mathrm{ampicillin}}$/mL). We used three different models - namely: Freundlich, Langmuir, and Temkin - to fit the experimental adsorption data. Fig. 6a shows the adsorption isotherm fitted by the Freundlich equation [64–67]:

$$L_A = K_F C_r^{1/n} \tag{1}$$

where K_F (mL/g) and 1/n (dimensionless) are the Freundlich constants, that is, empirical parameters specific for each adsorbent-adsorbate pair at a given temperature. The Freundlich model considers a heterogeneous adsorbent surface with non-identical adsorption sites. This results in the formation of a multi layer of adsorbed molecules. K_F is the support capacity, while l/n is the heterogeneity factor. The closer the latter is to 0 the more heterogeneous the adsorbent surface. Fig. 6b shows the fitting obtained with the Langmuir model:

$$L_A = \frac{L_0 K_L C_r}{1 + K_L C_r} \tag{2}$$

where L_0 and K_{L} are the maximum mono-layer coverage capacity and the Langmuir constant, respectively. Differently by the previous model, here only a monolayer of adsorbed molecules is allowed. Moreover, Langmuir isotherm refers to homogeneous adsorption, that is, it can only occur at a finite number of identical and equivalent localized sites, with no lateral interaction and steric hindrance between the adsorbed molecules, even on adjacent sites.

Finally, Fig. 6c shows the fitting obtained with the Temkin model:

$$L_A = \frac{RT}{b_T} \ln A_T C_r \tag{3}$$

where b_{T} is the Temkin constant and A_{T} is the isotherm equilibrium binding constant.

These models were chosen among many available since they resulted in quite good fittings of our experimental results. In particular, as shown in Table 2, Freundlich and Langmuir fittings were better than Temkin as confirmed by their higher correlation coefficients (R). In Fig. 6, adsorption isotherm curves have higher slopes for MCM-41 respect to SBA-15. This resulted, in our experimental conditions, in the maximal loadings of 278 mg/g and 237 mg/g for MCM-41 and SBA-15 respectively. The materials are both pure silica, but with different particle and pore size (see Fig. 2 and Table 1). This result seems to mean that the wider pore size of

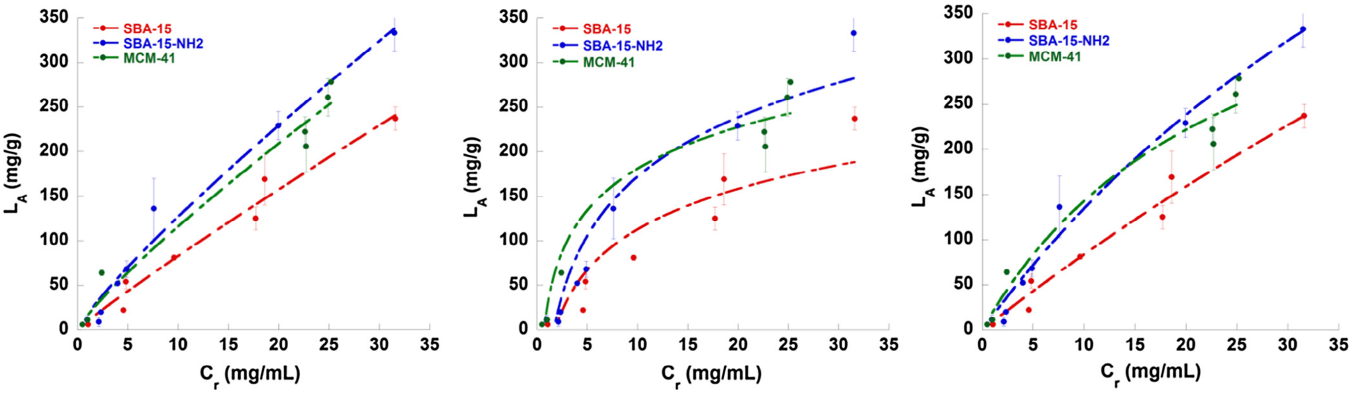

Fig. 6. Adsorption isotherms of ampicillin on SBA-15, SBA-15-NH$_2$ and MCM-41 (T = 298 K; pH 7.4) fitted with Freundlich (a), Langmuir (b), and Temkin (c) models.

Table 2
Isotherm parameters for ampicillin adsorption on OMS samples.

	Freundlich			Langmuir			Temkin		
Sample	K_F (mL/g)	1/n	R	L_0 (mg/g)	K_L (dm^3/mg)	R	b_T	A_T (L/g)	R
SBA-15	10	0.9	0.985	1588	0.006	0.986	38	0.6	0.906
SBA-15-NH$_2$	18	0.85	0.988	1035	0.015	0.991	26	0.6	0.949
MCM-41	16	0.9	0.986	495	0.04	0.984	37	1.5	0.976

SBA-15, compared to that of MCM-41, does not necessarily result in a higher ampicillin loading.

On the contrary, a lower pore size results in a higher surface area which is, evidently, widely available for ampicillin adsorption. However, also surface area does not seem to be the distinctive feature for obtaining a high loading. Indeed, SBA-15-NH$_2$ sample, with a S_{BET} = 408 m^2/g 'only', resulted in the highest loading (333 mg/g). Our hypothesis is that this result is due to the chemical nature of SBA-15-NH$_2$ surface. This gives rise to attractive forces between the adsorbent and the adsorbate. Indeed at pH 7.4 SBA-15-NH$_2$ carries a positive surface charge (Fig. 5), hence we expect a favorable electrostatic interaction with the carboxylate group of ampicillin. Singh et al. immobilized ampicillin on aminated mesoporous silica nanotubes (mSiNTs) [53]. They found that the loading capacity was affected by the presence of CTAB during the synthesis since it increased both pore size and surface area of the obtained material. In particular a loading of 110 mg/g was obtained for the material synthesized without CTAB, whereas a loading capacity of 180 mg/g in the presence of CTAB. Both values were, nevertheless, lower than those obtained with our adsorbents.

We also investigated the adsorption kinetics of ampicillin on OMSs samples (Fig. 7). The slope of the curve gives an estimation of the adsorption rate. This follow the series MCM-41 > SBA-15 > SBA-15-NH$_2$. The adsorption of molecules on mesoporous silica particles is a multistep process (1. External diffusion; 2. Internal diffusion; 3. Adsorbent-adsorbate interaction). We ascribe the trends shown in Fig. 7 to the lower particle size of MCM-41 which permits a faster diffusion, likely both external and internal (shorter channels). Nevertheless, ampicillin adsorption on SBA-15-NH$_2$, although occurred with a slower rate, reached the highest loading.

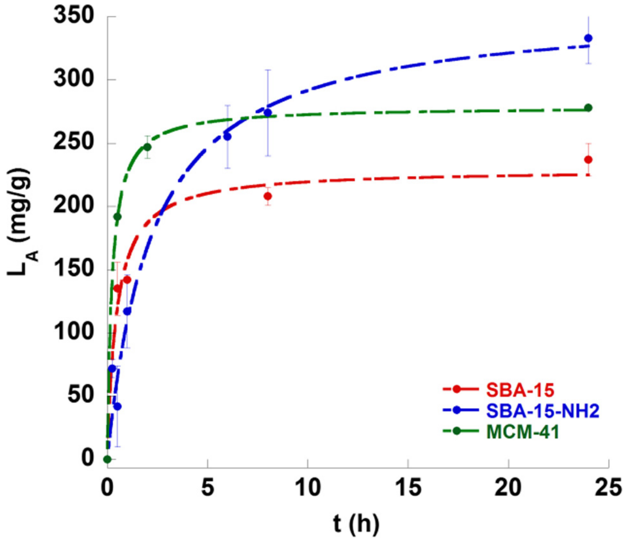

Fig. 7. Adsorption kinetics of ampicillin on SBA-15, SBA-15-NH$_2$ and MCM-41 (T = 298 K; pH 7.4).

3.3. FTIR characterization of ampicillin-loaded OMS samples

The adsorption of ampicillin on OMS samples was also confirmed by FTIR spectra (Fig. 8). Fig. 8a shows the chemical structure of ampicillin molecule while the relative FTIR spectrum, in the whole spectral range 4000–400 cm^{-1}, is shown in Fig. 8b. Fig. 8c shows a comparison among the FTIR spectra of free ampicillin and the ampicillin-loaded OMS samples in the range between 1900 cm^{-1} and 1300 cm^{-1}. In that figure, the peaks at 1764 cm^{-1} and 1693 cm^{-1} are attributed to the —C=O of the beta-lactam ring and of the amide bond respectively, those at 1640 cm^{-1} and 1378 cm^{-1} are instead related to the symmetric and asymmetric stretching of —COOH. Finally, the peaks at 1582 cm^{-1}, 1525 cm^{-1}, and 1455 cm^{-1} are assigned to the N—H deformation of the amide bond, the —NH$_2$ bending, and the —C=C—C stretching of aromatic ring, respectively [25,63,68]. Fig. 8c displays also the FTIR spectra of the ampicillin-loaded OMS samples (MCM-41, SBA-15, and SBA-15-NH$_2$). We notice that most peaks occurring in the spectrum of the free ampicillin occur also in the FTIR spectra of ampicillin-loaded OMS samples. In particular, we observe the peaks at 1765 cm^{-1} (—C=O of the beta-lactam ring) and the shoulder at 1685 cm^{-1} (amide bond) [63], and those at 1640 and

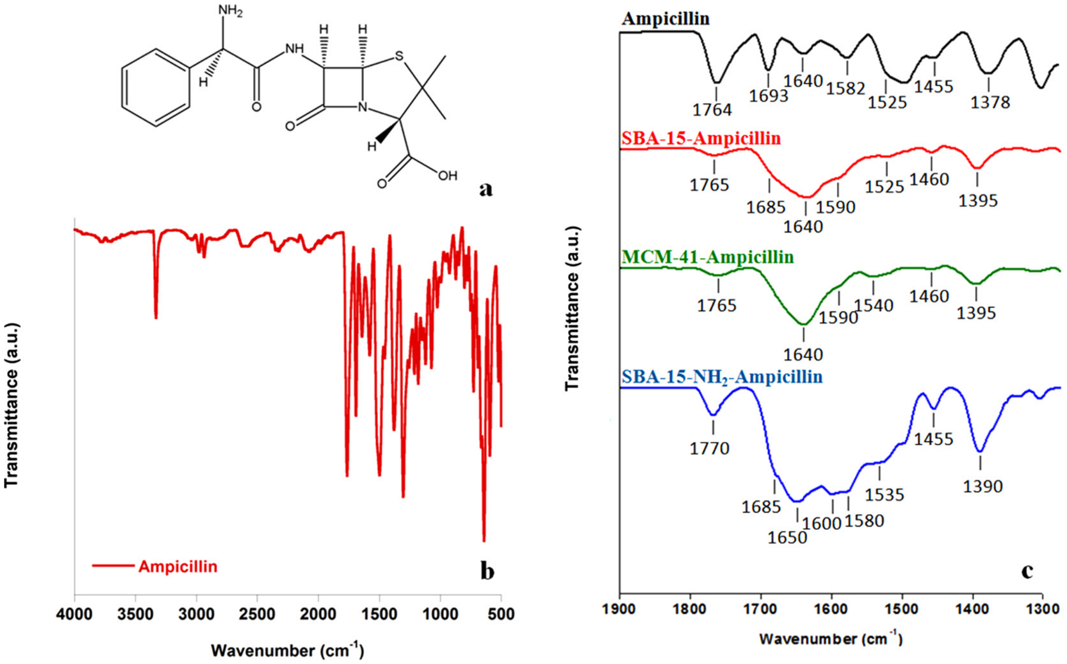

Fig. 8. Chemical structure of ampicillin (a). FTIR spectra of free ampicillin (b), and ampicillin-loaded on SBA-15, SBA-15-NH$_2$, and MCM-41 (c).

1395 cm^{-1} (symmetric and asymmetric stretching of —COOH) [27,37] and the shoulder at 1590 cm^{-1} (N—H deformation) [25].

Finally, we observe the peaks in the range 1525–1540 cm^{-1} (—NH$_2$ bending) and that at 1460 cm^{-1} (C=C—C stretching of the aromatic ring) [25,63]. We also notice that the spectrum of ampicillin loaded on SBA-15-NH$_2$ looks different from those of the drug loaded on SBA-15 and MCM-41. In particular, the broad band between 1700 and 1500 cm^{-1} shows additional peaks, like that at 1600 cm^{-1} and 1580 cm^{-1}, likely due to an electrostatic interaction between the protonated amino group of SBA-15-NH$_2$ and the carboxylate of ampicillin [25].

In summary, FTIR measurements confirm that ampicillin is successfully adsorbed on all OMS samples and that the chemical nature of the surface groups, that is, silanols (MCM-41 and SBA-15) or amino (SBA-15-NH$_2$), results in a different intermolecular interaction between the drug and the adsorbent. Indeed, at pH 7.4 the carboxylate of ampicillin is fully dissociated ($pK_{aCOOH} = 2.96$), whereas the —NH$_2$ group is only partially protonated ($pK_{aNH2} = 7.22$)[63]. Therefore we expect an attractive electrostatic interaction between the carboxylate of ampicillin with the protonated amino group of SBA-15-NH$_2$ (see Fig. 5). On the contrary, electrostatics would be much less important for the interaction between the only partially charged amino group of ampicillin and the slightly negatively charged silica (SBA-15, MCM-41) surface.

3.4. Ampicillin release from OMS samples

The release of ampicillin from SBA-15, SBA-15-NH$_2$ and MCM-41 matrices was then studied. The ampicillin-loaded OMS samples, with similar ampicillin loadings around 200 mg/g, were suspended in PBS (pH 7.4) at 37 °C, and the concentration of released ampicillin was measured at different times according to the procedure described above (see Section 2.3). We should specify that loadings cannot exactly be the same for the three samples, since they can only approximately be controlled due to the different ampicillin/OMS affinity. Nonetheless, any difference in the initial loading becomes not important since the release kinetics is expressed in mass% according to the following equation [26,57,69]:

$$\frac{M_t}{M_0}\% = A_{Max}(1 - e^{-kt}) \tag{4}$$

where M_t is the mass released at time t, M_0 is the total mass of ampicillin adsorbed in the material, A_{Max} is the maximal mass (%) released, k is the release rate constant, and t is the time. Fig. 9 shows the kinetics of ampicillin release from the different OMS samples.

MCM-41 and SBA-15 materials gave rise to a burst release, reaching a maximal amount of released drug of $A_{Max} = 56\%$ and 42% respectively within the first two hours (Fig. 9). Differently, SBA-15-NH$_2$ resulted in a more gradual release, reaching a release maximum $A_{Max} = 30\%$ after about 8 h. The maximal amount of released drug corresponds to an ampicillin concentration in the release solution of 327 µg/mL, 210 µg/mL, and 145 µg/mL for MCM-41, SBA-15, and SBA-15-NH$_2$, respectively. We observe that the latter value (SBA-15-NH$_2$) is comparable to the concentration of ampicillin in the serum of both adults and children [50,51].

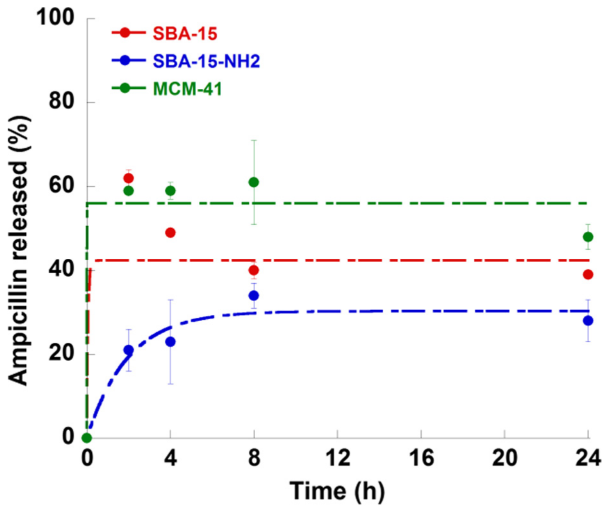

Fig. 9. Ampicillin release from SBA-15, SBA-15-NH$_2$ and MCM-41.

Similar release kinetics were reported for amoxicillin release from pure and functionalized SBA-15 and MCM-41 [25,41]. Also in those cases the maximal amount of drug was released in the first hours. The authors justified their results considering that the sustained release is regulated by a diffusion mechanism which is affected by steric hindrance. We propose that in our system, the release is affected by the competition between the affinity of ampicillin for the adsorbent surface and its solubility in the release medium (PBS) [70]. This results in a quick desorption particularly from the silica surfaces as a result of a weak electrostatic interaction (both attractive and repulsive). Differently, the electrostatic attraction between ampicillin and SBA-15-NH_2 surface, prevents a quick and significant release. Indeed the occurrence of an attractive electrostatic interaction between the protonated amino groups of SBA-15-NH_2 and the carboxylate groups of ampicillin is clearly seen in the FTIR spectra in Fig. 8c.

4. Conclusions

In this work the adsorption and the release of ampicillin from mesoporous silica matrices, differing in pore size and chemical proprieties due to surface functionalization, were studied. Results show that complex mechanisms and interactions address drug loading and release. The materials we compared had either different pore size but similar surface charge (SBA-15 and MCM-41), or similar pore size but different surface charge (SBA-15 and SBA-15-NH_2). It emerges that both ampicillin adsorption (isotherms and kinetics) and release are affected by the surface charge more than by the pore size. The interaction between a specific drug and a specific adsorbent is a very peculiar phenomenon. To the best of our knowledge, what found here for ampicillin/OMS systems was not previously available in the literature. The low negative surface charge of the two pure silica SBA-15 and MCM-41 matrices favors a rapid and efficient release at pH 7.4, this being slightly higher for MCM-41. Indeed, MCM-41 particles are much smaller than those of SBA-15 therefore a larger amount of adsorbed drug is likely to be located on the external surface or close to the pore openings. In the case of SBA-15-NH_2 matrix, electrostatic interactions favor a sustained release of ampicillin antibiotic. Indeed release from amino-functionalized material is slower than that measured for pure silica. The sustained release is likely due the presence of protonated amino groups that favorably interact with the negatively charged carboxylate of ampicillin. Future work will be necessary to investigate the use of SBA-15-NH_2 matrix for the fabrication of a depot system for a locally sustained release of ampicillin.

Acknowledgments

FIR 2016 and Fondazione di Sardegna (L.R. 7/2007 year 2016 – DGR 28/21 17.05.2015) is thanked for financial support. The Scientific Park 'Sardegna Ricerche' (Pula, CA, Italy) is acknowledged for free access to SAXS, FT-IR and potentiometric titration facilities. Prof. M.F. Casula is acknowledged for TEM images of OMS samples.

References

[1] A.D. Pye, D.E.A. Lockhart, M.P. Dawson, C.A. Murray, A.J. Smith, A review of dental implants and infection, J. Hosp. Infect. 72 (2009) 104–110, http://dx.doi.org/10.1016/j.jhin.2009.02.010.

[2] H.-A. Hansson, T. Albrektsson, P.-I. Branemark, Structural aspects of the interface between tissue and titanium implants, J. Prosthet. Dent. 50 (1983) 108–113.

[3] A. Mombelli, P.N. Lang, The diagnosis and treatment of peri-implantitis, Periodontology 17 (1998) 63–76.

[4] D. Molina-Manso, M. Manzano, J.C. Doadrio, G. Del Prado, A. Ortiz-Pérez, M. Vallet-Regì, E. Gòmez-Barrena, J. Esteban, Usefulness of SBA-15 mesoporous ceramics as a delivery system for vancomycin, rifampicin and linezolid: a preliminary report, Int. J. Antimicrob. Agents 40 (2012) 252–256, http://dx.doi.org/10.1016/j.ijantimicag.2012.05.013.

[5] M. Catauro, F. Papale, G. Roviello, C. Ferone, F. Bollino, M. Trifuoggi, C. Aurilio, Synthesis of SiO_2 and CaO rich calcium silicate systems via sol-gel process: bioactivity, biocompatibility, and drug delivery tests, J. Biomed. Mater. Res. – Part A 102 (2014) 3087–3092, http://dx.doi.org/10.1002/jbm.a.34978.

[6] S. Kamath, S. Sinha, E. Shaari, D. Young, A.C. Campbell, Role of topical antibiotics in hip surgery: a prospective randomised study, Injury 36 (2005) 783–787, http://dx.doi.org/10.1016/j.injury.2005.01.001.

[7] P. Huiras, J.K. Logan, S. Papadopoulos, D. Whitney, Local antimicrobial administration for prophylaxis of surgical site infections, Pharmacotherapy 32 (2012) 1006–1019, http://dx.doi.org/10.1002/phar.1135.

[8] A. Chaudhari, M.V. Cardoso, J. Martens, K. Vandamme, I. Naert, J. Duyck, Bone tissue response to BMP-2 adsorbed on amorphous microporous silica implants, J. Clin. Periodontol. 39 (2012) 1206–1213, http://dx.doi.org/10.1111/jcpe.12005.

[9] A.J. Salinas, M. Vallet-Regí, Bioactive ceramics: from bone grafts to tissue engineering, RSC Adv. 3 (2013) 11116–11131, http://dx.doi.org/10.1039/c3ra00166k.

[10] M.V. Cabañas, J. Peña, J. Román, C. Ramírez-Santillán, M.C. Matesanz, M.J. Feito, M.T. Portolés, M. Vallet-Regí, Design of tunable protein-releasing nanoapatite/hydrogel scaffolds for hard tissue engineering, Mater. Chem. Phys. 144 (2014) 409–417, http://dx.doi.org/10.1016/j.matchemphys.2014.01.011.

[11] M. Vallet-Regí, Nanostructured mesoporous silica matrices in nanomedicine, J. Intern. Med. 267 (2010) 22–43, http://dx.doi.org/10.1111/j.1365-2796.2009.02190.x.

[12] C.T. Kresge, M.E. Leonowicz, W.J. Roth, J.C. Vartuli, J.S. Beck, Ordered mesoporous molecular sieves synthesized by liquid-crystal template mechanism, Nature 359 (1992) 710–712, http://dx.doi.org/10.1038/355242a0.

[13] C.J. Brinker, Y. Lu, A. Sellinger, H. Fan, Evaporation-induced self-assembly: nanostructures made easy, Adv. Mater. 11 (1999) 579–585.

[14] A. Baeza, M. Colilla, M. Vallet-Regí, Advances in mesoporous silica nanoparticles for targeted stimuli-responsive drug delivery, Expert Opin. Drug Deliv. 12 (2015) 319–337, http://dx.doi.org/10.1517/17425247.2014.953051.

[15] D. Berger, L. Bajenaru, S. Nastase, R.-A. Mitran, C. Munteanu, C. Matei, Influence of structural, textural and surface properties of mesostructured silica and aluminosilicate carriers on aminoglycoside uptake and in vitro delivery, Microporous Mesoporous Mater. 206 (2015) 150–160, http://dx.doi.org/10.1016/j.micromeso.2014.12.022.

[16] N.Ž. Knežević, J.-O. Durand, Large pore mesoporous silica nanomaterials for application in delivery of biomolecules, Nanoscale 7 (2015) 2199–2209, http://dx.doi.org/10.1039/C4NR06114D.

[17] A.L. Doadrio, J.M. Sánchez-Montero, J.C. Doadrio, A.J. Salinas, M. Vallet-Regí, A molecular model to explain the controlled release from SBA-15 functionalized with APTES, Microporous Mesoporous Mater. 195 (2014) 43–49, http://dx.doi.org/10.1016/j.micromeso.2014.04.019.

[18] V. Mamaeva, C. Sahlgren, M. Lindén, Mesoporous silica nanoparticles in medicine-Recent advances, Adv. Drug Deliv. Rev. 65 (2013) 689–702, http://dx.doi.org/10.1016/j.addr.2012.07.018.

[19] L. Maggini, I. Cabrera, A. Ruiz-Carretero, E.A. Prasetyanto, E. Robinet, L. De Cola, Breakable mesoporous silica nanoparticles for targeted drug delivery, Nanoscale 8 (2016) 7240–7247, http://dx.doi.org/10.1039/C5NR09112H.

[20] A. Bertucci, E.A. Prasetyanto, D. Septiadi, A. Manicardi, E. Brognara, R. Gambari, R. Corradini, L. De Cola, Combined delivery of temozolomide and anti-miR221 PNA using mesoporous silica nanoparticles induces apoptosis in resistant glioma cells, Small 11 (2015) 5687–5695, http://dx.doi.org/10.1002/smll.201500540.

[21] T. Kjellman, X. Xia, V. Alfredsson, A.E. Garcia-Bennett, Influence of microporosity in SBA-15 on the release properties of anticancer drug dasatinib, J. Mater. Chem. B 2 (2014) 5265–5271, http://dx.doi.org/10.1039/C4TB00418C.

[22] M. Monduzzi, S. Lampis, S. Murgia, A. Salis, From self-assembly fundamental knowledge to nanomedicine developments, Adv. Colloid Interface Sci. 205 (2014) 48–67, http://dx.doi.org/10.1016/j.cis.2013.10.009.

[23] M. Piludu, L. Medda, F. Cugia, M. Monduzzi, A. Salis, Silver enhancement for transmission electron microscopy imaging of antibody fragment-gold nanoparticles conjugates immobilized on ordered mesoporous silica, Langmuir 31 (2015) 9458–9463, http://dx.doi.org/10.1021/acs.langmuir.5b02830.

[24] Z. Tao, Mesoporous silica-based nanodevices for biological applications, RSC Adv. 4 (2014) 18961, http://dx.doi.org/10.1039/c3ra47166g.

[25] F. Sevimli, Y. Aysen, Surface functionalization of SBA-15 particles for amoxicillin delivery, Microporous Mesoporous Mater. 158 (2012) 281–291, http://dx.doi.org/10.1016/j.micromeso.2012.02.037.

[26] A. Nieto, M. Colilla, F. Balas, M. Vallet-Regì, Surface electrochemistry of mesoporous silicas as a key factor in the design of tailored delivery devices, Langmuir 26 (2010) 5038–5049, http://dx.doi.org/10.1021/la904820k.

[27] L. Medda, M.F. Casula, M. Monduzzi, A. Salis, Adsorption of lysozyme on hyaluronic acid functionalized SBA-15 mesoporous silica: a possible bioadhesive depot system, Langmuir 30 (2014) 12996–13004, http://dx.doi.org/10.1021/la503224n.

[28] Y. Liu, X. Ding, J. Li, Z. Luo, Y. Hu, J. Liu, L. Dai, J. Zhou, C. Hou, K. Cai, Enzyme responsive drug delivery system based on mesoporous silica nanoparticles for tumor therapy *in vivo*, Nanotechnology 26 (2015), http://dx.doi.org/10.1088/0957-4484/26/14/145102. 145102–14115.

[29] B. Lebeau, A. Galarneau, M. Linden, Introduction for 20 years of research on ordered mesoporous materials, Chem. Soc. Rev. 42 (2013) 3661–3662, http://dx.doi.org/10.1039/c3cs90005c.

[30] P. Kipkemboi, A. Fogden, V. Alfredsson, K. Flodström, Triblock copolymers as templates in mesoporous silica formation: Structural dependence on polymer chain length and synthesis temperature, Langmuir 17 (2001) 5398–5402, http://dx.doi.org/10.1021/la001715i.

[31] Z. Chen, Z. Li, Y. Lin, M. Yin, J. Ren, X. Qu, Bioresponsive hyaluronic acid-capped mesoporous silica nanoparticles for targeted drug delivery, Chem. Eur. J. 19 (2013) 1778–1783, http://dx.doi.org/10.1002/chem.201202038.

[32] S. Williams, A. Neumann, I. Bremer, Y. Su, G. Dräger, C. Kasper, P. Behrens, Nanoporous silica nanoparticles as biomaterials: evaluation of different strategies for the functionalization with polysialic acid by step-by-step cytocompatibility testing, J. Mater. Sci. – Mater. Med. 26 (2015), http://dx.doi.org/10.1007/s10856-015-5409-3.

[33] S.P. Hudson, R.F. Padera, R. Langer, D.S. Kohane, The biocompatibility of mesoporous silicates, Biomaterials 29 (2008) 4045–4055, http://dx.doi.org/10.1016/j.biomaterials.2008.07.007.

[34] K. Braun, A. Pochert, M. Beck, R. Fiedler, J. Gruber, M. Lindén, Dissolution kinetics of mesoporous silica nanoparticles in different simulated body fluids, J. Sol-Gel. Sci. Technol. 79 (2016) 319–327, http://dx.doi.org/10.1007/s10971-016-4053-9.

[35] M. Vallet-Regi, A. Rámila, R.P. Del Real, J. Pérez-Pariente, A new property of MCM-41: drug delivery system, Chem. Mater. 13 (2001) 308–311, http://dx.doi.org/10.1021/cm0011559.

[36] A. Szegedi, M. Popova, I. Goshev, S. Klébert, J. Mihály, Controlled drug release on amine functionalized spherical MCM-41, J. Solid State Chem. 194 (2012) 257–263, http://dx.doi.org/10.1016/j.jssc.2012.05.030.

[37] A. Szegedi, M. Popova, I. Goshev, J. Mihály, Effect of amine functionalization of spherical MCM-41 and SBA-15 on controlled drug release, J. Solid State Chem. 184 (2011) 1201–1207, http://dx.doi.org/10.1016/j.jssc.2011.03.005.

[38] Q. Gao, Y. Xu, D. Wu, W. Shen, F. Deng, Synthesis, characterization, and in vitro pH-controllable drug release from mesoporous silica spheres with switchable gates, Langmuir 26 (2010) 17133–17138, http://dx.doi.org/10.1021/la102952n.

[39] A.L. Doadrio, E.M.B. Sousa, J.C. Doadrio, J. Pérez Pariente, I. Izquierdo-Barba, M. Vallet-Regí, Mesoporous SBA-15 HPLC evaluation for controlled gentamicin drug delivery, J. Control. Release 97 (2004) 125–132, http://dx.doi.org/10.1016/j.jconrel.2004.03.005.

[40] M. Vallet-Regì, J.C. Doadrio, A.L. Doadrio, I. Izquierdo-Barba, J. Pérez-Pariente, Hexagonal ordered mesoporous material as a matrix for the controlled release of amoxicillin, Solid State Ionics 172 (2004) 435–439, http://dx.doi.org/10.1016/j.ssi.2004.04.036.

[41] Z. Li, K. Su, B. Cheng, Y. Deng, Organically modified MCM-type material preparation and its usage in controlled amoxicillin delivery, J. Colloid Interface Sci. 342 (2010) 607–613, http://dx.doi.org/10.1016/j.jcis.2009.10.073.

[42] Y. Jiao, S. Shen, Y. Sun, X. Jiang, W. Yang, A Functionalized hollow mesoporous silica nanoparticles-based controlled dual-drug delivery system for improved tumor cell cytotoxicity, Part. Part. Syst. Charact. 32 (2015) 222–233, http://dx.doi.org/10.1002/ppsc.201400115.

[43] E.I. Basaldella, M.S. Legnoverde, Functionalized silica matrices for controlled delivery of cephalexin, J. Sol-Gel. Sci. Technol. 56 (2010) 191–196, http://dx.doi.org/10.1007/s10971-010-2293-7.

[44] M.-Y. Yang, L. Tan, H.-X. Wu, C.-J. Liu, R.-X. Zhuo, Dual-stimuli-responsive polymer-coated mesoporous silica nanoparticles used for controlled drug delivery, J. Appl. Polym. Sci. 132 (2015) 42395–42403, http://dx.doi.org/10.1002/app.42395.

[45] Y. Yan, J. Fu, X. Liu, T. Wang, X. Lu, Acid-responsive intracellular doxorubicin release from click chemistry functionalized mesoporous silica nanoparticles, RSC Adv. 5 (2015) 30640–30646, http://dx.doi.org/10.1039/C5RA00059A.

[46] H.M. Lode, Rational antibiotic therapy and the position of ampicillin/sulbactam, Int. J. Antimicrob. Agents 32 (2008) 10–28, http://dx.doi.org/10.1016/j.ijantimicag.2008.02.004.

[47] H. Lode, Role of sultamicillin and ampicillin/sulbactam in the treatment of upper and lower bacterial respiratory tract infections, Int. J. Antimicrob. Agents 18 (2001) 199–209, http://dx.doi.org/10.1016/S0924-8579(01)00387-9.

[48] J.D. Williams, β-Lactamases and β-lactamase inhibitors, Int. J. Antimicrob. Agents 12 (1999) S3–S7, http://dx.doi.org/10.1016/S0924-8579(99)00085-0.

[49] J.D. Williams, β-Lactamase inhibition and in vitro activity of sulbactam and sulbactam/cefoperazone, Clin. Infect. Dis. 24 (1997) 494–497. 1058-4838/97/2403-0030$02.00.

[50] B.R. Meyers, P. Wilkinson, M.H. Mendelson, S. Walsh, C. Bournazos, S.Z. Hirschman, Pharmacokinetics of aztreonam in healthy elderly and young adult volunteers, Antimicrob. Agents Chemother. 35 (1991) 2098–2101. 0066-4804/91/102098-04$02.00/0.

[51] M.C. Nahata, V.I. Vashi, R.N. Swanson, M.A. Messig, M. Chung, Pharmacokinetics of ampicillin and sulbactam in pediatric patients, Antimicrob. Agents Chemother. 43 (1999) 1225–1229, http://dx.doi.org/10.1016/0002-9378(93)90515-K.

[52] F. De Gaetano, L. Ambrosio, M.G. Raucci, A. Marotta, M. Catauro, Sol-gel processing of drug delivery materials and release kinetics, J. Mater. Sci. – Mater. Med. 16 (2005) 261–265, http://dx.doi.org/10.1007/s10856-005-6688-x.

[53] R.K. Singh, T.-H. Kim, J.-J. Kim, E.-J. Lee, J.C. Knowles, H.-W. Kim, Mesoporous silica tubular nanocarriers for the delivery of therapeutic molecules, RSC Adv. 3 (2013) 8692–8704, http://dx.doi.org/10.1039/c3ra22975k.

[54] I.I. Slowing, B.G. Trewyn, V.S. Lin, Mesoporous silica nanoparticles for intracellular delivery of membrane-impermeable proteins, J. Am. Chem. Soc. (2007) 8845–8849.

[55] A. Salis, M. Fanti, L. Medda, V. Nairi, F. Cugia, M. Piludu, V. Sogos, M. Monduzzi, Mesoporous silica nanoparticles functionalized with hyaluronic acid and chitosan biopolymers effect of functionalization on cell internalization, ACS Biomater. Sci. Eng. 2 (2016) 741–751, http://dx.doi.org/10.1021/acsbiomaterials.5b00502.

[56] A. Salis, D.F. Parsons, M. Boström, L. Medda, B. Barse, B.W. Ninham, M. Monduzzi, Ion specific surface charge density of SBA-15 mesoporous silica, Langmuir 26 (2010) 2484–2490, http://dx.doi.org/10.1021/la902721a.

[57] D. Steri, M. Monduzzi, A. Salis, Ionic strength affects lysozyme adsorption and release from SBA-15 mesoporous silica, Microporous Mesoporous Mater. 170 (2013) 164–172, http://dx.doi.org/10.1016/j.micromeso.2012.12.002.

[58] B.A. Morrow, A.J. McFarlan, Surface vibrational modes of silanol groups on silica, J. Phys. Chem. 96 (1992) 1395–1400, http://dx.doi.org/10.1021/j100182a068.

[59] D. Scarano, A. Zecchina, S. Bordiga, F. Geobaldo, G. Spoto, G. Petrini, G. Leofanti, M. Padovan, G. Tozzola, Fourier-transform infrared and raman-spectra of pure and Al, B-, Ti- and Fe-substituted silicalites: stretching-mode region, J. Chem. Soc. Trans. 89 (1993) 4123–4130, http://dx.doi.org/10.1039/ft9938904123.

[60] S.W. Song, K. Hidajat, S. Kawi, Functionalized SBA-15 materials as carriers for controlled drug delivery: influence of surface properties on matrix-drug interactions, Langmuir 21 (2005) 9568–9575, http://dx.doi.org/10.1021/la051167e.

[61] E. Gianotti, V. Dellarocca, L. Marchese, G. Martra, S. Coluccia, T. Maschmeyer, NH3 adsorption on MCM-41 and Ti-grafted MCM-41. FTIR, DR UV-Vis-NIR and photoluminescence studies, Phys. Chem. Chem. Phys. 4 (2002) 6109–6115, http://dx.doi.org/10.1039/b207231a.

[62] J. Grams, N. Potrzebowska, J. Goscianska, B. Michalkiewicz, A.M. Ruppert, Mesoporous silicas as supports for Ni catalyst used in cellulose conversion to hydrogen rich gas, Int. J. Hydrogen Energy 41 (2016) 8656–8667, http://dx.doi.org/10.1016/j.ijhydene.2015.12.146.

[63] O. Rozas, D. Contreras, M.A. Mondaca, M. Pérez-Moya, H.D. Mansilla, Experimental design of Fenton and photo-Fenton reactions for the treatment of ampicillin solutions, J. Hazard. Mater. 177 (2010) 1025–1030, http://dx.doi.org/10.1016/j.jhazmat.2010.01.023.

[64] Y.-S. Ho, Selection of optimum sorption isotherm, Carbon N. Y. 42 (2004) 2115–2116, http://dx.doi.org/10.1016/j.carbon.2004.03.019.

[65] K. Gul, S. Sohni, M. Waqar, F. Ahmad, N.A.N. Norulaini, M. Omar, Functionalization of magnetic chitosan with graphene oxide for removal of cationic and anionic dyes from aqueous solution, Carbohydr. Polym. 152 (2016) 520–531, http://dx.doi.org/10.1016/j.carbpol.2016.06.045.

[66] J. Zhu, X. Zhu, J. Gu, L. Zhao, L. Jiang, Y. Qiu, Effective adsorption and concentration of carnosine by nickel species within mesoporous silica, LWT – Food Sci. Technol. 74 (2016) 211–218, http://dx.doi.org/10.1016/j.lwt.2016.07.016.

[67] E.A. Dil, M. Ghaedi, A. Asfaram, S. Hajati, F. Mehrabi, A. Goudarzi, Preparation of nanomaterials for the ultrasound-enhanced removal of Pb2+ ions and malachite green dye: chemometric optimization and modeling, Ultrason. Sonochem. 34 (2017) 677–691, http://dx.doi.org/10.1016/j.ultsonch.2016.07.001.

[68] J. Coates, Interpretation of Infrared Spectra, A Practical Approach, Encycl. Anal. Chem. John Wiley & Sons Ltd, Chichester, vol. 2000, 2000, pp. 10815–10837.

[69] M.S. Bhattacharyya, P. Hiwale, M. Piras, L. Medda, D. Steri, M. Piludu, A. Salis, M. Monduzzi, Lysozyme adsorption and release from ordered mesoporous materials, J. Phys. Chem. C 114 (2010) 19928–19934, http://dx.doi.org/10.1021/jp1078218.

[70] H. Liu, K.K. Leonas, Y. Zhao, Antimicrobial properties and release profile of ampicillin from electrospun poly (ε-caprolactone) nanofiber yarns, J. Eng. Fiber. Fabr. 5 (2010) 10–19.

Paper II

Reprinted with permission from:

Double Sequential Encrypted Targeting Sequence: A New Concept for Bone Cancer Treatment.

G. Villaverde, V. Nairi, A. Baeza and M. Vallet-Regì, *Chem.–Eur. J.*, 2017, 23, 7174-7179.

DOI: 10.1002/chem.201605947

ChemPubSoc Europe
DOI: 10.1002/chem.201605947
CHEMISTRY A European Journal Communication

Drug Delivery |*Hot Paper*|

Double Sequential Encrypted Targeting Sequence: A New Concept for Bone Cancer Treatment

Gonzalo Villaverde, Valentina Nairi, Alejandro Baeza,* and María Vallet-Regí*[a]

In memory of José Barluenga Mur

Abstract: The selective transportation of therapeutic agents to tumoral cells is usually achieved by their conjugation with targeting moieties able to recognize these cells. Unfortunately, simple and static targeting systems usually show a lack in selectivity. Herein, a double sequential encrypted targeting system is proposed as a stimuli-responsive targeting analogue for selectivity enhancement. The system is able to recognize diseased bone tissue in the first place, and once there, a hidden secondary targeting group is activated by the presence of an enzyme overproduced in the malignant tissue (cathepsin K), thereby triggering the recognition of diseased cells. Transporting the cell targeting agent in a hidden conformation that contains a high selective tissular primary targeting, could avoid not only its binding to similar cell receptors but also the apparition of the binding-site barrier effect, which can enhance the penetration of the therapeutic agent within the affected zone. This strategy could be applied not only to conjugate drugs but also to drug-loaded nanocarriers to improve the efficiency for bone cancer treatments.

The lack in selectivity of cytotoxic drugs results in their ineffective delivery to tumor tissues, which strongly reduces efficacy and causes the apparition of systemic toxicity in usual cancer treatments.[1] Moreover, even if the drug reaches the tumor area, it will face a complex scenario. A solid tumor is an extraordinary heterogeneous tissue formed by a myriad of different malignant, harmless, even supportive cells, which play different roles in tumor progression.[2] Therefore, it is necessary to design smart therapeutic agents with the ability to distinguish between healthy and tumor cells in order to enhance their efficiency through the concentration of their cytotoxic capacity exclusively in malignant cells. One of the promising alternatives for improving the selectivity of chemotherapy is the covalent conjugation of vectorization moieties or targeting systems directly on the surface of drug-loaded nanocarriers,[3] with both inorganic[4,5] and organic nature,[6,7] as well as to free drugs[8] generating vectorized drug conjugates. A wide variety of targeting systems, from big biomolecules like antibodies,[9] lipoproteins,[10] or oligonucleotide sequences[11] to small molecules such as vitamins,[12] sugars,[13] or synthetic molecules,[14] are known. These moieties are characterized by their capacity to recognize and specifically bind to membrane cell receptors which are only, or mainly, expressed by tumor cells. Unfortunately, the use of targeting moieties is not free of drawbacks, for example unwanted off-target effects caused by the protein corona,[15] non-desired modifications of the ligand during the conjugation process,[16] or cross interactions between the targeting group and cell receptors expressed in healthy cells. On the other hand, a strong binding affinity between the vectorization motif and its cell receptor severely hampers the penetration of the therapeutic agent within the tumor. The apparition of this well-known effect, called binding-site barrier, is common in both drug conjugates[17] and targeted nanoparticles[18] and compromises the efficacy of the therapy by accumulation of targeted systems mainly in the tumor periphery, inducing only weak local effects.

Hierarchical targeting has been recently proposed as a novel strategy able to overcome these limitations in the case of nanometric carriers.[19] However, using shielded targeting agents in this context makes the EPR (enhanced permeability and retention)[20,21] effect as solely responsible for nanocarrier accumulation in tumor tissues.[22] Therefore, the achieved gain regarding lower cross interactions and higher penetration could be counteracted by the lower amount of nanocarriers that reach the diseased zone. Additionally, this approach is hardly adaptable to the direct conjugation with small drugs, since these therapeutic agents do not present an EPR effect as a consequence of their smaller size.

Herein, we propose a novel approach equally applicable to both drug conjugates and nanocarriers. This concept is based on a double sequential encrypted targeting system (DSETS) capable to combine tissular and cellular targeting following an activatable cascade mechanism. As proof of concept, we have focused on bone tumors. Thereby, we have chosen an uncovered primary tissue targeting agent, bisphosphonate (BP), that is specific for exposed diseased bone tissue, and a secondary hidden cellular targeting moiety of the "RGD type". The peptide has been encrypted inside an oligopeptide sequence RPGR<u>DGR</u>C (Arg-Pr-Gly-Arg-Asp-Gly-Arg-Cys) and has been sterically covered with a polyethylenglycol 3500 Da (PEG) moiety, making it more inert in presence of its receptors. Then, the RGD pattern becomes exposed only in the presence of elevated concentrations of cathepsin K (CK), a characteristic condition in bone tissues with high osteoclast activity such as many primary and metastatic bone tumors[23,24] (Scheme 1). This novel targeting moiety is based on the combination of two widely employed targeting agents; alendronate[25] (ALN) and the RGD tripeptide[26,27]. Alendronate shows a high affinity for hydroxyapatite and, therefore, this molecule strongly binds to the mineral part of bone tissues.[28]

On the other hand, the RGD pattern is a well-known sequence that binds to α,β-integrin and Neuropilin (NRP)-1 receptors, which are usually overexpressed in many tumoral cell lines and also in tumoral blood vessels.[29]

However, integrin receptors are also present in many healthy cells and, therefore, the direct conjugation of RGD sequences on the transported species could misdirect the therapeutic cargo to unwanted locations. The combination of both vectorization capacities (tissular and cellular targeting) converts this modular targeting system into a promising prototype for deliv-

---

[a] *Dr. G. Villaverde, V. Nairi, Dr. A. Baeza, Prof. M. Vallet-Regí*
Depto. Química Inorgánica y Bioinorgánica, Facultad de Farmacia
Universidad Complutense de Madrid. Plaza Ramon y CajaLs/n.
Instituto de Investigación Sanitaria Hospital 12 de Octubre i + 12 ¡
Centro de Investigación Biomédica en Red de Bioingeniería,
Biomateriales y Nanomedicina (CIBER-BBN), Madrid (Spain)
E-mail: abaezaga@ucm.es
vallet@ucm.es

Supporting information for this article, containing synthetic proccedures, NMR and MALDI-TOF/TOF spectra, cell culture protcols, and flow cytometry measurements, can be found under: http://dx.doi.org/10.1002/chem.201605947.

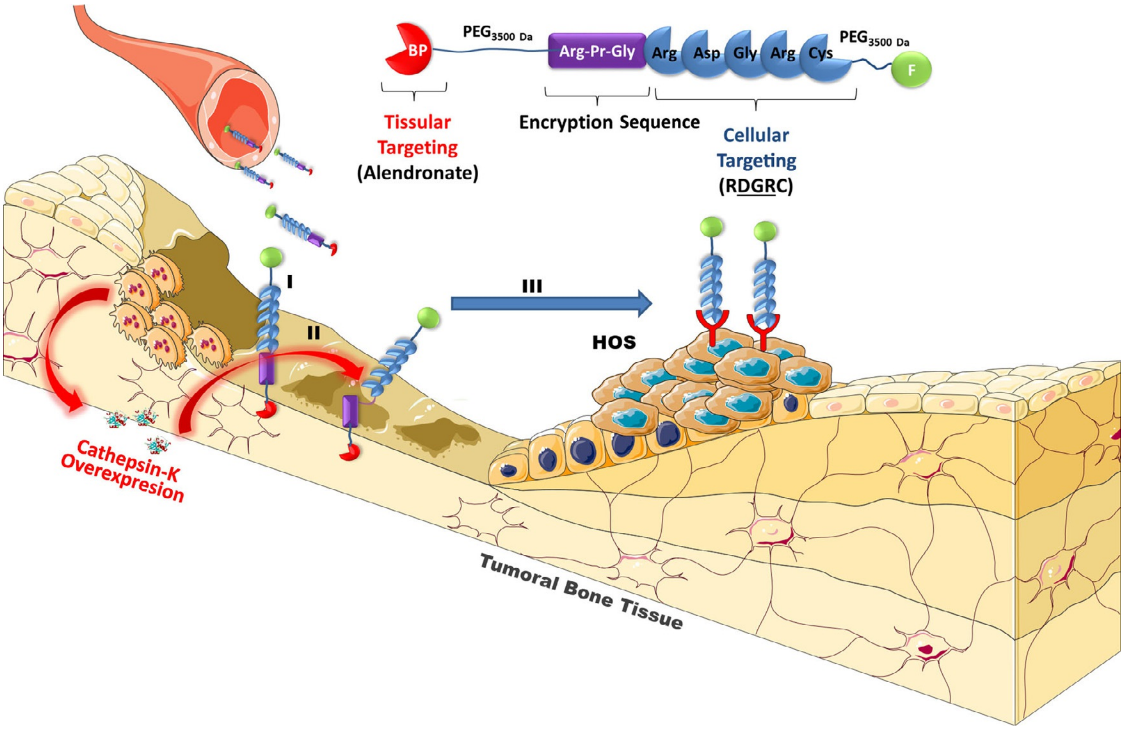

Scheme 1. Mode of action of the double sequential targeting system in osteosarcoma diseased bone. I) Bone targeting of BP (bisphosphonate) to HA (hydroxyapatite). II) Cathepsin K (CK) induced peptide proteolysis. III) RGD peptide recognition by HOS (human osteosarcoma) cell wall and subsequent internalization.

ering therapeutic agents to bone tumors. For affording the targeting device, the first step was the synthesis of the polypeptide strand, which was made using solid-phase chemistry starting from a Fmoc-Arg(Pbf)-Wang resin (see the Supporting Information for the detailed protocol).

Following the typical Fmoc-deprotection and HBTU/HOBT-mediated carboxylic acid activation steps, each individual amino acid was added to the peptide strand (Scheme 2a). The tripeptide Arg-Pr-Gly motif was introduced in the sequence for providing selective responsivity to CK. This enzyme performs the proteolysis of collagen I, catalyzing almost exclusively the rupture of the amide bond present in the helix after a Pr-Gly motif.[30,31]

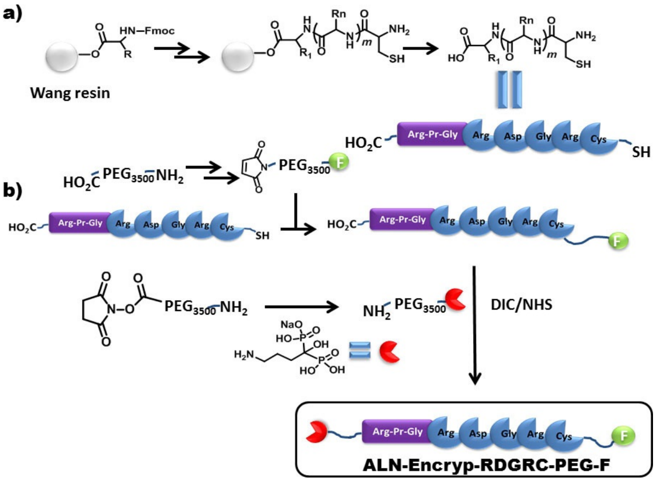

Scheme 2. Synthetic pathway affording the fluorescent dual-targeting moiety.

To evaluate the sensitivity and selectivity against CK, a small amount of the peptide strand (10 mg) was exposed to an acidic solution of this enzyme (pH 5) for 2 h at 37 °C, replicating osteoclast lacuna conditions, whereas the other batch was only exposed to mild acidic medium. After the isolation process, the resulting crude products were analyzed by matrix-assisted laser desorption/ionization (MALDI) time-of-flight/time-of-flight (TOF/TOF) spectrometry. As expected, when the peptide was exposed to CK, Arg-Asp-Gly-Arg-Cys was the mayor product, which corresponds to an amide bond rupture after glycine in Pr-Gly (Figure S10 in the Supporting Information). This result confirms that CK induces the responsive behavior of the peptide strand in comparison to its stability showed under enzyme-free conditions. A fluorescently labeled polyethylenglycol (F-PEG) was employed as the therapeutic cargo model. This polymeric strand mimics the role of the nanometric drug-loaded carrier or therapeutic macromolecule allowing an easy visualization and quantification of the system internalization within malignant cells, as it has been reported elsewhere.[32] F-PEG-Maleimide was attached to the cysteine end through thiol-ene reaction. Alendronate was conjugated via carbodiimide chemistry to the carboxylic acid end of a bifunctional HO_2C-PEG-NH_2 chain of a molecular weight of 3500 Da to shield the cellular targeting moiety more properly. Finally, this system was attached to the fluorescent peptide strand using again a carbodiimide as carboxylic acid activator (Scheme 2b).

Once the system was prepared, its performance was evaluated step by step. First, its capacity to bind to apatite was tested by incubating the complete system in the presence of pure hydroxyapatite discs (HA) in PBS (pH 7.4) at 37 °C for 8 h to simulate body fluid conditions. The peptide sequence without the PEG-alendronate moiety was employed as control. After completion of the incubation time, the discs were thoroughly washed with buffer to eliminate physically adsorbed systems and their presence was determined by fluorescence microscopy. As expected, the peptides without alendronate were not able to bind to the surface of the HA discs, whereas the peptides with alendronate were strongly retained on the HA surfaces (Figure 1 a). Further, the binding capacity was also evaluated in the presence of Ca^{2+} at a concentration of 2.5 mм, which is naturally present in the bone tissue surroundings. HA discs with the complete system were incubated in the presence of physiological concentrations of Ca^{2+}, showing the retention of the fluorescence in a similar amount than controls without Ca^{2+} (Figure 1 b). As shown in Figure 1 b, it was necessary to double this concentration to releasing a significant amount of the targeting moiety.

To prove that the binding capacity of the complete system was due to the complexation of alendronate on the HA surface, competition experiments with free alendronate were carried out. As shown in Figure 1 c, the systems ability to be retained on the HA surface decreased when the alendronate concentration was higher, due to free alendronate gradually replacing the complete targeting device from the surface. In all experiments, the targeting system release was confirmed by fluorescence measurements of the solutions before and after the alendronate exposition (Graphic S1 in the Supporting Information). In sight of these evidences, the active primary targeting moiety inside the complete system showed a good performance under close-to-reality conditions for vectorization to the diseased bone.

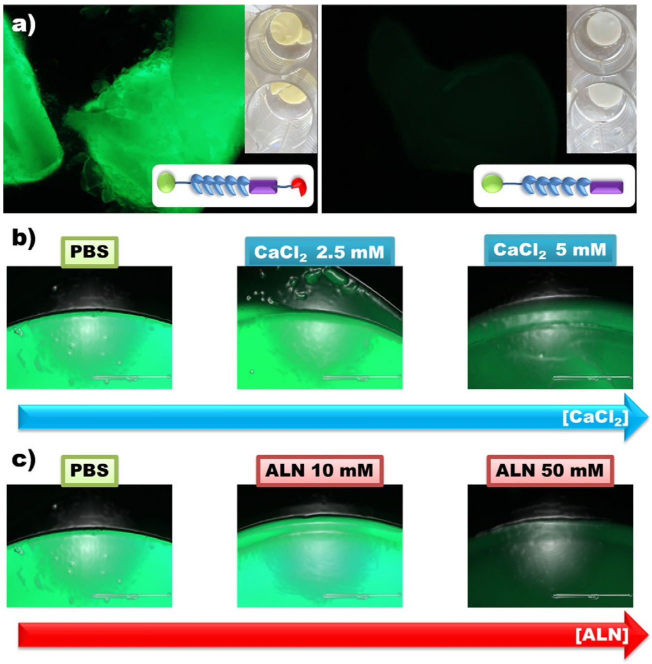

Figure 1. a) Fluorescence microscopy of HA discs exposed to the targeting molecule with and without PEG-ALN (polyethylenglycol-alendronate). Fluorescence microscopy of HA discs exposed to the complete targeting molecule in the presence of different concentrations of b) Ca^{2+} and c) free alendronate.

The next step was to evaluate the performance of the hidden secondary targeting sequence. For this aim, human osteosarcoma (HOS) cells were chosen as tumoral cell model because they usually overexpress α,β-integrin[33] and (NRP)-1 receptors,[34] which interact with the RGD pattern. Further, osteosarcoma is one of the most common non-hematologic neoplasm that affects bone tissues.[35] The capacity to hide the secondary targeting was evaluated by exposing HOS cells to a fixed concentration of the complete system (10 μg mL^{-1}) for 2 h. The same protocol was carried out employing a fluorescent PEG strand (F-PEG) as negative control and a fluorescent PEG strand decorated with CRGDR as positive control (F-PEG-CRGDR). The percentage of cells that internalize the fluorescent strands in each case was measured using flow cytometry. Almost 20 % of HOS cells internalize the fragment that contains the unshielded RGD pattern in comparison with only 8 % that engulf the fluorescent PEG, which confirms that the RGD sequence enhances the internalization within malignant cells (Figure 2). Interestingly, the targeting uptake was only 12 % (all data normalized with control) when the complete system containing the shield pattern was employed, which corresponds to a decrease of the targeting internalization of around 40 %. Thus, these results point out a good performance of both encryption and cell targeting capacity of the hybrid strand.

Finally, the complete system was tested employing a "bone/culture in vitro model". In this model, HA discs were previously incubated with a PBS solution that contains 300 μg mL^{-1} of the complete system. After 8 h, the discs were thoroughly washed with buffer to remove physisorbed peptides. Once washed, the discs were placed on the upper sheet of transwells and the cells were cultured on the bottom. Then, the wells were incubated in mild-acidic media for 2 h, three with addition of CK and three without. After the incubation time, the HA discs were removed and the cell cultures were washed with PBS and incubated with medium for another 24 h.

The targeting internalization in each well was analyzed by flow cytometry showing that, in the samples to which cathepsin K was added, around 90 % of the cells showed fluorescence, which indicates the internalization of the labeled peptide. On the contrary, in the wells incubated without CK, only around 10 % of the cells exhibited fluorescence. The presence of the peptide in each disc was observed by fluorescence microscopy. The discs that were treated with incubated proteolytic enzyme lost all fluorescence, whereas those without the enzyme almost completely retained their fluorescence (Figure 3).

Osteosarcoma has been chosen as proof of concept of a common solid tumor and therefore, the primary and secondary targeting groups were selected accordingly. But it is worth noting that this strategy could be easily adapted to different tumors that affect different organs or tissues. In conclusion, encrypted targeting agents would avoid the misdirection

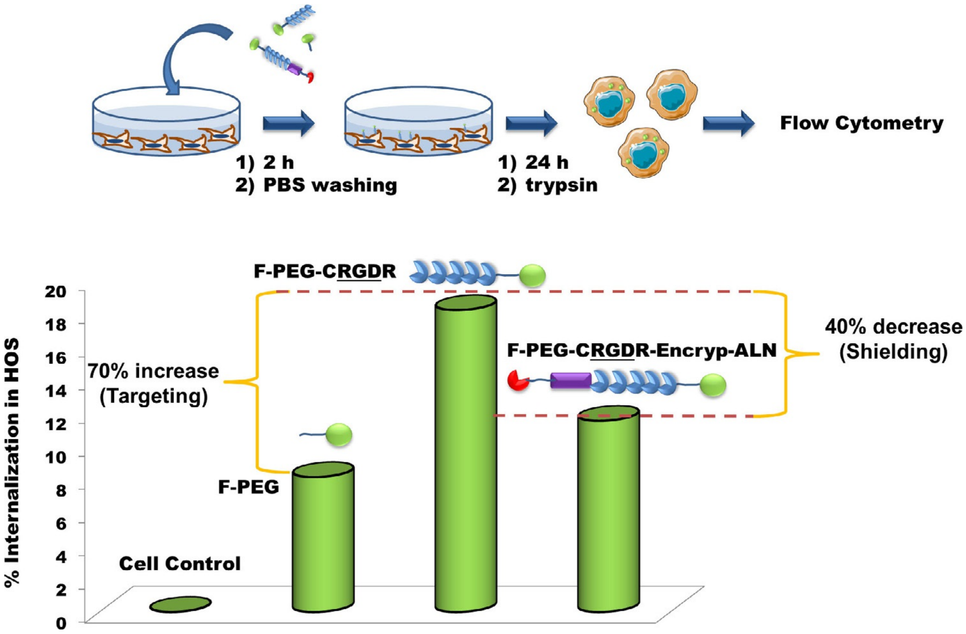

Figure 2. Studies of the internalization capacity of F-PEG (fluorescently labeled PEG), F-PEG-CRGDR and F-PEG-CRGDR-Encryp-ALN in HOS. Error data and statistical analysis can be found in the Supporting Information. CRGDR = Cys-Arg-Gly-Asp-Arg. CRGDR-Encryp = Cys-Arg-Gly-Asp-Arg-Gly-Pro-Arg.

of the transported species to other tissues, thereby reducing the apparition of side effects or systemic toxicity. Additionally, the primary targeting group located at the end of the full system provides the guiding capacity to the affected tissue.

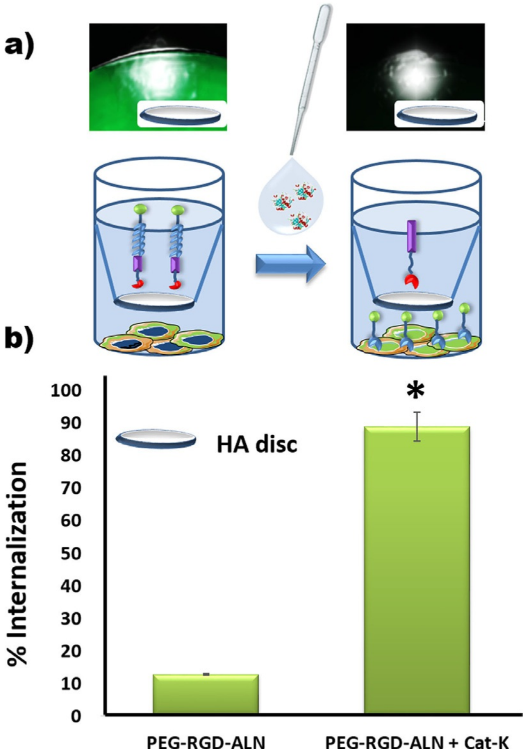

Figure 3. Cat-K responsive behavior of F-PEG-CRGDR-Encryp-ALN in HOS. a) Fluorescence microscopy of the HA discs with F-PEG-CRGDR-Encryp-ALN before and after Cat-K treatment. b) Percentage of cells that have engulfed the fluorescent label. * $P < 0.01$.

This novel targeting system represents a new approach for the selectivity enhancement in drug delivery processes and could be applied for several types of drug conjugates, drug-loaded nanocarriers, or imaging agents, increasing the available arsenal in the fight against tumors.

Acknowledgements

This work was supported by the European Research Council (Advanced Grant VERDI; ERC-2015-AdG Proposal No. 694160) and the project MAT2015-64831-R. The authors want to thanks Prof. Maura Monduzzi for her support along this work. For the elaboration of Figures and Schemes, some templates from http://www.servier.com/Powerpoint-image-bank have been used.

Conflict of interest

The authors declare no conflict of interest.

Keywords: cancer · drug delivery · dual targeting · encrypted peptide · stimuli-responsive targeting

[1] K. D. Miller, R. L. Siegel, C. C. Lin, A. B. Mariotto, J. L. Kramer, J. H. Rowland, K. D. Stein, R. Alteri, A. Jemal, *CA. Cancer J. Clin.* **2016**, *66*, 271–289.
[2] M. Egeblad, E. S. Nakasone, Z. Werb, *Dev. Cell* **2010**, *18*, 884–901.
[3] R. Bazak, M. Houri, S. El Achy, S. Kamel, T. Refaat, *J. Cancer Res. Clin. Oncol.* **2015**, *141*, 769–784.
[4] M. Vallet-Regi, A. Rámila, R. P. del Real, J. Pérez-Pariente, *Chem. Mater.* **2001**, *13*, 308–311.
[5] M. Vallet-Regí, F. Balas, D. Arcos, *Angew. Chem. Int. Ed. Engl.* **2007**, *46*, 7548–58.

[6] M. Talelli, M. Barz, C. J. F. Rijcken, F. Kiessling, W. E. Hennink, T. Lammers, *Nano Today* **2015**, *10*, 93 – 117.
[7] M. C. Parrott, J. C. Luft, J. D. Byrne, J. H. Fain, M. E. Napier, J. M. DeSimone, *J. Am. Chem. Soc.* **2010**, *132*, 17928 – 17932.
[8] E. L. Sievers, P. D. Senter, *Annu. Rev. Med.* **2013**, *64*, 15 – 29.
[9] Q. Dai, Y. Yan, C. Ang, K. Kempe, M. M. J. Kamphuis, S. J. Dodds, F. Caruso, *ACS Nano* **2015**, *9*, 2876 – 2885.
[10] S. Lara, F. Alnasser, E. Polo, D. Garry, M. C. Lo Giudice, D. R. Hristov, L. Rocks, A. Salvati, Y. Yan, K. A. Dawson, *ACS Nano* **2017**, *11*, 1884 – 1893.
[11] Y. Lao, K. K. L. Phua, K. W. Leong, *ACS Nano* **2015**, *9*, 2235 – 2254.
[12] H. Elnakat, M. Ratnam, *Adv. Drug Deliv. Rev.* **2004**, *56*, 1067 – 1084.
[13] H. Nguyen, P. Katavic, N. A. H. Bashah, V. Ferro, *ChemistrySelect* **2016**, *1*, 31 – 35.
[14] G. Villaverde, A. Baeza, G. J. Melen, A. Alfranca, M. Ramirez, M. Vallet-Regí, *J. Mater. Chem. B* **2015**, *3*, 4831 – 4842.
[15] A. Salvati, A. S. Pitek, M. P. Monopoli, K. Prapainop, F. B. Bombelli, D. R. Hristov, P. M. Kelly, C. Åberg, E. Mahon, K. A. Dawson, *Nat. Nanotechnol.* **2013**, *8*, 137 – 143.
[16] L. M. Herda, D. R. Hristov, M. C. Lo Giudice, E. Polo, K. A. Dawson, *J. Am. Chem. Soc.* **2017**, *139*, 111 – 114.
[17] R. Bakhtiar, *Biotechnol. Lett.* **2016**, *38*, 1655.
[18] T. Lammers, F. Kiessling, W. E. Hennink, G. Storm, *J. Control. Release* **2012**, *161*, 175 – 187.
[19] S. Wang, P. Huang, X. Chen, *Adv. Mater.* **2016**, *28*, 7340 – 7364.
[20] J. Fang, H. Nakamura, H. Maeda, *Adv. Drug Deliv. Rev.* **2011**, *63*, 136 – 151.
[21] H. Nakamura, F. Jun, H. Maeda, *Expert Opin. Drug Delivery* **2015**, *12*, 53 – 64.
[22] J. Zhang, Z.-F. Yuan, Y. Wang, W.-H. Chen, G.-F. Luo, S.-X. Cheng, R.-X. Zhuo, X.-Z. Zhang, *J. Am. Chem. Soc.* **2013**, *135*, 5068 – 5073.
[23] K. Husmann, R. Muff, M. E. Bolander, G. Sarkar, W. Born, B. Fuchs, *Mol. Carcinog.* **2008**, *47*, 66 – 73.
[24] G. Bonzi, S. Salmaso, A. Scomparin, A. Eldar-Boock, R. Satchi-Fainaro, P. Caliceti, *Bioconjug. Chem.* **2015**, *26*, 489 – 501.
[25] H. Uludag, J. Yang, *Biotechnol. Prog.* **2002**, *18*, 604 – 611.
[26] S. Kunjachan, R. Pola, F. Gremse, B. Theek, J. Ehling, D. Moeckel, B. Hermanns-Sachweh, M. Pechar, K. Ulbrich, W. E. Hennink, *Nano Lett.* **2014**, *14*, 972 – 981.
[27] D. J. Burkhart, B. T. Kalet, M. P. Coleman, G. C. Post, T. H. Koch, *Mol. Cancer Ther.* **2004**, *3*, 1593 – 1604.
[28] W. Jahnke, C. Henry, *ChemMedChem* **2010**, *5*, 770 – 776.
[29] S. Zitzmann, V. Ehemann, M. Schwab, *Cancer Res.* **2002**, *62*, 5139 – 5143.
[30] Y. Choe, F. Leonetti, D. C. Greenbaum, F. Lecaille, M. Bogyo, D. Brömme, J. A. Ellman, C. S. Craik, *J. Biol. Chem.* **2006**, *281*, 12824 – 12832.
[31] S. R. Wilson, C. Peters, P. Saftig, D. Brömme, *J. Biol. Chem.* **2009**, *284*, 2584 – 2592.
[32] E. Vlashi, L. E. Kelderhouse, J. E. Sturgis, P. S. Low, *ACS Nano* **2013**, *7*, 8573 – 8582.
[33] X. Duan, S.-F. Jia, Z. Zhou, R. R. Langley, M. F. Bolontrade, E. S. Kleinerman, *Clin. Exp. Metastasis* **2005**, *21*, 747 – 753.
[34] H. Zhu, H. Cai, M. Tang, J. Tang, *Clin. Transl. Oncol.* **2014**, *16*, 732 – 738.
[35] J. D. Lamplot, S. Denduluri, J. Qin, R. Li, X. Liu, H. Zhang, X. Chen, N. Wang, A. Pratt, W. Shui, X. Luo, G. Nan, Z.-L. Deng, J. Luo, R. C. Hydon, T.-C. He, H. H. Luu, *Curr. Cancer Ther. Rev.* **2013**, *9*, 55 – 77.

Manuscript received: January 11, 2017
Accepted manuscript online: February 22, 2017
Version of record online: March 28, 2017

CHEMISTRY
A European Journal

Supporting Information

Double Sequential Encrypted Targeting Sequence: A New Concept for Bone Cancer Treatment

Gonzalo Villaverde, Valentina Nairi, Alejandro Baeza,* and María Vallet-Regí*[a]

chem_201605947_sm_miscellaneous_information.pdf

1. Peptide Solid phase synthesis general steps

I) Amino group Fmoc deprotection: A solution of piperidine (20 %) in DMF was added to the peptide functionalized resin. The suspension mixture was shaken in the solid phase reactor by wrist-shaker overnight. Finally, the solid was filtered and washed with DMF.

II) Peptide amide bond formation: A solution of HOBt (3 eq), HBTU (3 eq) and the corresponding amino acid (2 eq) in DMF (2 mL) was added to the washed resin, after slight shaking finally DIPEA (6 eq) was added. The mixture was shaken in the reactor with a wrist-shaker overnight. Finally, the solid is filtered and washed with DMF.

III) Final peptide release from the resin: Once added the last amino acid of the chain and deprotected the last Fmoc amine group, the solid was filtered, washed with DMF and dried under vacuum. A solution of trifluoroacetic acid (95%), triisopropylsilane (2.5%) and water (1%) was added dropwise. The mixture was mechanical stirred for 4 hours. Then filtered and washed with another milliliter of the same previous mixture. Both filtered solution were mixed.

The product is obtained, in all cases, by precipitation of the filtered solution with cold ether. Then the product is added slowly dropwise to cool ether. After one hour, the suspension was centrifuged at T = 4 ° C at 14000 r.p.m. The solid is then dried overnight under vacuum oven at room temperature.

IV) Final peptide isolation by chromatography: The solid obtained is solved in the minimum amount of water and purified by flash column for molecular exclusion chromatography (stationary phase: Sephadex® G-25; mobile phase: water). All phases are then frozen at -80 ° C and lyophilized.

RDGRC Arg-Asp-Gly-Arg-Cys (RGD-Active)

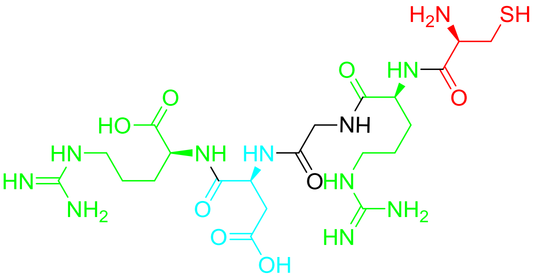

Reagent	PM (g/mol)	eq
HOBt	135.12	3
HBTU	379.24	3
DIPEA	129.24	6
Asp-Fmoc	411.45	2
Gly-Fmoc	297.31	2
Arg_Fmoc	648.78	2
Cys-Fmoc	585.72	2

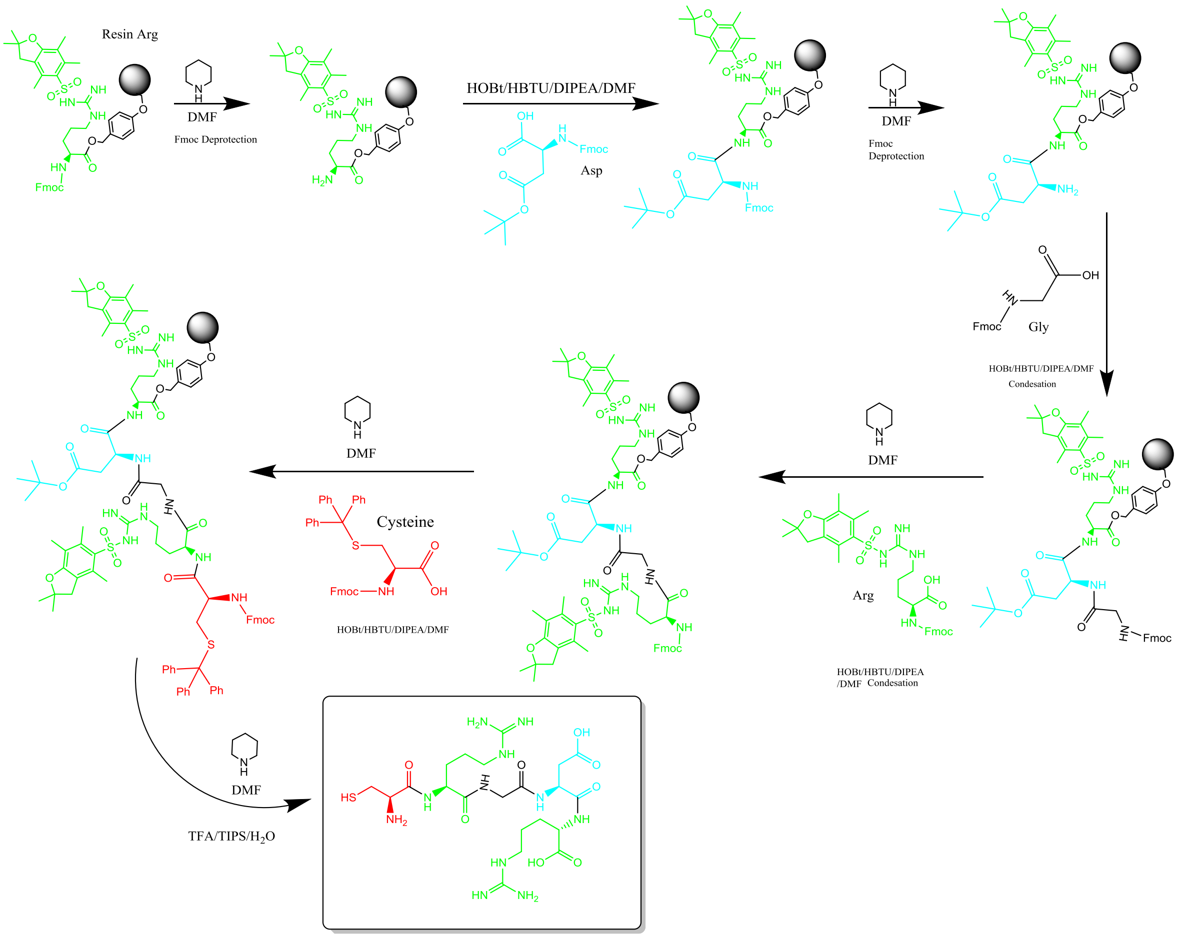

Figure S1: Scheme of RDGRC synthesis.

RDGRC Arg-Asp-Gly-Arg-Cys (RGD-Active): TOF/TOF (m/z): 606.220 [M+1] (100%); 607.224 (26%); 608.219 (9%). ^{1}H NMR (250 MHz, D$_2$O) δ 4.61 (1H, CH, Asp, from COSY)), 4.18 (1H, CH, Cys, from COSY), 4.39 – 4.13 (m, 2H, 2xCH, Arg), 3.90 – 3.79 (m, 2H, CH$_2$, Gly), 3.08 (t, J = 7.9 Hz, 4H, 2xCH$_2$, Arg), 3.03 – 2.87 (m, 2H, CH$_2$, Cys), 2.84 – 2.59 (m, 2H, CH$_2$, Asp), 1.89 – 1.65 (m, 4H, 2xCH$_2$, Arg), 1.64 – 1. 47 (m, 4H, 2xCH$_2$, Arg).

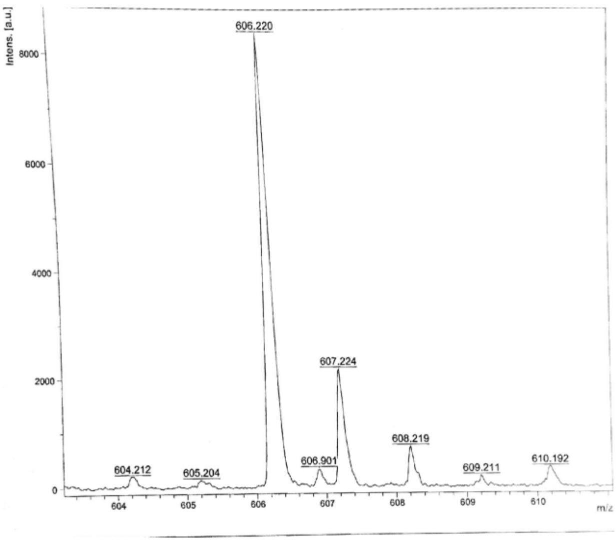

Figure S2: RDGRC TOF/TOF (m/z): 606.220 [M+1] (100%); 607.224 (26%); 608.219 (9%).

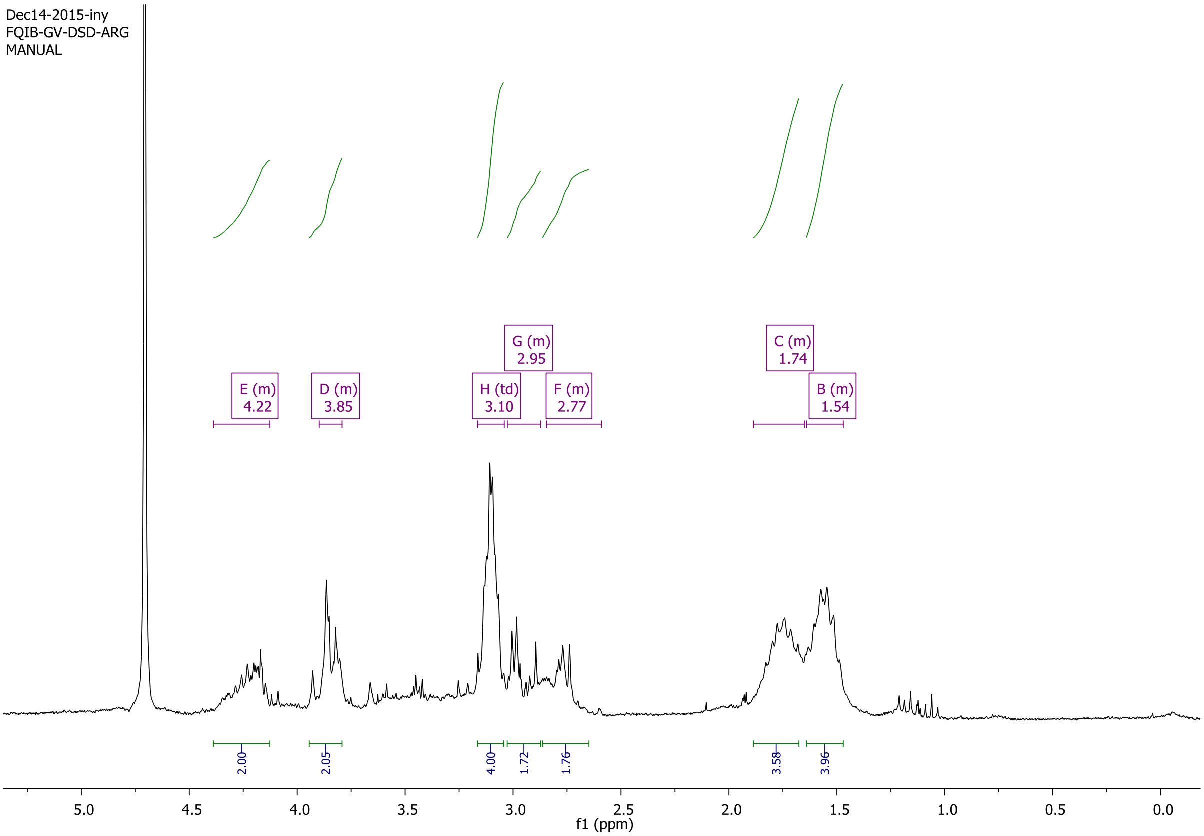

Figure S3: ^{1}H-NMR (D_2O) Arg-Asp-Gly-Arg-Cys

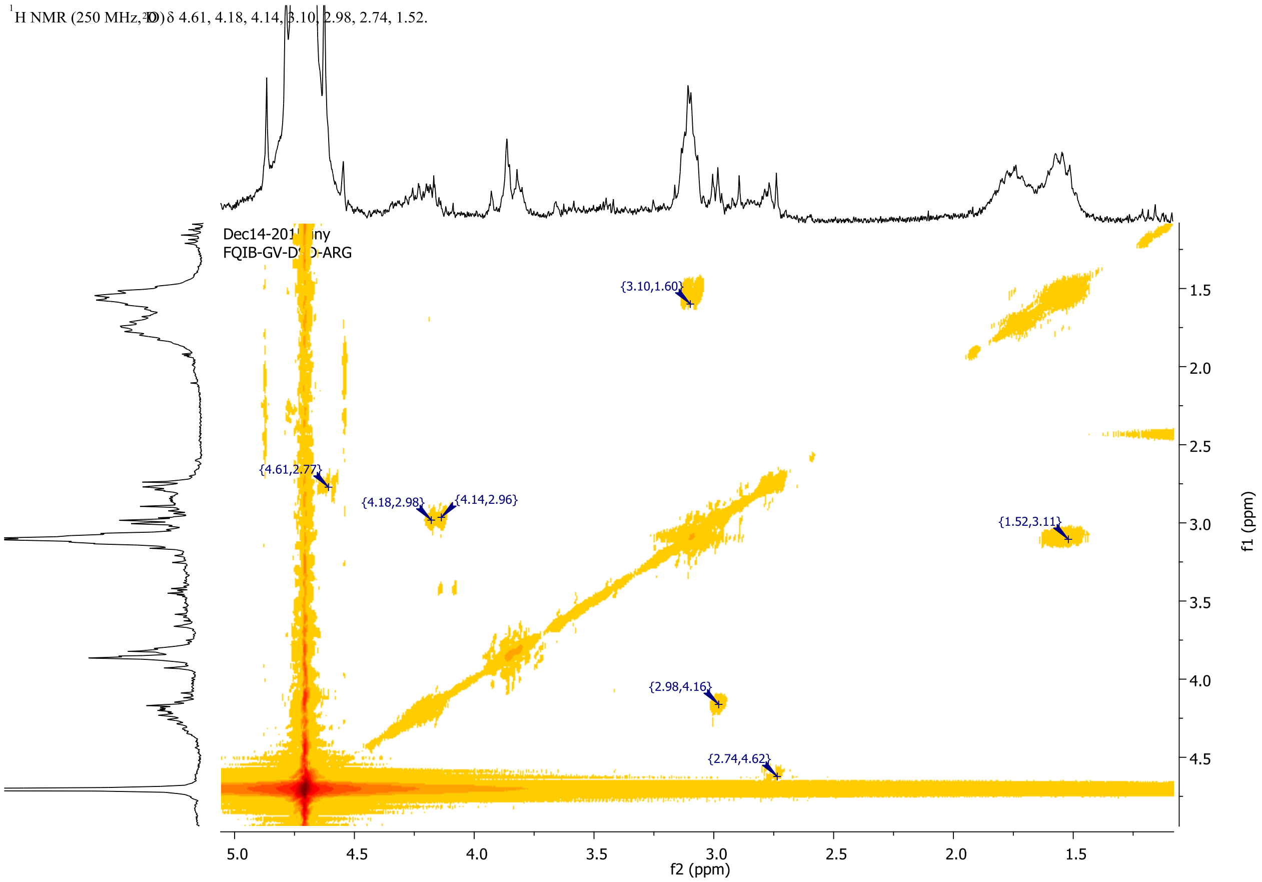

Figure S4: ^{1}H-NMR COSY (D_2O) Arg-Asp-Gly-Arg-Cys

RPGRDGRC Arg-Pr-Gly-Arg-Asp-Gly-Arg-Cys Sequence (RGD-Encrypted)

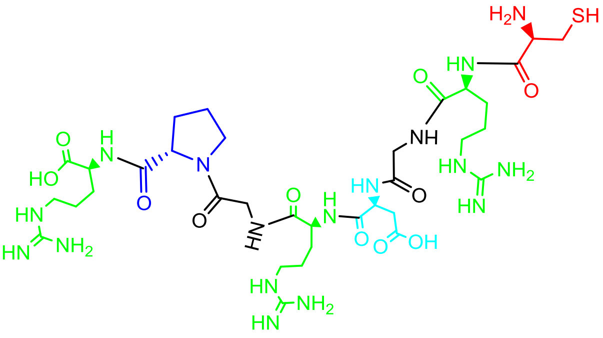

Reagent/Reactant	PM (g/mol)	eq
HOBt	135.12	3
HBTU	379.24	3
DIPEA	129.24	6
Pr-Fmoc	337.13	2
Gly-Fmoc	297.31	2
Arg_Fmoc	648.78	2
Asp-Fmoc	411.45	2
Gly-Fmoc	297.31	2
Arg_Fmoc	648.78	2
Cys-Fmoc	585.72	2

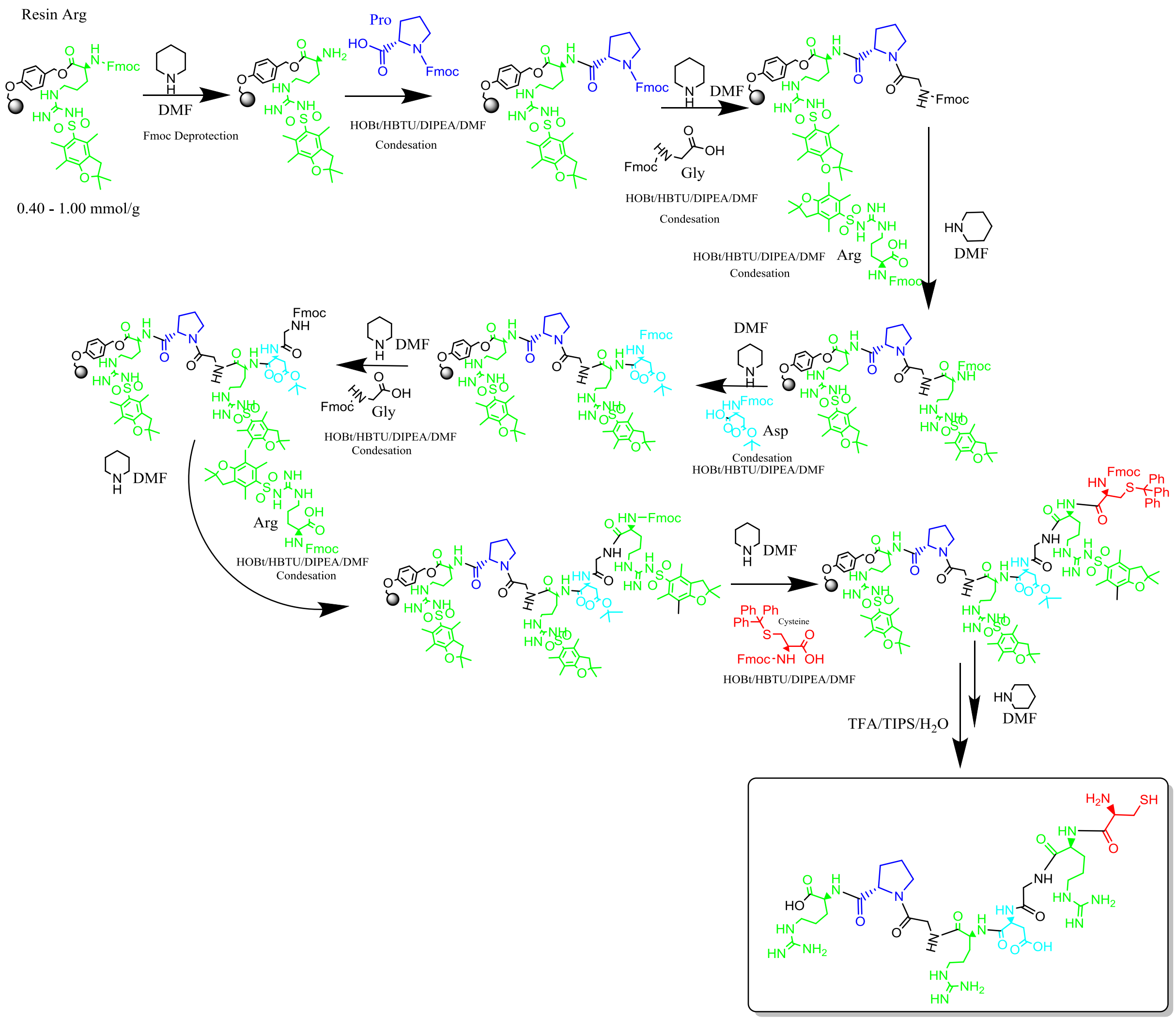

Figure S5: Scheme of RGD-Encrypted synthesis

RPGRDGRC Arg-Pr-Gly-Arg-Asp-Gly-Arg-Cys Sequence (RGD-Encrypted): TOF/TOF (m/z): 915 [M+] (100%); 916.565 (40%) 917.548 (10%). ^{1}H NMR (250 MHz, D_2O) δ 4.59 (1H, CH, Asp, from COSY), 4.48 – 4.15 (m, 4H, 3x CH, Arg and 4.32 (1H, CH, Pr, from COSY)), 4.12 – 4.02 (s, broad, 2H, CH_2, Gly), 4.00 – 3.89 (s, broad, 2H, CH_2, Gly), 3.74 – 3.34 (m, 2H, CH_2, Pr), 3.13 (d, *J* = 22.9 Hz, 6H, $3xCH_2$, Arg), 3.01 – 2.75 (m, 4H, CH_2, Asp and CH_2, Cys), 2.38 – 2.15 (m, 1H, CHH, Pr), 2.05 – 1.83 (m, 3H, CH_2 and CHH, Pr), 1.81 – 1.49 (m, 12H, $3xCH_2$-CH_2, Arg).

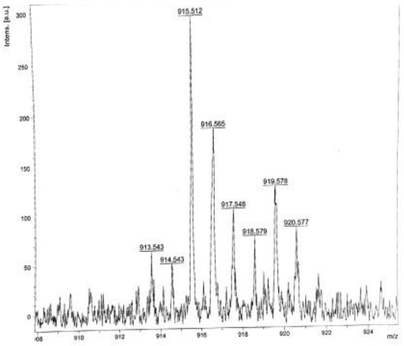

Figure S6: Arg-Pr-Gly-Arg-Asp-Gly-Arg-Cys TOF/TOF (m/z): 915 [M+] (100%); 916.565 (40%) 917.548 (10%).

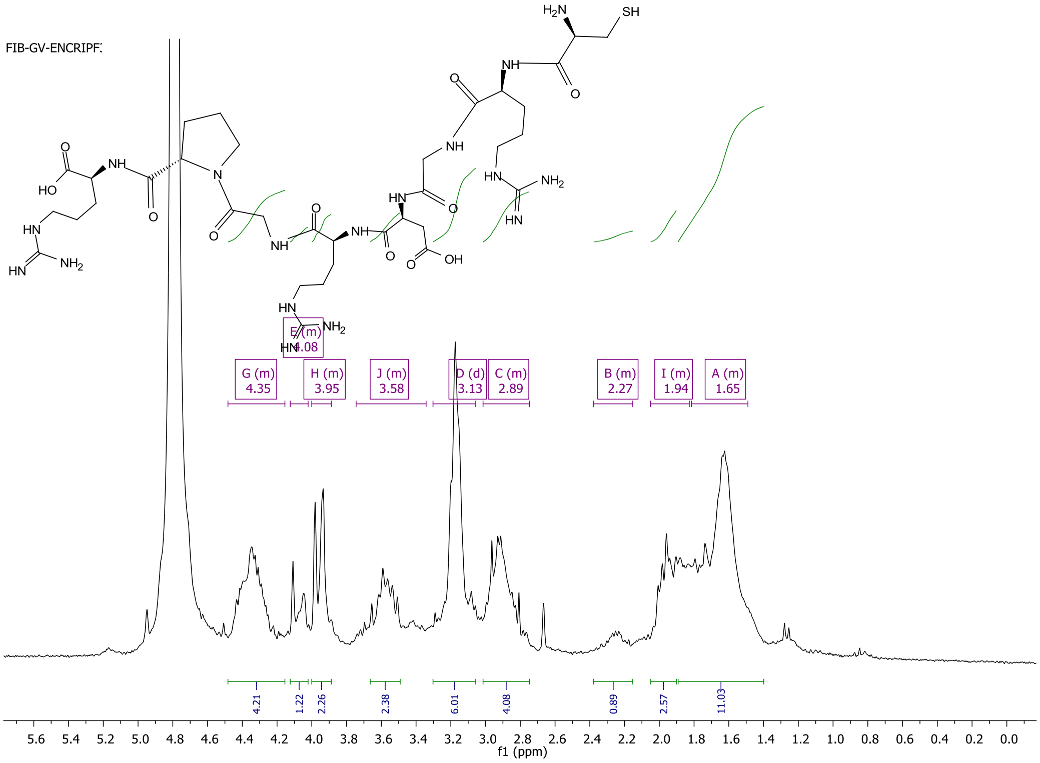

Figure S7: ^{1}H-NMR (D_2O) Arg-Pr-Gly-Arg-Asp-Gly-Arg-Cys

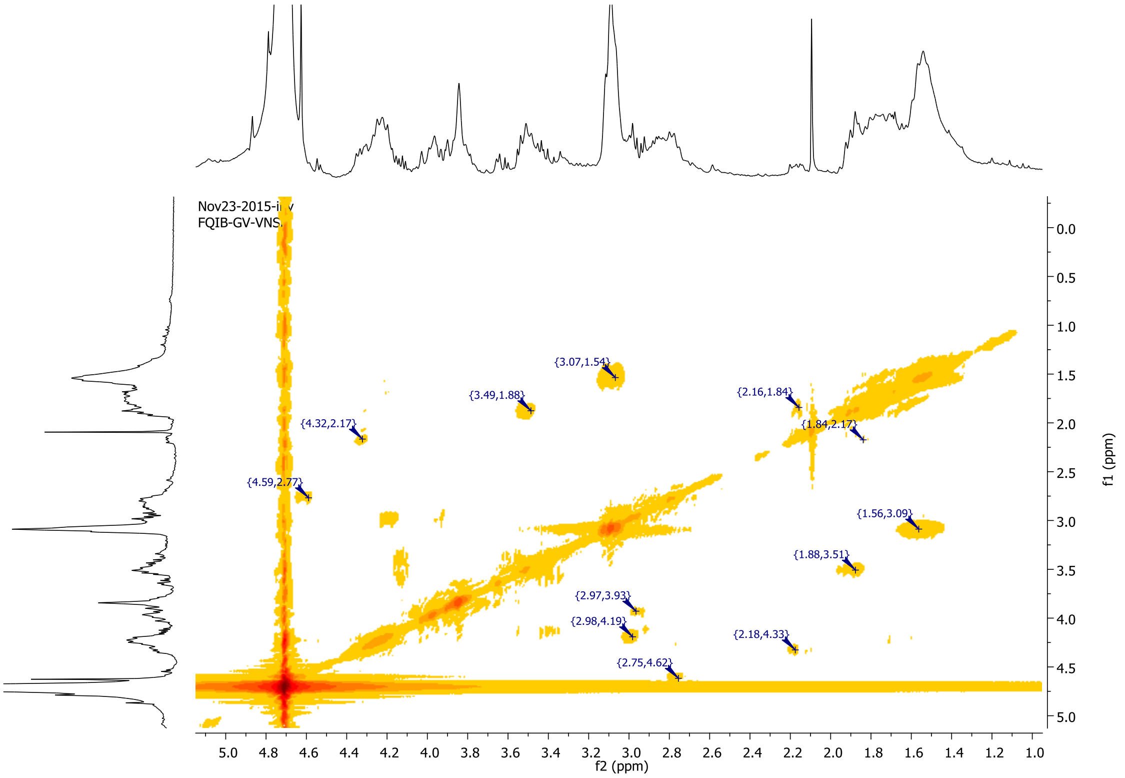

Figure S8: ^{1}H-NMR COSY (D_2O) Arg-Pr-Gly-Arg-Asp-Gly-Arg-Cys

^{13}C NMR (250 MHz, D_2O) δ 4.61, 4.32, 4.28, 4.26, 4.00, 3.87, 3.87, 3.58, 3.50, 3.11, 3.08, 3.02, 2.91, 2.86, 2.78, 1.91, 1.78, 1.61, 1.55.

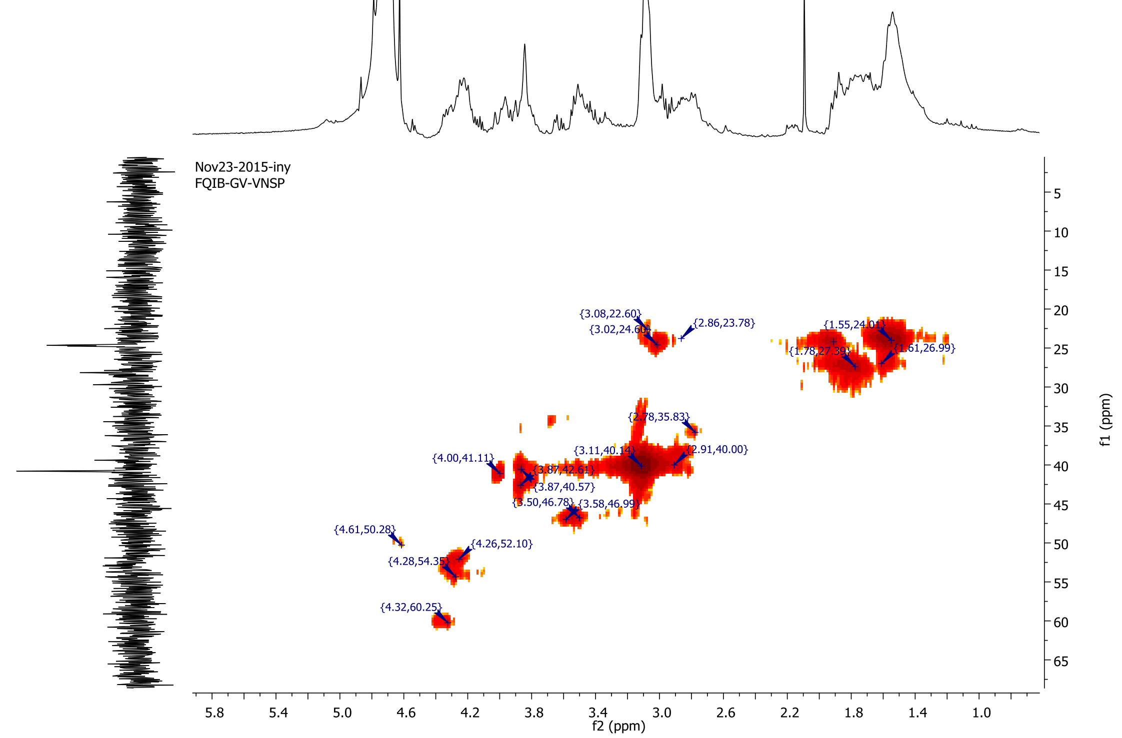

Figure S9: HMBC (D_2O) Arg-Pr-Gly-Arg-Asp-Gly-Arg-Cys.

2. Synthesis of F-PEG analogs

a. F-PEG-COOH

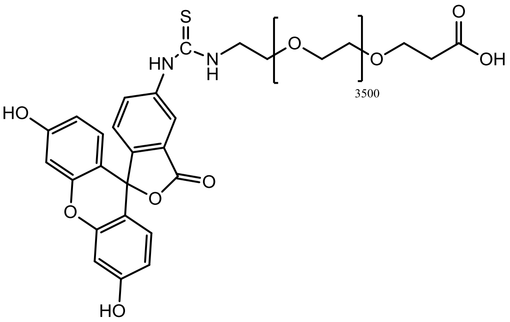

DIPEA was added (6 eq, 18uL) to a solution of 50 mg of O- (2-Aminoethyl) -O '- (2-carboxyethyl) polyethylene glycol hydrochloride (3500 Da) in a minimum volume of DMF (≈2 mL). The mixture was gentle stirred under inert atmosphere for one hour. A solution of FITC (10 eq, 64.9 mg) in DMF (≈1 mL) was added dropwise. The reaction mixture was stirred under inert atmosphere at room temperature overnight.

The final product was obtained by successive precipitation in cold ether (centrifuge to assisted the precipitation at T = - 4 ° C, in r.p.m. = 9000, t = 30 min).

The yellow powder afforded was purified through molecular exclusion chromatography (G-25 / H_2O).

TOF/TOF: 3859 z/m. ^{1}H NMR (250 MHz, D_2O) δ 7.71-7.50 (m, 2H, CH_{Ar}, Fluorescein), 7.31 – 7.05 (m, 3H, CH_{Ar}, Fluorescein), 6.57 (m, 4H, CH_{Ar}, Fluorescein), 3.82 (s, broad, 2H, CH_2, PEG), 3.79 – 3.36 (s, broad, 248 H, CH_2, PEG), 3.29 (s, broad, 2H, CH_2, PEG-CH_2-COOH).

b. F-PEG-Ma

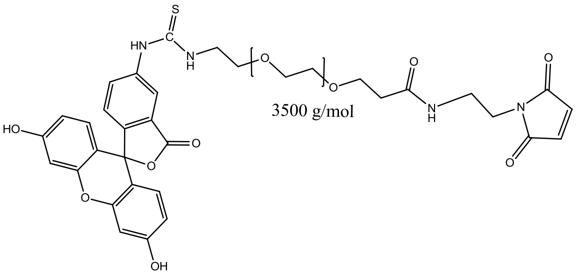

F-PEG-COOH (20 mg)), NHS (1.5 eq) and DIC (6 eq) were solved in DCM (minimum quantity, ≈2 mL. Further, DIPEA (6 eq) were added, and the mixture was stirred under inert atmosphere during 4 hours. *N*-(2-aminoethyl) maleimide trifluoroacetate salt in a DCM solution (1 eq) was added and the reaction stirred for additional 24 hours at room temperature. The final product was obtained by precipitation in cold ether.

TOF/TOF: 3859 z/m.

c. Boc-NH-PEG-ALN

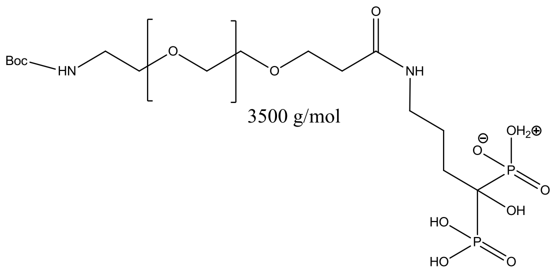

O-[2-(Boc-amino) ethyl]-*O′*-[3-(*N*-succinimidyloxy)-3-oxopropyl] polyethylene glycol (3500 Da) (153 mg) and sodium alendronate (30 mg) were solved in a mixture of DMSO/H_2O 60:40. Triethylamine (30 µL) was added and the temperature rose to 50 ºC. The reaction was stirred overnight under inert atmosphere.

The product was precipitated in cool ether and purified by flash molecular exclusion chromatography (G-25/H_2O).

^1H NMR (250 MHz, D_2O) δ 3.92 – 3.81 (m, 2H, CH_2, PEG), 3.59 (s, 324H, CH_2, PEG), 3.33 – 3.24 (m, 2H, CH_2, PEG), 3.20 – 3.01 (m, 4H, 2xCH_2, PEG), 2.19 (t, *J* = 7.5 Hz, 2H, CH_2, alendronate), 1.76 (dd, *J* = 12.4, 4.9 Hz, 4H, 2xCH_2, alendronate), 1.32 (s, 9H, 3xCH_3, Boc).

d. NH_2-PEG-ALN

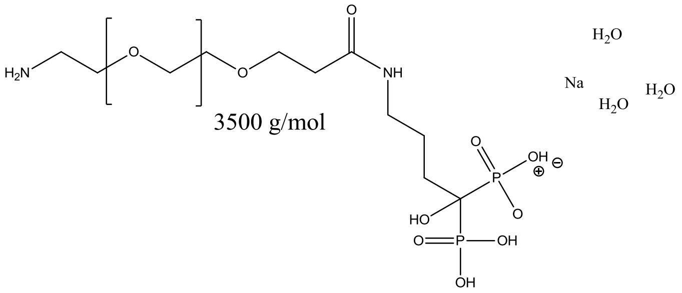

Boc-NH-PEG-ALN was solved in a solution of DCM/TFA 1%. The mixture was stirred at room temperature 1 hour. The product was obtained by precipitation in cold ether.

^1H NMR (250 MHz, D_2O) δ 3.59 (s, broad, 340H, CH_2, PEG), 3.09 (s, 2H, CH_2, PEG)), 2.20 (t, *J* = 7.4 Hz, 2H, CH_2, alendronate), 1.77 (d, *J* = 6.6 Hz, 4H, 2xCH_2, alendronate).

e. F-PEG-RGD

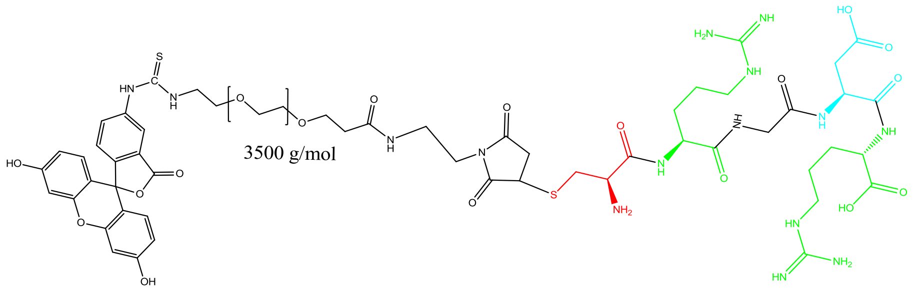

F-PEG-Ma (9 mg) and RGD-Active (2 mg) were solved under inert conditions in dried MeOH. The mixture was stirred overnight at room temperature, then the solvent was removed under vacuum and the crude precipitated on cold ethyl ether. The final product was purified by size exclusion flash chromatography (G-25/H_2O).

TOF/TOF: 3920 z/m

f. F-PEG-RGD-Encrypted

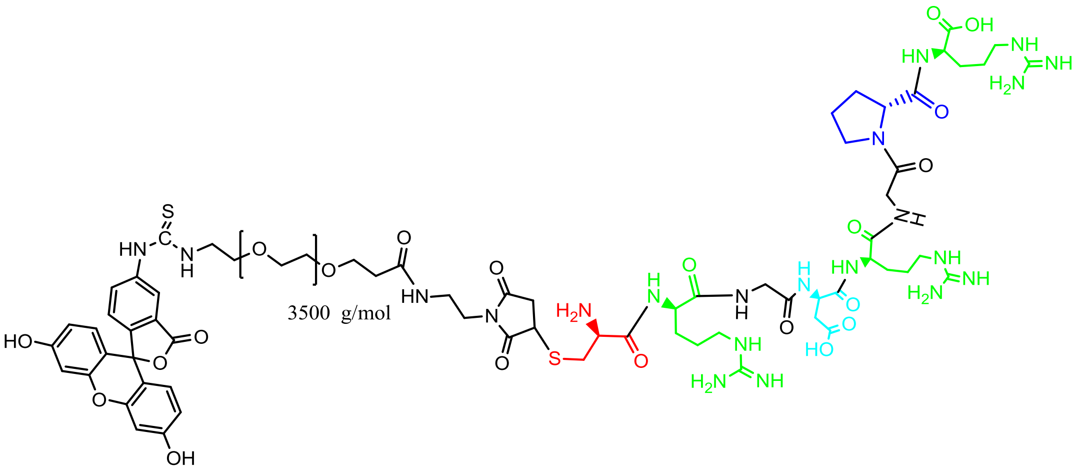

F-PEG-Ma (17 mg) and of RGD-Encrypted (4.1 mg) were solved under inert conditions in dried MeOH. The mixture was stirred overnight at room temperature, then, the solvent was removed under vacuum and the crude precipitated on cold ethyl ether. The final product was purified by size exclusion flash chromatography (G-25/H_2O).

TOF/TOF: 4022 z/m

g. F-PEG-RGD-Encrypted-ALN

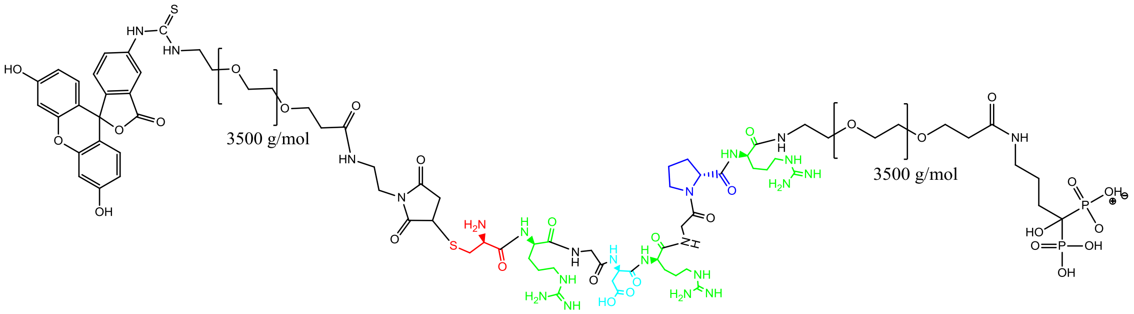

To a solution of F-PEG-RGD-Encrypted in the minimum amount of DMF, NHS (1.3 eq) and DIC (1.3 eq) were added under inert atmosphere. The mixture was stirred at room temperature and the reaction mixture was slowly added over NH_2-PEG-BF (1 eq) and DIPEA (6 eq) in DMF (minimum volume) solution. The mixture was gentle stirred overnight at room temperature under inert atmosphere. The final product was obtained by precipitation in cold ether and subsequent purification by molecular exclusion flash chromatography (G-25 / H_2O).

TOF/TOF: 7705.903 z/m

3. Cathepsin-K peptide selective proteolysis analysis

Procathepsin-K has been activated by adding an equal volume of 100 mM NaAc pH 4.9, 10 mM DTT, 5 mM EDTA (1ml of total volume) followed by incubation for 40 min at room temperature. Two samples of **RPGRDGRC** (Arg-Pr-Gly-Arg-Asp-Gly-Arg-Cys) (10 mg) were solved in 300 μL of Acetic acid solution (pH=5). Free of enzyme activation cocktail was added in control sample as reference. In the other hand, activated enzyme (200μg/mL) was added in sample. The proteolysis reactions were incubated for 2 hours at 37ºC 100 rpm. The reactions were filtered through Amicon Ultra cut-off 30KDa in order to remove the enzyme rests. The peptide fractions were lyophilized and the resulting crude was analyzed by TOF/TOF.

As shown Figure S10, the peptide treated with acid media free of Cathepsin-K suffers the proteolysis affording the desired activated RGD cleavage product in minor concentrations. However, the Cathepsin-K catalyzed process resulted quantitative at same conditions getting the decrypted peptide in quantitative numbers. Further ESI (+) analysis reveals in both cases the presence of bi-peptide rest Ar-Pr after enzymatic proteolysis.

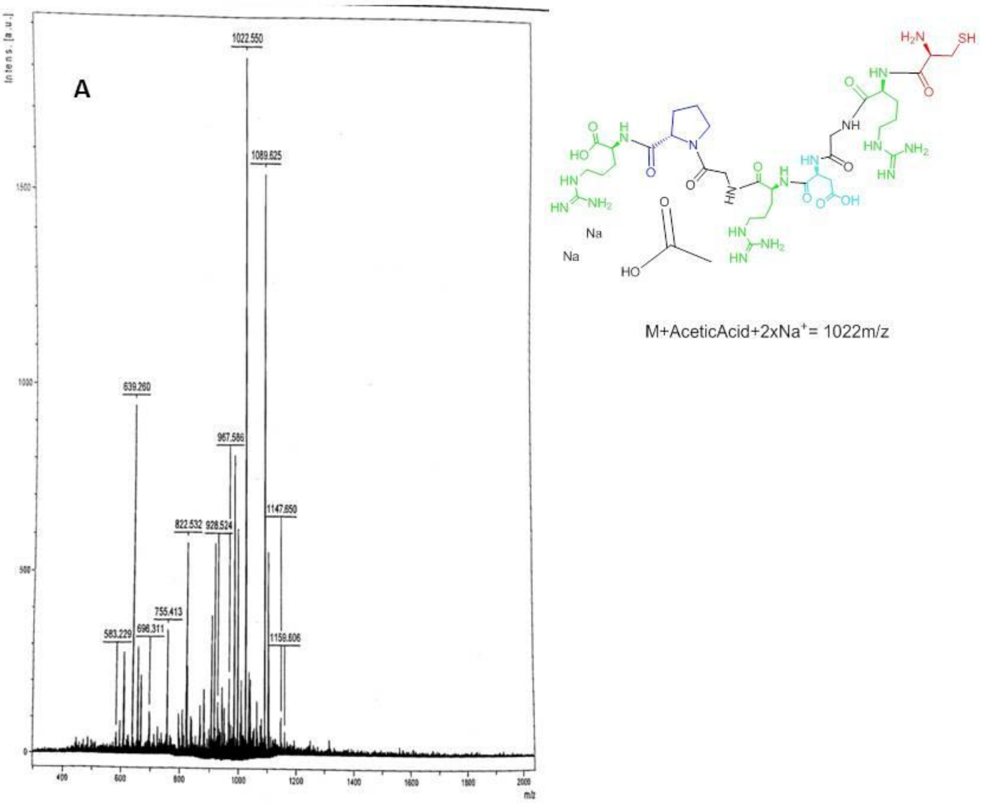

M+AceticAcid+2xNa$^+$= 1022m/z

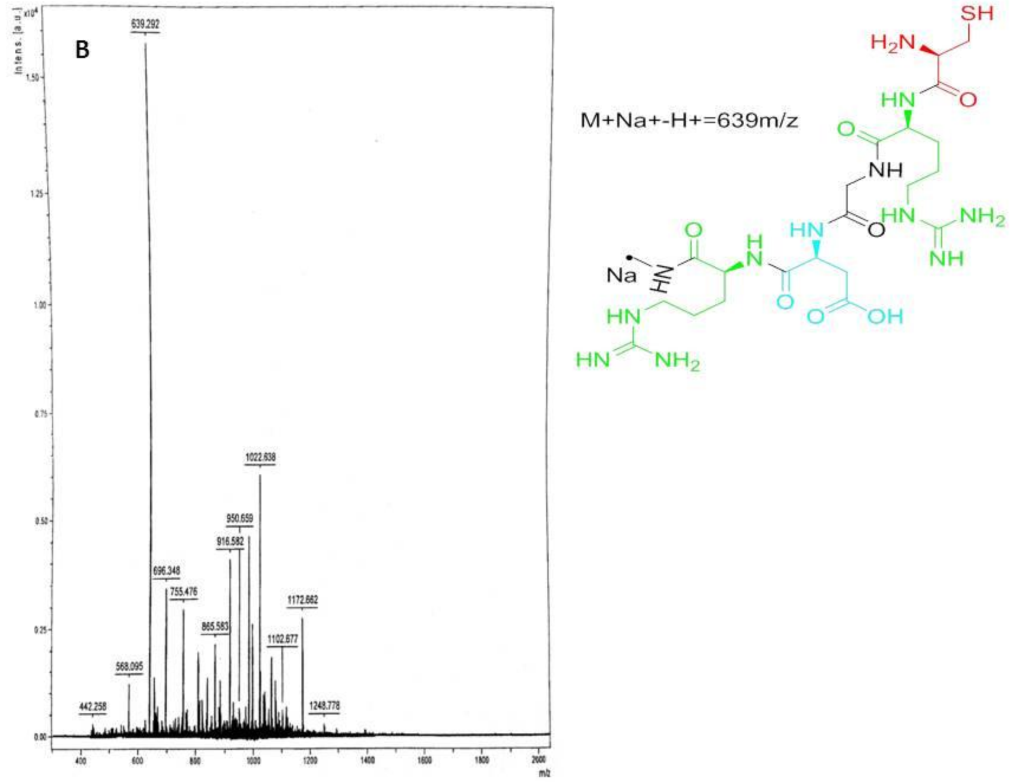

M+Na+-H+=639m/z

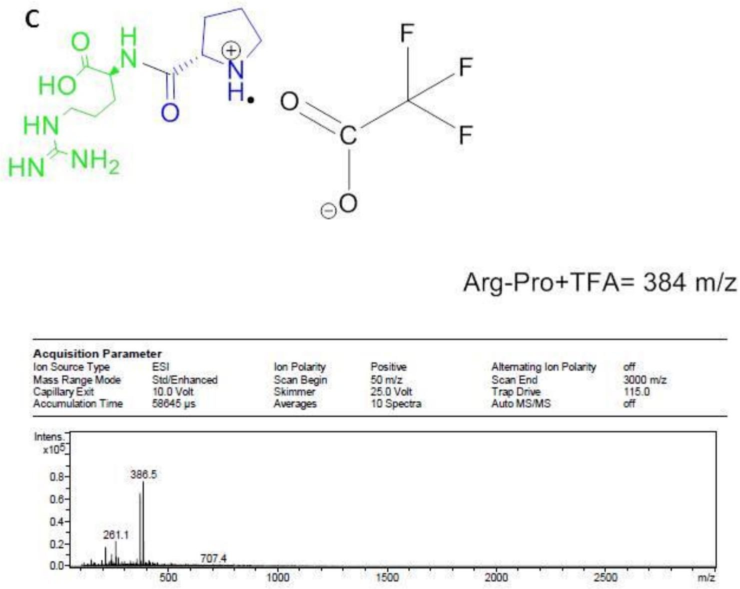

Acquisition Parameter

Ion Source Type	ESI	Ion Polarity	Positive	Alternating Ion Polarity	off
Mass Range Mode	Std/Enhanced	Scan Begin	50 m/z	Scan End	3000 m/z
Capillary Exit	10.0 Volt	Skimmer	25.0 Volt	Trap Drive	115.0
Accumulation Time	58645 µs	Averages	10 Spectra	Auto MS/MS	off

Figure S10: TOF/TOF peptide proteolysis reaction analysis. A. Acid media, B. Acid media and Cathepsin–K induced. C. ESI (+) of side product bi-peptide Arg-Pr after proteolysis.

4. HA-BF fixing assays

a. **Incubation:** 500 µL of a solution of 1mg/mL of the system to be analyzed in PBS 1X (pH= 7.2) was incubated with a commercial HA (50 mg) tablet (previously prepared by powder compaction) at 37 ºC and 100 rpm during 8h. The supernatant was measured by fluorescent spectrometry (λex 492 nm; λem 518 nm (green)) and the tabled washed 3 times in PBS 1X (1.5 mL) and lixiviated 48 hours at 37 ºC and 100 rpm. Further, the piece was washed 4 times with PBS 1X (1mL).

b. **Competition:** The previously incubated tablet with the system to be studied was incubated with 1 mL of a solution of $CaCl_2$ (2.5 mM and 5 mM) and sodium alendronate tri-hydrate (10 mM and 50 mM), further control samples were incubated with PBS 1X at 37ºC 100 rpm during 24 hours. The supernatant was measured by fluorescent spectrometry and the tablet washed 3 times in PBS 1X (1.5 mL) and lixiviated 48 hours at 37 ºC and 100 rpm. Further, the piece was washed 4 times with PBS 1X (1mL).

c. **Cathepsin-K cleavage**: The previously incubated tablet with the system to study was incubated with 300 µL of acetic acid (pH=5) and 200µL of Cathepsin K in activation cocktail (previously activated) for samples or activation cocktail free of enzyme for control. The cleavage reaction was carried out during 2h at 37ºC. The supernatant was measured by fluorescent spectrometry and the tablet washed 3 times in PBS 1X (1.5 mL) and lixiviated 48 hours at 37 ºC and 100 rpm. Further, the piece was washed 4 times with PBS 1X (1mL).

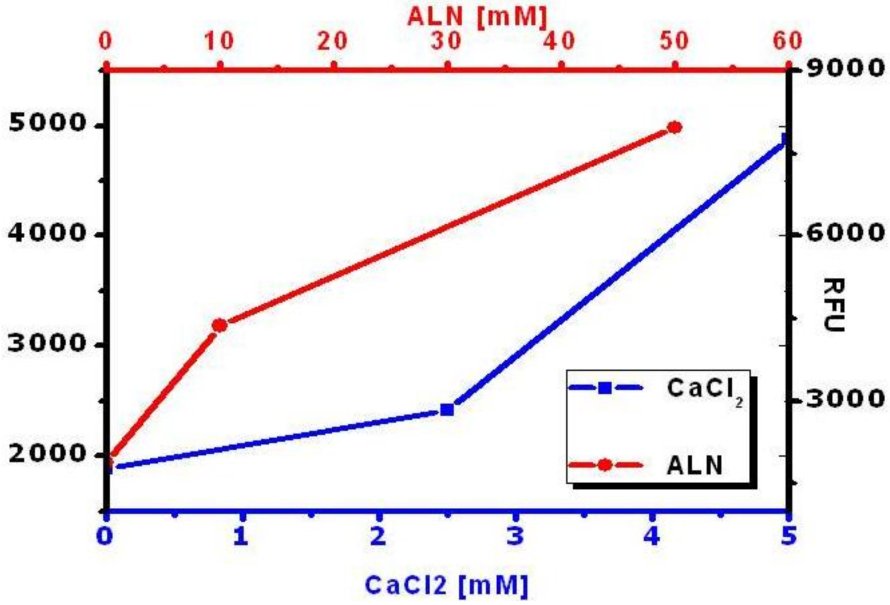

Graphic S1: Fluorescence variations on HA tablet surface after incubation, competition experiments with alendronate and calcium.

5. Culture and cellular uptake analysis.

a. Culture and uptake assays with analogues

Human Osteosarcoma cancer cell line HOS were seeded in a concentration of $4x10^4$ cell/well in a 12 well pate. The cultures were carried out in Dulbecco's Modified Eagle Medium (DMEM) completed with fetal bovine serum and antibiotic. After 48 hours the medium were removed, the cells washed twice with PBS 1X, and substituted by a solution of the fluorescein marked analogue to be studied at fixed concentration of 10µg/mL in medium. After 4 hours, the medium were removed and the cells washed twice with PBS 1X, further, fresh medium was added and cells incubated 24 hours. Cells were washed twice with PBS and trypsinized. After centrifugation and wash in PBS 1X, pellets were suspended in PBS/trypan blue. The data of the percentage of fluorescent cells (FITC %) were collected in FACS Calibur cytometer (Becton Dickinson) and analyzed using Flowing software 2.5.1.

10µg/mL FITC (%)			
	Mean	Sd	Normalized
CONTROL	11.9	1.79	0.445
*F-PEG	20.1	0.850	8.56
*F-PEG-CRGDR	30.2	0.989	18.6
*F-PEG-CRGDR-Encrypted-ALN	23.5	0.588	11.9

Table. S1. n=3, *$P < 0.05$

b. Uptake studies with HA Tablet and Cathepsin K activation.

Human Osteosarcoma cancer cell line HOS were seeded in a concentration of $4x10^4$ cell/well in a 12 well pate. The cultures were carried out in Dulbecco's Modified Eagle Medium (DMEM) completed with fetal bovine serum and antibiotic. After 48 hours the medium were removed, the cells washed twice with PBS 1X. Transwells were introduced in the wells with the HA tablets in their surfaces. Culture mediums were added until to cover along all the system. Activated Cathepsin-K or activation cocktail free of enzyme were added in each case. After 4 hours of incubation Transwells and medium were removed and cells washed twice with PBS. Cells were incubated 24 hours. Cells were washed twice with PBS and trypsinized. After centrifugation and wash in PBS, pellets were suspended in PBS/trypan blue. The data of the percentage of fluorescent cells (FITC %) were collected in FACS Calibur cytometer (Becton Dickinson) and analyzed using Flowing software 2.5.1.

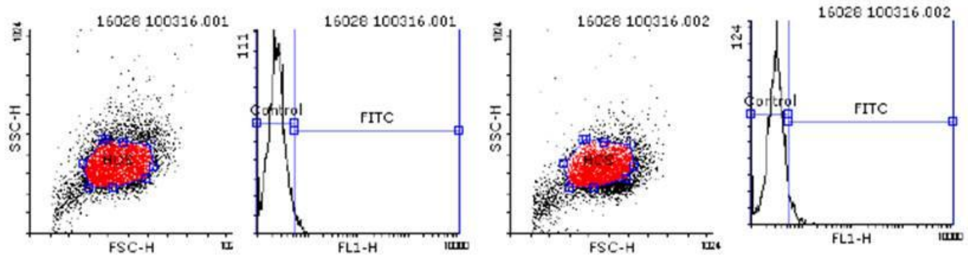

HOS control

F-PEG

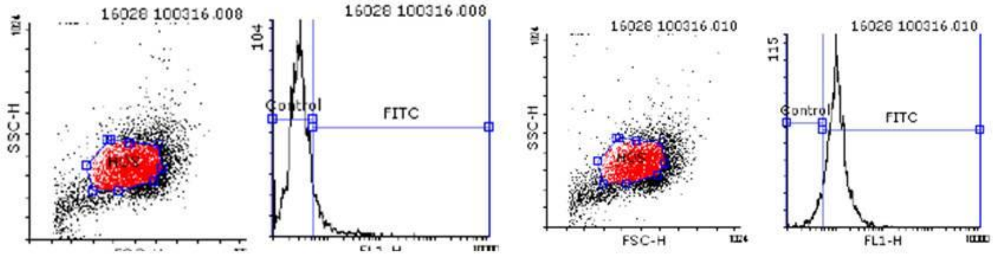

F-PEG-RGD-Encrypted-ALN

F-PEG-RGD-Encrypted-ALN
Cathepsin-K Activated

FITC (%)			
	Mean	Sd	Normalized
CONTROL	-	-	-
*F-PEG-RGD-Encrypted-ALN	12.8	0.21	9.4
*F-PEG-RGD-Encrypted-ALN (C-K activated)	88.3	3.0	85.0

Table S2. Cytometry experiments bone/culture in vitro system. *$P < 0.01$

Paper III

Reprinted with permission from:

Mesoporous Silica Nanoparticles Functionalized with Hyaluronic Acid and Chitosan Biopolymers. Effect of Functionalization on Cell Internalization.

A. Salis, M. Fanti, L. Medda, V. Nairi, F. Cugia, M. Piludu, V. Sogos and M. Monduzzi *ACS Biomater. Sci. Eng.*, 2016, 2, 741-751.

DOI: 10.1021/acsbiomaterials.5b00502

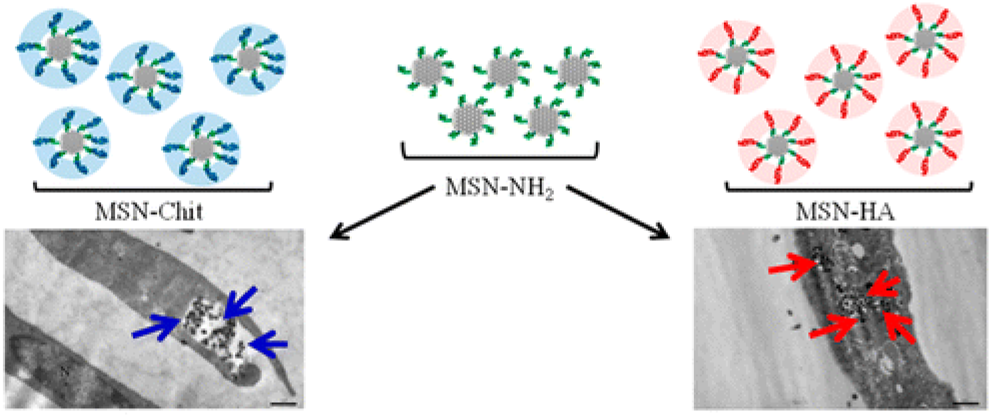

ACS Biomaterials Science & Engineering
Article
pubs.acs.org/journal/abseba

Mesoporous Silica Nanoparticles Functionalized with Hyaluronic Acid and Chitosan Biopolymers. Effect of Functionalization on Cell Internalization

Andrea Salis,*,[‡] Maura Fanti,[†] Luca Medda,[‡] Valentina Nairi,[‡] Francesca Cugia,[‡] Marco Piludu,[†] Valeria Sogos,[†] and Maura Monduzzi*,[‡]

[‡]Department of Chemical and Geological Sciences, University of Cagliari-CSGI and CNBS, Cittadella Universitaria, S.S. 554 bivio Sestu, 09042 Monserrato, Cagliari, Italy

[†]Department of Biomedical Sciences, University of Cagliari, Cittadella Universitaria, S.S. 554 bivio Sestu, 09042 Monserrato Cagliari, Italy

S *Supporting Information*

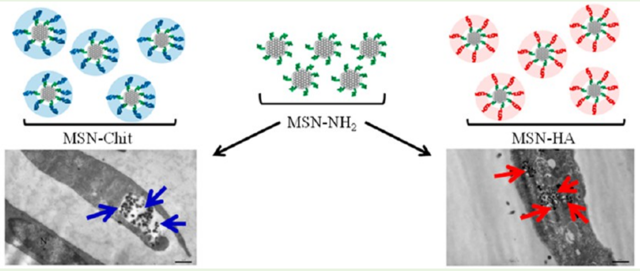

ABSTRACT: Mesoporous silica nanoparticles (MSNs), based on the MCM-41 matrix, were functionalized with amino groups, and then with hyaluronic acid (HA) or chitosan (CHIT) to fabricate bioactive conjugates. The role of the functional groups toward cytotoxicity and cellular uptake was investigated using 3T3 mouse fibroblast cells. A very high biocompatibility of MSN-NH$_2$, MSN-HA and MSN-CHIT matrices was assessed through the MTS biological assay and Coulter counter evaluation. No significant differences in cytotoxicity data arise from the presence of different functional groups in the investigated MSNs. Fluorescence microscopy experiments performed using fluorescein isothiocyanate-conjugated MSN-NH$_2$, MSN-HA, and MSN-CHIT, and transmission electron microscopy experiments performed on slices of the investigated systems embedded in epoxy resins give evidence of significant differences due to type of functionalization in terms of cellular uptake and stability of the particles in the biological medium. MSN-NH$_2$ and MSN-HA conjugates are easily internalized, the uptake of the HA-functionalized MSNs being much higher than that of the -NH$_2$-functionalized MSNs. Differently, MSN-CHIT conjugates tend to give large aggregates dispersed in the medium or localized at the external surface of the cell membranes. Both fluorescence microscopy and TEM images show that the MSNs are distributed in the cytoplasm of the cells in the case of MSN-NH$_2$ and MSN-HA, whereas only a few particles are internalized in the case of MSN-CHIT. Flow cytometry experiments confirmed quantitatively the selectively high cellular uptake of MSN-HA particles.

KEYWORDS: *nanomedicine, mesoporous silica nanoparticles, functionalization, biopolymers, hyaluronic acid, chitosan, cytotoxicity, transmission electron microscopy*

1. INTRODUCTION

Functionalization of materials is an art and has become a must in the development of smart nanodevices for a huge variety of applications, particularly in the challenging topics related to nanomedicine.[1−4] Indeed the design of a drug delivery formulation, and the fabrication of composite materials for either tissue engineering or theranostic, and stimuli responsive drug carriers, should carefully consider the nature of biological barriers. A favorable interaction between an external object and biological entities is addressed by bioadhesion processes which, at a nanoscopic level, can be regarded as a molecular recognition event. Therefore, as described by Gagner et al.,[5] nanomaterials for biomedical applications require suitable functionalization to favor the interaction with the biomolecules. An increased awareness of the involvement of glycoproteins and oligosaccharides in many molecular recognition/inhibition biological processes has addressed the fabrication of bioconjugates functionalized with saccharide biopolymers, proteins, and peptides.[6,7] In this context, several recent works have considered functionalized mesoporous silica nanoparticles (MSNs) as a very promising matrix to build a hybrid organic−inorganic bioconjugate that can modulate weak, but very important, interactions that play significant roles in biology, those that occur when proteins bind to extracellular carbohydrates. Such protein−carbohydrate interactions are essential participants in many physiological cell−cell recognition processes, including fertilization, bacterial, and viral pathogenesis, and the inflammatory response.[8−10]

Ordered mesoporous silica-based functional materials have raised great interest since their discovery in the nineties because of the easiness and the flexibility of the synthesis, the reproducibility of the texture, and of the morphology.[11] Besides

Received: November 24, 2015
Accepted: April 5, 2016
Published: April 5, 2016

ACS Publications

DOI: 10.1021/acsbiomaterials.5b00502

the easy synthesis, other intrinsic peculiar features such as high surface area, uniform pore size distribution, high pore volume as well as the wide possibility to introduce functional groups have attracted an extraordinary interest in these materials.

In the last 20 years, several different long-range ordered structures such as hexagonal, cubic, or lamellar have been built.[12] Several research groups have produced interesting advances in the use of silica materials for nanomedicine applications.[1,2,4,13,14] Another interesting feature is the fact that the silica-based ordered mesoporous materials display a high propensity to selectively adsorb proteins, peptides, and enzymes.[15−17] This was clearly demonstrated through peculiar TEM experiments based either on a standard immunochemical method[18] or a silver enhancement procedure.[19]

In the past few years, we have explored the peculiarities of ordered mesoporous materials to pursue a deep knowledge on the different interactions occurring between charged interfaces such as silica matrices and proteins. Particularly, we investigated the role of pH and ionic strength as well as specific electrolyte effects on the adsorption on, and the release from SBA-15 silica matrices of lysozyme.[15−17] Indeed proteins undergo dramatic specific ion effects in the presence of both weak (buffers) and strong electrolytes.[20−23] These findings highlighted the important role of weak and strong electrolytes when dealing with charged inorganic surfaces or proteins in relation to the complex nature of biological fluids. However, it should be remarked that non functionalized silica particles generally show very high toxicity, up to death, when injected in vivo via intravenous or intraperitoneal administration route.[24] Only subcutaneous injections were recognized as generally safe. Substantially, at present the use of MSNs is limited to the fabrication of drug depot systems or to bone regeneration treatments.[14,25−27] Remarkably, the role of biological fluids has not yet deeply been investigated. As emphasized by many authors[1,2,28−32] functionalization of MSNs constitutes a solid possibility not only for specific cell targeting but also for reducing toxicity and improving biodistribution.[33] To this aim, functionalization based on bioactive moieties such as biopolymers and polyelectrolytes was shown to be a very promising choice.[34] Very recently, we analyzed the adsorption of lysozyme on hyaluronic acid-functionalized SBA-15.[35] The experimental findings suggested that a high level of functionalization of the silica surface almost prevents lysozyme adsorption, whereas a low degree of functionalization of the silica allows for a large lysozyme adsorption. Interestingly, it was ascertained that during enzymatic degradation of HA-drug conjugated systems CD44 receptors favor the internalization of HA-conjugated nanoparticles by cells that enable intracellular delivery of drugs.[36−38] Focusing on functionalizations based on polysaccharides, it is worth mentioning that pH-responsive alginate/chitosan MSN conjugates allow for drug release as pH decreases. This turned out to be very useful for tumor chemotherapeutics delivery both in vitro and in vivo experiments.[39] In addition, it was found that anticancer drugs loaded inside MSNs end-capped with chitosan can be released and internalized in tumor cells not only because of acidic pHs but also as a result of the high concentration of lysozyme, produced in large excess by cancer cells.[40] Indeed chitosan is easily hydrolyzed into monomers either by acidic pHs or by the catalytic activity of lysozyme, afterward the drug can be released. In that case a dual stimuli-responsive drug carrier was fabricated.

This work focuses on MSNs based on MCM-41 matrices functionalized either with hyaluronic acid (HA) or chitosan (CHIT) and on the evaluation of their cytotoxicity toward 3T3 mouse fibroblast cell lines. As reported in recent works,[41−43] the functionalization with HA and CHIT should produce MSNs characterized by negative and positive charged interfaces respectively, at physiological pHs. However, it should be remarked that many changes can occur when particles get in contact with biological environments. Particularly, the role of the composition of the growing media for cell proliferation on the particle surface charge can become a very complex task. Indeed, here we will demonstrate that cell internalization of functionalized MSNs strongly depends on the type of functionalization. In this context, it is worth citing a recent paper by Treccani et al.,[44] where the interaction between biological fluids and charged particles was carefully investigated.

2. MATERIALS AND METHODS

2.1. Chemicals. Tetraethoxysilane (TEOS, 98%), hexadecyltrimethylammonium bromide (CTAB, > 99%), anhydrous toluene (99.8%), 3-aminopropyl-triethoxysilane (APTES, > 98%), triethylamine (>99%), hyaluronic acid sodium salt from *Streptococcus equi* (cod. 53747), chitosan (cod. 740063, MW 60−120 kDa), NaH_2PO_4 (99%), Na_2HPO_4 (99%), and fluorescein isothiocyanate (FITC) were purchased from Sigma-Aldrich (Milan, Italy). *N*-hydroxysuccinimide (NHS, > 97%), and *N*-(3-(dimethylamino)propyl)-*N*′-ethylcarbodiimide hydrochloride (EDC, > 98%) were purchased from Fluka. 3T3 were cultured in complete medium: DMEM (#6429,Sigma-Aldrich) supplemented with 10% fetal bovine serum (#F6178,Sigma-Aldrich), 1 μM L-glutamine (#G7513,Sigma-Aldrich), 100 U/mL penicillin and 100 μg/mL streptomycin (#4333,Sigma-Aldrich). MTS: CellTiter 96 AQueous One Solution Reagent (#G3581, Promega).

2.2. Synthesis of Mesoporous Silica Nanoparticles (MSNs). 1g of CTAB was dissolved in 480 g of Millipore water at room temperature by using an overhead stirrer. A volume of 3.5 mL of NaOH (2 M) was added to the surfactant solution, the temperature was then increased at 80 °C and, after 2 h, 5.0 mL of TEOS were added dropwise. The solution was stirred for other 2 h and then the resultant white precipitate was collected by vacuum filtration and dried overnight at room temperature. The removal of CTAB surfactant was carried out by weighing 1.0 g of the synthesized material and adding 100 mL of a methanolic solution with 0.75 mL of hydrochloric acid (37%) and stirring for 6 h at 50 °C. The mesoporous silica nanoparticles (MSNs) were then recovered via filtration and dried under vacuum at room temperature.[45,46] The grafting of the amino group on the surface of the MSNs was carried out by dispersing 1 g of the sample in 30 mL of anhydrous toluene and then by adding dropwise 1.0 mL of APTES. The dispersion was heated under reflux for 15 h. The resulting MSN-NH_2 sample was collected by filtration, washed with acetone, and dried overnight at room temperature under vacuum.

2.3. Functionalization and Characterization of MSN-NH_2 Particles. *2.3.1. Functionalization of MSNs with Hyaluronic Acid (HA).* A mass of 100 mg of MSN-NH_2 sample was dispersed in 100 mL of Millipore water. In another reaction vessel, 20 mL of an aqueous solution containing NHS (0.37 g) and EDC (0.2 g) was mixed with 60 mL of an aqueous solution containing 113 mg of HA. The two solutions were mixed and the pH was adjusted to 9.0 by adding triethylamine. Finally, the mixture was stirred at 38 °C overnight. The HA-modified MSNs (MSN-HA) were collected after centrifugation, three washings with Millipore water, and dried under vacuum and at room temperature overnight.[34]

2.3.2. Functionalization of MSNs with Chitosan (CHIT). Chitosan has a free aminogroup per unit of sugar. The grafting of the chitosan biopolymer to MSN-NH_2 was achieved by linking the amino groups of both the biopolymer and the particles with glutaraldehyde bifunctional reagent. 0.1 g of MSN-NH_2 sample were soaked for 1 h in a solution composed by 100 μL of aqueous glutaraldehyde (50%) and 2.5 mL of

Scheme 1. Steps Involved in the Functionalization of Mesoporous Silica Nanoparticles (MSNs) To Obtain Amino- (MSN-NH_2), Hyaluronic Acid- (MSN-HA), Chitosan- (MSN-CHIT), and Fluorescin Isothiocyanate-Mesoporous Silica Nanoparticles

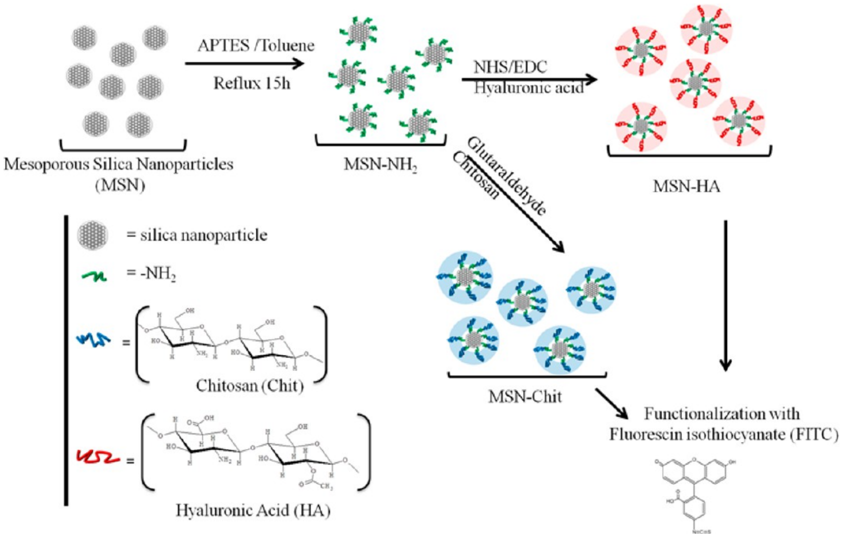

0.1 M phosphate buffer solution (pH 7.5). The activated material was washed for three times under stirring with the same buffer (2.5 mL), centrifuged and the supernatant was removed through a Pasteur pipet. The MSN-NH_2 dispersion was then mixed with a suspension of chitosan containing 50 mg of chitosan in 2.5 mL of 0.1 M HCl solution to allow chitosan solubilization. The mixture was gently stirred overnight at 25 °C and then the material was collected by filtration and washed with a slightly basic buffer solution (pH 8) to remove the excess of chitosan. The material was dried under vacuum and at room temperature overnight.

2.3.3. Labeling of MSN-NH_2, MSN-HA, and MSN-CHIT with FITC. A mass of 20 mg of MSNs (MSN-NH_2, MSN-HA, MSN-CHIT) was suspended in 3 mL of Millipore water, and mixed with 5 mL of a 0.3 mg/mL FITC ethanol solution. The suspension was stirred at room temperature in dark conditions for 6h and the particles were centrifuged, then washed three times with ethanol. The FITC labeled particles were used for fluorescence microscope observations and flow cytofluorimetry.[34]

2.3.4. Physicochemical Characterization of Functionalized MSNs. Thermogravimetric analysis (TGA) was carried out on a Mettler-Toledo TGA/STDA 851. Thermal analysis data were collected in the 25−1000 °C range, under oxygen flow (heating rate = 10 °C min^{-1}; flow rate =50 mL min^{-1}). The hydrodynamic diameter and the zeta potential of MSNs were measured using a Zetasizer nano ZSP (Malvern Instruments) in backscatter configuration ($\theta = 173°$) at laser wavelength of $\lambda = 633$ nm. The scattering cell temperature was fixed at 37 °C and the data were analyzed with the Zetasizer software 7.03 version. For both zeta potential and DLS measurements the sample was prepared by suspending MSNs (1 mg/mL) in filtered (0.2 μm polypropylene filter, Whatman) Milli-Q water. Samples were sonicated for 30 min and left under agitation overnight. Samples were sonicated for other 30 min and then the measurements were carried out.

2.4. Biological Methods. *2.4.1. In Vitro Viability Assay.* Cytotoxicity of MSNs was determined by the MTS assay. 3T3 mouse fibroblast cells were cultured in complete medium at 37 °C in a 5% CO_2 humidified environment. 3T3 cells were plated at a density of 3×10^5/mL in 96-well plates for 24 h, and then incubated with serial concentrations of MSN-NH_2, MSN-HA, and MSN-CHIT (from 200 μg/mL to 6.2 μg/mL) ($t = 0$). After 24 h, MSNs were removed and replaced with fresh complete medium. Cell viability was quantified by adding 20 μL of Cell-Titer 96 Aqueous One Solution Reagent (MTS) to the cultures for 2 h at 37 °C, immediately ($t = 24$ h), then after 24 ($t = 24$ h + 24 h) and 48 ($t = 24$ h + 48 h) hours after MSNs removal. Samples were read at $\lambda = 490$ nm for colorimetric assessment. All the experiments were performed at least in triplicate for each group.

2.4.2. Cell Growth Curve. 3T3 cells were plated 4×10^4/mL in 12-well plates. The day after ($t = 0$) cells were treated with 100 μg/mL of MSNs for the analysis of cell growth. After 24 h MSNs (MSN-NH_2, MSN-HA, and MSN-CHIT) were removed, and cells were cultured with fresh medium. Cell counts were performed immediately ($t = 24$ h), then after 24 ($t = 24$ h + 24 h) and 48 ($t = 24$ h + 48 h) hours after MSNs removal, using a Beckman Coulter counter. All the experiments were performed at least in triplicate for each group.

2.4.3. Intracellular Uptake through Fluorescence Microscopy. 3T3 cells were plated at a density of 3×10^5/mL on glass coverslips. After 24 h from seeding, cells were incubated with 100 μg/mL FITC-labeled MSN-NH_2, MSN-HA, and MSN-CHIT for 24 h. After treatment, MSNs were removed and cells maintained in fresh complete medium for further 24 h. Then, cells were washed with PBS, stained for 30 min with Hoechst dye 33342 for nuclei, and observed using an Olympus BX41 fluorescence microscope equipped with an appropriate filter for FITC detection ($\lambda_{Ex} = 490$ nm; $\lambda_{Em} = 517$ nm).

2.4.4. Intracellular Uptake through Flow Cytometry. 3T3 cells, after treatment with FITC-labeled MSNs as described above, were dissociated by 0.25% trypsin/EDTA and resuspended in PBS. MSN uptake was analyzed using a BD FACSCANTO II flow cytometer (Becton Dickinson Biosciences, CA). At least 10 000 cells were analyzed in each sample. Cells without nanoparticle treatment were used as controls.

2.5. Transmission Electron Microscopy. Samples of 3T3 cells were treated with 100 μg/mL of MSN-NH_2, MSN-HA, and MSN-CHIT for 24 h. After treatment, MSNs were removed and cells maintained in fresh complete medium for further 24 h. Then, cells were fixed for 2 h in a mixture of 1%(para)formaldehyde (Electron Microscopy Sciences) and 1.25% glutaraldehyde (Electron Microscopy Sciences) in 0.1 M sodium cacodylate (Electron Microscopy Sciences) buffer (pH 7.4). Cells were rinsed in the same buffer after fixation, postfixed in 1% osmium tetroxide for 1h and finally stained in aqueous uranyl acetate 0.25% overnight at 4 °C. The next day the cells were processed by standard methods for embedding in epoxy resin.[47] In detail, they were dehydrated in a graded series of ethanol and xylene and infiltrated overnight in Epon 812/xylene mixtures at room temperature. Cells were finally embedded in pure Epon 812 resin, transferred to dry beam capsules or flat embedding molds previously filled with embedding medium and polymerized in a oven at 60 °C for 24 h. Embedded cells were trimmed and sectioned after the resin blocks returned to room temperature. Ultrathin sections of the above samples (60−90 nm thick) were cut with a LKB ultratome 8800 ultramicrotome and collected on Formvar-coated grids. They were poststained with uranyl acetate and bismuth subnitrate, washed three times with distilled water, and finally observed and photographed in a transmission electron microscope (JEOL 100S model, Tokyo, Japan) operating at 80 kV.

3. RESULTS

3.1. Characterization of Functionalized MSNs. Mesoporous silica nanoparticles (MSNs) were synthesized according to Yu et al.[34] A detailed characterization of MSN is reported in the Figure S1. It includes the textural characterization (Figure S1A) obtained by the nitrogen adsorption/desorption isotherms which allowed to measure the surface area (S_{BET} = 1193 m^2/g), pore volume (V_p = 0.87 cm^3/g) and the maximum of pore size distribution (d_p = 22 Å). The structural characterization was carried out by means of small angle X-rays scattering (Figure S1C) and transmission electron microscopy (Figure S1D). Both techniques confirm the occurrence of the hexagonal array of pores the synthesized MSNs. Additionally, the TEM image in Figure S1D allows to estimate a particle size in the range 100−130 nm.

Scheme 1 summarizes the steps involved in the functionalization of MSNs. A reaction with aminopropyltriethoxysilane (APTES) introduces the amino group on the surface. This group is needed for the subsequent functionalization steps with hyaluronic acid (HA) and chitosan (CHIT) respectively. HA binding requires the use of two additional reagents, namely NHS and EDC.[35] CHIT binding was carried out similarly to what currently done in the covalent immobilization of enzymes on solid supports[48] using glutaraldehyde, a bifunctional reagent, which is able to react with the amino groups of MSN-NH_2 and those of chitosan biopolymer.

Functionalization of MSNs was proved by means of thermogravimetric analysis (TGA). Figure 1 compares the percentage mass loss profiles as a function of temperature for functionalized MSNs.

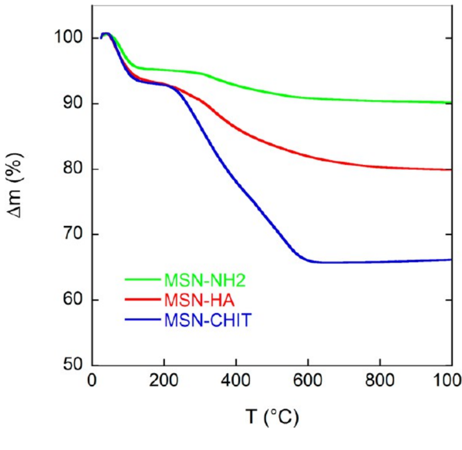

Figure 1. Percentage mass loss profiles as a function of temperature for functionalized MSNs (MSN-NH_2, MSN-HA, and MSN-CHIT).

The values of partial mass loss below and above 200 °C are reported in Table 1. For temperatures below 200 °C, a mass loss of 4.9% is obtained for MSN-NH_2 particles. This mass loss can be ascribed to the removal of humidity and to the condensation of surface silanols. Above 200 °C, the mass loss is due to the burning of organic groups. At T > 200 °C, a Δm = 5.0%, is obtained for MSN-NH_2. The functionalization with HA produces mass loss of about 7% for both MSN-HA and MSN-CHIT at T < 200 °C. Instead, at T > 200 °C Δm is 13.1% for MSN-HA and of 26.7% for MSN-CHIT, respectively. The higher mass loss found for MSN-CHIT respect to MSN-HA suggests that the former sample has a higher degree of grafted biopolymer compared to the latter.

Additional characterization of the functionalized samples was carried out through FTIR spectroscopy. Figure S2 compares the FTIR spectra of MSN-NH_2 with those of MSN-HA and MSN-CHIT and the text in the Supporting Information gives a description of band assignment. Substantially, TGA and FTIR techniques confirm the success of the functionalization procedure.

These functionalizations are expected to produce differently charged MSNs. Particularly once dispersed in an aqueous medium, positive charges for MSN-NH_2 and MSN-CHIT, and negative charges for MSN-HA surfaces would occur. This was confirmed by zeta potential measurements (Table 1). Indeed the values of ζ are positive (9.7 ± 0.8 mV) for MSN-NH_2 but changes sign after functionalization with HA (−7.2 ± 0.8 mV). Finally, the functionalization with positively charged polymer chitosan makes the nanoparticles even more positively charged (40 ± 1 mV). This would result in a very highly stable suspension in distilled water. Similar measurements were carried out using the cell culture medium as particle dispersant. This was done because one of the main aims of the work was the evaluation of the interactions between the different MSNs and the 3T3 mouse fibroblast cells. Thus, functionalized MSNs were prepared using the cell culture broth as dispersing medium. This medium is constituted by high glucose DMEM, 10 v% Fetal Bovine Serum and 0.5 v% antibiotics, and any attempt to measure the zeta potential of our MSNs failed: both medium and MSNs, independently of the functionalization, gave a zeta potential around −10 mV as already observed by Treccani et al.[44] These findings are clearly related to the complexity of the culture medium, particularly to the high ionic strength and to the presence of DMEM amino acids and FBS proteins, which can adsorb at the particle surface and eventually form a protein corona.[31,44]

The functionalized particles were characterized with dynamic light scattering for the determination of the hydrodynamic diameter, d_H, (Table 1 and Figure S3) both in Milli-Q water and cell culture medium. In Milli-Q water, the size (d_H) of MSN-NH_2 is 126 ± 2 nm and becomes 156 ± 3 nm (MSN-HA) and 169 ± 3 nm (MSN-CHIT) after biopolymer functionalization. This size increase is consistent with a

Table 1. Characterization of Functionalized MSNs by Means of TGA (Δm%), Zeta Potential (ζ), and Hydrodynamic Diameter (d_H)

	TGA (Δm %)		Milli-Q water		cell culture medium	
sample	<200 °C	>200 °C	ζ (mV)	d_H (nm)-Number	ζ (mV)	d_H (nm)-Number
MSN-NH_2	4.9	5.0	9.7 ± 0.8	126 ± 2	−11.3 ± 0.6	131 ± 2
MSN-HA	7.0	13.1	−7.2 ± 0.8	156 ± 3	−10 ± 1	138 ± 1
MSN-CHIT	7.1	26.7	40 ± 1	169 ± 3	−6.7 ± 0.9	157 ± 4

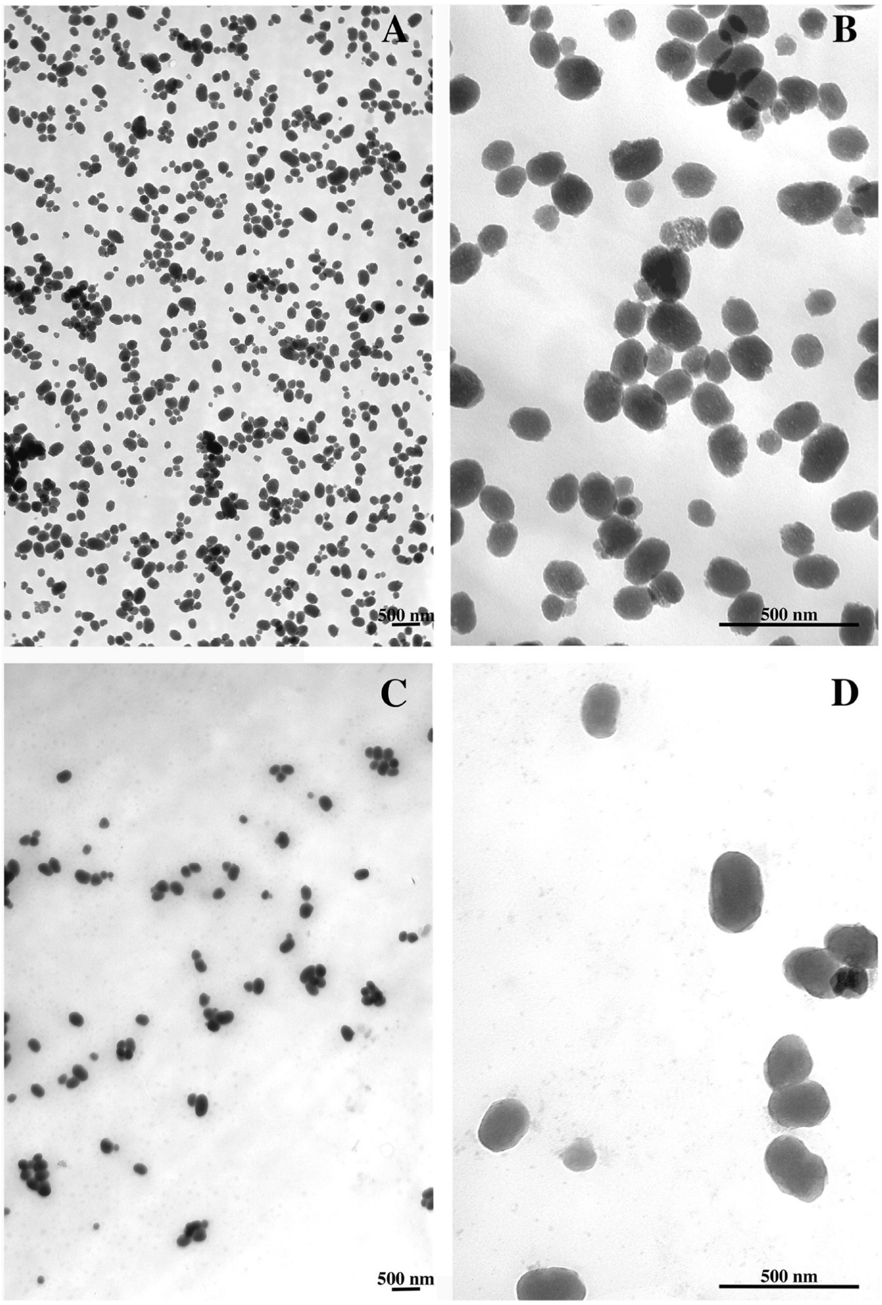

Figure 2. TEM images of functionalized MSNs. (A, B) MSN-HA; (C, D) MSN-CHIT.

successful functionalization of mesoporous silica nanoparticles. In the cell culture medium, the size of the MSNs is not significantly different for MSN-NH_2, whereas it is slightly lower for MSN-CHIT (157 ± 4 nm) and even lower for MSN-HA (138 ± 1 nm). A possible explanation is that the electrolytes occurring in the culture medium, besides affecting the measured zeta potential, also play a role to decreasing the hydrodynamic diameter of the biopolymer-functionalized MSNs.

Figure 2 shows the TEM images at low magnification of the functionalized MSNs. We observe that there is a good correspondence, at least at the qualitative level, between particle sizes obtained with DLS and TEM techniques.

To improve the ultrastructural details of functionalized particles by standard transmission electron microscopic techniques, we have treated nanoparticles with phosphotungstic acid solution. To date, the phosphotungstic acid staining is a rapid and easy method employed during electron microscopic investigations of isolated particles,[49] virus,[50] and organelles,[51] which usually appear brilliant in a amorphous electron-dense layer. As negative staining, it mainly allows the analysis of the superficial details of nanoparticles and individual macromolecules at electron microscopy level.

After treatment with phosphotungstic acid solution, we observed the presence of an electron lucent halo surrounding the MSN-HA and the MSN-CHIT particles (Figure S4). That halo was not observed for MSN-NH_2. Although the nature of the electron lucent halo detected on the above particles needs to be completely ascertained by additional and more specific EM counterstaining techniques, its presence could be ascribed to the HA and CHIT functionalization processes, respectively.

3.2. Cell Viability and Counts. The effect of MSNs on 3T3 cell viability and proliferation profiles were evaluated using

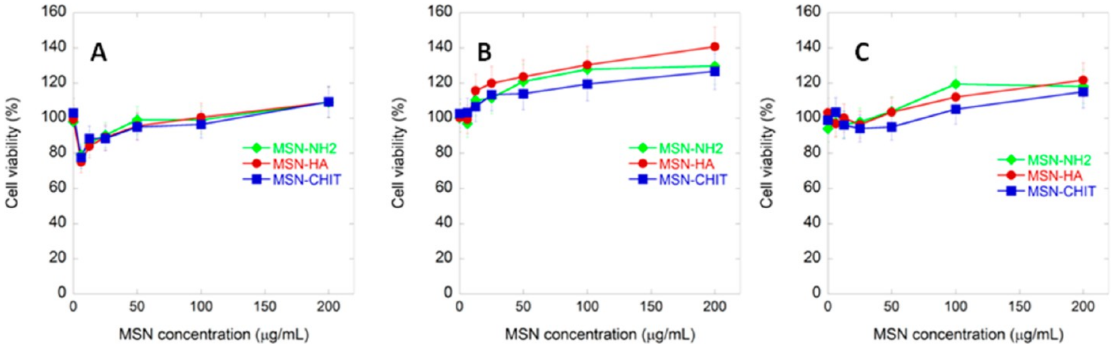

Figure 3. Effect of MSN-NH$_2$, MSN-HA, and MSN-CHIT on the viability/proliferation of 3T3 cell line incubated with the different MSNs for 24 h. Viability measurement through MTS assay: (A) immediately after MSNs removal; (B) 24 h after MSNs removal, and (C) 48 h after MSNs removal according to the protocol in section 2.4.1.Values are expressed as percentage of control wells containing culture medium without MSNs. Results represent the mean ± standard deviation of three independent experiments.

MTS assay and Coulter counter assay. Cell viability was measured after exposure to different concentrations of MSN-NH$_2$, MSN-HA, or MSN-CHIT for 24 h. Figure 3 shows the viability measured with respect to controls (%) for concentrations of MSNs up to 200 μg/mL. Figure 3A shows the viability determined immediately after MSNs removal. Figures 3B and 3C show the viability measured after MSNs removal for 3T3 cells allowed to grow in the medium for other 24 or 48 h, respectively. The experiments performed immediately after MSNs removal show a small decrease of viability with the lowest concentrations of MSNs (Figure 3A). On the contrary, no decrease of cell viability was observed for experiments carried out after 24 or 48 h (Figures 3B−C).

In addition, we note that viability measured for MSNs concentration of 200 μg/mL becomes very high compared to control, particularly for MSN-HA 24 h after MSNs removal (Figure 3B), and for all MSNs when cells are left to grow in the medium for 48 h after MSNs removal (Figure 3C). We can suggest that MTS assays are commonly used, and certainly reliable in relation to the evaluation of biocompatibility, but more at a qualitative rather than at a quantitative level. However, these findings confirm the good safety of MSNs used in this study toward 3T3 fibroblast cells. Indeed, it has been suggested that the presence of inorganic objects such as our MSNs (particles internalized or located on the cell membranes), may originate interference with the colorimetric assay as observed by Bancos et al.[52] Clearly the MTS assay can prove the general viability but, at a quantitative level, cell counts are more reliable. The experiments of cell counts were performed using the same conditions used for MTS assay in terms of contact time and following measurements. The MSNs concentration of 100 μg/mL was considered. Figure 4 shows the results of cell counts obtained for the different MSNs compared to the control. All measurements were performed in triplicate, and the quantitative results demonstrate again the safety of our MSNs, and also the fact that the highest growing speed of the cells is observed when cells are left to grow for 24 h after the incubation with MSNs. It is remarkable that both cytotoxycity and cell proliferation are not influenced by the type of functionalization of the MSNs.

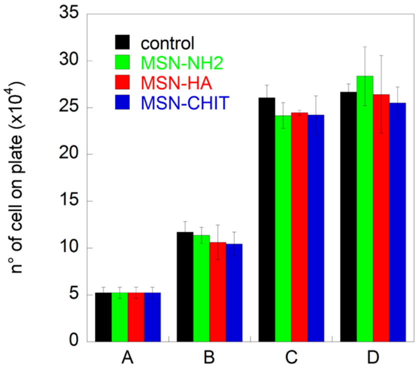

Figure 4. Effect of MSN-NH$_2$, MSN-HA, MSN-CHIT, and controls on the proliferation capacity of 3T3 cell line incubated with the different MSNs for 24 h, and then left in contact with the culture medium for different times. Cell count: (A) number of cells before treatment (t = 0); (B) number of cells immediately after MSNs removal (t = 24 h); (C) number of cells 24 h after MSNs removal (t = 24 h + 24 h); (D) number of cells 48 h after MSNs removal (t = 24 h + 48 h) according to protocol in section 2.4.2.

3.3. Intracellular Uptake. The cellular uptake performance of the MSNs was visualized by fluorescence and transmission electron microscopes. Figure 5 shows the fluorescence microscopy panels of 3T3 cells incubated with the FITC-labeled MSNs for 24 h, afterward MSNs were removed, and cells were left to grow in the culture medium for 24 h before performing the fluorescence microscopy analysis. Differently from the proliferation experiments, the cellular uptake performance depends significantly on MSN functionalization.

Indeed, we observed that about half of the cells incubated with FITC-MSN-NH$_2$ display significant amounts of internalized MSNs (Figure 5A, B), almost all the cells incubated with FITC-MSN-HA display high amounts of MSNs in their cytoplasm (Figure 5C, D), whereas only few cells incubated with FITC-MSN-CHIT show a very low number of internalized MSNs (Figure 5E, F). Indeed FITC-MSN-CHIT nanoparticles tend to form large aggregates outside or over the cells as demonstrated by the presence of big fluorescent spots in Figure 5E, F.

The qualitative observations of fluorescence microscopy were supported by flow cytometry analysis that determined the cellular uptake of FITC-MSNs into 3T3 cells by the incorporated fluorescence intensity. Figure 6 shows representative flow cytometry assessment of controls cells and cells treated with FITC-MSN-HA, indicating a very efficient uptake of nanoparticles. FITC-MSN-HA were efficiently internalized by all the cells, whereas the uptake of FITC-MSN-NH$_2$ was lower, since about 79% of cells were FITC positive. Finally, the uptake of FITC-MSN-CHIT is not shown because unreliable results due to the formation of big aggregates into the cell

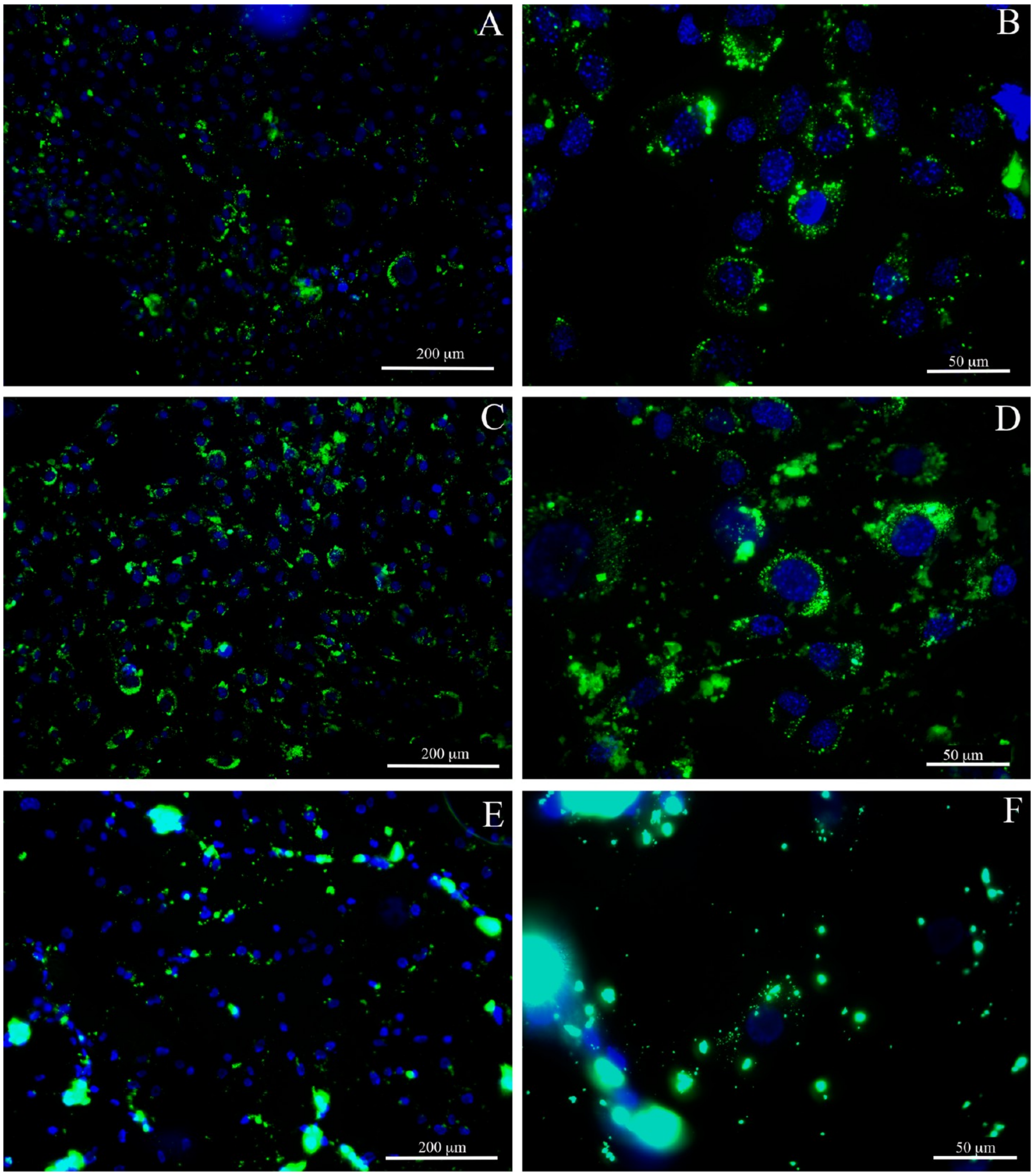

Figure 5. Internalization of MSNs using fluorescence microscopy. Images at different magnification (bars: left side 200 μm, right side 50 μm) of 3T3 mouse fibroblasts incubated for 24 h with 100 μg/mL of MSNs, and then left to grow for other 24 h in the culture medium (see section 2.4.3). (A, B) MSN-NH_2, (C, D) MSN-HA, (E, F) MSN-CHIT. Blue, nuclei (Hoechst assay); green fluorescence, FITC-MSNs.

culture medium were obtained. However, this behavior is consistent with what observed in Figure 5E, F.

3.4. Electronic Microscopy. Electron microscopy analysis confirmed and extended the results obtained by means of fluorescence microscopy. TEM highlighted at ultrastructural level significant differences in the morphological events that occurred in 3T3 cell cultures after exposure to the different types of functionalized MSNs. Figure 7 shows some significant TEM images (see also Figure S5). In detail, 3T3 cells following MSN-NH_2 treatment exhibited only few cytoplasmic vesicles containing MSN particles (Figure 7A, B). Differently, 3T3 cells treated with MSN-HA particles exhibited a unique morphology of their cytoplasm that was mainly characterized by the presence of a large amount of vesicles filled with MSN-HA particles (Figure 7C, D). In both samples, the vesicles were delimited by a single membrane with size up to 1−2 μm in diameter (Figure 7A−D), suggesting an internalization by endocytosis. Although most internalized MSNs were seen to be confined inside the cytoplasmic vesicles, additional MSNs particles were found free in the cytosol. In contrast, MSN-CHIT particles exhibited a significant different pattern in 3T3 cells, where they were often observed strictly associated with the external cell surfaces or forming large aggregates in the culture medium (Figure 7E, F). Occasionally, very few MSN-CHIT particles were internalized in the cytoplasmic compartment (Figure 7F). Moreover, in all 3T3 samples examined in this study, the nucleus was always found devoid of MSN particles, which remained restricted to the cytoplasmic compartment. The higher resolving power of the TEM technique highlighted the cell structure of the 3T3 cells

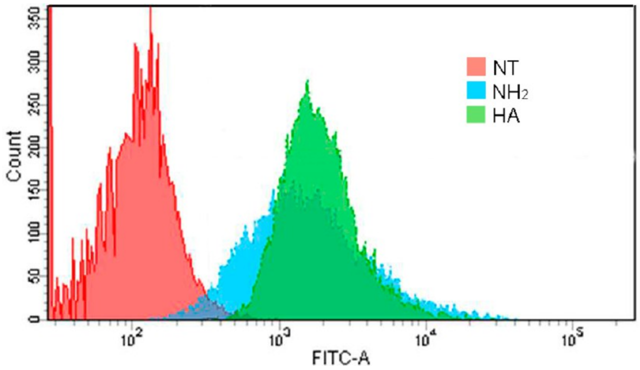

Figure 6. Flow cytometry: Histogram plot of control cells (red) and cells incubated with FITC-labeled MSN-NH_2 (blue) or MSN-HA (green).

incubated with MSNs particles. Independently of the type of functionalized MSNs used, the typical cell ultrastructure was preserved, being characterized by well developed Golgi apparatus, endoplasmic reticulum and mitochondria. No significant morphological alterations were detected when compared to control samples (see Figure S6).

4. DISCUSSION

As demonstrated by fluorescence microscopy, TEM images also document the significant dissimilarities in the MSNs patterns that take place in 3T3 cells following treatment with the different functionalized MSNs. The type of functionalization does not seem to affect the cellular architecture of the 3T3 mouse fibroblasts that was always well preserved and characterized by the presence of well-developed cellular organelles. This agrees with the cell viability experiments. However, the different amounts of MSNs particles internalized in the cytoplasm of 3T3 cells following a specific MSN

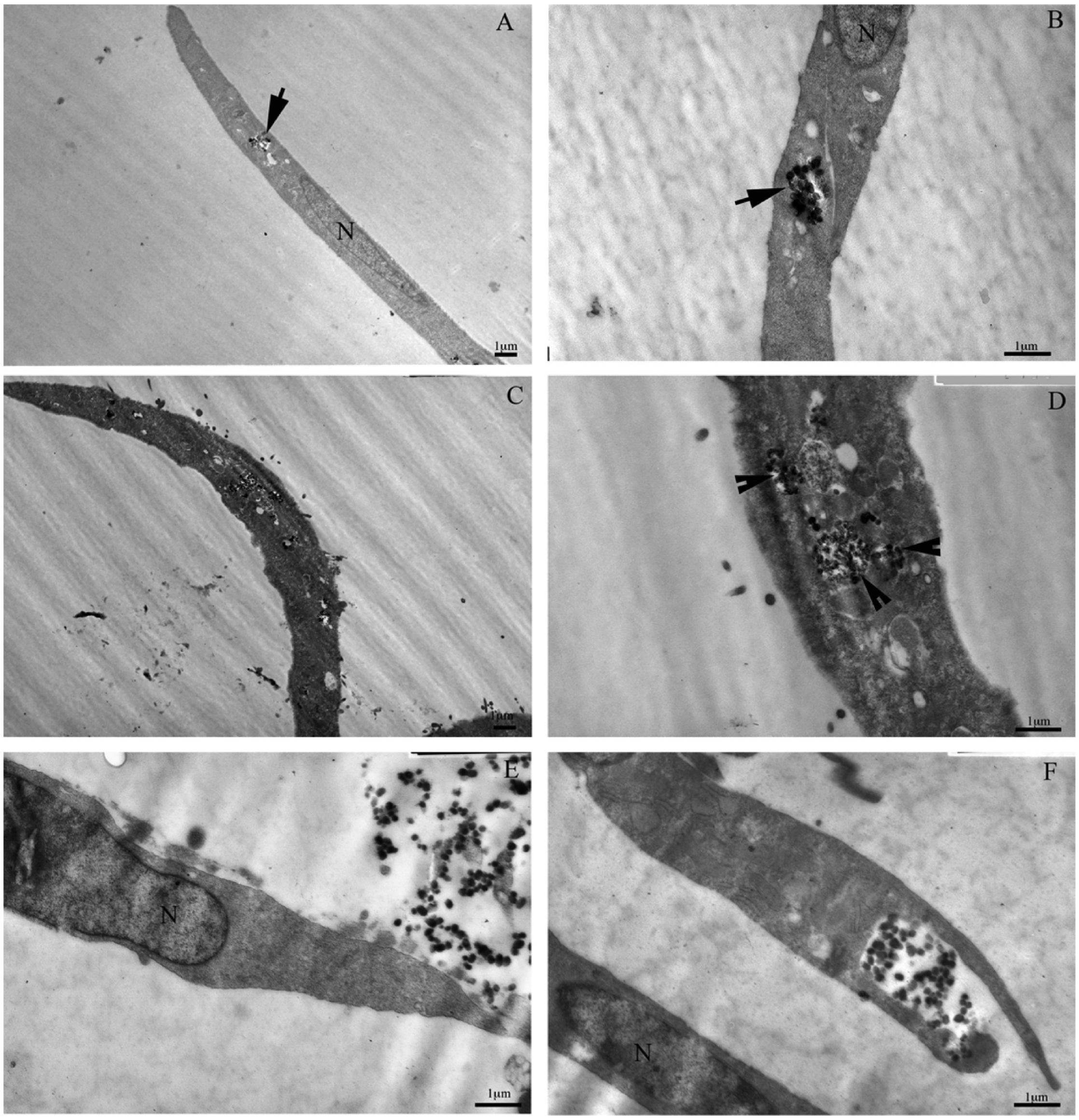

Figure 7. Electron micrographs of mouse fibroblasts 3T3 incubated for 24 h with 100 μg/mL of MSNs, and then left to grow for other 24 h in the culture medium before the other treatments (see section 2.5). (A, B) MSN-NH_2, (C, D) MSN-HA, (E, F) MSN-CHIT. Arrows and arrowheads indicate internalized MSN-NH_2 and MSN-HA nanoparticles, respectively. N = nucleus. Additional TEM images are shown in Figure S5.

treatment point out the significant role of the functionalization groups of the MSNs in the cellular uptake. Both fluorescence and electron microscopy demonstrate that 3T3 cells can easily internalize MSN-HA particles much more efficiently than functionalized MSN-NH_2, suggesting a specific uptake, probably via hyaluronic acid receptor mediated endocytosis. These marked differences can be explained considering that a variety of cellular mechanisms regulate the interactions of the plasma membrane with the external materials. The endocytosis is a complex process that controls not only the internalization of extracellular materials but also the expression of specific cell-surface receptors and is deeply involved in the cellular trafficking of macromolecules and particles through the cellular compartments.[53] The unique biological properties of hyaluronic acid may account for the high biocompatibility of MSN-HA with 3T3 cells. Hyaluronic acid is an ubiquitous extracellular matrix component[54] synthesized by fibroblasts, whose interaction with its specific cell surface receptor CD44 mediates a wide range of physiological roles including cell adhesion and migration.[55]

In the present work, although the cellular mechanisms involved in MSNs internalization cannot clearly be ascertained, we may point out some considerations. The cytoplasmic vesicles visualized by electron microscopy in 3T3 cells represent the cellular organelles that participate in the intracellular trafficking of MSN particles, being one of the steps of the sorting process that takes place soon after internalization. Moreover, we observed some MSNs that are not encapsulated into vesicles, suggesting that they are able to escape from the endocytic system and translocate into the cytosol.

In contrast, MSN-CHIT particles are strictly associated with the external cellular surfaces or dispersed as large aggregates in the culture medium, and only occasionally, are able to penetrate the cells. The low rate of intracellular uptake of MSN-CHIT may be ascribed to the large size of aggregates that cannot be endocyted by 3T3 cells.

However, although their inefficiency to penetrate the cellular compartment, the peculiar pattern that MSN-CHIT particles exhibit at the electron microscopic level raises interesting questions concerning their possible biological properties and function. The MSN-CHIT affinity for the external cellular surfaces clearly depends on the specific physicochemical properties of both chitosan and plasma membrane and could account for a potential role of chitosan in the modulation of the cellular adhesion to synthetic substrates. Lately, the growing interest in the development of biologically active coatings has led to significant improvements in the design of specific scaffolds for tissue engineering and new hypothesis are coming forth.[56−58] The fluorescence and TEM results highlight the morpho-functional events that characterize the interactions of artificial functionalized substrates with cell surfaces and represent a first step toward the deep understanding of the mechanisms involved in this process, but this is only the tip of the iceberg and many questions remain to be ascertained.

5. CONCLUSIONS

MSNs functionalized with amino groups (MSN-NH_2) were further functionalized at the external surface introducing a layer based on hyaluronic acid or chitosan polysaccharides, in order to obtain stimuli-responsive objects endowed with higher bioadhesion properties than non functionalized MSNs. The high level of the viability of 3T3 cells, determined through the MTS assay after a contact with the MSNs for 24 h, was confirmed by the cell growth curve obtained through Coulter counter. The whole results clearly assess the high biocompatibility of all types of functionalized MSNs, without any significant effect because of the different functionalizations. Significant differences due to type of functionalization were instead observed in the fluorescence microscopy experiments performed with the FITC-labeled MSN-NH_2, MSN-HA, and MSN-CHIT, which strikingly agree with the results of TEM experiments. Using an exposure time of 24 h and 100 μg/mL of MSNs, followed by another 24 h in contact with the culture medium only, different types of interactions between MSNs and 3T3 cells can be demonstrated: MSN-NH_2 and MSN-HA are easily internalized (at different extent), whereas MSN-CHIT tends to give large aggregates dispersed in the medium or localized at external surface of the cell membranes. Both fluorescence microscopy and TEM images give clear evidence that the MSN particles are localized in the cytoplasm in the case of NH_2 and HA functionalizations, as shown in Figure 5A−D, as well as in Figure 7A−D. In the case of CHIT functionalization, only a few particles are internalized as demonstrated in Figures 5E, F and 7E, F. These results permit us to emphasize some concluding remarks: (i) the importance of the external functionalization with HA allows for a very large cellular uptake: (ii) the external functionalization with CHIT seems to prevent a massive uptake from 3T3 cells. In principle, it may be suggested that MSN-CHIT undergoes strong interactions with the medium components that evidently screen the original (quite high) positive surface potential (see Table 1), thus resulting in a significant particle aggregation. In both cases, the formation of a serum protein corona may play a role.[44] These results, however, do not exclude the usefulness of CHIT functionalization for delivering anticancer drugs to tumor cells (the acidic pH would favor release as a result of CHIT hydrolysis) because massive adhesion to cellular membranes occurs as clearly shown in Figure 7F. In addition, the functionalization with CHIT, that is a positively charged polyelectrolyte, may decrease the retention of MSNs within the endosome which affects the efficiency of drug release, particularly in the case of sensitive therapeutic moieties such as proteins, antibodies, or DNA fragments. This was ascertained in the case of MSNs functionalized with the polyethylenimine polymer.[59]

In conclusion, the different cellular uptake observed in our in vitro experiments for MSNs functionalized with HA and CHIT suggests the need of further investigations not only with additional cell lines, but also a deeper evaluation of the interactions of MSNs with different dispersing media as well as the most suitable degree of functionalization. Indeed, our functionalized particles may be regarded as a stimuli-responsive platform to be tuned depending on the medium and type of cells with which particles are expected to interact.

■ ASSOCIATED CONTENT

Ⓢ Supporting Information

The Supporting Information is available free of charge on the ACS Publications website at DOI: 10.1021/acsbiomaterials.5b00502.

Additional characterizations (TGA, DLS) of MSNs samples and TEM images of control samples (PDF)

AUTHOR INFORMATION

Corresponding Authors

*E-mail: asalis@unica.it. Tel.: +39070675 4362/4385. Fax: +39 0706754388.

*E-mail: monduzzi@unica.it.

Notes

The authors declare no competing financial interest.

ACKNOWLEDGMENTS

MIUR, PRIN 2010-2011 Grant 2010BJ23MN-002, and Fondazione Banco di Sardegna are thanked for financial support. Prof. M. Casula is thanked for TGA measurements. Marco Sanna and Gino Paolo Asuni are thanked for experimental support.

REFERENCES

(1) Baeza, A.; Colilla, M.; Vallet-Regí, M. Advances in mesoporous silica nanoparticles for targeted stimuli-responsive drug delivery. *Expert Opin. Drug Delivery* **2015**, *12* (2), 319−337.

(2) Mamaeva, V.; Sahlgren, C.; Lindén, M. Mesoporous silica nanoparticles in medicine-recent advances. *Adv. Drug Delivery Rev.* **2013**, *65* (5), 689−702.

(3) Monduzzi, M.; Lampis, S.; Murgia, S.; Salis, A. From self-assembly fundamental knowledge to nanomedicine developments. *Adv. Colloid Interface Sci.* **2014**, *205*, 48−67.

(4) Lebeau, B.; Galarneau, A.; Linden, M. Introduction for 20 years of research on ordered mesoporous materials. *Chem. Soc. Rev.* **2013**, *42* (9), 3661−3662.

(5) Gagner, J. E.; Shrivastava, S.; Qian, X.; Dordick, J. S.; Siegel, R. W. Engineering Nanomaterials for Biomedical Applications Requires Understanding the Nano-Bio Interface: A Perspective. *J. Phys. Chem. Lett.* **2012**, *3* (21), 3149−3158.

(6) Feizi, T. Oligosaccharides in molecular recognition. *Biochem. Soc. Trans.* **1988**, *16* (6), 930−934.

(7) Wang, E.; Lew, K.; Barecki, M.; Casciano, C. N.; Clement, R. P.; Johnson, W. W. Quantitative Distinctions of Active Site Molecular Recognition by P-Glycoprotein and Cytochrome P450 3A4. *Chem. Res. Toxicol.* **2001**, *14* (12), 1596−1603.

(8) Slowing, I. I.; Vivero-Escoto, J. L.; Wu, C.-W.; Lin, V. S.-Y. Mesoporous silica nanoparticles as controlled release drug delivery and gene transfection carriers. *Adv. Drug Delivery Rev.* **2008**, *60* (11), 1278−1288.

(9) Wang, Y.; Zhao, Q.; Han, N.; Bai, L.; Li, J.; Liu, J.; Che, E.; Hu, L.; Zhang, Q.; Jiang, T.; et al. Mesoporous silica nanoparticles in drug delivery and biomedical applications. *Nanomedicine* **2015**, *11* (2), 313−327.

(10) Fu, C.; Liu, T.; Li, L.; Liu, H.; Chen, D.; Tang, F. The absorption, distribution, excretion and toxicity of mesoporous silica nanoparticles in mice following different exposure routes. *Biomaterials* **2013**, *34* (10), 2565−2575.

(11) Kresge, C. T.; Roth, W. J. The discovery of mesoporous molecular sieves from the twenty year perspective. *Chem. Soc. Rev.* **2013**, *42* (9), 3663−3670.

(12) Hoffmann, F.; Cornelius, M.; Morell, J.; Fröba, M. Silica-based mesoporous organic-inorganic hybrid materials. *Angew. Chem., Int. Ed.* **2006**, *45* (20), 3216−3251.

(13) Böcking, D.; Wiltschka, O.; Niinimäki, J.; Shokry, H.; Brenner, R.; Lindén, M.; Sahlgren, C. Mesoporous silica nanoparticle-based substrates for cell directed delivery of Notch signalling modulators to control myoblast differentiation. *Nanoscale* **2014**, *6* (3), 1490−1498.

(14) Gomez-Cerezo, N.; Izquierdo-Barba, I.; Arcos, D.; Vallet-Regi, M. Tailoring the biological response of mesoporous bioactive materials. *J. Mater. Chem. B* **2015**, *3* (18), 3810−3819.

(15) Bhattacharyya, M. S.; Hiwale, P.; Piras, M.; Medda, L.; Steri, D.; Piludu, M.; Salis, A.; Monduzzi, M. Lysozyme adsorption and release from ordered mesoporous materials. *J. Phys. Chem. C* **2010**, *114*, 19928−19934.

(16) Steri, D.; Monduzzi, M.; Salis, A. Ionic strength affects lysozyme adsorption and release from SBA-15 mesoporous silica. *Microporous Mesoporous Mater.* **2013**, *170*, 164−172.

(17) Salis, A.; Medda, L.; Cugia, F.; Monduzzi, M. Effect of electrolytes on proteins physisorption on ordered mesoporous silica materials. *Colloids Surf., B* **2016**, *137*, 77−90.

(18) Piras, M.; Salis, A.; Piludu, M.; Steri, D.; Monduzzi, M. 3D vision of human lysozyme adsorbed onto a SBA-15 nanostructured matrix. *Chem. Commun.* **2011**, *47* (26), 7338−7440.

(19) Piludu, M.; Medda, L.; Cugia, F.; Monduzzi, M.; Salis, A. Silver-Enhancement for TEM Imaging of Antibody Fragment-Gold Nanoparticles Conjugates Immobilized on Ordered Mesoporous Silica. *Langmuir* **2015**, *31* (34), 9458−9463.

(20) Medda, L.; Monduzzi, M.; Salis, A. The molecular motion of bovine serum albumin under physiological conditions is ion specific. *Chem. Commun.* **2015**, *51* (30), 6663−6666.

(21) Salis, A.; Ninham, B. W. Models and mechanisms of Hofmeister effects in electrolyte solutions, and colloid and protein systems revisited. *Chem. Soc. Rev.* **2014**, *43* (21), 7358−7377.

(22) Cugia, F.; Monduzzi, M.; Ninham, B. W.; Salis, A. Interplay of ion specificity, pH and buffers: insights from electrophoretic mobility and pH measurements of lysozyme solutions. *RSC Adv.* **2013**, *3* (17), 5882−5888.

(23) Medda, L.; Carucci, C.; Parsons, D. F.; Ninham, B. W.; Monduzzi, M.; Salis, A. Specific cation effects on hemoglobin aggregation below and at physiological salt concentration. *Langmuir* **2013**, *29* (49), 15350−15358.

(24) Hudson, S. P.; Padera, R. F.; Langer, R.; Kohane, D. S. The biocompatibility of mesoporous silicates. *Biomaterials* **2008**, *29* (30), 4045−4055.

(25) Vallet-Regí, M.; Izquierdo-Barba, I.; Rámila, A.; Pérez-Pariente, J.; Babonneau, F.; González-Calbet, J. M. Phosphorous-doped MCM-41 as bioactive material. *Solid State Sci.* **2005**, *7* (2), 233−237.

(26) Balas, F.; Manzano, M.; Colilla, M.; Vallet-Regí, M. L-Trp adsorption into silica mesoporous materials to promote bone formation. *Acta Biomater.* **2008**, *4* (3), 514−522.

(27) Vallet-Regi, M.; Ruiz-Gonzalez, L.; Izquierdo-Barba, I.; Gonzalez-Calbet, J. M. Revisiting silica based ordered mesoporous materials: medical applications. *J. Mater. Chem.* **2006**, *16* (1), 26−31.

(28) Li, L.; Tang, F.; Liu, H.; Liu, T.; Hao, N.; Chen, D.; Teng, X.; He, J. In Vivo Delivery of Silica Nanorattle Encapsulated Docetaxel for Liver Cancer Therapy with Low Toxicity and High Efficacy. *ACS Nano* **2010**, *4* (11), 6874−6882.

(29) Yu, T.; Greish, K.; McGill, L. D.; Ray, A.; Ghandehari, H. Influence of Geometry, Porosity, and Surface Characteristics of Silica Nanoparticles on Acute Toxicity: Their Vasculature Effect and Tolerance Threshold. *ACS Nano* **2012**, *6* (3), 2289−2301.

(30) Meng, H.; Xue, M.; Xia, T.; Ji, Z.; Tarn, D. Y.; Zink, J. I.; Nel, A. E. Use of Size and a Copolymer Design Feature To Improve the Biodistribution and the Enhanced Permeability and Retention Effect of Doxorubicin-Loaded Mesoporous Silica Nanoparticles in a Murine Xenograft Tumor Model. *ACS Nano* **2011**, *5* (5), 4131−4144.

(31) Salvati, A.; Pitek, A. S.; Monopoli, M. P.; Prapainop, K.; Bombelli, F. B.; Hristov, D. R.; Kelly, P. M.; Aberg, C.; Mahon, E.; Dawson, K. A. Transferrin-functionalized nanoparticles lose their targeting capabilities when a biomolecule corona adsorbs on the surface. *Nat. Nanotechnol.* **2013**, *8* (2), 137−143.

(32) Guarnieri, D.; Malvindi, M. A.; Belli, V.; Pompa, P. P.; Netti, P. Effect of silica nanoparticles with variable size and surface functionalization on human endothelial cell viability and angiogenic activity. *J. Nanopart. Res.*, 2014, *16*, 2, Article ID: 2229, DOI: 10.1007/s11051-013-2229-6.

(33) Chen, Y.; Chen, H.; Shi, J. In Vivo Bio-Safety Evaluations and Diagnostic/Therapeutic Applications of Chemically Designed Mesoporous Silica Nanoparticles. *Adv. Mater.* **2013**, *25* (23), 3144−3176.

(34) Yu, M.; Jambhrunkar, S.; Thorn, P.; Chen, J.; Gu, W.; Yu, C. Hyaluronic acid modified mesoporous silica nanoparticles for targeted drug delivery to CD44-overexpressing cancer cells. *Nanoscale* **2013**, *5* (1), 178−183.

(35) Medda, L.; Casula, M. F.; Monduzzi, M.; Salis, A. Adsorption of lysozyme on hyaluronic acid functionalized SBA-15 mesoporous silica: a possible bioadhesive depot system. *Langmuir* **2014**, *30* (43), 12996−13004.

(36) Vasi, A. M.; Popa, M. I.; Butnaru, M.; Dodi, G.; Verestiuc, L. Chemical functionalization of hyaluronic acid for drug delivery applications. *Mater. Sci. Eng., C* **2014**, *38* (1), 177−185.

(37) Knudson, W.; Peterson, R. S. The hyalorunan 388 receptor: CD44. In *Chemistry and Biology of Hyalorunan*; Garg, H. G., Hales, C. A., Eds.; Elsevier: Oxford, U.K., 2004; pp 83−124.

(38) Girish, K. S.; Kemparaju, K. The magic glue hyaluronan and its eraser hyaluronidase: a biological overview. *Life Sci.* **2007**, *80* (21), 1921−1943.

(39) Feng, W.; Nie, W.; He, C.; Zhou, X.; Chen, L.; Qiu, K.; Wang, W.; Yin, Z. Effect of pH-responsive alginate/chitosan multilayers coating on delivery efficiency, cellular uptake and biodistribution of mesoporous silica nanoparticles based nanocarriers. *ACS Appl. Mater. Interfaces* **2014**, *6* (11), 8447−8460.

(40) Hakeem, A.; Duan, R.; Zahid, F.; Dong, C.; Wang, B.; Hong, F.; Ou, X.; Jia, Y.; Lou, X.; Xia, F. Dual stimuli-responsive nano-vehicles for controlled drug delivery: mesoporous silica nanoparticles end-capped with natural chitosan. *Chem. Commun.* **2014**, *50* (87), 13268−13271.

(41) Zhao, Q.; Geng, H.; Wang, Y.; Gao, Y.; Huang, J.; Wang, Y.; Zhang, J.; Wang, S. Hyaluronic Acid Oligosaccharide Modified Redox-Responsive Mesoporous Silica Nanoparticles for Targeted Drug Delivery. *ACS Appl. Mater. Interfaces* **2014**, *6* (22), 20290−20299.

(42) Senthilkumar, R.; Karaman, D. Ş.; Paul, P.; Björk, E. M.; Odén, M.; Eriksson, J. E.; Rosenholm, J. M. Targeted delivery of a novel anticancer compound anisomelic acid using chitosan-coated porous silica nanorods for enhancing the apoptotic effect. *Biomater. Sci.* **2015**, *3* (1), 103−111.

(43) Chen, Z.; Li, Z.; Lin, Y.; Yin, M.; Ren, J.; Qu, X. Bioresponsive hyaluronic acid-capped mesoporous silica nanoparticles for targeted drug delivery. *Chem. - Eur. J.* **2013**, *19* (5), 1778−1783.

(44) Shahabi, S.; Treccani, L.; Dringen, R.; Rezwan, K. Modulation of Silica Nanoparticle Uptake into Human Osteoblast Cells by Variation of the Ratio of Amino and Sulfonate Surface Groups: Effects of Serum. *ACS Appl. Mater. Interfaces* **2015**, *7*, 13821−13833.

(45) Slowing, I.; Trewyn, B. G.; Lin, V. S.-Y. Effect of Surface Functionalization of MCM-41-Type Mesoporous Silica Nanoparticles on the Endocytosis by Human Cancer Cells. *J. Am. Chem. Soc.* **2006**, *128* (46), 14792−14793.

(46) Slowing, I. I.; Trewyn, B. G.; Lin, V. S.-Y. Mesoporous Silica Nanoparticles for Intracellular Delivery of Membrane-Impermeable Proteins. *J. Am. Chem. Soc.* **2007**, *129* (28), 8845−8849.

(47) Luft, J. H. Improvements in epoxy resin embedding methods. *J. Cell Biol.* **1961**, *9* (2), 409−414.

(48) Salis, A.; Casula, M. F.; Bhattacharyya, M. S.; Pinna, M.; Solinas, V.; Monduzzi, M. Physical and Chemical Lipase Adsorption on SBA-15: Effect of Different Interactions on Enzyme Loading and Catalytic Performance. *ChemCatChem* **2010**, *2* (3), 322−329.

(49) Harris, J. R.; Roos, C.; Djalali, R.; Rheingans, O.; Maskos, M.; Schmidt, M. Application of the negative staining technique to both aqueous and organic solvent solutions of polymer particles. *Micron* **1999**, *30* (4), 289−298.

(50) Ponomarev, A. P.; Molchanova, A. I.; Uziumov, V. L. [Effect of the contrast conditions using solutions of phosphotungstic acid on the electron microscopic image of the foot-and-mouth disease virus]. *Vopr. Virusol.* **1979**, *5*, 470−476.

(51) Silverman, L.; Glick, D. The reactivity and staining of tissue proteins with phosphotungstic acid. *J. Cell Biol.* **1969**, *40* (3), 761−767.

(52) Bancos, S.; Tsai, D.-H.; Hackley, V.; Weaver, J. L.; Tyner, K. M. Evaluation of Viability and Proliferation Profiles on Macrophages Treated with Silica Nanoparticles In Vitro via Plate-Based, Flow Cytometry, and Coulter Counter Assays. *ISRN Nanotechnol.* **2012**, *2012*, 454072.

(53) Doherty, G. J.; McMahon, H. T. Mechanisms of endocytosis. *Annu. Rev. Biochem.* **2009**, *78*, 857−902.

(54) Necas, J.; Bartosikova, L.; Brauner, P.; Kolar, J. Hyaluronic acid (hyaluronan): A review. *Vet. Med.* **2008**, *53* (8), 397−411.

(55) Jordan, A. R.; Racine, R. R.; Hennig, M. J. P.; Lokeshwar, V. B. The Role of CD44 in Disease Pathophysiology And Targeted Treatment. *Front. Immunol.*, 2015, *6*, article 182.

(56) Kornu, R.; Smith, R. L.; Maloney, W. J.; Kelly, M. A. Osteoblast adhesion to orthopaedic implant alloys: Effects of cell adhesion molecules and diamond-like carbon coating. *J. Orthop. Res.* **1996**, *14* (6), 871−877.

(57) El-Ghannam, A.; Ducheyne, P.; Shapiro, I. M. Effect of serum proteins on osteoblast adhesion to surface-modified bioactive glass and hydroxyapatite. *J. Orthop. Res.* **1999**, *17* (3), 340−345.

(58) Decuzzi, P.; Ferrari, M. Modulating cellular adhesion through nanotopography. *Biomaterials* **2010**, *31* (1), 173−179.

(59) Li, X.; Chen, Y.; Wang, M.; Ma, Y.; Xia, W.; Gu, H. A mesoporous silica nanoparticle - PEI - fusogenic peptide system for siRNA delivery in cancer therapy. *Biomaterials* **2013**, *34* (4), 1391−1401.

Supporting Information

Mesoporous Silica Nanoparticles Functionalized with Hyaluronic Acid and Chitosan Biopolymers. Effect of Functionalization on Cell Internalization

Andrea Salis[‡,*] *Maura Fanti,*[†] *Luca Medda,*[‡] *Valentina Nairi,* [‡] *Francesca Cugia,*[‡] *Marco Piludu,*[†]
Valeria Sogos, [†] *Maura Monduzzi,*[‡,*]

[‡] Department of Chemical and Geological Sciences, University of Cagliari-CSGI and CNBS, Cittadella Universitaria, S.S. 554 bivio Sestu, 09042- Monserrato (CA), Italy; [†] Department of Biomedical Sciences, University of Cagliari, Cittadella Universitaria, S.S. 554 bivio Sestu, 09042-Monserrato (CA), Italy.

Physico-chemical characterization of MSNs.

Textural analysis was carried out on a Thermoquest-Sorptomatic 1990 instrument, by determining the N_2 adsorption/desorption isotherms at 77 K. Before analysis, pure silica samples (MSNs) were heated up to 250 °C at a rate of 1°C/min under vacuum, while the functionalized samples (MSN-NH_2, MSN-HA, and MSN-CHIT) were outgassed overnight at 40°C. The specific surface area, and the pore size distribution were assessed by the Brunauer-Emmett-Teller (BET) and BJH methods, respectively.

Small-angle X-ray scattering (SAXS) was recorded with a S3-MICRO SWAXS camera system (HECUS X-ray Systems, Graz, Austria). CuKα radiation of wavelength 1.542 Å was provided by a GeniX X-ray generator, operating at 30 kV and 0.4 mA. A 1D-PSD-50 M system (HECUS X-ray Systems, Graz, Austria) containing 1024 channels of width 54.0 μm was used for detection of scattered X-rays in the small-angle region. The working q-range (Å^{-1}) was $0.003 \leq q \leq 0.6$, where $q=4\pi \sin(\theta)\lambda^{-1}$ is the modulus of the scattering wave vector. Thin-walled 2 mm glass capillaries were filled with the sample for the scattering experiments. The scattering patterns were recorded for 1h.

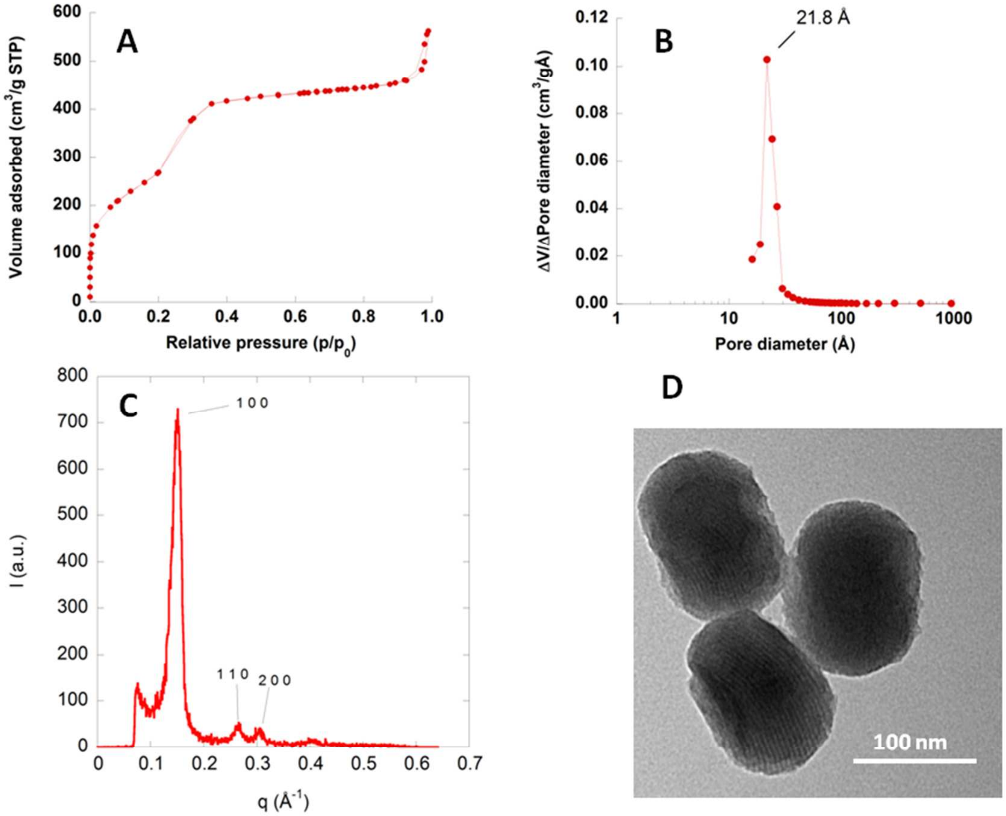

Figure S1. Textural and structural characterization of MSNs (MCM-41 nanoparticles). A) Nitrogen adsorption/desorption isotherm; B) Pore size distribution; C) SAXS pattern; D) TEM image.

The textural characterization obtained by the nitrogen adsorption–desorption isotherm of the MSNs, displayed in Figure S1A, exhibits a typical type IV isotherm and a steep capillary condensation step occurring at a relative pressure (P/P_0) of 0.3. This corresponds to a narrow pore size distribution (d_{BJH}) centered at about 22 Å (Figure S1B). The use of BJH method has been criticized because it underestimates pore size.[1] But more accurate methods (i.e. the NLDFT[1]) are still not widespread, and available only in most recent instrumental facilities. Hence we take 22 Å as a rough, but nevertheless useful, estimation of pore size distribution of our sample. The calculated surface area (S_{BET}) and pore volume are 1193 m^2/g and 0.87 cm^3/g respectively. The structural characterization was carried out by SAXS and TEM techniques. The SAXS pattern of the MSNs (Figure S1C) shows three typical well resolved diffraction peaks due to the 100, 110 and 200 planes of a highly ordered two dimensional hexagonal mesophase. SAXS analysis provides a lattice parameter $a = 48$ Å. The TEM image in Figure S1D confirms that the MSNs are nanoparticles with well-ordered mesopores and allows to estimate a particle size in the range 100–130 nm.

FTIR Characterization.

ATR-FTIR measurements were conducted with a Bruker Tensor 27 spectrophotometer equipped with a diamond-ATR accessory and a DTGS detector. A number of 256 scans at a resolution of 2 cm^{-1} were averaged from wavenumber 4000 to 400 cm^{-1}. The Opus software was used for data handling. Figure S2 compares the FTIR spectra of MSN-NH_2 with those of MSN-HA and MSN-CHIT. All samples show two characteristic bands at 1060 cm^{-1} and 800 cm^{-1} due to the Si−O stretching ($\nu_{\mathrm{Si-O}}$), and one band at 450 cm^{-1} due to the Si−O−Si bending ($\delta_{\mathrm{Si-O-Si}}$). All samples exhibit a broad O–H stretching band with two peaks centered around 3400 and 3230 cm^{-1} respectively. MSN-NH_2 sample shows a band at 2920 cm^{-1} due to the C-H stretching of the propylamino group. A very intense band for MSN-HA (2950 cm^{-1}) and two close bands for MSN-CHIT (2970 and 2880 cm^{-1}) can also be assigned. The MSN-NH_2 sample (Figure 2A) displays a band at 1520 cm^{-1}, which disappears after the functionalization with HA and CHIT (Figures 2B and 2C), that can be assigned to N−H bending ($\delta_{\mathrm{N-H}}$). In addition, the functionalization with HA is confirmed by the peaks at 1570-1470 cm^{-1} due to the stretching of the COO^- group.[2] The band around 1630-1650cm^{-1} observed for the three samples cannot clearly be assigned. Indeed, it can be either due to the bending mode of physisorbed water (MSN-NH_2) or to the C=O stretching of amide groups (MSN-HA and MSN-CHIT).[3]

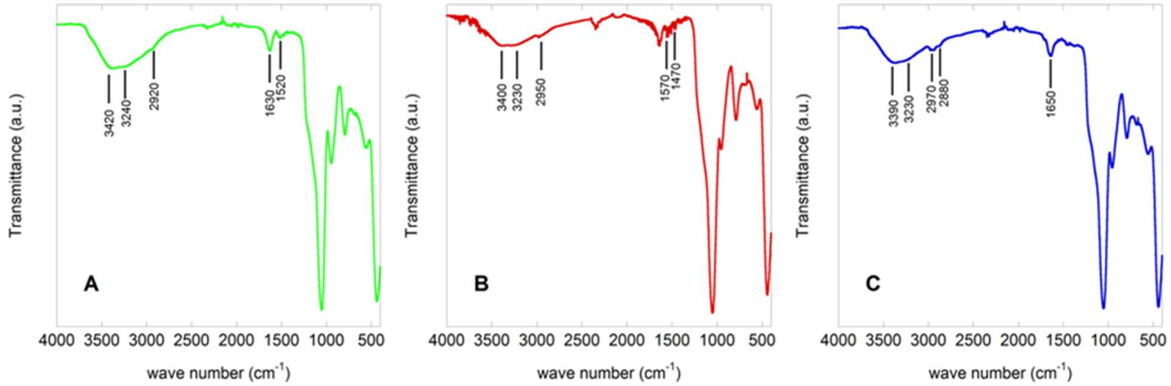

Figure S2. FTIR Spectra of A) MSN-NH_2, B) MSN-HA, and C) MSN-CHIT.

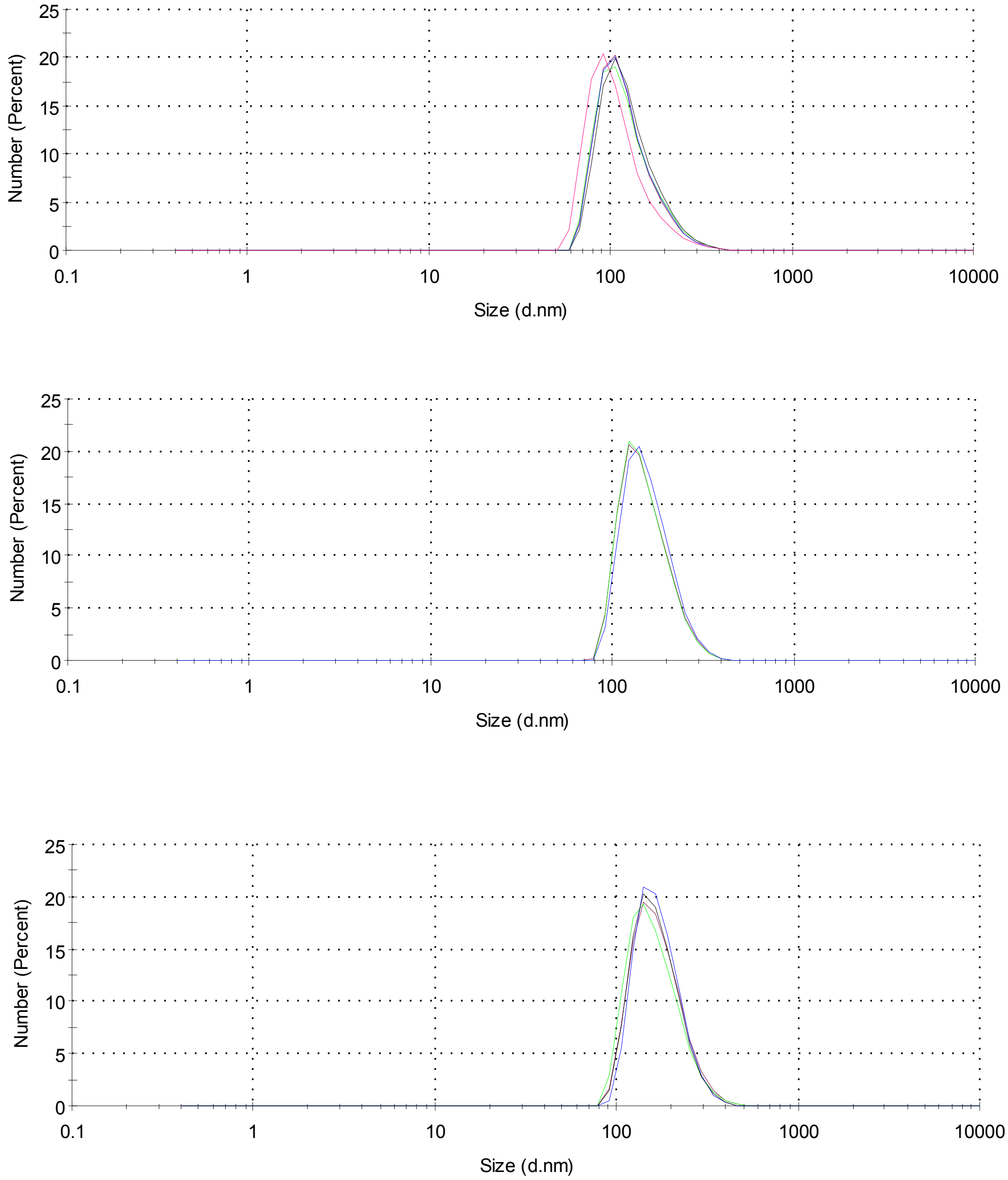

Figure S3. Particle size distribution (Number) obtained by DLS measurements for A) MSN-NH$_2$; B) MSN-HA; and C) MSN-CHIT. The different colours of the curves are associated to different DLS measurements of the same sample.

MSNs staining with phosphotungstic acid.

Appropriated dilutions of MSN-NH$_2$, MSN-HA and MSN-CHIT particles were stained with phosphotungstic acid 2% solution, placed on formavar coated 100 mesh grids. Excess of suspension was adsorbed touching the edge of the grids with filter paper. The grids were air dried and finally observed and photographed with a Jeol 100S transmission electron microscope.

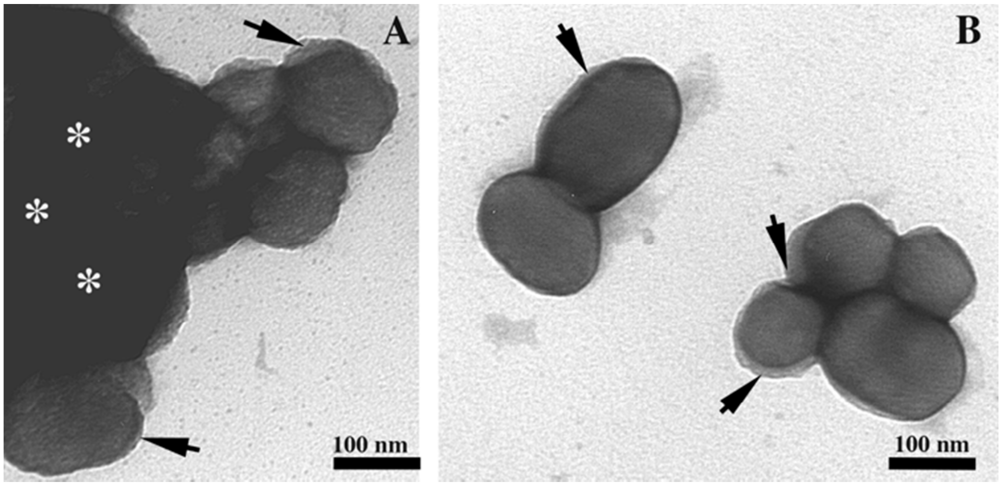

Figure S4. Transmission electron micrographs of MSN-HA (A), and MSN-CHIT (B) particles after staining with phosphotungstic acid solution. Note the presence of electron lucent halo (arrows) surrounding the MSN-HA (A), and MSN-CHIT (B) particles that could be ascribed to the functionalization with HA and CHIT respectively. The dark areas (asterisks) are probably due to the phosphotungstic acid staining process or to the electron beam passing through large aggregates of MSN-HA particles.

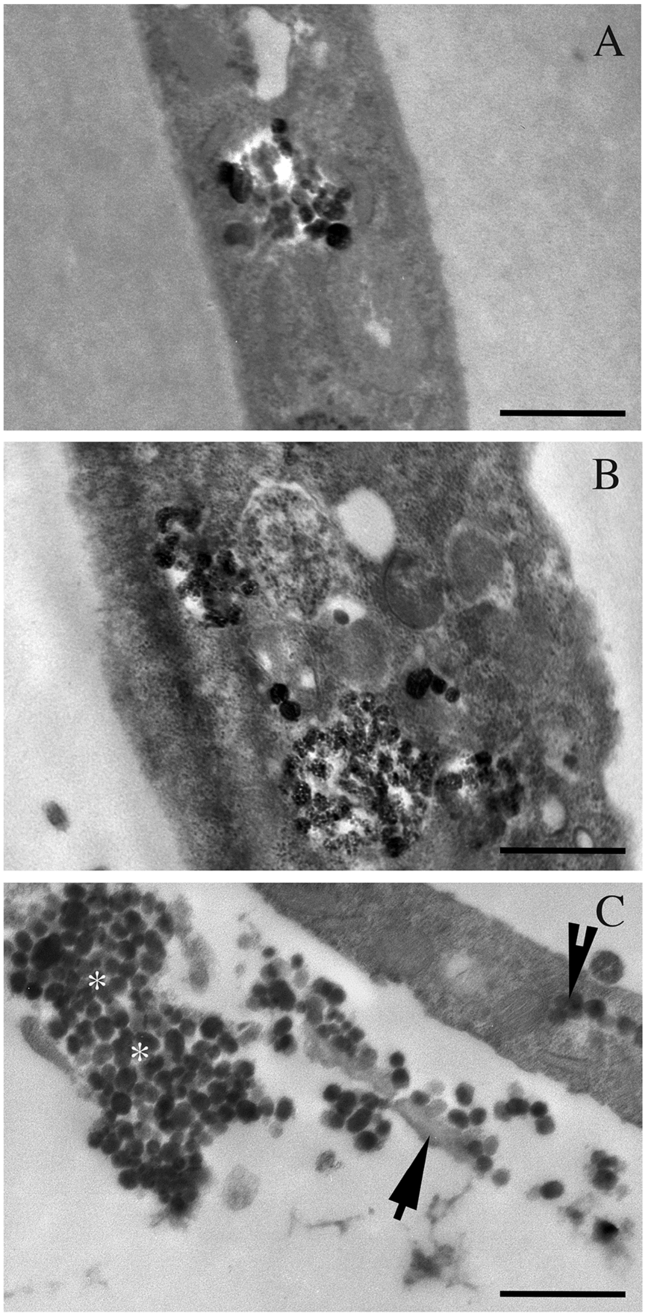

Figure S5. Electron micrographic details of mouse fibroblasts 3T3 incubated for 24 hours with 100 μg/mL of MSNs, and then left to grow for other 24 hours in the growing medium before the other treatments (see par. 2.6). Panel A: MSM-NH$_2$, Panel B: MSN-HA, Panel C: MSN-CHIT. Note that MSN-CHIT particles are associated to the external cell surfaces (arrow) or forming large aggregates in the culture medium (asterisks), whereas only few MSN-CHIT particles are internalized in the cytoplasmic compartment (arrowhead). Bars = 1μm

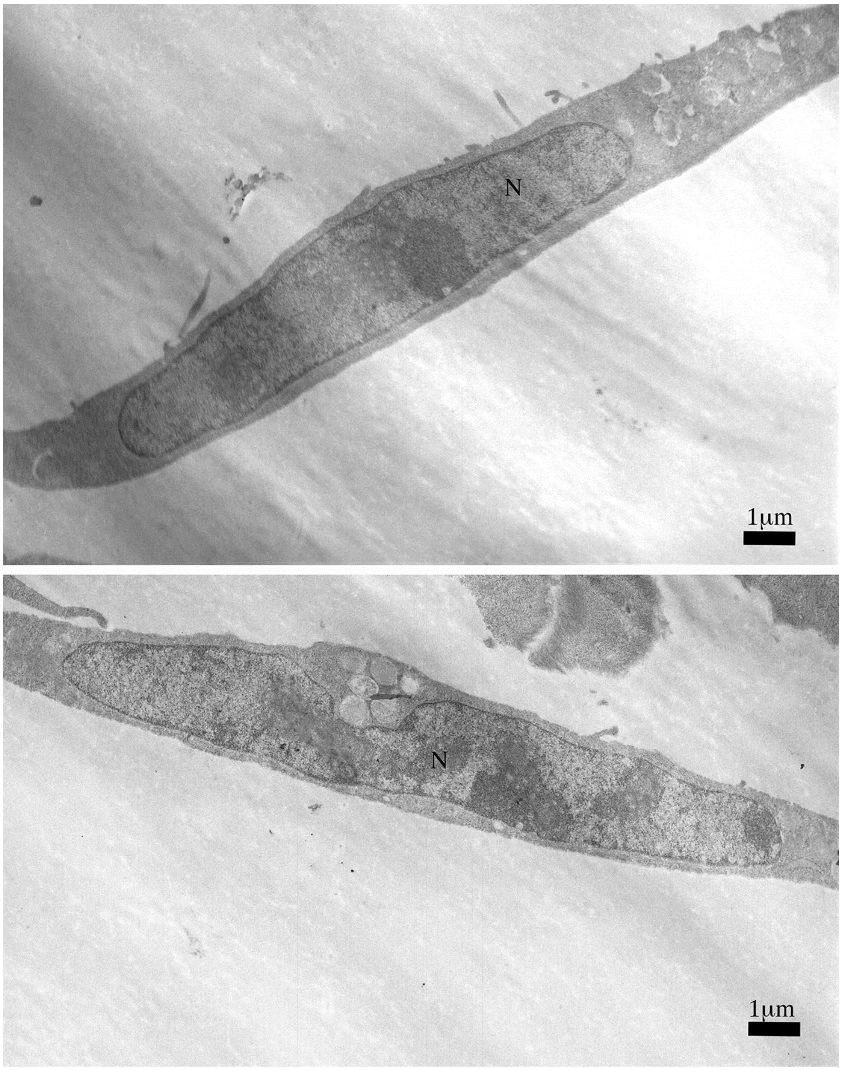

Figure S6. Electron micrographs of 3T3 cell control samples. N= nucleus

References

(1) Ravikovitch, P. I.; Wei, D.; Chueh, W. T.; Haller, G. L.; Neimark, a. V. Evaluation of pore structure parameters of MCM-41 catalyst supports and catalysts by means of nitrogen and argon adsorption. *J. Phys. Chem. B* **1997**, *101* (19), 3671–3679 DOI: 10.1021/jp9625321.

(2) Medda, L.; Casula, M. F.; Monduzzi, M.; Salis, A. Adsorption of lysozyme on hyaluronic acid functionalized SBA-15 mesoporous silica: a possible bioadhesive depot system. *Langmuir* **2014**, *30* (43), 12996–13004 DOI: 10.1021/la503224n.

(3) Hakeem, A.; Duan, R.; Zahid, F.; Dong, C.; Wang, B.; Hong, F.; Ou, X.; Jia, Y.; Lou, X.; Xia, F. Dual stimuli-responsive nano-vehicles for controlled drug delivery: mesoporous silica nanoparticles end-capped with natural chitosan. *Chem. Commun.* **2014**, *50* (87), 13268–13271 DOI: 10.1039/c4cc04383a.

Paper IV

Reprinted with permission from:

Interaction between bovine serum albumin and mesoporous silica nanoparticles functionalized with biopolymers.

Valentina Nairi, Sara Medda, Marco Piludu, Maria Francesca Casula, Maria Vallet-Regì, Maura Monduzzi, and Andrea Salis. *Chem. Eng. J.* (2018) In press

DOI: 10.1016/j.cej.2018.01.011.

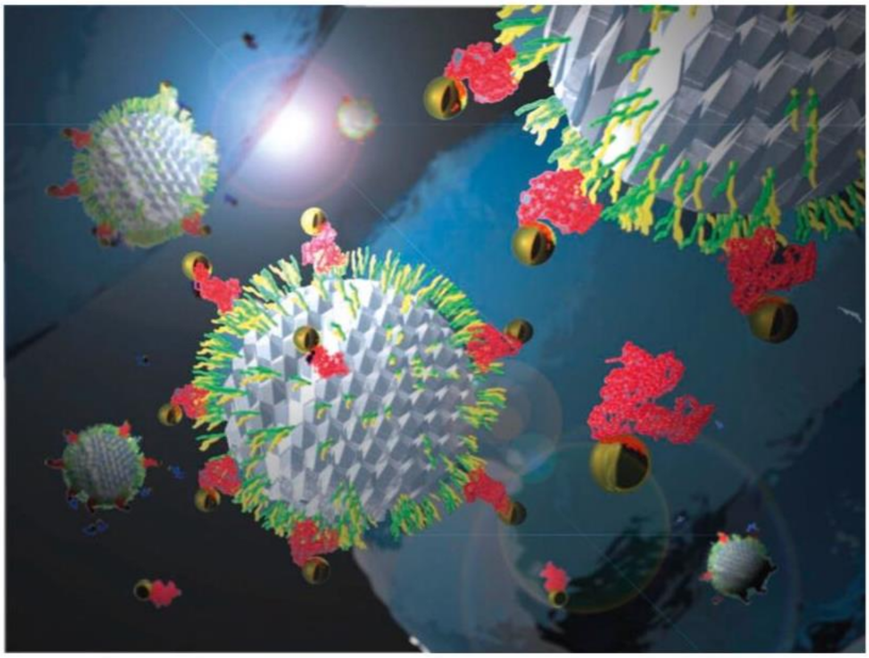

Chemical Engineering Journal xxx (xxxx) xxx–xxx

Contents lists available at ScienceDirect

Chemical Engineering Journal

journal homepage: www.elsevier.com/locate/cej

Interactions between bovine serum albumin and mesoporous silica nanoparticles functionalized with biopolymers

Valentina Nairi[a], Sara Medda[a], Marco Piludu[b], Maria Francesca Casula[a], Maria Vallet-Regì[c,*], Maura Monduzzi[a,*], Andrea Salis[a,*]

[a] *Dipartimento di Scienze Chimiche e Geologiche, Università di Cagliari-CSGI and CNBS, Cittadella Universitaria, S.S. 554 bivio Sestu, 09042 Monserrato, Cagliari, Italy*
[b] *Dipartimento di Scienze Biomediche, Università di Cagliari, Cittadella Universitaria, S.S. 554 bivio Sestu, 09042 Monserrato, Cagliari, Italy*
[c] *Departamento de Quimica Inorganica y Bioinorganica, Facultad de Farmacia, Universidad Complutense de Madrid, Plaza Ramon y Cajal s/n, Instituto de Investigacion Sanitaria Hospital 12 de Octubre i+12 ¡ Centro de Investigacion Biomedica en Red de Bioingenieria, Biomateriales y Nanomedicina (CIBER-BBN), Madrid, Spain*

HIGHLIGHTS

- Mesoporous silica nanoparticles (MSNs) were functionalized with two biopolymers.
- The surface charge of functionalized MSNs modulates the interactions with BSA.
- van der Waals forces play an important role in the overall MSNs-BSA interactions.
- BSA-gold NP conjugates were used to visualize the formation of a protein corona.

GRAPHICAL ABSTRACT

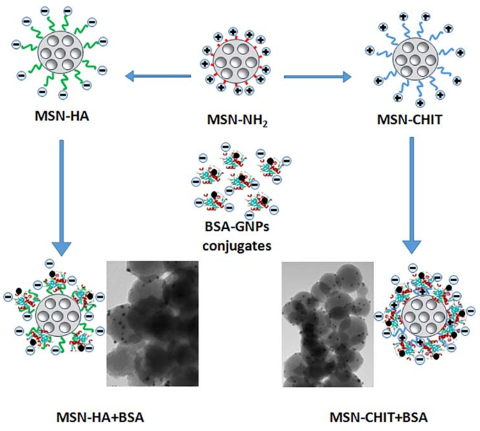

ARTICLE INFO

Keywords:
Mesoporous silica nanoparticles
Hyaluronic acid
Chitosan
Bovine serum albumin
Protein corona
Gold nano particles

ABSTRACT

Biomedical application of nanoparticles is largely associated to their fate in biological media which, in turn, is related to their surface properties. Surface functionalization plays a key role in determining biodegradation, cytotoxicity and biodistribution through interactions which may be mediated by the macromolecules occurring in biological media. A typical example is given by several proteins which lead to the formation of coated nanoparticles referred as protein corona. In this work we focus on mesoporous silica nanoparticles which, due to their intrinsic textural features, show potential as carriers for sustained drug release. Mesoporous silica nanoparticles functionalized by different biopolymers such as hyaluronic acid and chitosan were synthesized and characterized through small angle X-rays scattering, thermal analysis, and infrared spectroscopy. Biopolymer-coated mesoporous silica nanoparticles were used to investigate the interaction with bovine serum albumin, and to point out the role of different biopolymer coating. Gold-conjugated-bovine serum albumin was used to gain evidence on the occurrence of surface bound proteins enabling direct observation by transmission electron

---

* Corresponding authors.
E-mail address: asalis@unica.it (A. Salis).

https://doi.org/10.1016/j.cej.2018.01.011

Please cite this article as: Nairi, V., Chemical Engineering Journal (2018), https://doi.org/10.1016/j.cej.2018.01.011

microscopy. Our findings provide insights on how different biopolymers affect the formation of a protein corona around functionalized mesoporous silica nanoparticles.

1. Introduction

Cancer is treated with chemotherapeutic drugs which are able to restrain tumor's growth but are also toxic for healthy cells, thus resulting in adverse side effects [1,2]. The use of smart pharmaceutical formulations, which release the drug at the target diseased tissue only, would permit to reduce undesired side effects of the chemotherapeutics [3–6]. In this context, researchers are focusing on nanomaterials as smart carriers for targeted drug delivery and stimuli-responsive systems, useful for the treatment of cancer [7–13].

Ordered mesoporous silicates, synthesized for the first time in the early 1990s [14], are nanostructured materials with a big potential in nanomedicine applications [15–20]. Among them mesoporous silica nanoparticles (MSNs) are likely the best drug carrier candidates for the realization of innovative pharmaceutical formulations [11,21–24], as a result of their characteristic textural and structural features. Indeed, their high surface area (up to 1400 m^2/g), the narrow distribution of pore size (1–2 Å), and the high pore volume (1–3 cm^3/g), allow to load high amounts of drugs which can then be released with a sustained rate [24–26]. Moreover, the external surface of MSNs can easily be functionalized with target biomolecules, i.e. proteins/antibodies [27–29], peptides [30,31] or saccharides [32–34], that can be recognized by receptors overexpressed by tumor cells [35–37]. Alternatively, these macromolecules can modify their conformation, as a response to a change of environmental conditions (i.e. pH), thus acting as a stimuli-responsive system [38,39]. In general, the external functionalization affects MSNs biocompatibility, biodistribution, pharmacokinetics, particle stability, circulation time, tumor accumulation, cellular uptake, and therapeutic efficacy [32,40,41]. Relevant examples of biopolymers for the external functionalization of MSNs surface are offered by hyaluronic acid (HA) and chitosan (CHIT). The first was used by Zhan et al. to obtain a MSNs-based target system. Indeed, tumor cells overexpress CD-44 receptors which recognize HA chains promoting HA-functionalized MSNs' endocytosis, and thus drug internalization in the tumor tissue [1]. CHIT biopolymer, due to its capacity to change conformation depending on pH, was used to realize a pH-responsive system that allows for drug release at the acidic pH of tumor cells [42].

When dispersed in a biological medium, nanoparticles (NPs) seek to lower their surface energy by adsorbing biomolecules such as proteins, peptides, or glycolipids. This surface layer of biomolecules, known as the "protein corona" (PC), is due to the physico-chemical interactions established between the NPs and the biomolecules occurring in the biological fluid [43,44]. The nature of the PC depends on several NPs features [45], such as, their chemical composition [46], size [47], shape [48], surface charge [49–51], and hydrophilic/hydrophobic character [49]. PC also depends on the composition of the biological medium, and on proteins concentration in blood plasma, temperature, administration route as well as composition of the cell membrane [43,51]. Overall, the formation of the PC on NPs surface modifies their physico-chemical properties [11] that is, surface charge and hydrophilic/hydrophobic character, thus affecting the fate of NPs in terms of cellular uptake, [52] and cytotoxicity [53]. Two types of protein corona can occur, the "*hard corona*" (HC), characterized by strong interactions between NPs and proteins, and the "*soft corona*" (SC) consisting of weakly bound proteins [44,52,54]. The formation of either HC or SC depends on medium composition including protein concentration, but also on the NPs external charge, and the affinity of proteins for the NPs surface [51]. Proteins like serum albumins, and immunoglobulins have high concentrations in the blood, therefore they are initially present in the SC of NPs, but they can be replaced, at later time, by other proteins which occur with lower concentrations but show higher affinities toward NPs [55]. These changes of composition in the PC are known as the "Vroman effect" [55,56]. An important factor for the formation of the protein corona is the surface charge of NPs. As demonstrated by Shahabi et al. positive MSNs, functionalized with amine or polyethylene imine, promote the interaction with BSA. On the contrary neutral or negative MSNs, modified with polyethylene glycol or sulfonate, contrast the adsorption of BSA due to the establishment of unfavorable interactions [57]. Recently, we investigated the different behavior of MSNs functionalized with HA or CHIT (MSN-HA and MSN-CHIT respectively) toward cell internalization [32]. In vitro studies showed that the MSN-HA were easily internalized by 3T3 mouse fibroblast cells whereas MSN-CHIT gave rise to large aggregates in the cell medium which prevented an effective cell internalization. A possible reason of this behavior is that the components of the cell medium are adsorbed at a different extent on the functionalized MSNs due to their opposite surface charge. That is negative and positive for MSN-HA and MSN-CHIT respectively. Albumins are negatively charged at pH 7 (IEP ~ 4.7) and are abundant in the cell medium. We hypothesized therefore that albumins would adsorb more effectively on MSN-CHIT than on MSN-HA when forming a PC. This would reduce MSN-CHIT colloidal stability by promoting aggregation [32].

Here the interactions between bovine serum albumin (BSA) with MSN-HA and MSN-CHIT samples are investigated. The aim of the work is to study a model system which may provide new insights on the formation of a PC around MSNs functionalized with oppositely charged biopolymers (HA *vs* CHIT). To this purpose the adsorption of BSA on differently functionalized MSNs ($MSN\text{-}NH_2$, MSN-HA and MSN-CHIT) was investigated through FTIR, zeta potential, and thermogravimetric analysis. Finally, gold nanoparticles conjugated to bovine serum albumin (BSA-GNPs) were used to visualize the bound proteins on MSNs surface by mean of transmission electron microscopy (Scheme 1).

2. Materials and methods

2.1. Chemicals

Tetraethoxysilane (TEOS, 98%), hexadecyltrimethylammonium

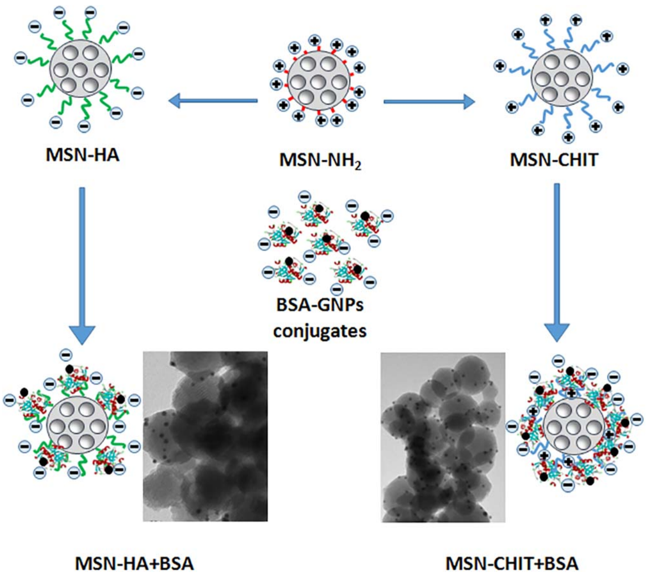

Scheme 1. Direct visualization of BSA-GNP conjugates on the surface of biopolymer-modified MSNs (MSN-HA and MSN-CHIT).

bromide (CTAB, > 99%), anhydrous toluene (99.8%), 3-aminopropyltriethoxysilane (APTES, > 98%), triethylamine (> 99%), chitosan (cod. 740,063, MW = 60–120 kDa), NaH_2PO_4 (99%), Na_2HPO_4 (99%), hydrochloride acid (37%), and glutaraldehyde (50% aqueous solution) were purchased from Sigma-Aldrich (Milan, Italy). *N*-hydroxysuccinimide (NHS, > 97%), and *N*-(3-dimethylaminopropyl)-*N′*-ethylcarbodiimide hydrochloride (EDC, > 98%) were purchased from Fluka. Sodium hyaluronate (MW = 90–130 kDa) was purchased from Contipro Biotech a.s. (Czech Republic). Bovine serum albumin conjugated with gold nanoparticles (BSA-GNPs) was purchased from British BioCell International.

2.2. Synthesis and functionalization of MSNs with HA and CHIT biopolymers

MSNs were synthesized by a silica precursor (TEOS) and an organic surfactant (CTAB) as reported in ref.s [25,32]. After surfactant removal MSNs were functionalized with APTES (0.5 mL for 1 g of MSNs) with a post-synthesis functionalization [25,32]. The resulting MSN-NH_2 sample was collected by filtration, washed with toluene and acetone, and dried overnight at room temperature under vacuum. HA-grafted MSNs (MSN-HA) were synthesized as described in ref. [32]. Briefly, an aqueous solution of NHS (0.186 g), EDC (0.113 g) and HA (0.060 g) was added to a dispersion of 0.5 g of MSN-NH_2 in water. The pH was adjusted to 9.0 by adding triethylamine and the mixture was stirred at 38 °C overnight. The obtained white powder was centrifuged, washed with water, and dried under vacuum at room temperature overnight. CHIT-grafting was carried out as reported in ref. [32], by adding to a dispersion of 0.5 g of MSN-NH_2 at pH = 7.5 1 mL of aqueous glutaraldehyde (50%). Then, the obtained red powder was dispersed in an aqueous solution containing chitosan (0.055 g) and HCl 0.1 M to promote the solubilization of the biopolymer. The obtained MSN-CHIT was collected by centrifugation, washed with a basic buffer solution (pH = 8), and dried overnight under vacuum at room temperature.

2.3. Adsorption of bovine serum albumin (BSA)

2.3.1. Adsorption of BSA on MSNs

A mass of 25 mg of MSNs previously functionalized (MSN-NH_2, MSN-HA or MSN-CHIT) was suspended in 5 mL of a 20 mg/mL solution of BSA in 10 mM phosphate buffer saline (PBS) solution (pH = 7.4 and 0.15 M NaCl) for 24 h at 25 °C. The powder was centrifuged, washed with PBS for three times and dried under vacuum at room temperature overnight. These BSA-loaded materials (MSN-NH_2, MSN-HA and MSN-CHIT + BSA) were submitted to FTIR, TGA and light scattering characterization.

2.3.2. Adsorption of BSA-GNPs on MSNs

A mass of 5 mg of MSNs previously functionalized (MSN-NH_2, MSN-HA or MSN-CHIT) was suspended in 100 µL of BSA-GNPs and 100 µL of 10 mM PBS solution (pH = 7.4 and 0.15 M NaCl) and left under agitation for 2 h at 25 °C. After supernatant removal the powder was suspended in 100 µL of fresh PBS and 50 µL of glutaraldehyde 50% w/w for fixing the protein to MSNs. The suspension was gently stirred for another hour at 25 °C. The obtained red powder was centrifuged, washed with PBS and dried overnight under vacuum at room temperature [58]. BSA-GNPs loaded samples were then used for TEM analysis.

2.4. Characterization of functionalized MSNs

The textural characterization was carried out on an ASAP 2020 instrument, by determining the N_2 adsorption/desorption isotherm at 77 K. Before analysis MSN-NH_2 samples was heated at 110 °C at a rate of 1 °C/min under vacuum for 24 h, whereas polymer-functionalized sample (MSN-HA and MSN-CHIT) were outgassed under the same conditions while heating at 40 °C for 60 h. The hexagonal structure was determined by small-angle X-rays scattering (SAXS) analysis. Patterns were recorded for 1 h with a S3-MICRO SWAXS camera system (HECUS X-ray Systems, Graz, Austria). CuKα radiation of wavelength 1.542 Å was provided by a Genix X-ray generator, operating at 30 kV and

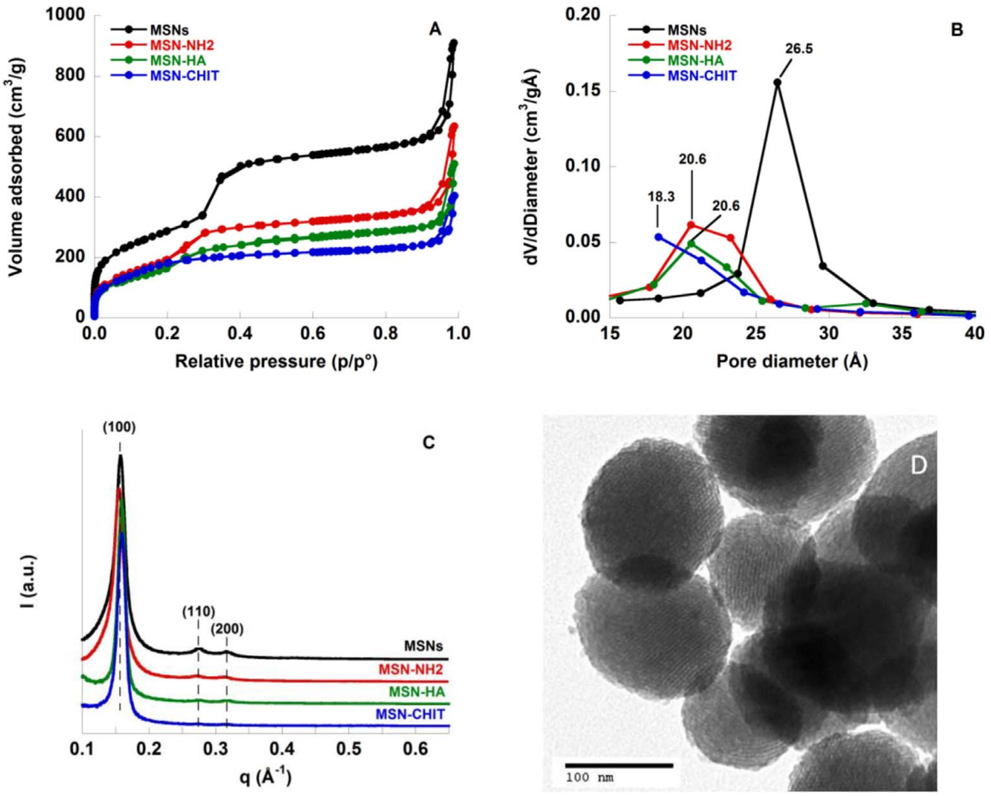

Fig. 1. Characterization of MSNs (black), MSN-NH_2 (red), MSN-HA (green), and MSN-CHIT (blue) samples: (A) adsorption/desorption N_2 isotherms; (B) pore size distribution; (C) SAXS patterns. (D) TEM micrograph of MSN-NH_2 sample.

0.4 mA.

Transmission electron microscopy (TEM) analysis was carried out placing appropriate amounts of finely ground powder samples onto carbon-coated copper grids that were observed and photographed by a Hitachi H-7000 microscope equipped with a thermionic gun operating at 100 kV. Digital images were acquired by an AMT DVC CCD camera.

Thermogravimetric analysis (TGA) was carried out on a Mettler-Toledo TGA/STDA 851. Thermal analysis data were collected in the 25–1000 °C range, under oxygen flow (heating rate = 10 °C·min^{-1}; flow rate = 50 mL·min^{-1}) using argon as the carrier.

The hydrodynamic diameter and the zeta potential of MSNs were measured using a Zetasizer nano ZSP (Malvern Instruments) in back-scatter configuration (θ = 173°) at laser wavelength of λ = 633 nm. The scattering cell temperature was fixed at 37 °C and the data were analysed with the Zetasizer software 7.03 version. For both zeta potential and hydrodynamic diameter measurements the samples were prepared by suspending MSNs (1 mg/mL) in filtered (0.2 μm polypropylene filter, Whatman) millipore water. Before measurements the samples were left under agitation overnight and sonicated for 30 min.

The surface functionalization was confirmed through Fourier transform infrared (FTIR) studies conducted with a Bruker Tensor 27 spectrophotometer equipped with a diamond-ATR accessory and a DTGS detector. A number of 256 scans at a resolution of 2 cm^{-1} were averaged in the spectral range 4000 cm^{-1}–400 cm^{-1}.

3. Results and discussion

3.1. Characterization of MSNs

The synthesized MSNs were initially functionalized with APTES to obtain MSN-NH_2, and then with hyaluronic acid (HA) and chitosan (CHIT) biopolymers obtaining MSN-HA and MSN-CHIT samples. The samples were then characterized through different physico-chemical techniques. Fig. 1A shows nitrogen adsorption/desorption isotherms. All samples exhibit a typical type IV isotherm with a small hysteresis cycle at $p/p^\circ > 0.9$ due to the capillary condensation of nitrogen into the mesopores. Table 1 reports the textural parameters: the surface area was calculated through the BET method (S_{BET}) [25,59], whereas the pore size distributions were obtained by the BJH method [25,60]. The hysteresis of the functionalized samples lies at lower adsorbed nitrogen volumes than the original MSNs, due to a decrease of pore volume induced by the functionalization. This is paralleled by the decrease of the pore size as shown in Fig. 1B. SAXS patterns (Fig. 1C) show for all samples an intense peak, due to the reflection of (1 0 0) plane, and two weak peaks due to the reflection of (1 1 0) and (2 0 0) planes respectively. These patterns are associated to materials with a hexagonal array of pores. The lattice parameters, *a*, shown in Table 1, confirm that both the amino- and the polymer-functionalization do not alter the ordered structure of the MSNs. TEM micrograph for MSN-NH_2 (Fig. 1D) shows almost spherical nanoparticles with size in the range 80–130 nm, and confirms the occurrence of an ordered hexagonal array of pores. The hydrodynamic diameter (d_H) of MSNs samples dispersed in distilled water at 37 °C was measured through dynamic light scattering (DLS). The d_H values obtained for the different MSN samples, reported in Table 1, are in agreement with TEM data.

FTIR spectra (Fig. 2) show the characteristic peaks of silica materials for all samples. That is, two intense peaks at 1070 cm^{-1} and 795 cm^{-1} attributed to the asymmetric and symmetric stretching vibration of Si-O-Si, respectively. Other two peaks at 965 cm^{-1} and 450 cm^{-1} are related to Si-OH bending and to the deformation modes of the O-Si-O, respectively. MSN-NH_2 spectrum shows an additional peak at 1547 cm^{-1} due to the asymmetric –NH_2 bending, which confirms the amino-functionalization. MSN-HA sample displays a peak at 1636 cm^{-1} assigned to C=O stretching [40,61]. Finally, MSN-CHIT spectrum shows two peaks at 1649 cm^{-1} and 1556 cm^{-1} due to C=N stretching and the asymmetric bending of amino groups in the biopolymer chain [61].

Thermogravimetric analysis (TGA) was then carried out. Fig. 3 shows the graphs of mass loss (Δm %) as a function of temperature for the original and the functionalized MSN samples. At temperatures below 200 °C the mass loss can be ascribed to the removal of humidity and to the condensation of surface silanols. Above 200 °C, Δm values can be directly related to the extent of surface functionalization.

The mass loss values are reported in Table 2. Remarkably, the similar Δm % values obtained for MSN-HA and MSN-CHIT samples suggest that a similar degree of biopolymer functionalization was achieved. Electrophoretic light scattering measurements in distilled water result in a different surface potential depending on surface functionalization. Zeta potential (ζ) values are strongly negative for pure silica (−20.0 mV) and become positive after amino-functionalization (+30.6 mV). Likewise, ζ values for MSN-HA and MSN-CHIT are negative and positive, due to the occurrence of dissociated carboxylic groups of hyaluronic acid and protonated amino groups of chitosan chains, respectively. An additional evidence of surface functionalization is provided by the increase of hydrodynamic diameter (d_H) for the functionalized MSNs, as reported in Table 1.

3.2. Adsorption of BSA on biopolymer-modified MSNs

The biopolymer-functionalized materials were then suspended in a 20 mg/mL BSA solution in PBS (pH 7.4, NaCl 150 mM) to simulate the formation of the protein corona in physiological systems [57,62]. In order to evaluate the extent of BSA adsorption on the surface of the biopolymer-functionalized materials, MSN-NH_2 + BSA, MSN-HA + BSA and MSN-CHIT + BSA samples were characterized through FTIR, TGA and electrophoretic light scattering (ELS) measurements. Fig. 4 shows FTIR spectra of pure BSA and BSA-loaded MSNs (MSN-HA + BSA and MSN-CHIT + BSA). The FTIR spectrum of BSA protein displays two characteristic bands at 1642 cm^{-1} and 1522 cm^{-1} named amide I (C=O stretching) and amide II (C-N stretching and N-H bending), respectively [63–65]. The occurrence of these two characteristic bands proves the successful adsorption of a protein on a solid support [19,66,67]. In Fig. 4 we observe two bands at 1651 cm^{-1} and 1547 cm^{-1} in the pure-BSA sample. In the FTIR spectra of MSN-BSA samples, it is difficult to assign univocally those bands to amide I and amide II due to the occurrence of vibrations of the functional groups of HA and CHIT biopolymers grafted on MSNs in the same spectral region (compare Figs. 2 and 4). It is likely that for MSN-HA + BSA and MSN-CHIT + BSA samples those bands are overlapped, preventing therefore unambiguous peak assignment.

However, BSA adsorption on biopolymer-functionalized MSNs can be assessed by TGA measurements shown in Fig. 5A-C. For all samples an increase of Δm (%) after BSA adsorption is observed (Table 2). These values are higher for biopolymer-functionalized materials, MSN-HA (26.3%) and MSN-CHIT (29.7%) than for the amino-functionalized MSN-NH_2 (18.1%). The corresponding values of BSA loading (L_{BSA}),

Table 1
Surface area (S_{BET}), pore diameter (d_{BJH}), pore volume (V_p), and lattice parameter (*a*) and hydrodynamic diameter (d_H) in distilled water at 37 °C of MSNs.

Sample	$^a S_{BET}$ (m^2/g)	$^b d_{Des,BJH}$ (Å)	$^c V_{pDes,BJH}$ (cm^3/g)	$^d a$ (Å)	$^e d_H$ (nm)
MSN	1061	26.5	1.41	45.4	140 ± 12
MSN-NH_2	894	20.6	0.98	45.9	160 ± 6
MSN-HA	735	20.6	0.79	45.4	168 ± 11
MSN-CHIT	623	18.3	0.63	45.4	186 ± 7

[a] Surface area calculated by the BET method.
[b] Pore diameter from desorption branch calculated by BJH method.
[c] Pore volume calculated at $p/p^\circ = 0.99$.
[d] Lattice parameter obtained by SAXS.
[e] Hydrodynamic diameter obtained by DLS.

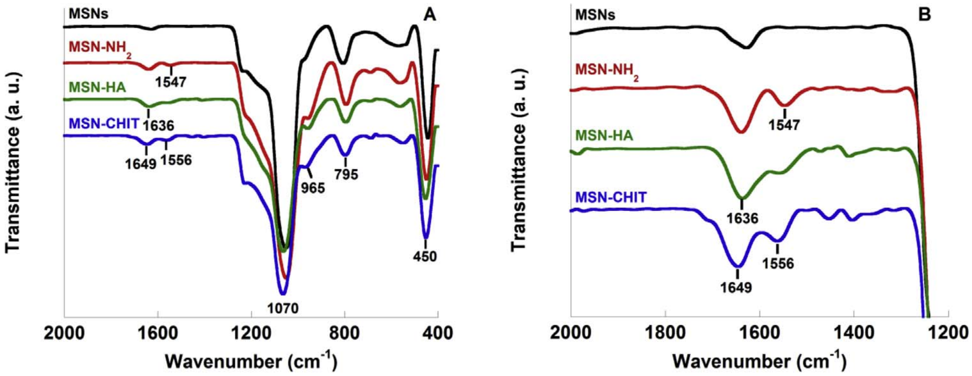

Fig. 2. FTIR spectra of original and functionalized MSN samples.

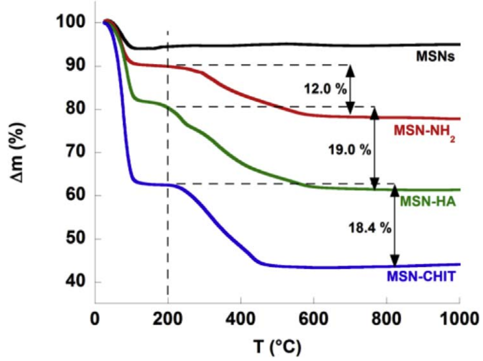

Fig. 3. Thermogravimentric analysis (TGA) of MSNs, MSN-NH$_2$, MSN-HA and MSN-CHIT samples.

Table 2
Characterization of biopolymer-functionalized MSNs and BSA-loaded MSNs. Percentage mass loss (Δm) below and above 200 °C. Zeta potential (ζ) and hydrodynamic diameter (d_H) in distilled water at 37 °C. Loading of BSA (L_{BSA}).

Sample	Δm (%)		ζ (mV)	L_{BSA} (mg/g)
	< 200 °C	> 200 °C		
MSN	7.6	4.0	−20.0 ± 0.2	–
MSN-NH$_2$	10.2	12.0	+30.6 ± 0.5	–
MSN-HA	19.6	19.0	−14.8 ± 0.9	–
MSN-CHIT	37.6	18.4	+10.1 ± 0.3	–
MSN-NH$_2$ + BSA	11.4	18.1	+9.3 ± 0.3	65
MSN-HA + BSA	15.2	26.3	−18.5 ± 0.4	79
MSN-CHIT + BSA	11.9	29.7	−7.7 ± 0.6	127

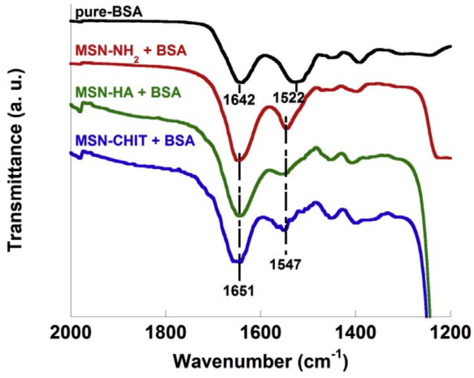

Fig. 4. FTIR spectra of functionalized MSNs loaded with BSA.

calculated from Δm (%) values, are L_{BSA} = 65 mg/g, 79 mg/g, and 127 mg/g for MSN-NH$_2$, MSN-HA and MSN-CHIT, respectively. These results confirm that BSA protein is effectively adsorbed on MSNs surface and that, under our experimental conditions (pH 7.4, ionic strength 0.15 M, T = 37 °C), the type of functionalization modulates the amount of adsorbed BSA. Indeed, the amount of BSA loading is in the order MSN-CHIT > MSN-HA > MSN-NH$_2$.

These trends can be interpreted by taking into account the different electrical charge carried by the biopolymers and the protein. Indeed under our adsorption conditions (PBS pH = 7.4 and 0.15 M NaCl) MSN-HA sample is negatively charged due the dissociation of carboxylic groups occurring in the HA chains. On the contrary, amino groups of CHIT biopolymer are protonated, and thus positively charged. Furthermore, in the same physiological conditions, BSA has a net negative charge since its isoelectric point (IEP) is about 4.7 [68,69]. Assuming that only the electrostatic interaction is operating, we would expect a high BSA loading for MSN-CHIT and a negligible or low BSA loading for MSN-HA. BSA loading indeed decreases in the order MSN-CHIT > MSN-HA > MSN-NH$_2$. The non-negligible BSA loading recorded on MSN-HA, however, suggests that electrostatics is likely not the only interaction at work. Once BSA has been adsorbed on the MSNs surface, it changes the physico-chemical features of the NPs [11], as demonstrated by electrophoretic light scattering results reported in Table 2. Indeed, ζ-potential values for all samples are strongly affected by the presence of adsorbed BSA molecules. In particular, we observe a decrease of ζ values for MSN-NH$_2$ – from +30.6 to +9.3 mV – and a charge reversal for MSN-CHIT from +10.1 mV to −7.7 mV. This can be explained by a strong interaction between the negatively charged BSA and the positively charged particles, in our adsorption conditions. In the case of MSN-HA we observed a slightly more negative value of ζ from −14.8 mV to −18.5 mV. Such a change of ζ value is consistent with the adsorption of negatively charged BSA molecules on the negatively charged MSN-HA particles, as already confirmed by TGA data. Although the attraction of two species with like charges might sound counterintuitive, it should be recalled that BSA adsorption might take place on positively charged patches occurring also above its IEP [70]. Moreover, we should also consider that under physiological conditions electrostatics is screened. It is easy to calculate that at a 100 mM NaCl concentration the Debye length is about 1 nm. This means that a surface potential of 100 mV is reduced by charge screening to about 5–10 mV within the diffuse layer. Hence, above 100 mM salt concentration the intensity of the electrostatic force is comparable to that of non-electrostatic van der Waals interactions [71]. Therefore, due to electrolyte-induced surface potential screening, the ubiquitous attractive van der Waals forces between uncharged BSA and hyaluronic patches are likely responsible of the BSA loading of 79 mg/g. The fact that besides electrostatics also other interactions are operating is demonstrated by the lower BSA loading (65 mg/g) reached by the positively charged MSN-NH$_2$ (Scheme 2).

What obtained here seems to confirm the findings observed in a previous work where the internalization of functionalized MSNs on 3 T3 mouse fibroblast cells was investigated [32]. Indeed, in the protein-rich cell culture medium MSN-NH$_2$ and MSN-HA particles were easily

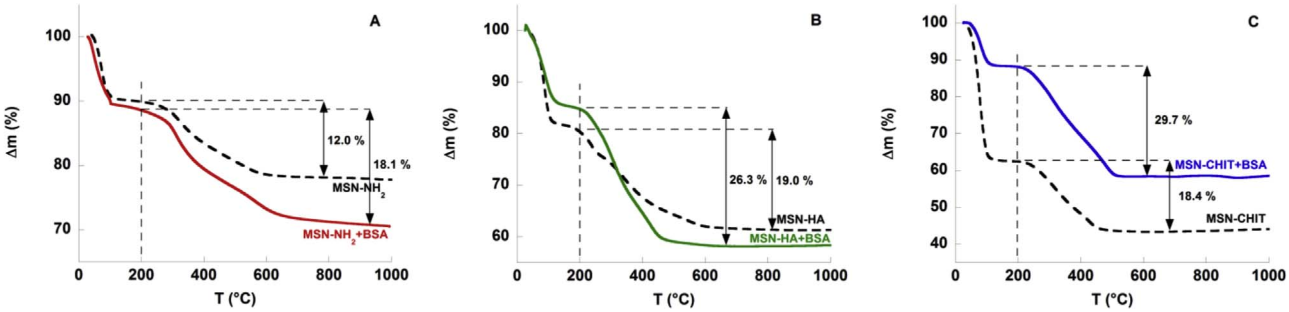

Fig. 5. Percentage mass loss profiles as a function of temperature for MSN-NH$_2$ (A), MSN-HA (B) and MSN-CHIT (C) and the corresponding BSA-loaded samples as determined by TGA.

internalized whereas MSN-CHIT resulted in the formation of large aggregates which could not be internalized by 3 T3 cells. The high BSA loading on MSN-CHIT, obtained by TGA measurements, is consistent with the drastic change of zeta potential (Table 2) which is likely the cause of the formation of those particle aggregates [32].

3.3. *Transmission electron microscopy analysis*

TEM characterization was used to highlight the inner mesoporous structure of all samples and confirm BSA adsorption on surfaces of most of MSN samples examined in this investigation. In detail, in order to detect the presence of BSA on the MSNs, we used a specific gold labelling technique that consisted mainly of BSA conjugated with gold nanoparticles (GNPs). The use of GNP-antibody conjugates was previously used to localize human lysozyme [72] and an antibody fragment [58] within the pores of SBA-15 mesoporous silica. Here, the BSA-GNPs conjugates allowed the visualization of BSA adsorbed on MSNs. Both MSN-HA and MSN-CHIT samples showed similar BSA-GNPs patterns that were mainly characterized by the presence of an evident and intense gold labelling decorating the MSN surfaces (Fig. 6). However, variability of gold labelling intensity was occasionally observed. Overall, by a careful examination of several samples, a qualitative higher abundance of gold labelling was observed for MSN-CHIT than for MSN-HA in agreement with TGA data. The lower abundance of gold labelling for MSN-NH$_2$ sample is also in qualitative agreement with the lowest BSA loading, quantified through TGA (Table 2).

4. Conclusions

Taking into consideration the results of this study we can remark that the choice of a simple model provided interesting information on the interaction between BSA and functionalized MSNs. Our system was constituted by HA/CHIT-functionalized MSNs suspended in a 20 mg/mL BSA aqueous solution (phosphate buffer solution at pH 7.4 and NaCl 150 mM) at T = 37 °C. Within these conditions BSA interacts with the MSNs surface covered by the biopolymer. BSA is able to interact with both types of sample even though they carry opposite electric charges. This is an additional proof of the importance of non-electrostatic van der Waals interactions particularly in biological systems [71]. In fact, electrostatic and non electrostatic interactions likely cooperate to get the highest BSA loading on MSN-CHIT sample. For MSN-HA, instead, the two types of interactions have opposite effects which, nonetheless, overall result in a relatively high BSA loading. The effective adsorption of BSA is clearly demonstrated by TEM images of the samples treated with a GNP labelling procedure. Once BSA covers functionalized MSNs surface, the resulting surface potential is quite different from that of bare particles. That is a relevant finding which can influence the formation of the protein corona, and results in a different destiny of functionalized MSNs, once dispersed in a cellular medium or in a body fluid.

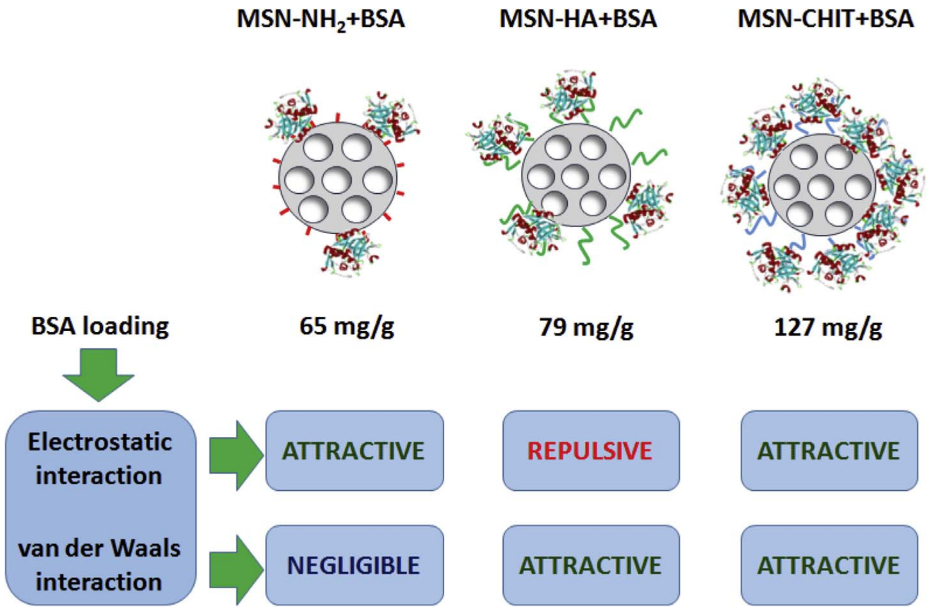

Scheme 2. Interactions responsible of the formation of the protein corona on functionalized MSNs.

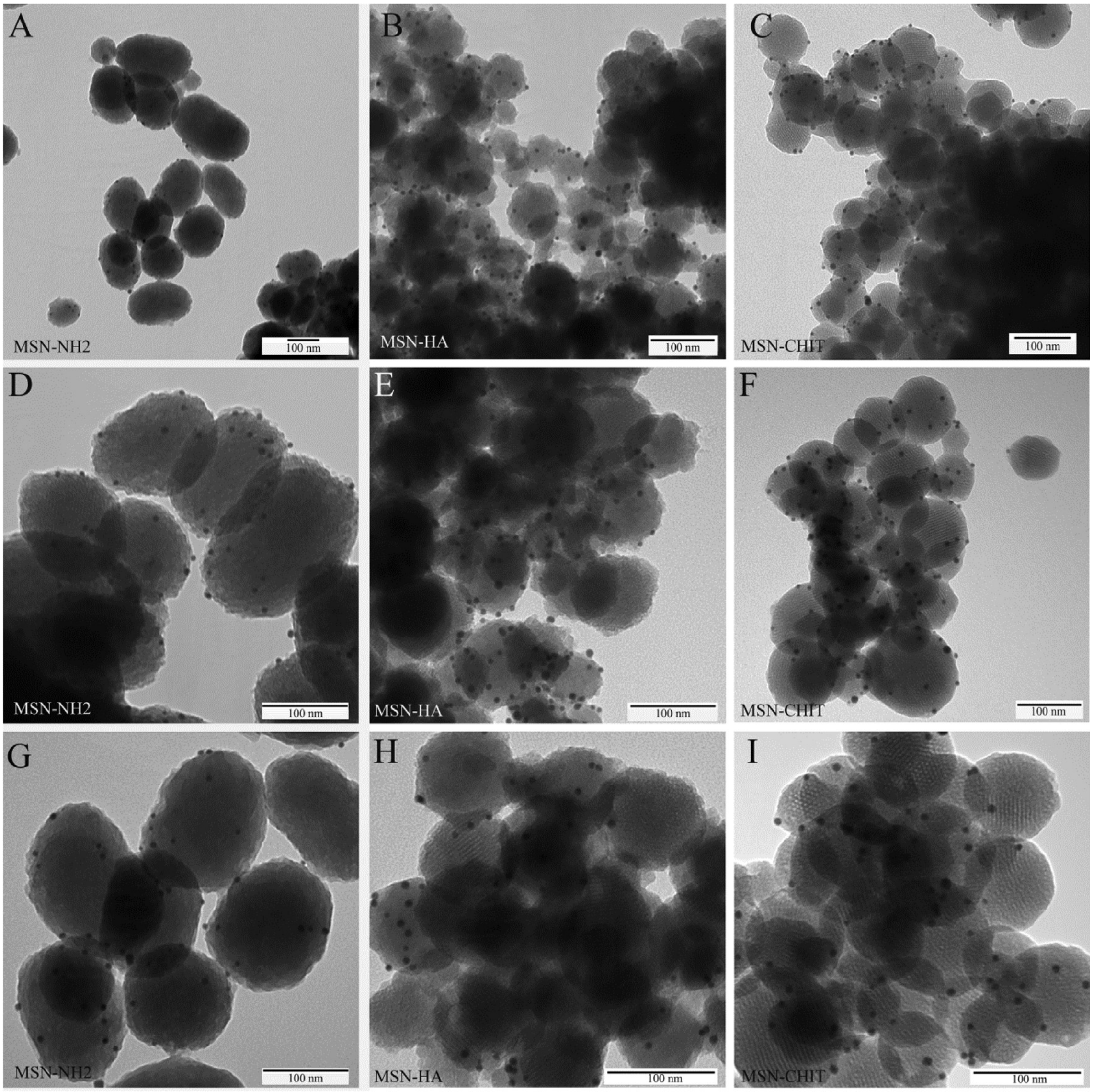

Fig. 6. TEM micrographs of MSN-NH_2 + BSA-GNPs (A, D, G) MSN-HA + BSA-GNPs (B, E, H) and MSN-CHIT + BSA-GNPs (C, F , I).

Acknowledgments

Financial support from FIR 2017, RAS/FdS (CUP F72F16003070002, 2017), European Research Council (Advanced Grant VERDI; ERC-2015-AdG Proposal No. 694160) is gratefully acknowledged.

References

[1] J. Zhang, Y. Sun, B. Tian, K. Li, L. Wang, Y. Liang, J. Han, Multifunctional mesoporous silica nanoparticles modified with tumor-shedable hyaluronic acid as carriers for doxorubicin, Colloids Surfaces. B 144 (2016) 293–302, http://dx.doi.org/10.1016/j.colsurfb.2016.04.015.

[2] S. Baek, R. Singh, D. Khanal, K.D. Patel, E.-J. Lee, K.W. Leong, W. Chrzanowski, H.-W. Kim, Smart multifunctional drug delivery towards anticancer therapy harmonized in mesoporous nanoparticles, Nanoscale 7 (2015) 14191–14216, http://dx.doi.org/10.1039/C5NR02730F.

[3] V. Keskar, P.S. Mohanty, E.J. Gemeinhart, R.A. Gemeinhart, Cervical cancer treatment with a locally insertable controlled release delivery system, J. Control Release 115 (2006) 280–288, http://dx.doi.org/10.1016/j.jconrel.2006.08.014.

[4] P. Nittayacharn, N. Nasongkla, Development of self-forming doxorubicin-loaded polymeric depots as an injectable drug delivery system for liver cancer chemotherapy, J. Mater. Sci. – Mater. Med. 28 (2017) 101–113, http://dx.doi.org/10.1007/s10856-017-5905-8.

[5] C. Monterrubio, G. Pascual-Pasto, F. Cano, M. Vila-Ubach, A. Manzanares, P. Schaiquevich, J.A. Tornero, A. Sosnik, J. Mora, A.M. Carcaboso, SN-38-loaded nanofiber matrices for local control of pediatric solid tumors after subtotal resection surgery, Biomaterials 79 (2016) 69–78, http://dx.doi.org/10.1016/j.biomaterials.2015.11.055.

[6] M. Norouzi, B. Nazari, D.W. Miller, Injectable hydrogel-based drug delivery systems for local cancer therapy, Drug Discovery Today 21 (2016) 1835–1849, http://dx.doi.org/10.1016/j.drudis.2016.07.006.

[7] A. Di Martino, O.A. Guselnikova, M.E. Trusova, P.S. Postnikov, V. Sedlarik, Organic-inorganic hybrid nanoparticles controlled delivery system for anticancer drugs, Int. J. Pharm. 526 (2017) 380–390, http://dx.doi.org/10.1016/j.ijpharm.2017.04.061.

[8] C. Ding, Z. Li, A review of drug release mechanisms from nanocarrier systems, Mater. Sci. Eng., C 76 (2017) 1440–1453, http://dx.doi.org/10.1016/j.msec.2017.03.130.

[9] Q. Zhang, Z. Wu, N. Li, Y. Pu, B. Wang, T. Zhang, J. Tao, Advanced review of graphene-based nanomaterials in drug delivery systems: synthesis, modification, toxicity and application, Mater. Sci. Eng., C 77 (2017) 1363–1375, http://dx.doi.org/10.1016/j.msec.2017.03.196.

[10] M. Bikram, A.M. Gobin, R.E. Whitmire, J.L. West, Temperature-sensitive hydrogels with SiO2-Au nanoshells for controlled drug delivery, J. Control. Release 123 (2007) 219–227, http://dx.doi.org/10.1016/j.jconrel.2007.08.013.

[11] G. Villaverde, A. Baeza, G.J. Melen, A. Alfranca, M. Ramirez, M. Vallet-Regí, A new targeting agent for the selective drug delivery of nanocarriers for treating neuroblastoma, J. Mater. Chem. B. 3 (2015) 4831–4842, http://dx.doi.org/10.1039/C5TB00287G.

[12] J. Jiao, X. Li, S. Zhang, J. Liu, D. Di, Y. Zhang, Q. Zhao, S. Wang, Redox and pH dual-responsive PEG and chitosan-conjugated hollow mesoporous silica for controlled drug release, Mater. Sci. Eng., C 67 (2016) 26–33, http://dx.doi.org/10.1016/j.msec.2016.04.091.

[13] M. Monduzzi, S. Lampis, S. Murgia, A. Salis, From self-assembly fundamental knowledge to nanomedicine developments, Adv. Colloid Interface Sci. 205 (2014)

48–67, http://dx.doi.org/10.1016/j.cis.2013.10.009.

[14] C.T. Kresge, M.E. Leonowicz, W.J. Roth, J.C. Vartuli, J.S. Beck, Ordered mesoporous molecular sieves synthesized by liquid-crystal template mechanism, Nature 359 (1992) 710–712, http://dx.doi.org/10.1038/355242a0.

[15] M. Vallet-Regi, A. Rámila, R.P. Del Real, J. Pérez-Pariente, A new property of MCM-41: Drug delivery system, Chem. Mater. 13 (2001) 308–311, http://dx.doi.org/10.1021/cm0011559.

[16] M. Vallet-Regì, J.C. Doadrio, A.L. Doadrio, I. Izquierdo-Barba, J. Perez-Pariente, Hexagonal ordered mesoporous material as a matrix for the controlled release of amoxicillin, Solid State Ionics 172 (2004) 435–439, http://dx.doi.org/10.1016/j.ssi.2004.04.036.

[17] D. Molina-Manso, M. Manzano, J.C. Doadrio, G. Del Prado, A. Ortiz-Pérez, M. Vallet-Regì, E. Gòmez-Barrena, J. Esteban, Usefulness of SBA-15 mesoporous ceramics as a delivery system for vancomycin, rifampicin and linezolid: a preliminary report, Int. J. Antimicrob. Agents 40 (2012) 252–256, http://dx.doi.org/10.1016/j.ijantimicag.2012.05.013.

[18] N. Gómez-Cerezo, I. Izquierdo-Barba, D. Arcos, M. Vallet-Regí, Tailoring the biological response of mesoporous bioactive materials, J. Mater. Chem. B. 3 (2015) 3810–3819, http://dx.doi.org/10.1039/C5TB00268K.

[19] M.S. Bhattacharyya, P. Hiwale, M. Piras, L. Medda, D. Steri, M. Piludu, A. Salis, M. Monduzzi, Lysozyme adsorption and release from ordered mesoporous materials, J. Phys. Chem. C. 114 (2010) 19928–19934, http://dx.doi.org/10.1021/jp1078218.

[20] D. Steri, M. Monduzzi, A. Salis, Ionic strength affects lysozyme adsorption and release from SBA-15 mesoporous silica, Microporous Mesoporous Mater. 170 (2013) 164–172, http://dx.doi.org/10.1016/j.micromeso.2012.12.002.

[21] R.R. Castillo, A. Baeza, M. Vallet-Regí, Recent applications of the combination of mesoporous silica nanoparticles with nucleic acids: development of bioresponsive devices, carriers and sensors, Biomater. Sci. 5 (2017) 353–377, http://dx.doi.org/10.1039/C6BM00872K.

[22] R.R. Castillo, M. Colilla, M. Vallet-Regí, Advances in mesoporous silica-based nanocarriers for co-delivery and combination therapy against cancer, Expert Opin. Drug Delivery. 14 (2017) 229–243, http://dx.doi.org/10.1080/17425247.2016.1211637.

[23] S. Rahmani, J.O. Durand, C. Charnay, L. Lichon, M. Férid, M. Garcia, M. Gary-Bobo, Synthesis of mesoporous silica nanoparticles and nanorods: Application to doxorubicin delivery, Solid State Sci. 68 (2017) 25–31, http://dx.doi.org/10.1016/j.solidstatesciences.2017.04.003.

[24] J.L. Paris, M.V. Cabanas, M. Manzano, M. Vallet-Regí, Polymer-grafted mesoporous silica nanoparticles as ultrasound-responsive drug carriers, ACS Nano 9 (2015) 11023–11033, http://dx.doi.org/10.1021/acsnano.5b04378.

[25] V. Nairi, L. Medda, M. Monduzzi, A. Salis, Adsorption and release of ampicillin antibiotic from ordered mesoporous silica, J. Colloid Interface Sci. 497 (2017) 217–225, http://dx.doi.org/10.1016/j.jcis.2017.03.021.

[26] F. Sevimli, A. Yılmaz, Surface functionalization of SBA-15 particles for amoxicillin delivery, Microporous Mesoporous Mater. 158 (2012) 281–291, http://dx.doi.org/10.1016/j.micromeso.2012.02.037.

[27] W. Fang, Z. Wang, S. Zong, H. Chen, D. Zhu, Y. Zhong, Y. Cui, Biosensors and Bioelectronics pH-controllable drug carrier with SERS activity for targeting cancer cells, Biosens. Bioelectron. 57 (2014) 10–15, http://dx.doi.org/10.1016/j.bios.2014.01.042.

[28] D.P. Ferris, J. Lu, C. Gothard, R. Yanes, C.R. Thomas, J. Olsen, J.F. Stoddart, F. Tamanoi, J.I. Zink, Synthesis of Biomolecule-Modified Mesoporous Silica Nanoparticles for Targeted Hydrophobic Drug Delivery to Cancer Cells, Small 7 (2011) 1816–1826, http://dx.doi.org/10.1002/smll.201002300.

[29] K. Cheng, S.R. Blumen, M.B. Macpherson, J.L. Steinbacher, B.T. Mossman, C.C. Landry, Enhanced uptake of porous silica microparticles by bifunctional surface biocompatible, Polymer 2 (2010) 2489–2495, http://dx.doi.org/10.1021/am100530t.

[30] Z.-Y. Li, J.-J. Hu, Q. Xu, S. Chen, H. Jia, Y.-X. Sun, R.-X. Zhuo, X.-Z. Zhang, A redox-responsive drug delivery system based on RGD containing peptide-capped mesoporous silica, J. Mater. Chem. B 3 (2015) 39–44, http://dx.doi.org/10.1039/C4TB01533A.

[31] J. Zhang, Z.-F. Yuan, Y. Wang, W.-H. Chen, G.-F. Luo, S.-X. Cheng, R. Zhuo, X. Zhang, Multifunctional envelope-type mesoporous silica nanoparticles for tumor-triggered targeting drug delivery, J. Am. Chem. Soc. 135 (2013) 5068–5073 do:/10.1021/ja312004m.

[32] A. Salis, M. Fanti, L. Medda, V. Nairi, F. Cugia, M. Piludu, V. Sogos, M. Monduzzi, Mesoporous silica nanoparticles functionalized with hyaluronic acid and chitosan biopolymers. effect of functionalization on cell internalization, ACS Biomater. Sci. Eng. 2 (2016) 741–751, http://dx.doi.org/10.1021/acsbiomaterials.5b00502.

[33] A. Popat, J. Liu, G.Q. (Max) Lu, S.Z. Qiao, A pH-responsive drug delivery system based on chitosan coated mesoporous silica nanoparticles, J. Mater. Chem. 22 (2012) 11173–11178, http://dx.doi.org/10.1039/c2jm30501a.

[34] W.T. Liu, Y. Yang, P.H. Shen, X.J. Gao, S.Q. He, H. Liu, C.S. Zhu, Facile and simple preparation of pH-sensitive chitosan-mesoporous silica nanoparticles for future breast cancer treatment, Express Polym. Lett. 9 (2015) 1068–1075, http://dx.doi.org/10.3144/expresspolymlett.2015.96.

[35] G. Villaverde, V. Nairi, A. Baeza, M. Vallet-Regí, Double sequential encrypted targeting sequence: a new concept for bone cancer treatment, Chem. – A Eur. J. 23 (2017) 7174–7179, http://dx.doi.org/10.1002/chem.201605947.

[36] Z. Wang, Y. Tian, H. Zhang, Y. Qin, D. Li, L. Gan, F. Wu, Using hyaluronic acid-functionalized pH stimuli-responsive mesoporous silica nanoparticles for targeted delivery to CD44-overexpressing cancer cells, Int. J. Nanomed. 11 (2016) 6485–6497, http://dx.doi.org/10.2147/IJN.S117184.

[37] M. Chang, F. Zhang, T. Wei, T. Zuo, Y. Guan, G. Lin, W. Shao, Smart linkers in polymer-drug conjugates for tumor-targeted delivery, J. Drug Target. 24 (2016) 475–491, http://dx.doi.org/10.3109/1061186X.2015.1108324.

[38] A. Baeza, M. Colilla, M. Vallet-Regí, Advances in mesoporous silica nanoparticles for targeted stimuli-responsive drug delivery, Expert Opin. Drug Delivery 12 (2015) 319–337, http://dx.doi.org/10.1517/17425247.2014.953051.

[39] G. Li, Y. Gao, Y. Cui, T. Zhang, R. Cui, Y. Jiang, J. Shi, Overexpression of CD44 is associated with the occurrence and migration of non-small cell lung cancer, Mol. Med. Rep. 14 (2016) 3159–3167, http://dx.doi.org/10.3892/mmr.2016.5636.

[40] L. Medda, M.F. Casula, M. Monduzzi, A. Salis, Adsorption of lysozyme on hyaluronic acid functionalized SBA-15 mesoporous silica: a possible bioadhesive depot system, Langmuir 43 (2014) 12996–13004, http://dx.doi.org/10.1021/la503224n.

[41] Y. Wang, Q. Zhao, N. Han, L. Bai, J. Li, J. Liu, E. Che, L. Hu, Q. Zhang, T. Jiang, S. Wang, Mesoporous silica nanoparticles in drug delivery and biomedical applications, Nanomedicine: Nanotechnology, Biol. Med. 11 (2015) 313–327, http://dx.doi.org/10.1016/j.nano.2014.09.014.

[42] J. Liu, Y. Huang, A. Kumar, A. Tan, S. Jin, A. Mozhi, X.J. Liang, PH-Sensitive nanosystems for drug delivery in cancer therapy, Biotechnol. Adv. 32 (2014) 693–710, http://dx.doi.org/10.1016/j.biotechadv.2013.11.009.

[43] L. Treuel, G.U. Nienhaus, Toward a molecular understanding of nanoparticle-protein interactions, Biophys. Rev. 4 (2012) 137–147, http://dx.doi.org/10.1007/s12551-012-0072-0.

[44] S. Laurent, C. Burtea, C. Thirifays, F. Rezaee, M. Mahmoudi, Significance of cell "observer" and protein source in nanobiosciences, J. Colloid Interface Sci. 392 (2013) 431–445, http://dx.doi.org/10.1016/j.jcis.2012.10.005.

[45] M. Mahmoudi, I. Lynch, M.R. Ejtehadi, M.P. Monopoli, F.B. Bombelli, S. Laurent, Protein – nanoparticle interactions: opportunities and challenges, Chem. Rev. 111 (2011) 5610–5637, http://dx.doi.org/10.1021/cr100440g.

[46] Z. Deng, G. Mortimer, T. Schiller, A. Masumeci, D. Martin, M. RF, Differential plasma protein binding to metal oxide nanoparticles, Nanotechnology 20 (2009) 455101–455109, http://dx.doi.org/10.1088/0957-4484/20/45/455101.

[47] S. Tenzer, D. Docter, S. Rosfa, A. Wlodarski, J. Kuharev, A. Rekik, S.K. Knauer, C. Bantz, T. Nawroth, C. Bier, J. Sirirattanapan, W. Mann, L. Treuel, R. Zellner, M. Maskos, H. Schild, R.H. Stauber, Nanoparticle size is a critical physicochemical determinant of the human blood plasma corona: a comprehensive quantitative proteomic analysis, ACS Nano 5 (2011) 7155–7167, http://dx.doi.org/10.1021/nn201950e.

[48] M.C. Cox, K.J. Barnham, T.A. Frenkiel, J.D. Hoeschele, A.B. Mason, Q.Y. He, R.C. Woodworth, P.J. Sadler, Identification of platination sites on human serum transferrin using (13)C and (15)N NMR spectroscopy., Journal of Biological Inorganic Chemistry : JBIC : A Publication of the Society of Biological, Inorg. Chem. 4 (1999) 621–631.

[49] P. Aggarwal, J.B. Hall, C.B. McLeland, M.A. Dobrovolskaia, S.E. McNeil, Nanoparticle interaction with plasma proteins as it relates to particle biodistribution, biocompatibility and therapeutic efficacy, Adv. Drug Deliv. Rev. 61 (2009) 428–437, http://dx.doi.org/10.1016/j.addr.2009.03.009.

[50] S. Laurent, M. Mahmoudi, Superparamagnetic iron oxide nanoparticles: Promises for diagnosis and treatment of cancer, Int. J. Mol. Epidemiol. Genet. 2 (2011) 367–390, http://dx.doi.org/10.1021/cn100100e.

[51] I. Lynch, K.A. Dawson, Protein-nanoparticle interactions, Nano Today 3 (2008) 40–47, http://dx.doi.org/10.1016/S1748-0132(08)70014-8.

[52] P. Foroozandeh, A.A. Aziz, Merging worlds of nanomaterials and biological environment: factors governing protein corona formation on nanoparticles and its biological consequences, Nanoscale Res. Lett. 10 (2015) 221–232, http://dx.doi.org/10.1186/s11671-015-0922-3.

[53] M.T. Ortega, J.E. Riviere, K. Choi, N.A. Monteiro-Riviere, Biocorona formation on gold nanoparticles modulates human proximal tubule kidney cell uptake, cytotoxicity and gene expression, Toxicol. In Vitro 42 (2017) 150–160, http://dx.doi.org/10.1016/j.tiv.2017.04.020.

[54] M. Lundqvist, J. Stigler, T. Cedervall, T. Berggård, M.B. Flanagan, I. Lynch, G. Elia, K. Dawson, The evolution of the protein corona around nanoparticles: a test study, ACS Nano 5 (2011) 7503–7509, http://dx.doi.org/10.1021/nn202458g.

[55] M.S. Ehrenberg, A.E. Friedman, J.N. Finkelstein, G. Oberdörster, J.L. McGrath, The influence of protein adsorption on nanoparticle association with cultured endothelial cells, Biomaterials 30 (2009) 603–610, http://dx.doi.org/10.1016/j.biomaterials.2008.09.050.

[56] L. Vroman, A.L. Adams, G.C. Fischer, P.C. Munoz, Interaction of high molecular weight Kininogen, Factor XII, and Fibrinogen in plasma at interfaces, 55 (1980) 156–159.

[57] S. Shahabi, S. Döscher, T. Bollhorst, L. Treccani, M. Maas, R. Dringen, K. Rezwan, Enhancing cellular uptake and doxorubicin delivery of mesoporous silica nanoparticles via surface functionalization: effects of serum, ACS Appl. Mater. Interfaces 7 (2015) 26880–26891, http://dx.doi.org/10.1021/acsami.5b09483.

[58] M. Piludu, L. Medda, F. Cugia, M. Monduzzi, A. Salis, Silver enhancement for transmission electron microscopy imaging of antibody fragment-gold nanoparticles conjugates immobilized on ordered mesoporous silica, Langmuir 31 (2015) 9458–9463, http://dx.doi.org/10.1021/acs.langmuir.5b02830.

[59] S. Brunauer, P.H. Emmett, E. Teller, Adsorption of gases in multimolecular layers, J. Am. Chem. Soc. 60 (1938) 309–319, http://dx.doi.org/10.1021/ja01269a023.

[60] E.P. Barrett, L.G. Joyner, P.P. Halenda, The determination of pore volume and area distributions in porous substances. I. computations from nitrogen isotherms, J. Am. Chem. Soc. 73 (1951) 373–380, http://dx.doi.org/10.1021/ja01145a126.

[61] J. Coates, Interpretation of Infrared Spectra, A Practical Approach, in: Encyclopedia of Analytical Chemistry, John Wiley & Sons, Ltd, Chichester, UK, 2000, pp. 10815–10837, , http://dx.doi.org/10.1002/9780470027318.a5606.

[62] T.-P. Liu, S.-H. Wu, Y.-P. Chen, C.-M. Chou, C.-T. Chen, Biosafety evaluations of well-dispersed mesoporous silica nanoparticles: towards in vivo-relevant

conditions, Nanoscale 7 (2015) 6471–6480, http://dx.doi.org/10.1039/C4NR07421A.

[63] M. Since, A Study of the Amide III Band by FT-IR Spectrometry of the Secondary Structure of Albumin, Myoglobin, and γ-Globulin, 41 (1987) 180–184.

[64] G. Sekar, S. Sugumar, A. Mukherjee, N. Chandrasekaran, Multiple spectroscopic studies of the structural conformational changes of human serum albumin — Essential oil based nanoemulsions conjugates, J. Lumin. 161 (2015) 187–197, http://dx.doi.org/10.1016/j.jlumin.2014.12.058.

[65] A. Pielesz, D. Binia, E. Sarna, J. Paluch, W. Waksma, Spectrochimica Acta Part A : molecular and biomolecular spectroscopy the role of topically applied L -ascorbic acid in ex-vivo examination of burn-injured human skin, 185 (2017) 279–285, http://dx.doi.org/10.1016/j.saa.2017.05.055.

[66] Z. Zhou, X. He, M. Zhou, F. Meng, Chemically induced alterations in the characteristics of fouling-causing bio-macromolecules – Implications for the chemical cleaning of fouled membranes, Water Res. 108 (2017) 115–123, http://dx.doi.org/10.1016/j.watres.2016.10.065.

[67] K. Kaiden, T. Matsui, S. Tanaka, A Study of the Amide III Band by FT-IR Spectrometry of the Secondary Structure of Albumin, Myoglobin, and γ –Globulin, Appl. Spectrosc. 41 (1987) 180–184, http://dx.doi.org/10.1366/000370287774986714.

[68] A. Salis, M. Boström, L. Medda, F. Cugia, B. Barse, D.F. Parsons, B.W. Ninham, M. Monduzzi, Measurements and theoretical interpretation of points of zero charge/potential of BSA protein, Langmuir 27 (2011) 11597–11604, http://dx.doi.org/10.1021/la2024605.

[69] S.H. Brewer, W.R. Glomm, M.C. Johnson, M.K. Knag, S. Franzen, Probing BSA binding to citrate-coated gold nanoparticles and surfaces, Langmuir 21 (2005) 9303–9307, http://dx.doi.org/10.1021/la050588t.

[70] L. Medda, B. Barse, F. Cugia, M. Boström, D.F. Parsons, B.W. Ninham, M. Monduzzi, A. Salis, Hofmeister challenges: ion binding and charge of the BSA protein as explicit examples, Langmuir 28 (2012) 16355–16363, http://dx.doi.org/10.1021/la3035984.

[71] D.F. Parsons, A. Salis, Hofmeister effects at low salt concentration due to surface charge transfer, Curr. Opin. Colloid Interface Sci. 23 (2016) 41–49, http://dx.doi.org/10.1016/j.cocis.2016.05.005.

[72] M. Piras, A. Salis, M. Piludu, D. Steri, M. Monduzzi, 3D vision of human lysozyme adsorbed onto a SBA-15 nanostructured matrix, Chem. Commun. 47 (2011) 7338–7340, http://dx.doi.org/10.1039/c1cc11840d.

Paper V

Reprinted with permission from:

Mesoporous Silica Nanoparticles Functionalized with Hyaluronic Acid. Effect of the Biopolymer Chain Length on Cell Internalization

Valentina Nairi, Silvia Magnolia, Marco Piludu, Mariella Nieddu, Cristian Antonio Caria, Valeria Sogos, Maria Vallet-Regì, Maura Monduzzi and Andrea Salis. *Colloids Surf. B* (2018). In press

DOI: 10.1016/j.colsurfb.2018.02.019

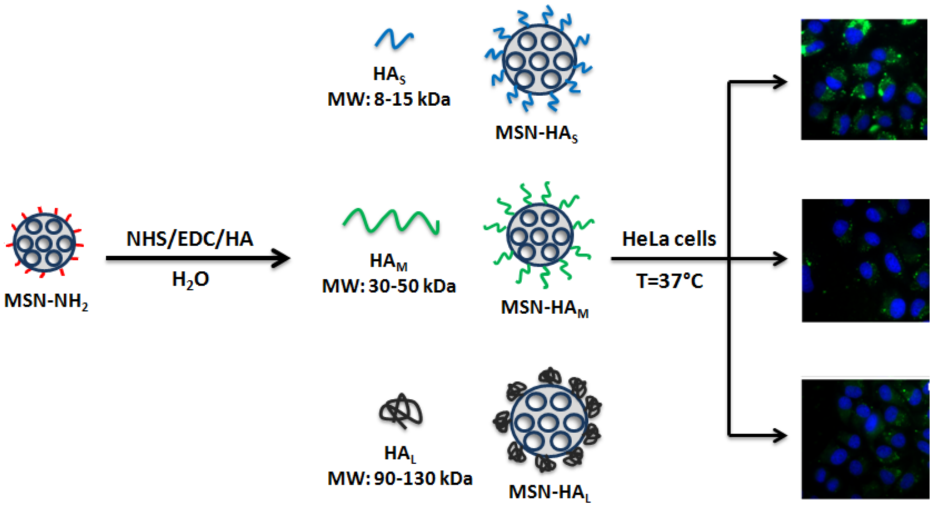

Colloids and Surfaces B: Biointerfaces xxx (2018) xxx–xxx

Contents lists available at ScienceDirect

Colloids and Surfaces B: Biointerfaces

journal homepage: www.elsevier.com/locate/colsurfb

Mesoporous silica nanoparticles functionalized with hyaluronic acid. Effect of the biopolymer chain length on cell internalization

Valentina Nairi[a], Silvia Magnolia[a], Marco Piludu[b], Mariella Nieddu[b], Cristian Antonio Caria[c], Valeria Sogos[b], Maria Vallet-Regì[d,*], Maura Monduzzi[a,*], Andrea Salis[a,*]

[a] Dipartmento di Scienze Chimiche e Geologiche, Università di Cagliari-CSGI and CNBS, Cittadella Universitaria, S.S. 554 bivio Sestu, 09042 Monserrato, CA, Italy
[b] Dipartimento di Scienze Biomediche, Università di Cagliari, Cittadella Universitaria, S.S. 554 bivio Sestu, 09042 Monserrato, CA, Italy
[c] Istituto di Ricerca Genetica e Biomedica, Consiglio Nazionale delle Ricerche, Cittadella Universitaria, S.S. 554 bivio Sestu, 09042 Monserrato, CA, Italy
[d] Departamento de Quimica Inorganica y Bioinorganica, Facultad de Farmacia, Universidad Complutense de Madrid, Plaza Ramon y Cajal s/n, Instituto de Investigacion Sanitaria Hospital 12 de Octubre i+12 ¡ Centro de Investigacion Biomedica en Red de Bioingenieria, Biomateriales y Nanomedicina (CIBER-BBN), Madrid, Spain

ARTICLE INFO

Article history:
Received 30 September 2017
Received in revised form 3 February 2018
Accepted 10 February 2018
Available online xxx

Keywords:
Mesoporous silica nanoparticles
Hyaluronic acid
Cellular uptake
Target system
Optical microscopy
Transmission electron microscopy

ABSTRACT

Mesoporous silica nanoparticles (MSNs) were functionalized with amino groups (MSN-NH_2) and then with hyaluronic acid, a biocompatible biopolymer which can be recognized by CD44 receptors in tumor cells, to obtain a targeting drug delivery system. To this purpose, three hyaluronic acid samples differing for the molecular weight, namely HA_S (8–15 kDa), HA_M (30–50 kDa) and HA_L (90–130 kDa), were used. The MSN-HA_S, MSN-HA_M, and MSN-HA_L materials were characterized through zeta potential and dynamic light scattering measurements at pH = 7.4 and T = 37 °C to simulate physiological conditions. While zeta potential showed an increasing negative value with the increase of the HA chain length, an anomalous value of the hydrodynamic diameter was observed for MSN-HA_L, which was smaller than that of MSN-HA_S and MSN-HA_M samples. The cellular uptake of MSN-HA samples on HeLa cells at 37 °C was studied by optical and electron microscopy. HA chain length affected significantly the cellular uptake that occurred at a higher extent for MSN-NH_2 and MSN-HA_S than for MSN-HA_M and MSN-HA_L samples. Cellular uptake experiments carried out at 4 °C showed that the internalization process was inhibited for MSN-HA samples but not for MSN-NH_2. This suggests the occurrence of two different mechanisms of internalization. For MSN-NH_2 the uptake is mainly driven by the attractive electrostatic interaction with membrane phospholipids, while MSN-HA internalization involves CD44 receptors overexpressed in HeLa cells.

1. Introduction

Cancer is a multifactorial widespread disease that represents a growing threat for human health [1]. The microenvironment of solid tumors is very similar to tissue repair sites of an injured tissue where activated platelets are involved in the release of vasoactive mediators, serum fibrinogen, growth factors, and proteins for the regeneration of a new healthy tissue. In particular epithelial and stromal cells are involved in a reciprocal signaling cross-talk responsible of the healing which is interrupted when the tissue is completely regenerated, while persists in tumor tissue allowing for the growth of tumor and stimulating the angiogenesis [2–4]. This phenomenon takes place in solid tumors when they reach 2 mm^3, and causes the formation of new blood vessels [5]. Long-circulating nanosized drug delivery systems (NDDS) can take advantage of the abnormal vascularization of tumor tissues. Indeed endothelial pores have dimensions between 10 and 1000 nm, and lymphatic vessels in tumor tissue are absent or nonfunctional, hence NDDS cannot efficiently be removed and are retained inside the endothelial pores. This passive phenomenon is known as Enhanced Permeability and Retention (EPR) effect [5].

Current therapies consist in the administration of chemotherapeutic drugs that are able to curb tumor growth, but these drugs are toxic for healthy cells and can produce several bad side effects [1,2]. In the recent years researchers widely focused on the possibility to

---

* Corresponding authors.
E-mail addresses: vallet@ucm.es (M. Vallet-Regì), monduzzi@unica.it (M. Monduzzi), asalis@unica.it (A. Salis).

https://doi.org/10.1016/j.colsurfb.2018.02.019

Please cite this article in press as: V. Nairi, et al., Mesoporous silica nanoparticles functionalized with hyaluronic acid. Effect of the biopolymer chain length on cell internalization, Colloids Surf. B: Biointerfaces (2018), https://doi.org/10.1016/j.colsurfb.2018.02.019

produce site-specific drug nanocarriers. Several smart drug delivery systems based on functionalized liposomes [6,7], micelles [8], mesoporous silica nanoparticles [9–12], carbon nanotubes [13], and inorganic nanoparticles [14] have been engineered. These systems allow to address the drug administration to the diseased tissue only [5,7], thus obtaining a reduction of the toxic effects of the drug along with an increase of the local drug concentration, and consequently an improvement of the therapeutic efficacy [15].

In this context ordered mesoporous silica was used for the first time in 2001 by Vallet-Regì and co-workers [16], and, as a result of peculiar features such as high surface area and pore volume that allow for drug adsorption and controlled release, received great attention since then [10,11,17–25]. Moreover, the possibility to introduce smart functional groups at the internal and/or the external mesoporous silica surface [9,26–28] allows to promote different types of specific interactions with biological entities. Focusing on mesoporous silica nanoparticles (MSNs), huge improvements were obtained on specific actions such as the MSNs' performance towards the sustained drug release [9,26–28], the reduction of toxicity, the increase of the biocompatibility [10,29,30] and cell internalization [31], as well as the citotoxicity towards tumor cells [32,33]. Indeed, several target molecules [10,17,30,34–37] and stimuli-responsive capping agents [27,34,38–41] can easily be grafted at the MSNs' surface. Target molecules allow the MSNs to reach the tumor tissue only through a molecular recognition mechanism. Then, once in the internal tissue, the stimuli-responsive capping agent [5,34] permits the release of the drug as a response to internal (change of pH [42–45], temperature [46–48], redox reactions [40,49–52]) or external (irradiation with light [53–55], magnetic field [55–57]) stimuli.

Hyaluronic acid (HA) is an anionic polysaccharide composed of D-glucuronic acid and N-acetyl-D-glucosamine units linked through alternating $\beta_{1,3}$ and $\beta_{1,4}$ glycosidic bonds [58,59]. HA is the main component of the extracellular matrix of the human connective tissue and one of the most important components of the skin. It also occurs at high concentrations in synovial joint fluids, vitreous humor of eyes, hyaline cartilage, intervertebral disc nucleus, and umbilical cord [59]. In humans HA is synthesized in plasma membrane by membrane-bound synthase (Has) [58]. This enzyme is present in three different isoforms: Has1 and Has2, responsible for the synthesis of high molecular weight HA ($\sim 2\cdot 10^6$ Da), and Has3, responsible of low molecular weight ($<3\cdot 10^5$ Da) [58,60,61]. HA has also many physiological roles related to its structure as for example regulation of water in tissues, lubrication, structural and space-filling properties. If modifications of HA ordered structure occur, the physico-chemical properties, being controlled by HA's secondary and tertiary structure, also change, particularly the rheological behavior [58]. Furthermore HA has a very good affinity for CD44 receptors overexpressed in several cancer cells, property that makes it a great active tumor target [2,62]. Recently HA was used to target different kinds of NDDS like HA-conjugated polyamidoamine dendrimers [63], micelles [64], and ceramides [65] or HA-grafted graphene quantum dots [66], carbon nanotubes [67,68] as well as mesoporous silica nanoparticles [69].

Herein the behavior of HA-grafted MSNs was investigated, focusing on the effects of the biopolymer's chain length towards cell internalization. MSNs were functionalized with HA having different molecular weight: HA_S: 8–15 kDa, HA_M: 30–50 kDa and HA_L: 90–130 kDa. Dynamic (DLS) and electrophoretic (ELS) light scattering measurements were used to characterize the different systems at pH = 7.4 at the temperature of 37 °C to simulate physiological conditions [45,70–72]. Fluorescence and electron microscopy experiments were then performed to highlight the effects of the polymer's chain length on the HA-grafted MSNs' internalization in HeLa cells.

2. Materials and methods

2.1. Chemicals

Tetraethoxysilane (TEOS, 98%), hexadecyltrimethylammonium bromide (CTAB, >99%), anhydrous toluene (99.8%), 3-aminopropyltriethoxysilane (APTES, >98%), hydrochloride acid (37%), fluorescein isothiocyanate (FITC) and triethylamine (>99%) were purchased from Sigma-Aldrich (Milan, Italy). NH_4NO_3 (>99.9%), NaH_2PO_4 (99%), Na_2HPO_4 (99%), acetic acid (>99.7%), NaOH (97%), *N*-(3-dimethylaminopropyl)-*N′*-ethylcarbodiimide hydrochloride (EDC, >98%), *N*-hydroxysuccinimide (NHS, >97%) were purchased from Fluka. Hyaluronic acid sodium salt (HA_S: 8–15 kDa, HA_M: 30–50 kDa and HA_L: 90–130 kDa) was purchased from Contipro Biotech a.s. (Czech Republic).

2.2. Synthesis of amino-functionalized Mesoporous Silica Nanoparticles (MSN-NH_2)

A mass of 1 g of CTAB was dissolved in 480 g of Millipore water and 3.5 mL of NaOH (2 M) and the resulting solution was stirred at 80 °C. After 2 h a volume of 10 mL of TEOS was added dropwise. The solution was stirred for other 2 h, and then the resulting white precipitate (MSN-T) was filtered under vacuum, washed with distilled water and methanol, and dried overnight at room temperature. The grafting of the amino group on the surface of the MSNs was carried out by dispersing 1 g of the MSN-T sample in 45 mL of anhydrous toluene, and then adding dropwise 0.5 mL of APTES. The dispersion was stirred and kept at 110 °C under reflux overnight. The resulting MSN-T-NH_2 sample was collected by filtration, washed with acetone, and dried overnight at room temperature under vacuum. CTAB surfactant was removed by dispersing the previously synthesized material in 1L of a 10 mg/mL NH_4NO_3 solution in ethanol:water (95:5), and then stirring the dispersion overnight under reflux. The functionalized mesoporous silica nanoparticles (MSN-NH_2) were recovered via filtration, washed with water and ethanol, and dried under vacuum at room temperature. The removal of CTAB is confirmed by the disappearance from FTIR spectra (Fig. S1) of the bands at 2930 cm^{-1} and 2840 cm^{-1} – assigned to asymmetric and symmetric stretching of C—H, respectively – the band at1490 cm^{-1}, due to the C—H bending, and that at 1220 cm^{-1} assigned to the C—N stretching of CTAB molecule.

2.3. Grafting of Hyaluronic Acid (HA) on MSN-NH_2

A mass of 0.5 g of MSN-NH_2 sample was dispersed in 50 mL of millipore water. In another vessel, 10 mL of an aqueous solution containing NHS (0.186 g) and EDC (0.113 g) were mixed with 30 mL of an aqueous solution containing 0.060 g of HA at different chain length (HA_S, HA_M and HA_L). The two solutions were mixed, and the pH was adjusted to 9.0 by adding triethylamine. Finally, the mixture was stirred at 38 °C overnight. The HA-modified MSNs (MSN-HA_S, MSN-HA_M and MSN-HA_L) were collected after centrifugation, washed extensively with millipore water, and dried under vacuum and at room temperature overnight.

FITC labeling of functionalized MSNs was carried out by dispersing

40 mg of MSN-NH_2 or HA-grafted MSNs (MSN-HA_S, MSN-HA_M and MSN-HA_L) in 5 mL of a 3.75 mM FITC solution in ethanol. The dispersion was stirred at room temperature under dark conditions for 3 h. The obtained yellow powder was centrifuged, washed with ethanol to remove the excess of FITC, and dried under vacuum. These FITC labeled MSNs were used for fluorescence microscopy.

Please cite this article in press as: V. Nairi, et al., Mesoporous silica nanoparticles functionalized with hyaluronic acid. Effect of the biopolymer chain length on cell internalization, Colloids Surf. B: Biointerfaces (2018), https://doi.org/10.1016/j.colsurfb.2018.02.019

2.4. Physico-chemical characterization of functionalized MSNs

Textural analysis was carried out on an ASAP 2020 instrument, by determining the N_2 adsorption/desorption isotherm at 77 K. Before analysis functionalized MSNs samples were heated at 40 °C, at the rate of 1 °C/min, under vacuum for 60 h. The Brunaeur-Emmett-Teller (BET) [73] and Barrett-Joyner-Halenda (BJH) [74] methods, calculated from adsorption and desorption branch of N_2 isotherm, were used to calculate surface area, pore volume and pore size distribution, respectively.

Small-angle X-ray scattering (SAXS) patterns were recorded through a S3-MICRO SWAXS camera system (HECUS X-ray Systems, Graz, Austria). CuKα radiation of wavelength 1.542 Å was provided by a GeniX-X-ray generator, operating at 30 kV and 0.4 mA. A 1D-PSD–50 M system (HECUS X-ray Systems, Graz, Austria) containing 1024 channels of width 54.0 μm was used for detection of scattered X-rays in the small-angle region. The working q-range ($Å^{-1}$) was $0.003 \leq q \leq 0.6$, where q ($=4\pi \sin\theta\ \lambda^{-1}$) is the modulus of the scattering wave vector and θ is the scattering angle. Thin-walled 2 mm glass capillaries were filled with the sample for the scattering experiments. The scattering patterns were recorded for 1 h.

Thermogravimetric analysis (TGA) was carried out on a TG-DTA 320 Seiko thermo-balance. Thermal analysis data were collected in the 25–1000 °C range, under oxygen flow (heating rate = 10 °C/min; flow rate = 50 mL min^{-1}).

The hydrodynamic diameter (d_H) and the zeta potential (ζ) of MSNs were measured using a Zetasizer Nano ZSP (Malvern Instruments) in backscatter configuration (θ = 173°), at laser wavelength of λ = 633 nm. The scattering cell temperature was fixed at 37 °C, and the data were analyzed with the Zetasizer software 7.03 version. For both d_H and ζ measurements the sample was prepared by suspending MSNs (1 mg/mL) in filtered (0.2 μm polypropylene filter, Whatman) milliQ water, 25 mM phosphate buffer (pH 7.4). Samples were sonicated for 30 min and left under stirring overnight. The samples were sonicated for other 30 min and then the measurements were carried out. ζ-potential values were calculated by mean of the Henry equation [75]:

$$\mu_E = \frac{2\varepsilon\zeta f(ka)}{3\eta} \tag{1}$$

where μ_E is the electrophoretic mobility, η is the viscosity of the dispersant, and $f(\kappa a)$ the Henry's function, ε ($=e_0 e_r$) is water permittivity and ε_0 (=8.85 pF/m) is vacuum permittivity. For our experiments we assumed as dispersant water ($\varepsilon_r = 78.5$ at 25 °C and 74.40 at 37 °C, and η = 0.89 cP at 25 °C and 0.69 cP at 37 °C) and $f(\kappa a) = 1.5$ in agreement with Smoluchowski approximation commonly used for nanoparticles larger than 0.2 μm dispersed in aqueous media and with electrolytes concentration higher than 10 mM.

Fourier transform infrared (FTIR) studies were carried out with a Bruker Tensor 27 spectrophotometer equipped with a diamond-ATR accessory and a DTGS detector. A number of 256 scans at a resolution of 2 cm^{-1} were averaged from wave number 4000–400 cm^{-1}. The Opus software was used for data handling.

2.5. Biological assays

The human cervical carcinoma HeLa cell line and 3T3 murine fibroblasts (kindly provided by Dr. A. Diana, University of Cagliari) were grown in DMEM medium supplemented with 10% fetal bovine serum (FBS), 2 mM L-Glutamine, penicillin (100U/mL) and streptomycin (100 μg/mL) at 37 °C in 5% CO_2.

Cell Growth was evaluated culturing 3×10^4/mL Hela cells in 12 well plates. The day after (t = 0) cells were treated with 50 μg/mL of MSN-NH_2, and with HA-modified MSNs (MSN-HA_S, MSN-HA_M and MSN-HA_L). After 24 h nanoparticles were removed, and cells were cultured with fresh medium. Cell counts were performed immediately (t = 24 h), after 24 (t = 24 h + 24 h) and 48 (t = 24 h + 48 h) h following nanoparticles removal, using a Scepter Cell Counter, Millipore. All the experiments were performed at least in triplicate for each group.

For fluorescence microscopy, HeLa cells were grown in Dulbecco's Modified Eagle's Medium (DMEM; Sigma Aldrich) supplemented with fetal calf serum (10%) at 37 °C in a humidified atmosphere containing 5% CO_2. Cells were seeded in 3 cm dishes containing glass coverslips at a density of 1×10^5/ mL, left to grow for 24 h, and then incubated with 50 μg/mL FITC-MSN-NH_2 or FITC-MSN-HA_X, where x = L (long), M (medium), and S (short) HA chain, for varying times (4 and 24 h) either at 37 °C or 4 °C. After incubation, the cells were washed with PBS to remove unbound nanoparticles, fixed with paraformaldehyde (4%), stained with the nuclear dye Hoechst 33342 and observed through a fluorescence microscope (Olympus BX41) or processed for immunocytochemistry.

For immunocytochemistry assay, cells on coverslips were preincubated with normal goat serum (1:5, Vector, Burlingame, CA, USA) for 30 min. Cells were then overlaid for 60 min at room temperature with the mouse anti-CD44 antibody (1:200, Chemicon). Then the cells were washed three times with PBS and subsequently incubated for 1 h with an anti-mouse IgG conjugated with Alexa Fluor 594 (1:500, Molecular Probes). Nuclei were counterstained with Hoechst 33342. Negative controls were routinely performed for each experiment, incubating the samples with non-immune serum and then with appropriate secondary antibody. Imaging was carried out using an Olympus BX41 fluorescence microscope.

A quantitative determination of the cellular uptake was provided by flow cytometry measurement. HeLa cells (1×10^5/mL) seeded in 6 cm plates were grown for 24 h and then treated with FITC-MSN-NH_2 or FITC-MSN-HA (HA_S, HA_M, HA_L) for 4 h either at 37 °C or 4 °C. After incubation, the cells were washed with PBS, harvested by trypsinization, suspended in PBS and analyzed by a FACSCANTO flow cytometer (BD-Bioscience) and analyzed with FACSDiva software Version 6.1.3 (BD Biosciences) and FloJo V7.6.5 software.

MSNs internalization was also visualized through Transmission Electron Microscopy. Samples of HeLa cells, incubated with MSN-NH_2, and with HA-modified MSNs (MSN-HA_S, MSN-HA_M and MSN-HA_L) for 24 h at 37°, were fixed for 2 h in a solution of 1% (para)formaldehyde (Electron Microscopy Sciences) and 1.25% glutaraldehyde (Electron Microscopy Sciences) in 0.1 M sodium cacodylate (Electron Microscopy Sciences) buffer, at pH 7.4. After rinsing in the same buffer after fixation, samples were postfixed in 1% osmium tetroxide for 1 h and stained in 0.25% aqueous uranyl acetate overnight at 4 °C. Dehydration of cell cultures in an ascending graded series of ethanol and xylene was followed by infiltration and embedding in Epon 812 resin. The specimens were transferred to flat embedding molds and polymerized in an oven at 60 °C for 24 h. Finally, thin sections (60–90 nm thick) were cut with a LKB ultratome 8800 ultramicrotome, post-stained with uranyl acetate and bismuth subnitrate, observed and photographed in a transmission electron microscope (JEOL 100S model, Tokyo, Japan) operating at 80 kV.

3. Results and discussion

Functionalized MSNs, prepared according to methods described in the previous section, were firstly characterized for their structural, textural and surface properties through TEM, SAXS, N_2 adsorption isotherms, along with FTIR, TGA, DLS and ELS experiments. Then, to evaluate biocompatibility and cell internalization

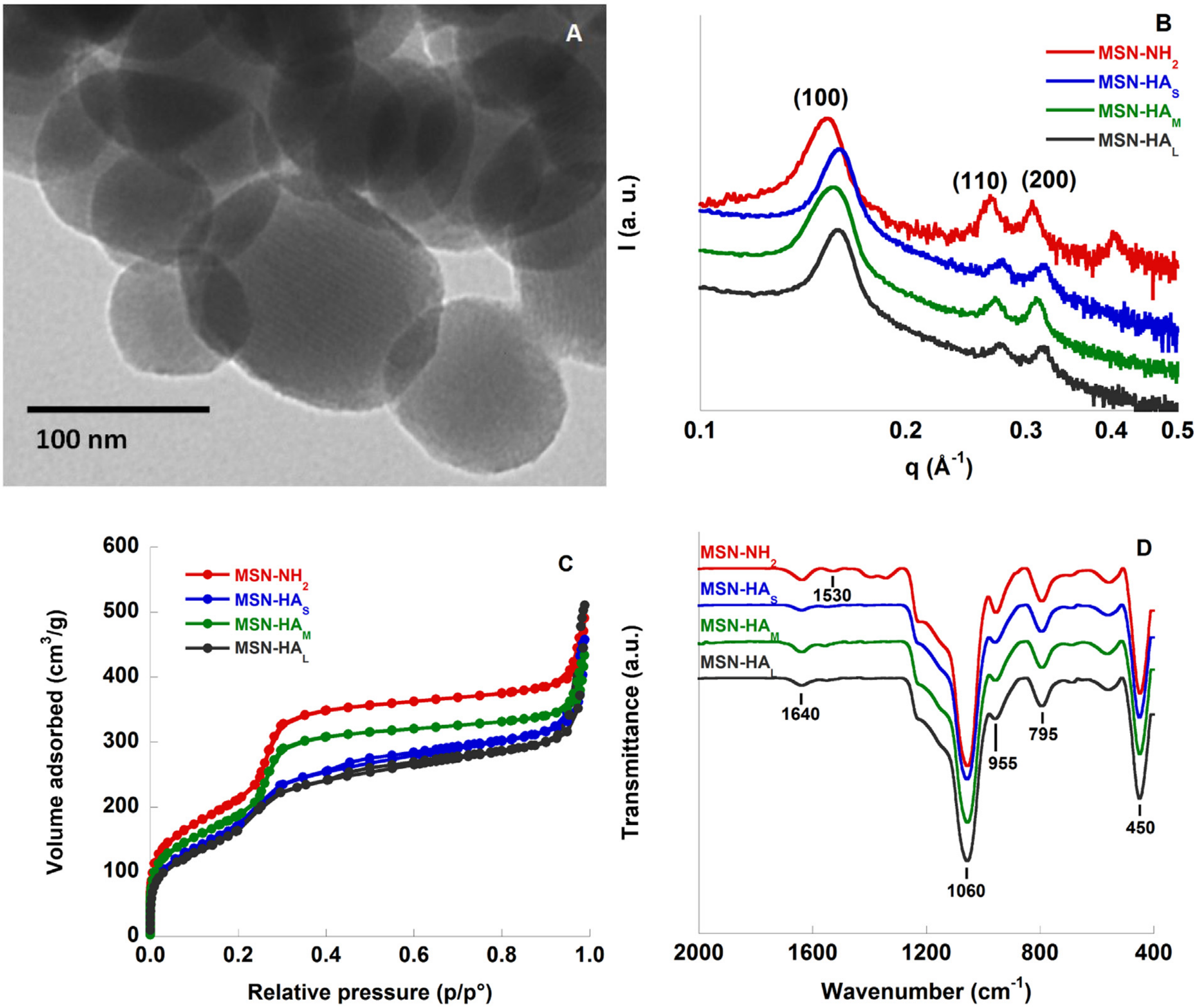

Fig. 1. Characterization of Functionalized MSNs: (A) TEM micrograph, (B) SAXS pattern, (C) N_2 Adsorption/desorption isotherms, and (D) FTIR spectra obtained for functionalized MSNs.

performance, biological assays on HeLa cells were performed using image techniques, namely optical and electron microscopy.

3.1. *Characterization of functionalized MSN samples*

A TEM micrograph of MSNs is shown in Fig. 1A. The particles are almost spherical and display, as expected, parallel pore channels. The SAXS patterns of MSN-NH_2, MSN-HA_S, MSN-HA_M and MSN-HA_L, shown in Fig. 1B, are typical of hexagonal structures, displaying an intense peak due to reflection of (100) plane and two weak peaks due to the reflection of (110) and (200) planes, respectively. This result confirms that the functionalization preserves the original ordered structure of the materials. The lattice parameters, calculated using the usual equation $a_{Hex} = (2/3^{.5}) \times (h^2 + k^2 + l^2)^{.5}$, are reported in Table 1. The N_2 adsorption/desorption isotherms of MSNs materials are reported in Fig. 1C. They exhibit the typical trend of type IV isotherms, with a sharp increase of gas volume adsorption at relative pressure values in the range 0.2–0.4 p/p°. Table 1 reports also the data of surface area (S_{BET}), pore diameter (d_{BJH}) and pore volume (V_{pBJH}), whereas Fig. S2A shows the pore size distribution obtained for the functionalized materials. The FTIR spectra reported in Fig. 1D for the same samples show the characteristic peaks of silica materials, two peaks at 1060 cm^{-1} and 800 cm^{-1} due to the asymmetric and symmetric stretching vibration of Si-O-Si, respectively, and other two at 450 cm^{-1} and 960 cm^{-1} that can be related to O-Si-O bending and Si-OH stretching, respectively [76,77]. Surface functionalization is confirmed by the presence of two peaks at 1530 and 1640 cm^{-1} that are related to $-NH_2$ bending [78] and C=O stretching [79] for NH_2- and HA-modified MSNs, respectively. Concerning the peak at 1640 cm^{-1}, it cannot be excluded that it could also be due to the C=O stretching of NHS used to activate the $-COOH$ groups of HA. Nonetheless, NHS is soluble in water and its excess has likely been fully removed during the last synthesis step where an extensive washing of the sample was carried out. In any case the functionalization of MSN-NH_2 with HA is confirmed by TGA and ELS measurements as described below. Fig. S2 B displays the percentage mass loss as a function of temperature for functionalized MSNs. Values of mass loss below and above 200 °C are reported in Table 1. For temperature below 200 °C mass loss is due to the removal of humidity and to the condensation of surface silanols. More interesting are the results at temperature above 200 °C when organic groups are burnt, although the mass loss measured for MSN-HA_L is relatively low compared to those found particularly for MSN-HA_M sample.

3.2. *Electrophoretic (ELS) and dynamic (DLS) and light scattering measurements*

The functionalized MSNs materials were also characterized through electrophoretic light scattering (ELS) (Fig. S2C) and

Please cite this article in press as: V. Nairi, et al., Mesoporous silica nanoparticles functionalized with hyaluronic acid. Effect of the biopolymer chain length on cell internalization, Colloids Surf. B: Biointerfaces (2018), https://doi.org/10.1016/j.colsurfb.2018.02.019

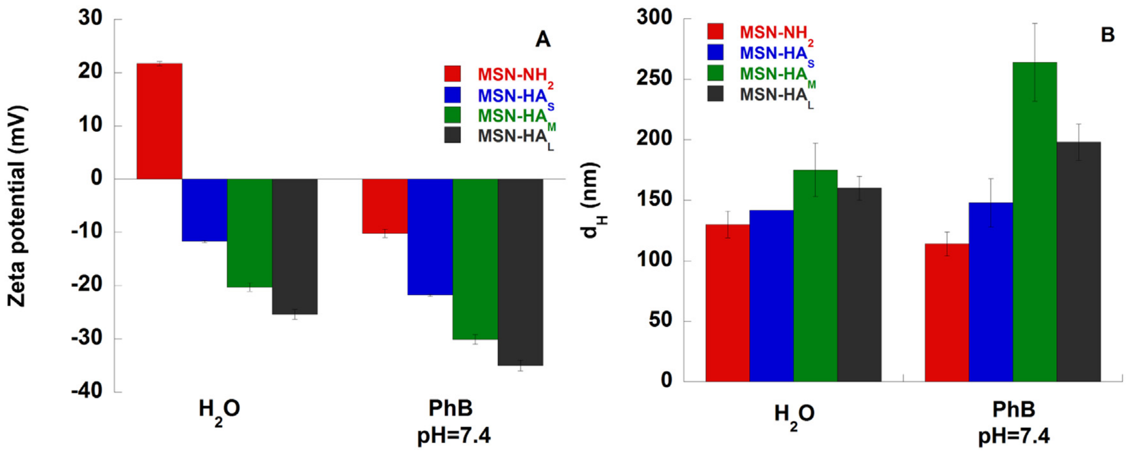

Fig. 2. Functionalized MSNs suspended in water and phosphate buffer PhB at pH 7.4. (A) Zeta potential and (B) hydrodinamic diameter, at 37 °C.

Table 1
Characterization of functionalized MSNs. Surface area (S_{BET}), pore diameter (d_{BJH}), pore volume (V_p), and lattice parameter (a) of Functionalized MSNs. TGA measurements: mass loss (%). pH, zeta potential (ζ) values from ELS, and hydrodynamic diameters (d_H) from DLS (in milliQ water at 25 °C).

Sample	$^{a}S_{BET}$ (m^2/g)	$^{b}d_{Des,BJH}$ (Å)	$^{c}V_{pDes,BJH}$ (cm^3/g)	^{d}a (Å)	^{e}Mass loss (%)	^{f}Mass loss (%)	pH	$^{e}\zeta$ (mV)	$^{e}d_H$ (nm)
MSN-NH$_2$	805	23.0	0.64	47.0	10.2	12.0	4.23	+34 ± 1	160 ± 6
MSN-HA$_S$	753	21.3	0.75	45.2	8.0	12.1	8.65	−11.3 ± 0.2	192 ± 15
MSN-HA$_M$	711	23.0	0.56	43.8	7.6	17.3	8.46	−17 ± 3	197 ± 8
MSN-HA$_L$	735	20.6	0.83	45.4	7.6	15.7	8.73	−20.4 ± 0.7	168 ± 11

[a] Surface area calculated by the BET method. [b] Pore diameter from the desorption branch calculated by BJH method. [c] Pore volume from the desorption branch calculated at $p/p^{\circ} = 0.99$ by BJH method. [d] Lattice parameter obtained by SAXS. [e] $T < 200$ °C. [f] $T > 200$ °C [e] Reported values are the average of at least three measurements.

dynamic light scattering DLS (Fig. S2D) measurements to highlight the effects of the external functionalization. As reported in Table 1 and in Fig. S2C, ζ values change as a result of the functionalization with the biopolymer. Indeed the positive value obtained for MSN-NH$_2$ (+34 mV) becomes negative for MSN-HA systems, due to the presence of carboxylic groups in the biopolymer's chain. Furthermore ζ values become more negative with increasing the length of HA's chain, and then the number of dissociated carboxylic groups as demonstrated by the basic pH values. From DLS measurements we would expect an increase, of the particle's size, $d_{H,}$ (Table 1, and Fig. S2D) along the series: MSN-NH$_2$ < MSN-HA$_S$ < MSN-HA$_M$ < MSN-HA$_L$. In fact, d_H increased going from MSN-NH$_2$ (160 ± 6 nm) to MSN-HA$_S$ (192 ± 15 nm), but remained unchanged for MSN-HA$_M$ (197 ± 8 nm), and decreased for MSN-HA$_L$ (168 ± 11 nm) as obtained through DLS analysis. The increase of biopolymer chain length, going from HA$_S$ (MW = 8–15 kDa) to HA$_M$ (MW = 30–50 kDa), and to HA$_L$ (MW = 90–130 kDa) increases the probability of a multi-point attachment of HA on MSN-NH$_2$ which simply does not allow the full disentanglement of the biopolymer chain. This is likely the reason of the counterintuitive trend of measured d_H values. However, independently of the hydrodynamic diameter and HA's MW, all grafted-HA MSNs produce the inversion of the zeta potential. This was ζ = +34 mV for MSN-NH$_2$ and became negative for MSN-HA samples (ζ = − 11, −17, −20 mV for short, medium, and long HA) paralleled by a strong increase of pH (from 4.2 to 8.5–8.7), as a result of a high number of dissociated carboxylic groups. The long biopolymer chains of HA$_L$, multi-point attached and entangled over the MSN-NH$_2$ surface may produce a thick layer that increases the negative ζ, but does not enlarge the average particle's diameter of MSN-HA$_L$ sample significantly.

In the perspective of using MSNs in biological media, the observation that HA grafting on the MSN-NH$_2$ surface produces a strong effect on the pH of the aqueous dispersions of the functionalized MSNs, suggested to deepen the characterizations evaluating the effect of pH using a pH buffer, at 37 °C. The functionalized MSNs suspended in water, 25 mM phosphate buffer at pH = 7.4 (PhB) were examined at 37 °C through ELS and DLS. The results are presented in Fig. 2 and Table S1.

As expected in water medium at 37 °C, ζ values are positive for MSN-NH$_2$ and negative for MSN-HA systems, being the values very similar to those determined at 25 °C. In phosphate buffer at pH 7.4 all functionalized MSNs display negative values of ζ, being the ζ values increasingly negative according to the following sequence: −NH$_2$ < −HA$_S$ < −HA$_M$ < −HA$_L$. Comparing these values to those measured in water a significant adsorption of the $H_2PO_4^-$ and HPO_4^{2-} anions at the solid surface can be suggested not only for MSN-NH$_2$ (that is expected as a result of strong electrostatic interactions induced particularly by divalent HPO_4^{2-} anions), but also for HA-grafted MSNs (see ζ values in Table S1): in the latter case the adsorption of buffer anions is likely due to specific interactions originated by van der Waals (non-electrostatic) forces [80–82]. Turning the attention to the particles' size d_H determined through DLS (see Fig. 2B) we may remark the rather high standard deviations of the obtained values (Table S2). Again we observe the apparently anomalous d_H values measured for MSN-HA$_L$ in both media (water, PhB at pH = 7.4), as in the case of data at 25 °C, reported in Table S1.

3.3. *Optical microscopy*

To evaluate the cellular uptake, HeLa cells were treated with FITC-conjugated MSN-HA particles and studied by fluorescence microscopy and cytofluorimetry. As shown in Fig. 3, after 4 h of treatment at 37 °C, all MSNs were internalized by cells. In particular, MSN-HA uptake is likely mediated by CD44 receptors, that are highly expressed in HeLa cells (Fig. 3). In fact, when a similar experiment was performed at 4 °C, nanoparticles were not internalized, suggesting that an ATP-dependent endocytosis is involved in MSN-HA uptake which is relatively inactive at low temperatures (Fig. 3) [83]. On the other hand, when HeLa cells were incubated with MSN-NH$_2$ at 4 °C, a strong fluorescence was observed on the surface of cells, likely due to an attractive interaction between positively charged nanoparticles and negatively charged phospholipids of cell membrane (Fig. 3) [84].

Please cite this article in press as: V. Nairi, et al., Mesoporous silica nanoparticles functionalized with hyaluronic acid. Effect of the biopolymer chain length on cell internalization, Colloids Surf. B: Biointerfaces (2018), https://doi.org/10.1016/j.colsurfb.2018.02.019

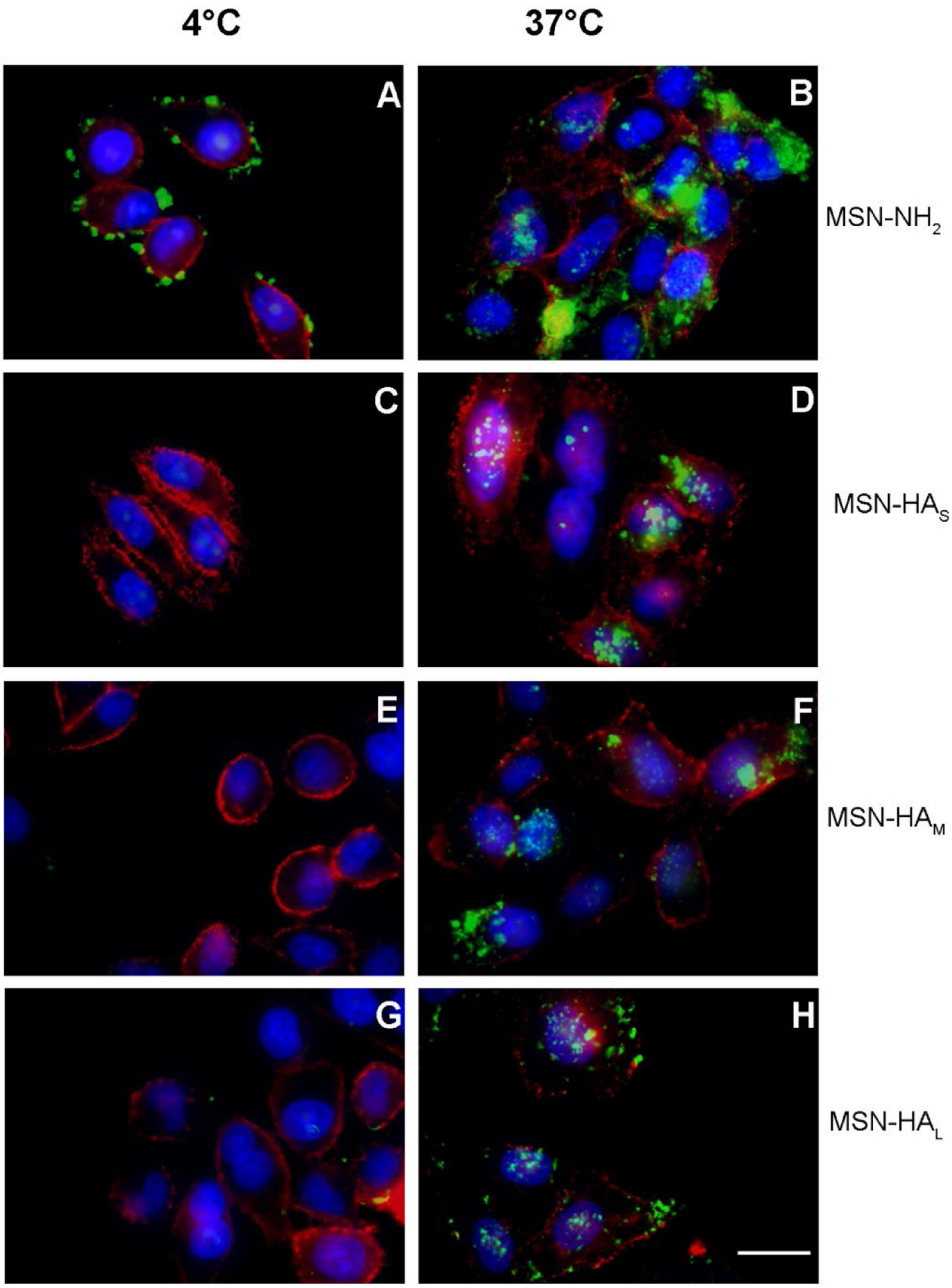

Fig. 3. Fluorescence microscopy images of HeLa cells treated for 4 h at different temperatures (4 °C and 37 °C) with FITC labeled MSNs. Cell membranes are immunostained with CD44 antibody (red) and nuclei are stained with Hoechst (blue). Bar: 20 μm. (For interpretation of the references to colour in this figure legend, the reader is referred to the web version of this article.)

Moreover, we compared the cell internalization of MSN-HA in HeLa cells and in a CD44 receptor-negative cell line (3T3 cells). In contrast to HeLa, the rate of MSNs internalization was very low in 3T3 cells after 4 h incubation with MSN- HA$_S$ (Fig. S3), as already observed by Zhao et al. [83] and Wang et al. [85]. This highlights the importance of CD44 receptors to mediate cell uptake. On the other hand, our previous results showed MSN-HA uptake by 3T3 after 24 h incubation [29], suggesting that alternative internalization mechanisms may take place in these cells following prolonged MSN-HA exposure.

A quantitative evaluation of the cellular uptake was provided by cytofluorimeter analysis that confirmed results obtained by microscopy (Fig. S4). In addition, cytofluorimetry showed a different rate of internalization, since MSN-NH$_2$ and MSN-HA$_S$ particles were internalized by all cells, whereas both MSN-HA$_M$ and MSN-HA$_L$ were detected only in about 50% of cells. These differences were detected also by fluorescence microscopy after 24 h treatment (Fig. S5). MSN particle internalization does not affect cell growth and proliferation as indicated by cell count results (Fig. S6).

3.4. Electron microscopy

TEM experiments highlighted a well preserved ultrastructure of HeLa cells after treatment with MSNs, being mainly characterized by the presence of a well-developed Golgi apparatus, endoplasmic reticulum and several mitochondria in their cytoplasm. TEM observations confirmed the fluorescence microscopy results, highlighting the presence of functionalized MSNs in the cytoplasm of the

Please cite this article in press as: V. Nairi, et al., Mesoporous silica nanoparticles functionalized with hyaluronic acid. Effect of the biopolymer chain length on cell internalization, Colloids Surf. B: Biointerfaces (2018), https://doi.org/10.1016/j.colsurfb.2018.02.019

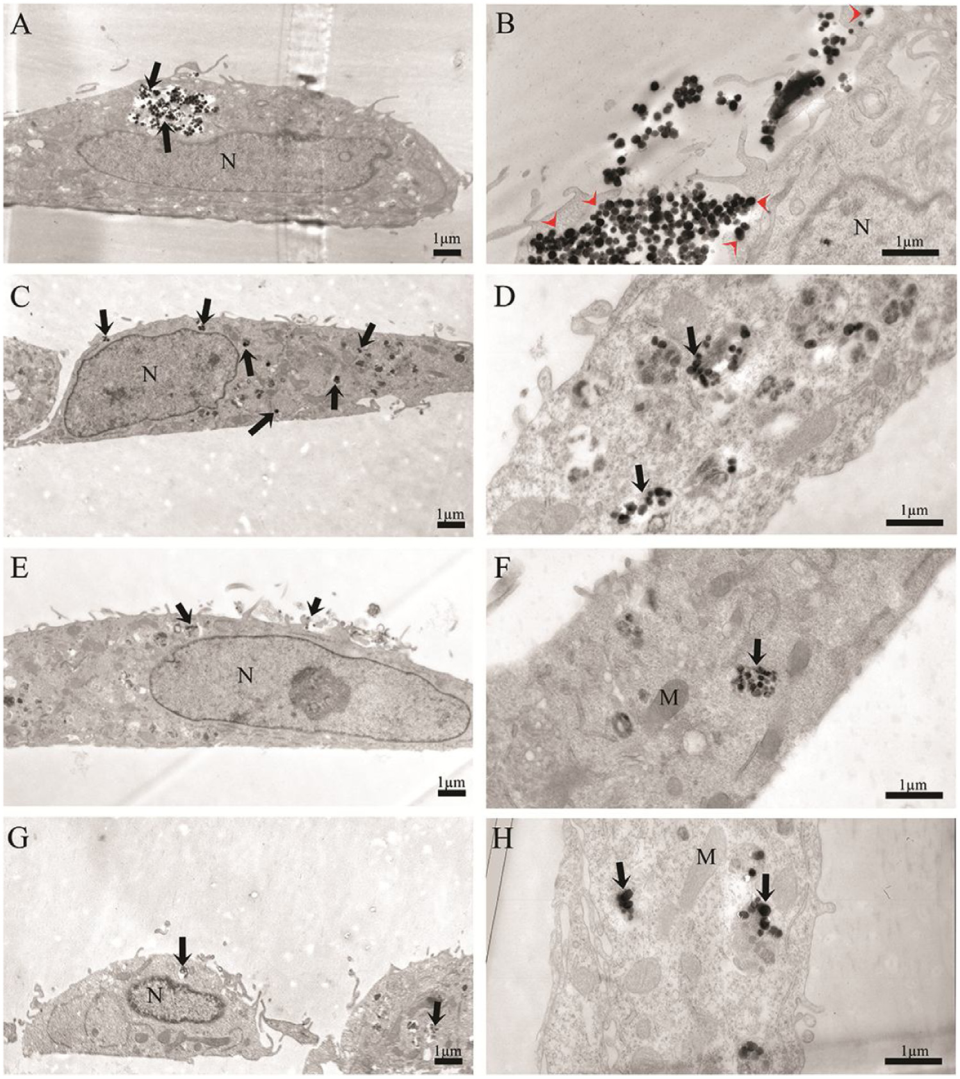

Fig. 4. Electron micrographs of HeLa cells incubated for 24 h: (A-B) MSN-NH_2, (C-D) MSN-HA_S, (E-F) MSN-HA_M, (G-H) MSN-HA_L. Black arrows show the presence of the internalized MSNs. (B) Detail of cytoplasmic portion of HeLa cell displaying intense MSN-NH_2 interaction with the external cellular surface (red arrowheads).

HeLa cells after treatment with all types of particles (Fig. 4) [31,86]. No MSNs were detected in the nuclear compartment (Fig. 4).

The MSNs were found confined within cytoplasmic vesicles delimited by a single membrane, suggesting an endocytosis process for all types of functionalized particles. This mechanism of internalization was proposed also by Guo and co-workers [87] which explained how particle size can affect the mechanism and the rate of cellular internalization. Indeed, MSNs with dimensions around 200 nm are easily internalized with an endocytosis process. However, differences concerning the amount of internalized MSNs were observed. In detail, the HeLa cells following the MSN-NH_2 and MSN-HA_S treatment exhibited the larger amount of internalized MSNs and cell surface interacting MSNs (Fig. 4A–D), whereas only few internalized MSNs were observed following MSN-HA_M, and MSN-HA_L exposure (Fig. 4E–H). Interestingly, a higher association of MSN-NH_2 to the cellular surface was observed (Fig. 4 B).

The Optical microscopy and TEM results indicate that two different internalization mechanisms occur for MSN-NH_2 and MSN-HA samples. Indeed, while for MSN-NH_2 the uptake is mediated by the electrostatic attraction between the positive surface charge of the material and the negatively charged cell membrane, for MSN-HA samples the uptake is likely mediated by CD44 receptors overexpressed in HeLa cells (Fig. 3). Indeed, the MSN-HA internalization process occurred at 37 °C only, whereas is inhibited at 4 °C, likely due to the inactivation of the ATP-dependent endocytosis at low temperature (see Figs 3–4).

4. Conclusions

In this work the behavior of different MSNs samples, functionalized with amino groups and HA with increasing chain length ($HA_{S} > HA_{M} > HA_{L}$), was investigated. They showed different ζ and hydrodynamic diameter in distilled water and at pH 7.4. We found an apparently anomalous d_H value of MSN-HA_L, which was smaller than values obtained for the other samples (MSN-HA_S and MSN-HA_M). These smaller d_H values observed for MSN-HA_L are likely due to the high MW and possible multi-point attachment of HA chains entangled over the solid surface [88]. The internalization of MSNs samples on HeLa cells was then evaluated. Cells were incubated at 37 °C and 4 °C with the MSNs and visualized through optical and electron microscopy. The image findings suggest important details on the internalization mechanism driven by the ATP-dependent endocytosis, and also by CD44 receptors in the case of HA functionalized MSNs. Remarkably, MSN-NH_2 adsorbs at HeLa surface (Fig. 3A) also at low temperature because of a favorable electrostatic interaction. Finally, the chain length has also an effect on

Please cite this article in press as: V. Nairi, et al., Mesoporous silica nanoparticles functionalized with hyaluronic acid. Effect of the biopolymer chain length on cell internalization, Colloids Surf. B: Biointerfaces (2018), https://doi.org/10.1016/j.colsurfb.2018.02.019

internalization efficiency since this was high for MSN-HA_S and low for MSN-HA_L. This is a relevant finding which is important for the realization of targeting drug delivery systems for cancer treatment.

Acknowledgments

Financial supports from, FIR 2016-17, RAS and Fondazione di Sardegna (CUP F72F16003070002, 2017) and MIUR (FFABR 2017) are gratefully acknowledged. V. Nairi thanks MIUR for financing her PhD scholarship. M. Vallet-Regì thanks The European Research Council (Advanced Grant VERDI; ERC-2015-AdG Proposal no. 694160) and Visiting Scientists 2016 program financed by RAS (Regione Autonoma della Sardegna).

Appendix A. Supplementary data

Supplementary data associated with this article can be found, in the online version, at https://doi.org/10.1016/j.colsurfb.2018.02.019.

References

[1] J. Zhang, Y. Sun, B. Tian, K. Li, L. Wang, Y. Liang, J. Han, Multifunctional mesoporous silica nanoparticles modified with tumor-shedable hyaluronic acid as carriers for doxorubicin, Colloids Surf. B, Biointerfaces 144 (2016) 293–302, http://dx.doi.org/10.1016/j.colsurfb.2016.04.015.

[2] S. Misra, P. Heldin, V.C. Hascall, N.K. Karamanos, S.S. Skandalis, R.R. Markwald, S. Ghatak, Hyaluronan-CD44 interactions as potential targets for cancer therapy, FEBS J. 278 (2011) 1429–1443, http://dx.doi.org/10.1111/j.1742-4658.2011.08071.x.

[3] A. Giordano, U. Galderisi, From the laboratory bench to the patient ' s bedside: an update on clinical trials with mesenchymal stem cells, J. Cell. Physio. (2006) 27–35, http://dx.doi.org/10.1002/jcp.20959.

[4] V. Sordi, M.L. Malosio, F. Marchesi, A. Mercalli, R. Melzi, T. Giordano, N. Belmonte, G. Ferrari, B.E. Leone, F. Bertuzzi, G. Zerbini, P. Allavena, E. Bonifacio, L. Piemonti, Bone marrow mesenchymal stem cells express a restricted set of functionally active chemokine receptors capable of promoting migration to pancreatic islets, Blood 106 (2017) 419–428, http://dx.doi.org/10.1182/blood-2004-09-3507 (Supported).

[5] F. Danhier, O. Feron, V. Préat, To exploit the tumor microenvironment: passive and active tumor targeting of nanocarriers for anti-cancer drug delivery, J. Controlled Release 148 (2010) 135–146, http://dx.doi.org/10.1016/j.jconrel.2010.08.027.

[6] D. Mehn, P. Iavicoli, N. Cabaleiro, S. Even, F. Caputo, O. Geiss, L. Calzolai, F. Rossi, D. Gilliland, Analytical ultracentrifugation for analysis of doxorubicin loaded liposomes, Int. J. Pharm. 523 (2017) 320–326, http://dx.doi.org/10.1016/j.ijpharm.2017.03.046.

[7] S. Matviykiv, M. Buscema, T. Mészáros, G. Gerganova, T. Pfohl, A. Zumbühl, J. Szebeni, B. Müller, Liposomes Bio-inspired nano-containers for physically triggered targeted drug delivery, Proc. SPIE – Int. Soc. Opt. Eng. 10162 (2017) 1–14, http://dx.doi.org/10.1117/12.2258378.

[8] P. Kumari, O.S. Muddineti, S.V.K. Rompicharla, P. Ghanta, A.K. B B N, B. Ghosh, S. Biswas, Cholesterol-conjugated poly(D, L-lactide)-based micelles as a nanocarrier system for effective delivery of curcumin in cancer therapy, Drug Deliv. 24 (2017) 209–223, http://dx.doi.org/10.1080/10717544.2016.1245365.

[9] V. Nairi, L. Medda, M. Monduzzi, A. Salis, Adsorption and release of ampicillin antibiotic from ordered mesoporous silica, J. Colloid Interface Sci. 497 (2017) 217–225, http://dx.doi.org/10.1016/j.jcis.2017.03.021.

[10] G. Villaverde, A. Baeza, G.J. Melen, A. Alfranca, M. Ramirez, M. Vallet-Regí, A new targeting agent for the selective drug delivery of nanocarriers for treating neuroblastoma, J. Mater. Chem. B 3 (2015) 4831–4842, http://dx.doi.org/10.1039/C5TB00287G.

[11] L.B. de O. Freitas, L. de M. Corgosinho, Faria J.A.Q.A, V.M. dos Santos, J.M. Resende, A.S. Leal, D.A. Gomes, E.M.B. de Sousa, Multifunctional mesoporous silica nanoparticles for cancer-targeted, controlled drug delivery and imaging, Microporous Mesoporous Mater. 242 (2017) 271–283, http://dx.doi.org/10.1016/j.micromeso.2017.01.036.

[12] V. Nairi, S. Medda, M. Piludu, M.F. Casula, M. Vallet-Regì, M. Monduzzi, A. Salis, Interactions between bovine serum albumin and mesoporous silica nanoparticles functionalized with biopolymers, Chem. Eng. J. (2018), http://dx.doi.org/10.1016/j.cej.2018.01.011, in press.

[13] R. ling Qi, X. jiao Tian, R. Guo, Y. Luo, M. wu Shen, J. yong Yu, X. yang Shi, Controlled release of doxorubicin from electrospun MWCNTs/PLGA hybrid nanofibers, Chin. J. Polymer Sci. (Engl. Ed.) 34 (2016) 1047–1059, http://dx.doi.org/10.1007/s10118-016-1827-z.

[14] A. Di Martino, O.A. Guselnikova, M.E. Trusova, P.S. Postnikov, V. Sedlarik, Organic-inorganic hybrid nanoparticles controlled delivery system for anticancer drugs, Int. J. Pharm. 526 (2017) 380–390, http://dx.doi.org/10.1016/j.ijpharm.2017.04.061.

[15] H. Chen, D. Liu, Z. Guo, Endogenous stimuli-responsive nanocarriers for drug delivery, Chem. Lett. 45 (2016) 242–249, http://dx.doi.org/10.1246/cl.151176.

[16] M. Vallet-Regi, A. Rámila, R.P. Del Real, J. Pérez-Pariente, A new property of MCM-41: drug delivery system, Chem. Mater. 13 (2001) 308–311, http://dx.doi.org/10.1021/cm0011559.

[17] L. Palanikumar, E.S. Choi, J.Y. Cheon, S.H. Joo, J.-H. Ryu, Noncovalent polymer-gatekeeper in mesoporous silica nanoparticles as a targeted drug delivery platform, Adv. Funct. Mater. 25 (2015) 957–965, http://dx.doi.org/10.1002/adfm.201402755.

[18] L. Chen, Z. Zhang, X. Yao, X. Chen, X. Chen, Intracellular pH-operated mechanized mesoporous silica nanoparticles as potential drug carries, Microporous Mesoporous Mater. 201 (2015) 169–175, http://dx.doi.org/10.1016/j.micromeso.2014.09.023.

[19] J.L. Paris, M.V. Cabanas, M. Manzano, M. Vallet-Regí, Polymer-Grafted mesoporous silica nanoparticles as ultrasound-responsive drug carriers, ACS Nano 9 (2015) 11023–11033, http://dx.doi.org/10.1021/acsnano.5b04378.

[20] A. Maleki, H. Kettiger, A. Schoubben, J.M. Rosenholm, V. Ambrogi, M. Hamidi, Mesoporous silica materials: from physico-chemical properties to enhanced dissolution of poorly water-soluble drugs, J. Controlled Release 262 (2017) 329–347, http://dx.doi.org/10.1016/j.jconrel.2017.07.047.

[21] M. Piras, A. Salis, M. Piludu, D. Steri, M. Monduzzi, 3D vision of human lysozyme adsorbed onto a SBA-15 nanostructured matrix, Chem. Commun. 47 (2011) 7338, http://dx.doi.org/10.1039/c1cc11840d.

[22] M. Piludu, L. Medda, F. Cugia, M. Monduzzi, A. Salis, Silver enhancement for transmission electron microscopy imaging of antibody fragment–gold nanoparticles conjugates immobilized on ordered mesoporous silica, Langmuir 31 (2015) 9458–9463, http://dx.doi.org/10.1021/acs.langmuir.5b02830.

[23] M. Monduzzi, S. Lampis, S. Murgia, A. Salis, From self-assembly fundamental knowledge to nanomedicine developments, Adv. Colloid Interface Sci. 205 (2014) 48–67, http://dx.doi.org/10.1016/j.cis.2013.10.009.

[24] M.S. Bhattacharyya, P. Hiwale, M. Piras, L. Medda, D. Steri, M. Piludu, A. Salis, M. Monduzzi, Lysozyme adsorption and release from ordered mesoporous materials, J. Phys. Chem. C 114 (2010) 19928–19934, http://dx.doi.org/10.1021/jp1078218.

[25] D. Steri, M. Monduzzi, A. Salis, Ionic strength affects lysozyme adsorption and release from SBA-15 mesoporous silica, Microporous Mesoporous Mater. 170 (2013) 164–172, http://dx.doi.org/10.1016/j.micromeso.2012.12.002.

[26] Y. Yan, J. Fu, X. Liu, T. Wang, X. Lu, Acid-responsive intracellular doxorubicin release from click chemistry functionalized mesoporous silica nanoparticles, RSC Adv. 5 (2015) 30640–30646, http://dx.doi.org/10.1039/C5RA00059A.

[27] Y. Wang, Q. Zhao, N. Han, L. Bai, J. Li, J. Liu, E. Che, L. Hu, Q. Zhang, T. Jiang, S. Wang, Mesoporous silica nanoparticles in drug delivery and biomedical applications, Nanomedicine: nanotechnology, Biol. Med. 11 (2015) 313–327, http://dx.doi.org/10.1016/j.nano.2014.09.014.

[28] P. Yang, S. Gai, J. Lin, Functionalized mesoporous silica materials for controlled drug delivery, Chem. Soc. Rev. 41 (2012) 3679–3698, http://dx.doi.org/10.1039/c2cs15308d.

[29] G. Zhou, L. Li, J. Xing, J. Cai, J. Chen, P. Liu, N. Gu, M. Ji, Layer-by-layer construction of lipid bilayer on mesoporous silica nanoparticle to improve its water suspensibility and hemocompatibility, J. Sol-Gel Sci. Technol. 82 (2017) 490–499, http://dx.doi.org/10.1007/s10971-017-4330-2.

[30] F. Danhier, O. Feron, V. Préat, To exploit the tumor microenvironment: passive and active tumor targeting of nanocarriers for anti-cancer drug delivery, J. Controlled Release 148 (2015) 135–146, http://dx.doi.org/10.1016/j.jconrel.2010.08.027.

[31] A. Salis, M. Fanti, L. Medda, V. Nairi, F. Cugia, M. Piludu, V. Sogos, M. Monduzzi, Mesoporous silica nanoparticles functionalized with hyaluronic acid and chitosan biopolymers. Effect of functionalization on cell internalization, ACS Biomater. Sci. Eng. 2 (2016) 741–751, http://dx.doi.org/10.1021/acsbiomaterials.5b00502.

[32] S. Williams, A. Neumann, I. Bremer, Y. Su, G. Dräger, C. Kasper, P. Behrens, Nanoporous silica nanoparticles as biomaterials: evaluation of different strategies for the functionalization with polysialic acid by step-by-step cytocompatibility testing, J. Mater. Sci. 26 (2015), http://dx.doi.org/10.1007/s10856-015-5409-3.

[33] Y. Yan, J. Fu, T. Wang, X. Lu, Controlled release of silyl ether camptothecin from thiol-ene click chemistry-functionalized mesoporous silica nanoparticles, Acta Biomater. 51 (2017) 471–478, http://dx.doi.org/10.1016/j.actbio.2017.01.062.

[34] A. Baeza, M. Colilla, M. Vallet-Regí, Advances in mesoporous silica nanoparticles for targeted stimuli-responsive drug delivery, Expert Opin. Drug Deliv. 12 (2015) 319–337, http://dx.doi.org/10.1517/17425247.2014.953051.

[35] C. de la Torre, I. Casanova, G. Acosta, C. Coll, M.J. Moreno, F. Albericio, E. Aznar, R. Mangues, M. Royo, F. Sancenón, R. Martínez-Máñez, Gated mesoporous silica nanoparticles using a double-role circular peptide for the controlled and target-preferential release of doxorubicin in CXCR4-expresing lymphoma cells, Adv. Funct. Mater. 25 (2015) 687–695, http://dx.doi.org/10.1002/adfm.201403822.

[36] Y.-J. Cheng, G.-F. Luo, J.-Y. Zhu, X.-D. Xu, X. Zeng, D.-B. Cheng, Y.-M. Li, Y. Wu, X.-Z. Zhang, R.-X. Zhuo, F. He, Enzyme-induced and tumor-targeted drug delivery system based on multifunctional mesoporous silica nanoparticles, ACS Appl. Mater. Interfaces 7 (2015) 9078–9087, http://dx.doi.org/10.1021/acsami.5b00752.

Please cite this article in press as: V. Nairi, et al., Mesoporous silica nanoparticles functionalized with hyaluronic acid. Effect of the biopolymer chain length on cell internalization, Colloids Surf. B: Biointerfaces (2018), https://doi.org/10.1016/j.colsurfb.2018.02.019

[37] M. Yu, S. Jambhrunkar, P. Thorn, J. Chen, W. Gu, C. Yu, Hyaluronic acid modified mesoporous silica nanoparticles for targeted drug delivery to CD44-overexpressing cancer cells, Nanoscale 5 (2013) 178–183, http://dx.doi.org/10.1039/c2nr32145a.

[38] A.F. Moreira, D.R. Dias, I.J. Correia, Stimuli-responsive mesoporous silica nanoparticles for cancer therapy: a review, Microporous Mesoporous Mater. 236 (2016) 141–157, http://dx.doi.org/10.1016/j.micromeso.2016.08.038.

[39] N. Zhao, X. Lin, Q. Zhang, Z. Ji, F.J. Xu, Redox-triggered gatekeeper-enveloped starlike hollow silica nanoparticles for intelligent delivery systems, Small 11 (2015) 6467–6479, http://dx.doi.org/10.1002/smll.201502760.

[40] X. Chen, H. Sun, J. Hu, X. Han, H. Liu, Y. Hu, Transferrin gated mesoporous silica nanoparticles for redox-responsive and targeted drug delivery, Colloids Surf. B: Biointerfaces 152 (2017) 77–84, http://dx.doi.org/10.1016/j.colsurfb.2017.01.010.

[41] L. Tan, H.-X. Wu, M.-Y. Yang, C.-J. Liu, R.-X. Zhuo, The dual-stimulated release of size-selected cargos from cyclodextrin-covered mesoporous silica nanoparticles, RSC Adv. 5 (2015) 10393–10399, http://dx.doi.org/10.1039/C4RA15574B.

[42] W.T. Liu, Y. Yang, P.H. Shen, X.J. Gao, S.Q. He, H. Liu, C.S. Zhu, Facile and simple preparation of pH-sensitive chitosan-mesoporous silica nanoparticles for future breast cancer treatment, Express Polymer Lett. 9 (2015) 1068–1075, http://dx.doi.org/10.3144/expresspolymlett.2015.96.

[43] D.R. Nogueira, L.E. Scheeren, L.B. Macedo, A.I.P. Marcolino, M. Pilar Vinardell, M. Mitjans, M. Rosa Infante, A.A. Farooqi, C.M.B. Rolim, Inclusion of a pH-responsive amino acid-based amphiphile in methotrexate-loaded chitosan nanoparticles as a delivery strategy in cancer therapy, Amino Acids 48 (2015) 157–168, http://dx.doi.org/10.1007/s00726-015-2075-1.

[44] Z. Li, D.L. Clemens, B.Y. Lee, B.J. Dillon, M.A. Horwitz, J.I. Zink, Mesoporous silica nanoparticles with pH-sensitive nanovalves for delivery of moxifloxacin provide improved treatment of lethal pneumonic Tularemia, ACS Nano 9 (2015) 10778–10789, http://dx.doi.org/10.1021/acsnano.5b04306.

[45] A. Popat, J. Liu, G.Q. (Max) Lu, S.Z. Qiao, A pH-responsive drug delivery system based on chitosan coated mesoporous silica nanoparticles, J. Mater. Chem. 22 (2012) 11173–11178, http://dx.doi.org/10.1039/c2jm30501a.

[46] X. Kang, Z. Cheng, D. Yang, P. Ma, M. Shang, C. Peng, Y. Dai, J. Lin, Design and synthesis of multifunctional drug carriers based on luminescent rattle-type mesoporous silica microspheres with a thermosensitive hydrogel as a controlled switch, Adv. Funct. Mater. 22 (2012) 1470–1481, http://dx.doi.org/10.1002/adfm.201102746.

[47] S. Baek, R.K. Singh, T.-H. Kim, J. Seo, U.S. Shin, W. Chrzanowski, H.-W. Kim, Triple hit with drug carriers: pH- and temperature-responsive theranostics for multimodal chemo- and photothermal therapy and diagnostic applications, ACS Appl. Mater. Interfaces 8 (2016) 8967–8979, http://dx.doi.org/10.1021/acsami.6b00963.

[48] E. Ugazio, L. Gastaldi, V. Brunella, D. Scalarone, S.A. Jadhav, S. Oliaro-Bosso, D. Zonari, G. Berlier, I. Miletto, S. Sapino, Thermoresponsive mesoporous silica nanoparticles as a carrier for skin delivery of quercetin, Int. J. Pharm. 511 (2016) 446–454, http://dx.doi.org/10.1016/j.ijpharm.2016.07.024.

[49] J.T. Lin, Z.K. Liu, Q.L. Zhu, X.H. Rong, C.L. Liang, J. Wang, D. Ma, J. Sun, G.H. Wang, Redox-responsive nanocarriers for drug and gene co-delivery based on chitosan derivatives modified mesoporous silica nanoparticles, Colloids Surf. B: Biointerfaces 155 (2017) 41–50, http://dx.doi.org/10.1016/j.colsurfb.2017.04.002.

[50] Q. Zhao, S. Wang, Y. Yang, X. Li, D. Di, C. Zhang, T. Jiang, S. Wang, Hyaluronic acid and carbon dots-gated hollow mesoporous silica for redox and enzyme-triggered targeted drug delivery and bioimaging, Mater. Sci. Eng.: C 78 (2017) 475–484, http://dx.doi.org/10.1016/j.msec.2017.04.059.

[51] K. Park, S.S. Park, Y.H. Yun, C.-S. Ha, Mesoporous silica nanoparticles functionalized with a redox-responsive biopolymer, J. Porous Mater. 24 (2017) 1215–1225, http://dx.doi.org/10.1007/s10934-017-0361-x.

[52] L. Chen, X. Zhou, W. Nie, Q. Zhang, W. Wang, Y. Zhang, C. He, Multifunctional redox-responsive mesoporous silica nanoparticles for efficient targeting drug delivery and magnetic resonance imaging, ACS Appl. Mater. Interfaces 8 (2016) 33829–33841, http://dx.doi.org/10.1021/acsami.6b11802.

[53] S. Chai, Y. Guo, Z. Zhang, Z. Chai, Y. Ma, L. Qi, Cyclodextrin-gated mesoporous silica nanoparticles as drug carriers for red light-induced drug release, Nanotechnology 28 (2017) 145101, http://dx.doi.org/10.1088/1361-6528/aa5e74.

[54] G. Wang, J. Dong, T. Yuan, J. Zhang, L. Wang, H. Wang, Visible light and pH responsive polymer-coated mesoporous silica nanohybrids for controlled release, Macromol. Biosci. 16 (2016) 990–994, http://dx.doi.org/10.1002/mabi.201600008.

[55] W. Li, P. Liao, C. Su, C. Yeh, Formation of oligonucleotide-gated silica shell-coated Fe 3 O 4 –Au core–shell nanotrisoctahedra for magnetically targeted and near-infrared light-responsive theranostic platform, J. Am. Chem. Soc. 136 (2014) 10062–10075, http://dx.doi.org/10.1021/ja504118q.

[56] W.-H. Chen, G.-F. Luo, Q. Lei, F.-Y. Cao, J.-X. Fan, W.-X. Qiu, H.-Z. Jia, S. Hong, F. Fang, X. Zeng, R.-X. Zhuo, X.-Z. Zhang, Rational design of multifunctional magnetic mesoporous silica nanoparticle for tumor-targeted magnetic resonance imaging and precise therapy, Biomaterials 76 (2016) 87–101, http://dx.doi.org/10.1016/j.biomaterials.2015.10.053.

[57] E. Che, Y. Gao, L. Wan, Y. Zhang, N. Han, J. Bai, J. Li, Z. Sha, S. Wang, Paclitaxel/gelatin coated magnetic mesoporous silica nanoparticles: preparation and antitumor efficacy in vivo, Microporous Mesoporous Mater. 204 (2015) 226–234, http://dx.doi.org/10.1016/j.micromeso.2014.11.013.

[58] Y.-H. Liao, S.A. Jones, B. Forbes, G.P. Martin, M.B. Brown, Hyaluronan: pharmaceutical characterization and drug delivery, Drug Deliv. 12 (2005) 327–342, http://dx.doi.org/10.1080/10717540590952555.

[59] E.D. Prè, G. Conti, A. Sbarbati, Hyaluronic acid (HA) scaffolds and multipotent stromal cells (MSCs) in regenerative medicine, Stem Cell Rev. Rep. 12 (2016) 664–681, http://dx.doi.org/10.1007/s12015-016-9684-2.

[60] N. Itano, K. Kimata, Mammalian hyaluronan synthases, IUBMB Life 1 (2002) 195–199, http://dx.doi.org/10.1080/15216540290114478.

[61] A.P. Spicer, T.K. Nguyen, Mammalian hyaluronan synthases: investigation of functional relationships in vivo, Biochem. Soc. Trans. 27 (1999) 109–115, http://dx.doi.org/10.1042/bst0270109.

[62] G. Mattheolabakis, L. Milane, A. Singh, M.M. Amiji, Hyaluronic acid targeting of CD44 for cancer therapy: from receptor biology to nanomedicine, J. Drug Target. 23 (2015) 605–618, http://dx.doi.org/10.3109/1061186X.2015.1052072.

[63] P. Kesharwani, L. Xie, S. Banerjee, G. Mao, S. Padhye, F.H. Sarkar, A.K. Iyer, Hyaluronic acid-conjugated polyamidoamine dendrimers for targeted delivery of 3 4-difluorobenzylidene curcumin to CD44 overexpressing pancreatic cancer cells, Colloids Surf. B: Biointerfaces 136 (2015) 413–423, http://dx.doi.org/10.1016/j.colsurfb.2015.09.043.

[64] Y. Zhong, K. Goltsche, L. Cheng, F. Xie, F. Meng, C. Deng, Z. Zhong, R. Haag, Hyaluronic acid-shelled acid-activatable paclitaxel prodrug micelles effectively target and treat CD44-overexpressing human breast tumor xenografts in vivo, Biomaterials 84 (2016) 250–261, http://dx.doi.org/10.1016/j.biomaterials.2016.01.049.

[65] J.-Y. Lee, U. Termsarasab, J.-H. Park, S.Y. Lee, S.-H. Ko, J.-S. Shim, S.-J. Chung, H.-J. Cho, D.-D. Kim, Dual CD44 and folate receptor-targeted nanoparticles for cancer diagnosis and anticancer drug delivery, J. Controlled Release 236 (2016) 38–46, http://dx.doi.org/10.1016/j.jconrel.2016.06.021.

[66] J.-E. Abdullah-Al-Nahain, I. Lee, H. In, K.D. Lee, J.H. Lee, S.Y. Jeong, Park, target delivery and cell imaging using hyaluronic acid-functionalized graphene quantum dots, Mol. Pharm. 10 (2013) 3736–3744, http://dx.doi.org/10.1021/mp400219u.

[67] H. Yao, Y. Zhang, L. Sun, Y. Liu, The effect of hyaluronic acid functionalized carbon nanotubes loaded with salinomycin on gastric cancer stem cells, Biomaterials 35 (2014) 9208–9223, http://dx.doi.org/10.1016/j.biomaterials.2014.07.033.

[68] X. Cao, L. Tao, S. Wen, W. Hou, X. Shi, Hyaluronic acid-modified multiwalled carbon nanotubes for targeted delivery of doxorubicin into cancer cells, Carbohydr. Res. 405 (2015) 70–77, http://dx.doi.org/10.1016/j.carres.2014.06.030.

[69] M. Yu, S. Jambhrunkar, P. Thorn, J. Chen, W. Gu, C. Yu, Hyaluronic acid modified mesoporous silica nanoparticles for targeted drug delivery to CD44-overexpressing cancer cells, Nanoscale 5 (2013) 178–183, http://dx.doi.org/10.1039/c2nr32145a.

[70] G. Yan, J. Wang, L. Hu, X. Wang, G. Yang, S. Fu, X. Cheng, P. Zhang, R. Tang, Stepwise targeted drug delivery to liver cancer cells for enhanced therapeutic efficacy by galactose-grafted, ultra-pH-sensitive micelles, Acta Biomater. 51 (2017) 363–373, http://dx.doi.org/10.1016/j.actbio.2017.01.031.

[71] C. Luo, J. Sun, B. Sun, Z. He, Prodrug-based nanoparticulate drug delivery strategies for cancer therapy, Trends Pharmacol. Sci. 35 (2014) 556–566, http://dx.doi.org/10.1016/j.tips.2014.09.008.

[72] S. Mura, J. Nicolas, P. Couvreur, Stimuli-responsive nanocarriers for drug delivery, Nat. Mater. 12 (2013) 991–1003, http://dx.doi.org/10.1038/nmat3776.

[73] S. Brunauer, P.H. Emmett, E. Teller, Adsorption of gases in multimolecular layers, J. Am. Chem. Soc. 60 (1938) 309–319, http://dx.doi.org/10.1021/ja01269a023.

[74] E.P. Barrett, L.G. Joyner, P.P. Halenda, The determination of pore volume and area distributions in porous substances. I. computations from nitrogen isotherm, J. Am. Chem. Soc. 73 (1951) 373–380, http://dx.doi.org/10.1021/ja01145a126.

[75] A. Tekrony, D. Cramb, Determination of the mobility of amine- and carboxy-terminated fluospheres and quantum dots by capillary electrophoresis, Can. J. Chem. 94 (2016) 430–435, http://dx.doi.org/10.1139/cjc-2015-0349.

[76] B.A. Morrow, A.J. McFarlan, Surface vibrational modes of silanol groups on silica, J. Phys. Chem. 96 (1992) 1395–1400, http://dx.doi.org/10.1021/j100182a068.

[77] D. Scarano, A. Zecchina, S. Bordiga, F. Geobaldo, G. Spoto, G. Petrini, G. Leofanti, M. Padovan, G. Tozzola, Fourier-Transform infrared and Raman-spectra of pure and Al, B-, Ti- and Fe-substituted silicalites: stretching-mode region, J. Chem. Soc.-Faraday Trans. 89 (1993) 4123–4130, http://dx.doi.org/10.1039/ft9938904123.

[78] F. Sevimli, A. Yılmaz, Surface functionalization of SBA-15 particles for amoxicillin delivery, Microporous Mesoporous Mater. 158 (2012) 281–291, http://dx.doi.org/10.1016/j.micromeso.2012.02.037.

[79] L. Medda, M.F. Casula, M. Monduzzi, A. Salis, Adsorption of lysozyme on hyaluronic acid functionalized SBA-15 mesoporous silica: a possible bioadhesive depot system, Langmuir 30 (2014) 12996–13004, http://dx.doi.org/10.1021/la503224n.

[80] F. Cugia, S. Sedda, F. Pitzalis, D.F. Parsons, M. Monduzzi, A. Salis, Are specific buffer effects the new frontier of Hofmeister phenomena? Insights from lysozyme adsorption on ordered mesoporous silica, RSC Adv. 6 (2016) 94617–94621, http://dx.doi.org/10.1039/C6RA17356J.

Please cite this article in press as: V. Nairi, et al., Mesoporous silica nanoparticles functionalized with hyaluronic acid. Effect of the biopolymer chain length on cell internalization, Colloids Surf. B: Biointerfaces (2018), https://doi.org/10.1016/j.colsurfb.2018.02.019

[81] A. Salis, L. Medda, F. Cugia, M. Monduzzi, Effect of electrolytes on proteins physisorption on ordered mesoporous silica materials, Colloids Surf. B: Biointerfaces 137 (2016) 77–90, http://dx.doi.org/10.1016/j.colsurfb.2015.04.068.

[82] A. Salis, M. Monduzzi, Not only pH. Specific buffer effects in biological systems, Curr. Opin. Colloid Interface Sci. 23 (2016) 1–9, http://dx.doi.org/10.1016/j.cocis.2016.04.004.

[83] Q. Zhao, J. Liu, W. Zhu, C. Sun, D. Di, Y. Zhang, P. Wang, Z. Wang, S. Wang, Dual-stimuli responsive hyaluronic acid-conjugated mesoporous silica for targeted delivery to CD44-overexpressing cancer cells, Acta Biomater. 23 (2015) 147–156, http://dx.doi.org/10.1016/j.actbio.2015.05.010.

[84] A. Verma, F. Stellacci, Effect of surface properties on nanoparticlea-cell interactions, Small 6 (2010) 12–21, http://dx.doi.org/10.1002/smll.200901158.

[85] Z. Wang, Y. Tian, H. Zhang, Y. Qin, D. Li, L. Gan, F. Wu, Using hyaluronic acid-functionalized pH stimuli-responsive mesoporous silica nanoparticles for targeted delivery to CD44-overexpressing cancer cells, Int. J. Nanomed. 11 (2016) 6485–6497, http://dx.doi.org/10.2147/IJN.S117184.

[86] Y. Xia, M. Li, T. Peng, W. Zhang, J. Xiong, Q. Hu, Z. Song, Q. Zheng, In vitro cytotoxicity of fluorescent silica nanoparticles hybridized with aggregation-induced emission luminogens for living cell imaging, Int. J. Mol. Sci. 14 (2013) 1080–1092, http://dx.doi.org/10.3390/ijms14011080.

[87] H. Guo, H. Qian, S. Sun, D. Sun, H. Yin, X. Cai, Z. Liu, J. Wu, T. Jiang, X. Liu, Hollow mesoporous silica nanoparticles for intracellular delivery of fluorescent dye, Chem. Cent. J. 5 (2011) 1–10, http://dx.doi.org/10.1186/1752-153X-5-1.

[88] S. Furlan, G. La Penna, A. Perico, A. Cesàro, Hyaluronan chain conformation and dynamics, Carbohydr. Res. 340 (2005) 959–970, http://dx.doi.org/10.1016/j.carres.2005.01.030.

Please cite this article in press as: V. Nairi, et al., Mesoporous silica nanoparticles functionalized with hyaluronic acid. Effect of the biopolymer chain length on cell internalization, Colloids Surf. B: Biointerfaces (2018), https://doi.org/10.1016/j.colsurfb.2018.02.019

Supporting Information

Mesoporous Silica Nanoparticles Functionalized with Hyaluronic Acid. Effect of the Biopolymer Chain Length on Cell Internalization

Valentina Nairi[1], Silvia Magnolia[1], Marco Piludu[2], Mariella Nieddu[2], Cristian Antonio Caria[3] , Valeria Sogos[2], Maria Vallet-Regì[4], Maura Monduzzi[1]* and Andrea Salis[1,]**

[1]Dipartmento di Scienze Chimiche e Geologiche, Università di Cagliari-CSGI and CNBS, Cittadella Universitaria, S.S. 554 bivio Sestu, 09042 Monserrato (CA), Italy
[2]Dipartimento di Scienze Biomediche, Università di Cagliari, Cittadella Universitaria, S.S. 554 bivio Sestu, 09042 Monserrato (CA), Italy
[3]Istituto di Ricerca Genetica e Biomedica, Consiglio Nazionale delle Ricerche, Cittadella Universitaria, S.S. 554 bivio Sestu, 09042 Monserrato (CA), Italy
[4]Departamento de Quimica Inorganica y Bioinorganica, Facultad de Farmacia, Universidad Complutense de Madrid, Plaza Ramon y Cajal s/n, Instituto de Investigacion Sanitaria Hospital 12 de Octubre i+12 ¡ Centro de Investigacion Biomedica en Red de Bioingenieria, Biomateriales y Nanomedicina (CIBER-BBN), Madrid, Spain

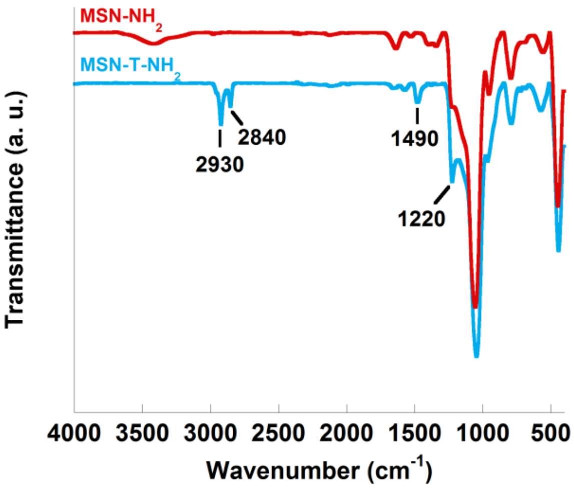

Fig. S1. FTIR spectra of before (MSN-T-NH$_2$) and after (MSN-NH$_2$) the removal of template.

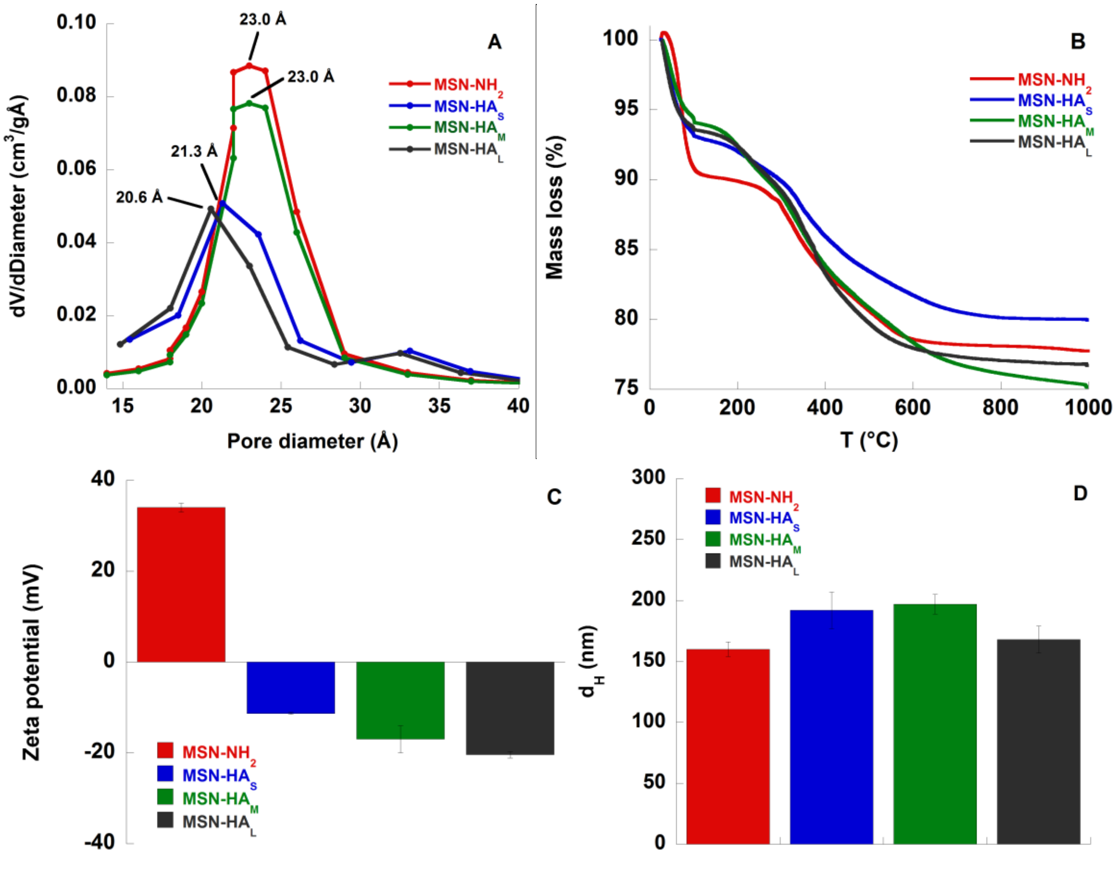

Fig. S2. (A) pore size distribution, (B) percentage mass loss profiles as a function of temperature, (C) Zeta potential (ζ) from ELS, and (D) hydrodynamic diameter (d$_H$) of functionalized MSNs.

Table S1. Values of ζ and d_H in water and 25 mM phosphate buffer (PhB) at pH=7.4 at 37°C for MSN-NH_2, MSN-HA_S, MSN-HA_M and MSN-HA_L.

	H_2O		**Ph-B pH=7.4**	
Sample	**ζ (mV)**	**d_H (nm)**	**ζ (mV)**	**d_H (nm)**
MSN-NH_2	+21.7±0.4	130±11	-10.2±0.8	114±10
MSN-HA_S	-11.7±0.2	142±14	-21.8±0.2	148±20
MSN-HA_M	-20.3±0.8	175±22	-30.1±0.9	264±32
MSN-HA_L	-25.4±0.9	160±10	-35±1	198±15

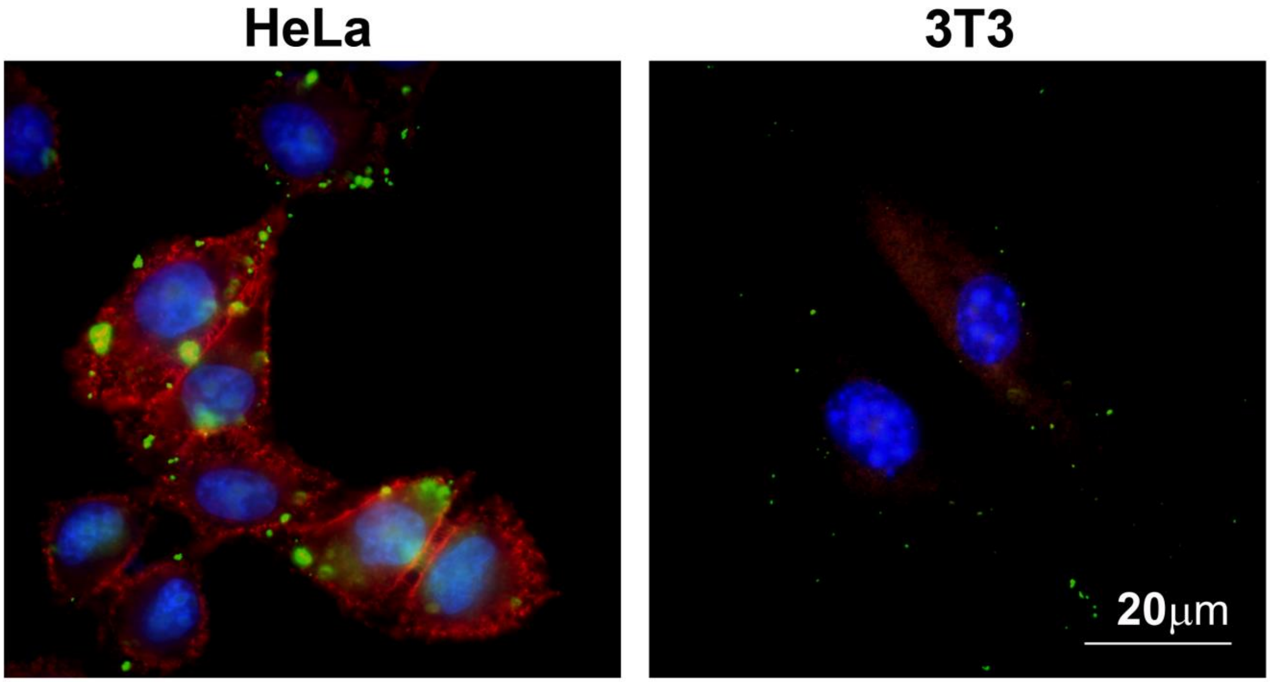

Fig. S3. Fluorescence microscopy images of 3T3 and HeLa cells treated for 4 h at 37°C with FITC labeled MSN-HAs. Cell membranes are immunostained with CD44 antibody (red) and nuclei are stained with Hoechst (blue). Bar: 20 µm.

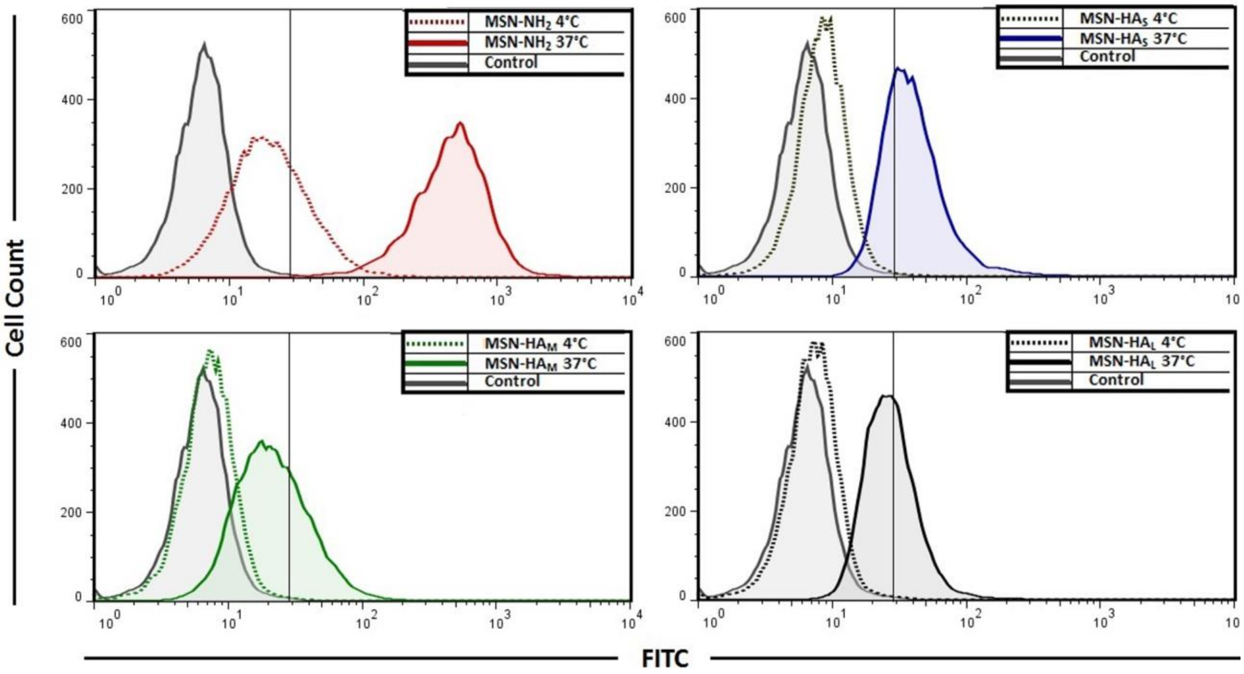

Fig. S4. Flow cytometry analysis on cells treated with FITC labeled MSN for 4h at different temperatures.

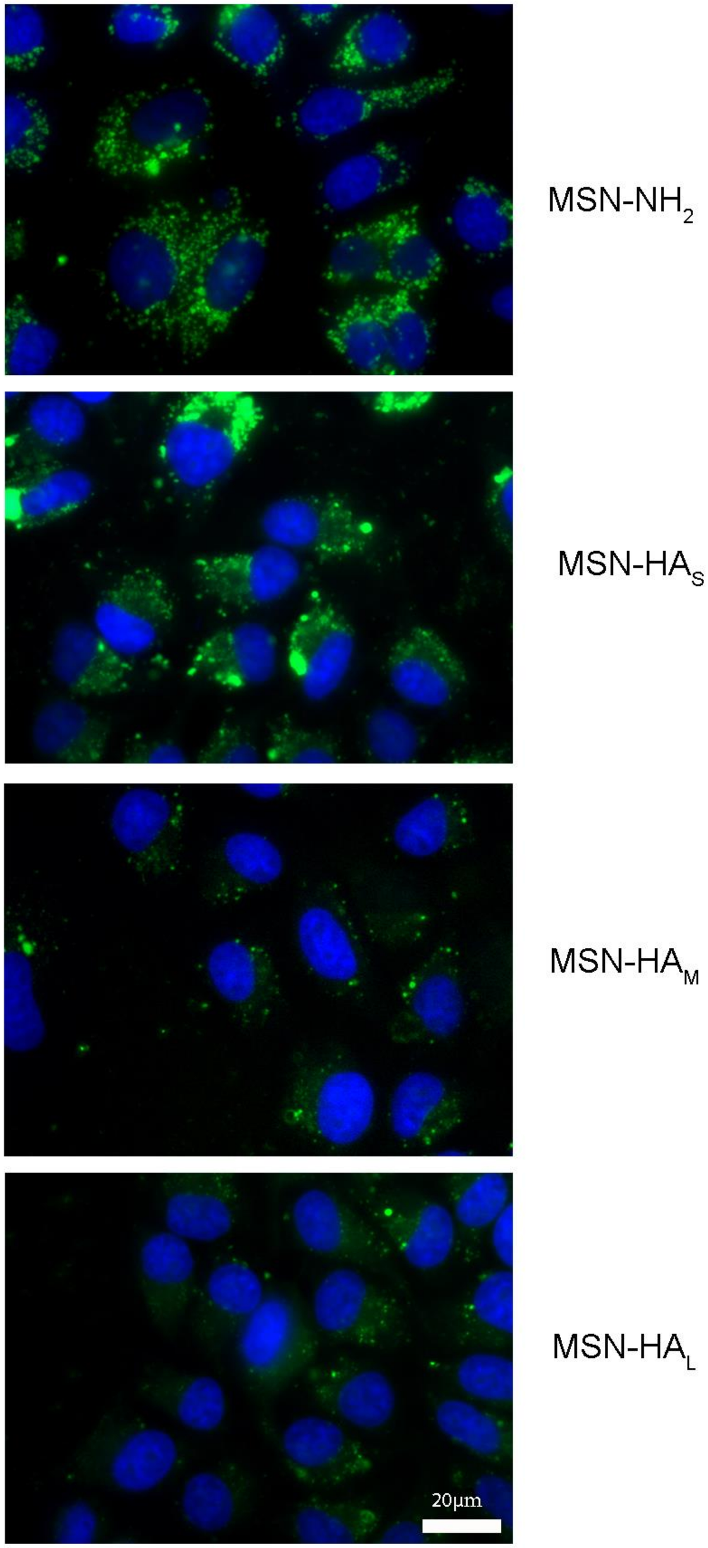

Fig. S5. Internalization of MSNs using fluorescence microscopy of HeLa cells incubated for 24 with 50 µg/mL of FITC-MSNs

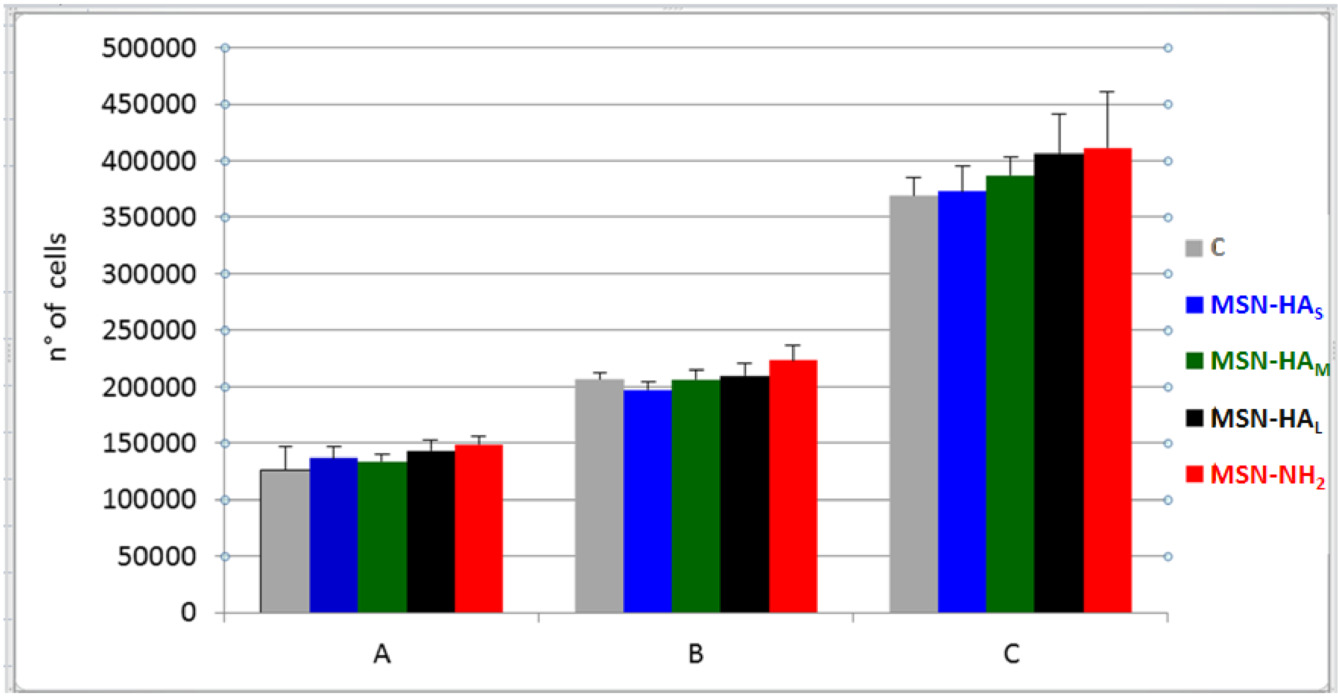

Fig. S6. Effect of MSNs on the proliferation capacity of Hela cell line incubated for 24 h, and then left in contact with the culture medium for different times. Cell count: (A) number of cells immediately after nanoparticles removal (t = 24 h); (B) number of cells 24 h after nanoparticle removal (t = 24 h + 24 h); (C) number of cells 48 h after nanoparticles removal (t = 24 h + 48 h) according to protocol.